Ministry of Energy and Water Resources
Geological Survey of Israel

Multi-site late Quaternary paleoseismology in the Dead Sea transform region: Independent recording by lake and cave sediments

Elisa Joy Kagan

This thesis was submitted for the degree "Doctor of Philosophy" to the senate of the Hebrew University of Jerusalem, Israel.

The study was carried out under the supervision of:
Prof. Amotz Agnon, The Hebrew University of Jerusalem, Jerusalem.
Prof. Mordechai Stein,The Geological Survey of Israel, Jerusalem.
Dr. Miryam Bar-Matthews, The Geological Survey of Israel, Jerusalem.

Report GSI/17/2012 Jerusalem, November 2012

Abstract

Paleoseismic data provide a long-term record of earthquake activity, crucial for hazard assessment. However, the establishment of precise and high-resolution chronology of paleo-earthquakes as well as an understanding of the behavior of earthquake markers (seismites) is essential to the establishment of a reliable paleoseismic record. Multi-archive and spatially extensive paleoseismic studies can help locate earthquake sources and assess magnitudes, compensate for hiatuses in single archives, highlight site effects, and emphasize distinctions in the "recording" of seismic events in various media.

This thesis comprises several investigations into the paleoseismic history of the Dead Sea rift and its vicinity during the late Quaternary. The geological archives embodying the earthquake deformations that were studied are the lacustrine sediment outcrops of the paleo-Dead Sea and its predecessor, Lake Lisan, and the Soreq and Har-Tuv karst caves and their speleothems. Addressing challenges posed in a region of fast and variegated developments of paleo-earthquake studies, the thesis is a contribution to the paleoseismic methodology.

In previous studies, the Holocene Ze'elim Formation and the last glacial Lisan Formation lake archives in Israel have proven to be sensitive long-term earthquake recorders, have produced a 70 kyr archive of earthquake-induced deformed layers, and have shown patterns of recurrence. Here, a comprehensive multi-site paleoseismic archive of the late Holocene Dead Sea basin (past 2500 years) is established by constructing two age-depth chronological models of two sedimentary sections exposed at the retreating shores of the modern Dead Sea. Two new paleoseismic sites studied are the Ein Feshkha Nature Reserve outcrop located at the northern part of the basin and close to an active underwater transverse fault, and the east Ze'elim Gully outcrop at the southern part of the basin. Age-depth regression models are calculated for these sections based on atmospheric radiocarbon ages of short-lived organic debris calibrated with a Bayesian model. The uncertainties on individual model ages are smaller than 100 years. Each depth (and each seismite) has an age extrapolated from the model. The new chronological records are compared to a published laminae-counting study of the Ein Gedi core located at the central Dead Sea basin. The Ein Feshkha outcrop, although being truncated ~500 a, yields the largest number of seismites (n = 52), while lower numbers of seismites are recovered from the Ze'elim outcrop and Ein Gedi core (n = 15 and 36, respectively). The seismites show no strong dependence on the limnological-sedimentological conditions in the particular sampling sites (they coappear in both shallow and deep water environments and in different sedimentary facies). During time intervals when the chronologies are comparable it appears that the number of seismites is significantly larger in the northern part of the basin (Ein Gedi and Ein Feshkha). Seismic quiescence intervals are apparent at all three sites from 2nd–4th century A.D. and at 500–150 B.C. at Ze'elim and Ein Gedi. Several synchronous seismites appear in all sections (termed here the intra basin seismites, IBS): 1927, 1293, 1202/1212, 749, 551, 419, and 33 A.D. and 31 and mid-2nd century B.C. The recurrence time of the IBS from the 2nd century B.C. to the 14th century A.D. is ~200 years, compared with <100 years for all earthquakes at the Ein Gedi or Ein Feshkha sites. On a diagram of epicentral distance versus magnitude, historic earthquakes that are correlated with IBS plot in a field of high local intensity. The farther and stronger IBS earthquakes require lower local intensities to be recorded.

The dates of the Dead Sea lacustrine seismites are calculated using the Bayesian statistical method of the OxCal v 4.1 program and age-depth models are constructed for a set of

accelerator mass spectrometry (AMS) radiocarbon ages of organic debris from the abovementioned sites. The Ein Feshkha model is tested for a case where no prior earthquake information is applied and for a case where there is incorporation of known ages of four prominent historic earthquakes as chronological anchor points along the section. While the anchor-based model provided a tightly constrained age-depth regression, the "nonanchored" model still produces a correlation where most of the 68% or 95% age ranges of the 52 seismites can be correlated to historic earthquakes. Since the unanchored model is almost as tighltly constrained and requires less assumptions than the anchored one, it is the prefered choice. This presents us with the opportunity for high-resolution paleoseismic analysis and comparison between various sites.

Speleothem seismites are investigated in this study at the Soreq Cave and the nearby Har-Tuv Cave, in the Jerusalem vicinity. Damaged cave deposits at these caves include collapsed stalactites, fallen stalagmites, standing but severed stalagmites, collapsed bedrock ceilings, cracked speleothems, and a collapsed soil mound. When dripping water and calcite precipitation continue after seismic events, the damaged deposits (pre-event age) are covered by regrowth (post-event age). The pre and post event carbonate is then dated by the U-Th MC-ICP-MS method. The Soreq-Har-Tuv caves provide a 400 ka earthquake history from forty-four samples in the field, which documented more than fifty-five seismites. For the past 200 millennia these collapses are grouped into 26 *events*, interpreted to be earthquakes. In all, there are 21 events that are defined by more than one collapse or by both pre and post ages. Seven quiescence intervals are discernible, with no pre or post collapse ages during that time. The 26 events from 200 ka to present lead to a mean recurrence interval of approximately 6.8 ky, with an aperiodicity value of 0.7 (aperiodicity is defined as the standard deviation/mean), indicative of quasi-periodic behavior. If only the 21 events dated by more than one date are used, the RI increases to 7.8-8.6 ky, and the aperiodicity values change slightly to 0.5-0.6 with the quasi-periodic behavior persisting. This RI is much longer than that interpreted from the lake archive earthquake history due to filtering out of the smaller earthquakes in the cave environment and the somewhat more removed location. Seismite ages appear to be spatially distributed randomly throughout the cave. Some of the different types of cave damage occurred at specific times in the past 200 millennia. These two observations support seismogenic origin of damage.

The Holocene portion of the Soreq-Har-Tuv speleoseismite archive, together with that of a cave in the Carmel Mountains (Denya Cave) is used for an analysis of the interaction between two sectors of the Dead Sea transform (DST) and its side branch - the Carmel fault (CF). The two sectors considered are the Dead Sea basin (DSB) and the Jordan Valley (JV). The two archive sites are potentially affected by the same fault system, yet separated by 110 km. A very strong seismo-tectonic event affecting the entire region would give the same ages (to within dating uncertainty) at both archives. Separate, local events from either sector would record separately in either archive. Nine pre-historical Holocene speleoseismites were identified in Denya Cave, interpreted to represent two seismic events (4.8±0.8 ka and 10.4±0.7 ka). For the same time period six speleoseismites were identified at the Judean Hills caves (Soreq-Har-Tuv caves) and cluster to two events (~5 ka, 8.6 ka). Together with other paleoseismic studies from the CF and JV regions, temporal correlation between cave archives implies coupling between the main fault sectors (DSB, JV), and CF branch. Specifically, an event at ~5 ka, is well-recorded at both the Haifa and Judean Hills caves. However, the penultimate Haifa cave event at ~10.5 ka seems to be limited to the northern region. Using a simplified model, we list possible earthquake scenarios in order to better understand the

tectonic regime of the region. Uncertainties may prevent differentiation of close events, but quiescent intervals and clustered earthquake events are resolved. The quiescent intervals identified for the largest events in the seismic cycle are between ~10 ka and ~5 ka in the cave in Haifa, and from ~5 ka to the historical period in the Judean Hills.

The multi-site approach taken in this work benefits from analysis and comparison of paleoseismic archives from various periods, regions, and media. The comparison of three Holocene lacustrine paleoseismic sites allowed interpretation of earthquake sources (and consequently magnitudes for known historic events) for some of the seismites. In addition, the multi-site approach introduced the concept of Intra-Basin Seismites (IBS) developed and provided a recurrence time for these out of the ordinary events. In the cave speleoseismite environment, the Carmel-Soreq comparison is another angle of the multi-site approach. In this case the two cave systems allowed an analysis of fault coupling. The different media (cave deposits and lake sediments) have thus far only been compared for the Late-Holocene period. During this time period there are two Soreq Cave seismites and tens of Ze'elim Formation disturbed layers. This is in accord with the hypothesis here that the lake sediment recorder is more sensitive than the cave sediment recorder to earthquake shaking, and therefore records smaller events.

This multi-site and diverse-environment study is a contribution towards the comparison of the long-term dated cave and lake paleoseismic archives. This comparison will resolve mega-earthquakes that affect the entire DSB area and traverse lithological confines and is currently underway. The new Lisan chronologies (in progress) will allow dating of all Lisan seismites, and this, together with the Soreq-Har-Tuv seismite event chronology, will achieve the multi-archive union. This study demonstrates that a painstaking effort is still needed for unraveling the seismic history of the Dead Sea basin. The results also indicate that such a study will likely be highly rewarding.

Acknowledgements

To Mira, Moti and Amotz, my advisors, I extend the warmest gratitude for teaching me so much about science and the science world. The three of you, each in your own way, have given me the precious tools for scientific, and especially geological, thinking. This guidance always came together with support, encouragement, time, patience, at times a shove in the right direction, and at times the freedom to pursue the path of my choice. Also, thank you for fascinating and enjoyable times in the field.

I would like to thank Avner Ayalon for his continued support and his help in anything I needed, especially with the bureaucratic complexities of the Geological Survey of Israel (GSI), for his encouragement at all stages, and for his scientific guidance regarding the petrography of the seismites. I appreciate the ongoing collaboration with Adi Torfstein in the field, in the lab, and throughout cyberspace, and thank him for his MATLAB scripts (including counsel) for the U-Th calculations.

I would like to thank Rivka Amit for use of her microscope (including her office) and for advice and encouragement throughout my work. I profited from valuable discussions and excursions with Revital Bookman, Anton Vaks, and Nicolas Waldmann. I thank Yael Braun for successful scientific collaboration and mutual compassion over coffee and beer. I appreciate the rewarding scientific collaboration with Frank Neumann and reminisce about those 3 a.m. wake-up calls for sweltering August field work. Benny Begin is thanked for his interest and encouragement in this work.

The GSI is thanked for providing me with the lab and fieldwork infrastructure for carrying out many aspects of this work. Irena Segal and Nataliya Teplyakov from the Geochemistry Department at the GSI are thanked for their enduring guidance, assistance, and patience with numerous laboratory procedures. Shlomo Ashkenazi, Eli Ram, Ya'akov Mizrachi, Anton Vaks, Dan Asael, Keren Sarusi, and Daniel Palhan provided assistance and company in the field and in various aspects of lab work. Special thanks to those of you who performed the arduous task of manually drilling cores into the harder-than-they-look cave deposits. Many other GSI technicians aided in field work at various stages of this work. Shmulik Zintronblat, Ira Peer, Ana Feigin, Masha Kahalani, Ora Shapira and the rest of the GSI administrative staff are thanked for their help. I thank Bat-Sheva Cohen, Chana Netzer-Cohen, and Nili Almog for their assistance and advice with graphical work and for a pleasant place to be when at the GSI (and always a little snack).

I would like to thank all the teachers at the Institute of Earth Sciences (HUJI) throughout the years who introduced me to, taught me about, and made me love geology. Shoshi Busheri, Magi Perkin, Batya Moshe, Dikla Hanuka, and Yossi Sherer are thanked warmly for their help in everything!

Thanks are due to my dissertation committee members – Shmulik Marco and Ari Matmon- and to the reviewers of the published papers, for their helpful and important remarks. Elisabetta Boaretto is thanked for her assistance with the radiocarbon samples. Christopher Bronk Ramsey is appreciated for his developing of the OxCal Radiocarbon calibration and analysis program and with his immediate and ongoing advice on the matter. Tina Niemi is thanked for a very thorough review of the chapter 3.1 manuscript. Oded Katz is appreciated for his thorough review of the chapter 3.3 manuscript. The staff members at the Avshalom Nature Reserve are thanked for their assistance and the Israel Nature and Parks Authority is appreciated for their permission to work in the caves.

I appreciate and remember Eli Tannenbaum (ז"ל) for introducing my advisors and me to the asphalt phenomena within the Lisan breccias.

In addition to the people mentioned above, my time at work was made more pleasurable by being with Keren K, Ronit K, Orly O, Yael K, Ornit M, Dan A, Josh S, Anton V, and others.

This work was funded in part by a grant from the Ministry of National Infrastructure of Israel (20-17-02), from the Israel Science Foundation (1006/2004) and from the German-Israel Foundation (GIF) for science and development (I-805.221.8/2003).

I wish to express my love and appreciation to my mother, my father, my brother, my bubby, my step-parents, my in-law family, and my close friends (like family) who helped, loved, encouraged, endured, cooked, picked-up kids, and proofread.

To my children, Aviv, Yotam, and Nadav, who were born during the course of this work, I love you and thank you for the laughs, the cries, and the perspective. And finally and most importantly Dani, for being there, lovingly, and unconditionally, and for understanding and believing that one day this project will end.

Table of Contents

List of Figures

List of Tables

List of Appendices

1. Introduction

"It's snowing still," said Eeyore gloomily. "So it is." "And freezing." "Is it?" "Yes," said Eeyore. "However," he said, brightening up a little, "we haven't had an earthquake lately.

A.A. Milne (1882-1956)

1.1 Overview

The nascent discipline of paleoseismology incorporates geological evidence of earthquakes from two facets of the earthquake phenomenon: the earthquake source record preserved in the fault zone ("on-fault") and the geological evidence of strong ground motion ("off-fault") [*McCalpin*, 1996; *Yeats et al.*, 1997]. Off-fault studies investigate the consequences of ground shaking, such as liquefied sands, landslides, slumps [*Obermeier et al.*, 2005], rockfalls and speleothem damage inside caves [*Gilli et al.*, 1999; *Kagan et al.*, 2005; *Matmon et al.*, 2005], tsunami and seiche induced deformation and deposits [*Cita et al.*, 1996; *Goodman-Tchernov et al.*, 2009; *Kastens and Cita*, 1981; *Reinhardt et al.*, 2006], lacustrine seiche waves that produce slump deposits [*Chapron et al.*, 1999; *Siegenthaler et al.*, 1987], and brecciation and resuspension of previously laminated lacustrine sediments [*Agnon et al.*, 2006; *Marco et al.*, 1996]. Multi-archive and spatially extensive paleoseismic studies can create long-term records, compensate for hiatuses in single records, highlight site effects, and emphasize distinctions in the "recording" of seismic events in various media.

The lacustrine and cave records are valuable earthquake recorders and are relatively well-preserved from erosion. The Dead Sea lake with its paleo-lake sediments has proven to be a sensitive long-term earthquake recorder, and has recorded 70 kyr of earthquakes, [*Agnon et al.*, 2006; *Marco et al.*, 1996]. The numerous outcrops of paleo-Dead Sea sediments (Figure 1.1) show different records, with different numbers of seismites and varying thicknesses and appearances. The study of collapses and other disturbances in the Soreq and Har-Tuv caves in central Israel (Fig. 1.1) has yielded a 185 kyr archive of large earthquakes [*Kagan et al.*, 2005]. The various off-fault archives are diverse in their location, sediment type, and probably in their sensitivity to earthquake shaking. These archives chronicle in different ways the same earthquake regime.

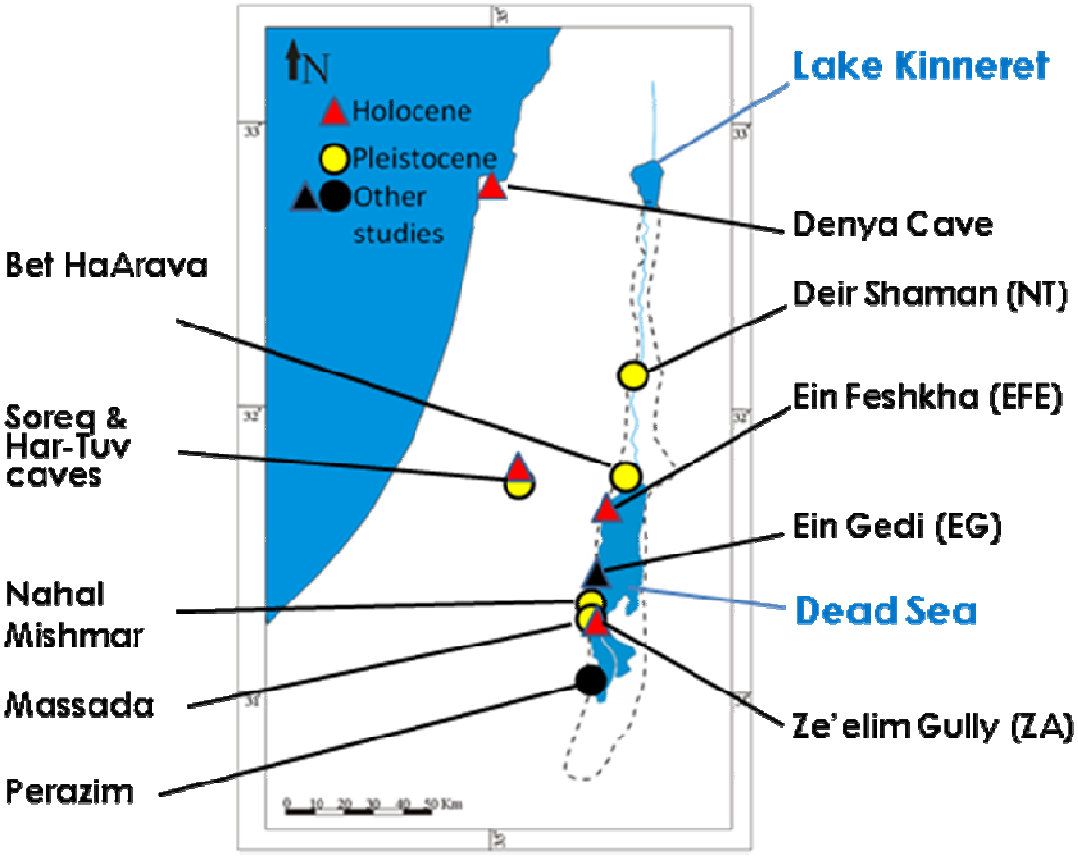

Figure 1.1. Location map of some sites discussed in this work (see text for details).

1.1.1 Lacustrine paleoseismology

The pioneering work of *Marco and Agnon* [1995] and [*Marco et al.*, 1996] on the intraclast breccia layers (termed there "*mixed layers*") in the Pleistocene Lisan Formation created the basis for lacustrine paleoseismic studies in the Dead Sea basin. They found that the intraclast breccias are temporally associated with surface faulting in places, strongly suggesting a genetic relationship between brecciation of the laminated sediment and surface faulting [*Marco and Agnon*, 1995; *Marco and Agnon*, 2005]. They found that secondary normal faults, with up to 2 m throw, caused earthquakes (M>5.5) simultaneously with breccia layer formation adjacent to, as well far away from, the fault scarp. [*Ken-Tor et al.*, 2001] and later [*Migowski et al.*, 2004] further strengthened this proposal by correlating historic earthquake dates to intraclast breccias and other seismites from the Late Holocene Ze'elim Formation, also in the Dead Sea basin. *Agnon et al.* [2006] define field criteria for the recognition of intraclast breccias, focusing on features diagnostic of a seismic origin. The field criteria stem from understanding of the mechanisms of breccia formation, which include ground acceleration, shearing, liquefaction, water escape, fluidization, and resuspension of the originally laminated mud. The undisturbed bedding in the Lisan Formation show dips of less than 1^0, which implies stable conditions [*Alsop and Marco*, 2011], supporting the hypothesis that folds and breccias were triggered by earthquake vibrations.

Studies in other locations in the area on liquefied sands and convoluted beds associated with earthquakes include *Bowman et al.* [2000], *Enzel et al.* [2000], and *Gluck* [2001]. *Levi et al.* [2006] used anisotropy of magnetic susceptibility to analyze the mechanism of formation of clastic dykes that cross-cut the Lisan sediments. Their results indicate that the dykes were emplaced by injection due to seismically triggered fluidization. *Heifetz et al.* [2005] assert that the seismites are probably the result of turbulence in the soft sediment, similar to Kelvin–Helmholtz Instability (KHI) mechanism, triggered by earthquake shaking, and that compaction profile, ground acceleration, and wave period all determine the threshold for onset of deformation. *Alsop and Marco* [2011] investigated soft-sediment slumps in the Lisan Formation and were able to recognize various generations of slumping, including overprinting on older slumps.

The recurrence pattern of earthquakes in the region was first extracted from the lake sediments by *Eli-Isa and Mustafa* [1986] and *Marco et al.* (1996) for the period of 70-20 ka and then by *Ken-Tor et al.* (2001) for the past 2000 years and *Migowski et al.* (2004) for the past 6000 years. Each one of these studies derived data from up to three different locations but the presented timetable of earthquakes was always derived from one location, the most complete and dated record. Comparison of the seismite recurrence patterns in lacustrine sections of various sites, which were deposited during the same time intervals, shows differences [*Begin et al.*, 2005; *Marco et al.*, 1996; *Migowski et al.*, 2004]. These differences must be scrutinized.

Marco et al. [1996]'s 50,000-year earthquake archive is based on three sites from the Lisan Formation.: PZ1 and PZ2 from the Perazim Valley and M1 from the Massada Plain. *Marco et al.* [1996], using preliminary U-Th chronology by Alexandra Schramm, interpreted the Perazim Valley seismite record to show clustering of 10 kyr periods. Based on the revised chronology of the PZ1 section [*Haase-Schramm et al.*, 2004], *Agnon et al.* [2006] divided the archive to six periods (2-13 kyr long), each with relatively uniform recurrence intervals (250 to >5000 yr).

In addition, the top of the Massada section has been dated by varve counting anchored by ^{14}C ages [*Prasad et al.*, 2004] while the lower section has a small number of published U-Th ages [*Bartov*, 2004]. The correlation between the Massada and the Perazim sections was tentative and mainly based on stratigraphic considerations [*Begin et al.*, 2005; *Marco*, 1996]. The new dating of these sections and others (Mishmar, Bet Ha'Arava, and Deir Shaman) (Torfstein et al., in press) will allow for better correlation and analysis of the temporal and spatial patterns of the seismites.

The Holocene paleoseismic archive has been studied in the Ze'elim Gully [*Bowman et al.*, 2001; *Ken-Tor et al.*, 2001] and Darga Gully [*Enzel et al.*, 2000] outcrops and in several boreholes drilled at Ein Gedi and Ein Feshkha [*Migowski*, 2001; *Migowski et al.*, 2004]. In the outcrops, eight deformed layers identified as seismites were correlated to historic earthquakes. Historic earthquakes "missing" from the outcrop records were attributed to hiatuses in the sedimentary record at the site [*Agnon et al.*, 2006; *Ken-Tor et al.*, 2001]. Migowski et al. (2004) found in the continuous Ein Gedi core, which was drilled in the more lacustrine environment of the lake, a more continuous paleoseismic archive containing the "missing" earthquakes from the Ze'elim section (Fig.1.2). This finding provided very strong support for the interpretation of the breccia layers as seismites. On the other hand, a core, being only a

few centimeters thick, is inherently spatially limited. Local spatial variations, important in understanding earthquake effects on sediments, are overlooked in cores.

Most studies of brecciated layers have concentrated on chronology and mechanisms of formation. Nonetheless the factors controlling seismite formation are numerous and as of yet difficult to specify. These factors, in addition to earthquake magnitude and location with respect to earthquake source, may include: water depth at site (mass of water above sediment), lithology, sediment compaction, sedimentation rate, gradient of lake bottom, and position with respect to basin structure. These factors can control the probability of seismite formation, and the appearance in the geological record (thickness and type: e.g. breccia, homogenite, or fold).

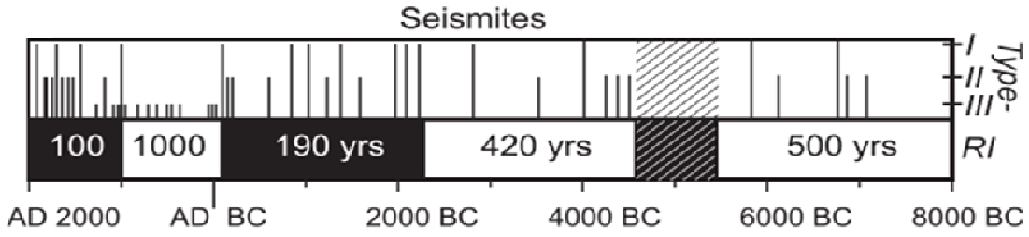

Figure 1.2. After *Migowski et al.*, 2004. Recurrence intervals of Late Holocene earthquakes based on Ein Gedi core seismites, types refer to seismite thicknesses (Type III are microscopic).

Begin et al. [2005; 2005] made a first effort to extract the strong earthquakes from the Lisan lacustrine record, using the data from the Perazim Valley (PZ1 and PZ2) sections. Their idea was that large earthquakes would induce limnological changes in the lake due to water waves that would lead to deposition of gypsum or detrital layers, immediately above the breccia layers. As well, they suggest that the thicker the brecciated bed the higher the probability that it is overlain by laminated gypsum and detritus or by detritus. *Begin et al.* [2005] also argue that site effects due to basin topography may have caused seismite thickness differences between the Massada and Perazim sections. The connection of breccia thickness to earthquake intensity is tentative and a better understanding of the formation mechanism is required. A detailed comparison of various dated Lisan sections from different depths in the paleo-basin, embarked on in this work, may shed light on this question.

Location of a paleoseismic site, with respect to earthquake source, has been considered with regard to seismite formation [*Migowski et al*., 2004; *Agnon et al*., 2006]. Topics such as water depth, lithology, degree of compaction, lake bottom gradient have not yet been studied with regard to seismite formation. Comparison of seismite records from various environments could potentially produce criteria for the identification of factors controlling seismite characteristics.

Several issues remain open with regard to lake seismites:

1. What are the temporal and spatial patterns of seismite appearance along the DST and what are the inferences for earthquake source location and recurrence?

2. Can paleo-mega-earthquakes be identified by tracing specific seismites along the DST and/or by correlating them to seismites outside the rift?

3. How do water depth, climatic conditions, lithology, degree of sediment compaction, basin topography, and proximity to epicenter effect seismite formation and pattern. (e.g. Ein Feshkha (lacustrine environment), Ze'elim (lacustrine-fluvial), Ein Gedi core (deep lacustrine))?

1.2 *Speleothem paleoseismology*

Sub-recent Quaternary formations are not always available in all places where large earthquakes have struck. Among the late Quaternary archives coral reefs were successfully used for the dating and reconstruction of paleo-earthquakes, mainly in coastal environments [*Edwards et al.*, 1988; *Grant et al.*, 1999; *Shaked et al.*, 2004; *Zachariasen et al.*, 1999]. Cave deposits (e.g. speleothems) have been considered as a new potential target for late Quaternary paleoseismic studies. Similar to corals the speleothems can provide precise U-Th ages in high-resolution sequences [e.g. *Kagan et al*., 2005]. Caves provide a closed environment protected from most erosive activity. The speleothem deposits have laminar growth patterns and therefore have the potential to apply karst caves and the deposits therein as a valuable recorder and preserver of delicate earthquakes evidence. Caves struck by earthquakes can undergo various types of damage (Figure 3.1.3) and reveal datable evidence. Such evidence may include collapsed ceiling blocks, severed stalagmites, collapsed stalactites, collapsed columns, change in growth axis, cracks and faults in cave walls and on speleothems, and creation or opening and closing of cracks according to their orientation relative to the seismotectonic stress field [*Braun*, 2009; *Delaby*, 2001; *Forti*, 1998; *Forti and Postpischl*, 1980; *Forti and Postpischl*, 1984; *Gilli*, 1999; *Gilli*, 2005; *Gilli et al.*, 1999; *Kagan et al.*, 2005; *Muirwood and King*, 1993; *Uysal et al.*, 2007]. Many of these features can be covered by post-damage regrowth. A modern-day example for caves damaged by tectonic activity is provided by a 1996 M5.2 earthquake in France that caused the collapse of thin stalactites in a cave 10 km from the epicenter [*Gilli et al.*, 1999].

In order to use speleothems as recorders of tectonic events it must be established that their disturbed state is a result of tectonic activity, and not of static load, anthropogenic, climatic, nor any other non-tectonic occurrence. Possible non-seismic damage of speleothems has been investigated by *Gilli* [2004] and *Crispim* [1999]. Investigation into possible climatic sources for cave damage must be carried out before earthquakes can be determined to be the cause [*Kempe*, 2004; *Pons-Branchu et al.*, 2004]. *Kempe* (2004) found ice movement to be a probable cause for speleothem damage in Slovenian caves during glacial periods. In addition the lack of speleothem growth in northern and central Europe during glacial periods prevents possible dating of seismic events to those periods. In the Soreq Cave and most other caves in the area temperatures were too high for icing during glacial periods [*Ayalon et al.*, 2004; *Bar-Matthews et al.*, 2003; *McGarry et al.*, 2004] and therefore ice movement can be ruled out as the cause for damage. However, exceptionally rainy periods could potentially cause massive soil movement into cracks [*Bar-Matthews et al.*, 1997] or perhaps in other ways cause speleothem damage. Possible correlation of damage events to drier periods was preliminarily negated by *Kagan* [2002]. During the past ~200 ka the Soreq speleothem depositional record is continuous with seemingly no periods of total drying [*Bar-Matthews et al.*, 2003]. Areas of

dripping migrate *within* the cave, and currently some areas are dry while others are wet. Morphological assessment, as part of the current study, shows that no speleothems have fallen due to extreme drying up and all broken speleothems in the cave have angular breaks.

The seismic response at different depths below ground varies greatly and may produce amplifications of up to a factor of six or attenuation, or it may show no distinct change from surface ground motions [*Bard and Tucker*, 1985; *Kanai et al.*, 1966]. No studies as of yet have been able to determine the actual intensity experienced in a specific cave during an earthquake. Direct magnitude assessment is therefore difficult, although this caveat may ultimately be alleviated by careful comparison with independent paleoseismic records, by real-time or immediately following earthquake observations, and by experimental studies.

Kagan et al. [2005] roughly estimated the magnitudes necessary to cause the damage found in the Soreq and Har-Tuv caves to be from an M7.5–8 event at the Dead Sea transform. The Soreq and Har-Tuv caves, located at a minimum distance of 40 km from the Dead Sea Transform, provide an off-fault archive. This relatively large distance from the active fault may act as a filter for smaller earthquakes, allowing only larger ones to be recorded in the cave seismite record. Previously estimated recurrence time for earthquakes large enough to cause significant damage in the study caves was found to be ~10 kyr [*Kagan et al.*, 2005; *Kagan*, 2002].

In a complimentary speleoseismite study by Braun [2009], the paleoseismology of the Carmel fault zone was studied by investigating seismites in the Denya Cave (Haifa). Thirty-two seismites from the Denya Cave were dated by U-Th mass spectrometry (MC-ICP-MS at the GSI). An isochron method was employed to correct for detrital Th. The isochron calculated ages obtained for groups of speleo-seismite samples indicated that each group records a seismic event. Nine age clusters were determined for speleoseismites from the Denya Cave, indicating the following ages of seismic events: 4.8±0.8 ka; 10.4±0.69 ka; 20.8±3.0 ka; 29.1±3.3; 38.0±2.7 ka; 57.9±5.2ka; 137±29 ka; 147.6±5.4 ka and 160±45 ka. *Braun* [2009] finds correlative paleoseismic evidence from other studies in the region. This study exemplifies the importance of the speleoseismite technique since the Carmel fault zone is understudied due to sparse exposed evidence.

Kagan [2002] and *Kagan et al.* [2005] are the first works of their kind in Israel and added new knowledge about the earthquake history of the area and also an understanding of the feasibility and difficulties of this paleoseismic technique (Figure 1.3). However, this archive was based on dates obtained by α-counting and stable isotope wiggle-matching, while currently a high resolution MC-ICP-MS mass spectrometer is available at the GSI for more precise ages on smaller sample sizes. This can provide earthquake ages with much smaller errors than previously reported from cave records. The new mass spectrometric ages can indeed improve the cave archive (see Tables 3.4.1, 3.4.2, 3.4.3), with shifting of some of the published wiggle-matching ages. This can also ease the obstacle existing in many paleoseismic archives of more than one earthquake being grouped as one event. The MC-ICP-MS method requires smaller sample size and therefore enables the use of small samples, previously not dateable. For example, soda straw stalactites can now be dated, enlarging the assemblage of phenomena accessible for studying. Also, the smaller sample size allows higher resolution sampling of the damage contact (*paleoseismic contact*), without contamination by much older or much younger material. The previous study was restricted to

two years and the number of seismites collected, examined, and dated was limited; not all areas of the cave were sampled. Field sampling and the more precise dating techniques here reveal that there are young events (< 1 ka) recorded in the Soreq cave (Table 3.4.1) which were not found in the previous study. The recurrence interval of 10-14 ky previously published [*Kagan et al., 2005*] does not take these young ages into account.

1.2.1 Comparison of the cave and lake sediment paleoseismic records

Multi-site earthquake histories can cover long time periods and can compensate for hiatuses in single-archive records. *Becker et al.* [2005] compared active faults, lake deposits, slope instabilities, and cave records in an attempt to create a complete paleoseismic record for Switzerland for the last 15,000 years. Historic earthquakes together with synchronous deformation features can be used to calibrate paleoseismic evidence. The large distance (40 km or more) of the Soreq and Har-Tuv caves to the probable source (DST) makes it less sensitive to earthquake deformation than the nearer Lisan and Ze'elim sediments. The two media (hard calcite speleothems versus soft marl lake bottom sediments) are inherently different and will likely react differently to earthquake shaking. A preliminary comparison [*Kagan et al.*, 2007] suggests mega-earthquakes at ~39±1 ka and ~52±2 ka affected both the Judean Hills and numerous sites along the Dead Seas basin, based on comparison of the previously published Lisan [*Marco et al.*, 1996] and Soreq [*Kagan et al.*, 2005] dated archives. These chronologies have subsequently been revised [this study, *Agnon et al.*, 2006; *Haase-Schramm et al.*, 2004; *Stein*, 2011].

Detailed comparison of the speleothem and lacustrine paleoseismic records in Israel can potentially help to: 1) Evaluate whether the cave destructions are related to earthquakes of specific magnitudes; (2) Extend the spatial and temporal history of earthquake activity in the region; (3) Compare earthquake responses and recoding in different media.

Within the scope of this thesis each archive is rigorously investigated and dated, while the cave-lake comparison is preliminary.

1.3 *Study area: Geology, tectonics, seismicity*

The Dead Sea Transform (DST) has a total left-lateral offset of about 105 km since about 18 Ma ago [*Freund et al.*, 1968]. Over 1100 km long, it trends from the spreading centre in the Red Sea to the Taurus collision zone in Turkey. Recent comprehensive geophysical investigations have illuminated the structure of the lithosphere and crust across pure transform and basinal segments (Wadi Araba and Dead Sea, respectively) [*Mechie et al.*, 2009; *ten Brink et al.*, 2006; *Weber et al.*, 2009]. Two GPS campaigns six years apart at seventeen stations straddling Wadi Araba yielded on-going slip rate calculations of 4.9 ± 1.4 mm/yr [*Le Beon et al.*, 2008]. Slip rates calculated by geological and archaeological markers, on varying time scales, yielded slip rates of 1.5-6.3 mm/yr [*Freund et al.*, 1968; *Garfunkel*, 1981; *Ginat et al.*, 1998; *Gomez et al.*, 2003; *Gomez et al.*, 2007; *Haynes et al.*, 2006; *Klinger et al.*, 2000; *Marco et al.*, 2005; *Niemi et al.*, 2001; *Sbeinati et al.*, 2010].

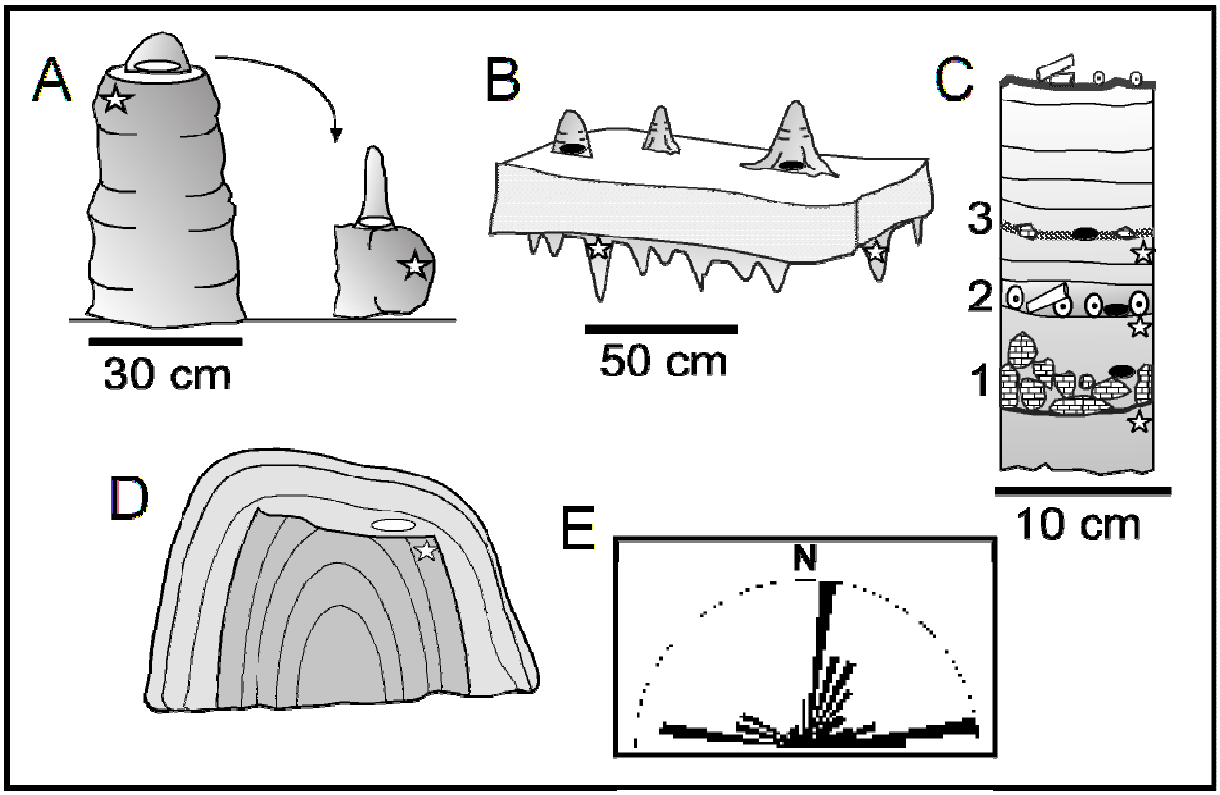

Figure 1.3. Modified after *Kagan et al.* [2005]. Speleothem seismite types in Soreq and Har-Tuv caves. Stars and ellipses mark pre-earthquake and post-earthquake deposits, respectively. Scale bars = 10 cm. A: Stalagmite with severed top and post-seismic regrowth. B: Collapsed ceiling with pre-collapse stalactites (below) and post-collapse stalagmites (above). C: Core in flowstone exposing three horizons representing earthquake events: fallen ceiling pieces (1), macaroni (soda-straw) stalactites (2), and debris layers (3). D: Section of severed stalagmite with post-seismic unconformable regrowth; E: Rose diagram shows orientations of long axes of 65 fallen stalactites and stalagmites cemented on subhorizontal surfaces in Soreq Cave.

Frequent seismic activity along the DST has been detected instrumentally in the last century and recorded historically and archaeologically over the last 4000 years [*Ambraseys*, 2009; *Ambraseys et al.*, 1994; *Ben-Menahem*, 1991; *Ellenblum et al.*, 1998; *Guidoboni and Comastri*, 2005; *Guidoboni et al.*, 1994; *Haynes et al.*, 2006; *Marco et al.*, 2006]. Other faults in the region are much less active and distant to the Dead Sea and are therefore less likely candidates for earthquake sources of the sediment deformation at the Dead Sea. The instrumentally recorded seismicity of the region for the past 111 years is presented in Figure 1.4.

One of the first major earthquakes on the DST to be recorded instrumentally was M6.2 on the 11th of July, 1927 in the northern Dead Sea [*Avni*, 1999]. The location of the event is given by an error uncertainty ellipse in Figure 3.1.1, which is based on best estimate of seismological data [*Shapira et al.*, 1993] and tectonic considerations. On the 11th of February, 2004 a M5.1 earthquake ruptured the northeast corner of the Dead Sea basin, with an aftershock sequence demarcating a transverse fault [*Hofstetter et al.*, 2008; *Lazar et al.*, 2006] (Figure 3.1.1). This fault is termed the Kalia fault [*Lazar et al.,* 2006].

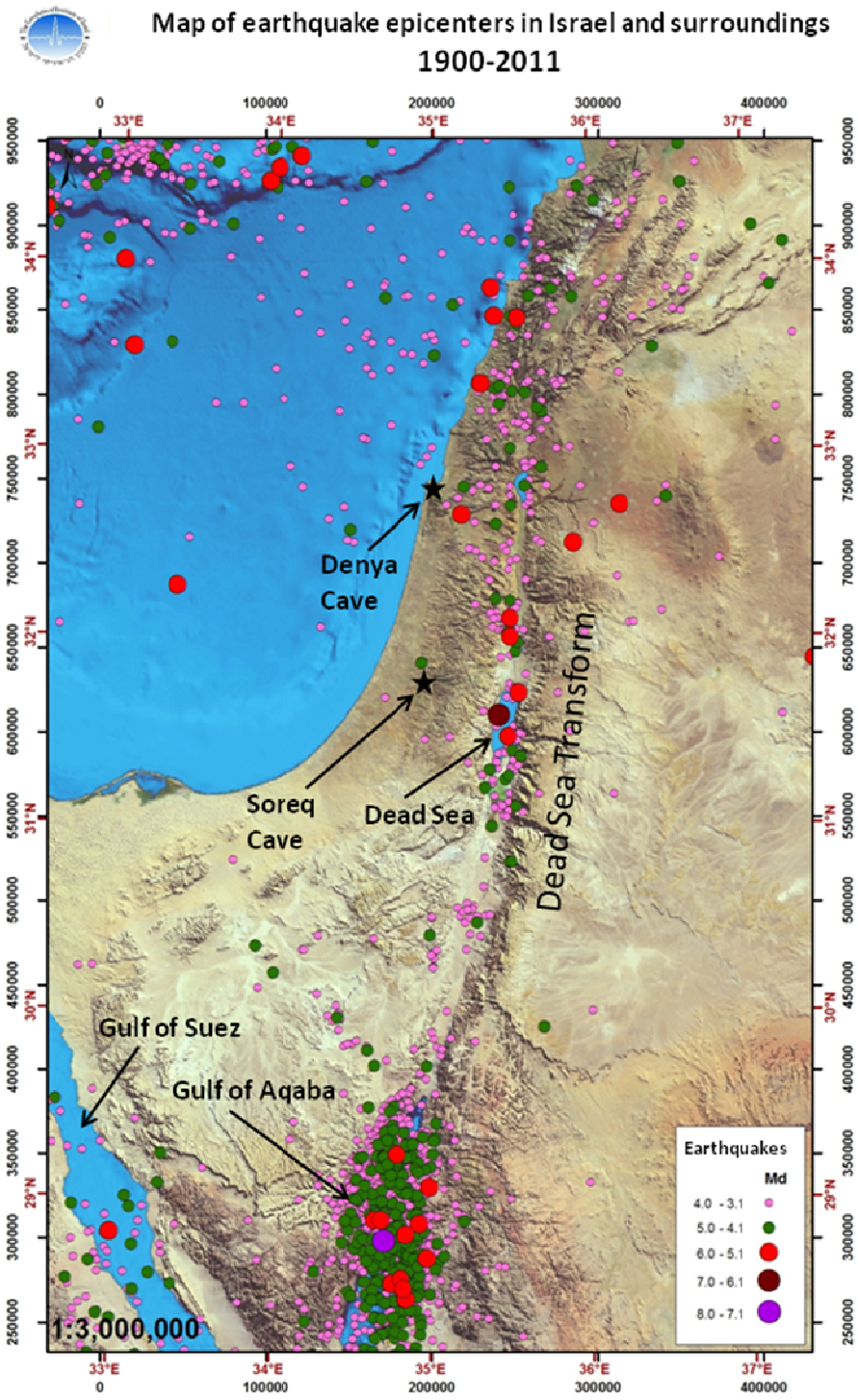

Figure 1.4. Instrumentally recorded earthquakes (M>3) in Israel and surroundings from the past 111 years (provided by the Geophysical Institute of Israel).

The Holocene Dead Sea is a terminal lake filling a deep tectonic depression along the boundary between the Sinai sub-plate and the Arabia plate, the DST. The Dead Sea basin is likely the largest pull-apart basin along the DST and one of the largest pull-apart basins on Earth [*Mechie et al.*, 2009]. Details of the Dead Sea basin fault system are given in Figure 3.1.1.

Although not directly on any of the seismogenic features, the Jerusalem/Judean Hills area has been affected by many earthquakes. Being continuously populated and a major religious and political center throughout historical times, the record of these earthquakes is extensive and well catalogued [*Ambraseys*, 2009; *Amiran et al.*, 1994; *Ben-Menahem*, 1991; *Guidoboni and Comastri*, 2005; *Guidoboni et al.*, 1994], with epicenters being estimated as Dead Sea Rift area, Carmel fault, and even as far as the Cypriotic Arc. At present it is not possible to exclude sources from intraplate events originating in closer faults (Figure 1.4). The Soreq and Har-Tuv area, like Jerusalem, is assumed to be affected by a number of source-faults, as documented in the historical catalogues listed above.

1.4 *Study sites*

1.4.1 Lacustrine study sites

The sediments of the Holocene Dead Sea comprise the Ze'elim Formation [*Yechieli*, 1993] of the Dead Sea Group [*Zak*, 1967]. The sediments represent various depositional environments: river, fan delta, shore, and lake [see detailed description in [*Bookman (Ken-Tor) et al.*, 2004]. The current (2011) lake level is 425 meters below sea level (mbsl), reflecting mainly anthropogenic diversion of freshwater inflow, while during the Holocene the natural (climate controlled) level varied from ~370 mbsl (e.g. ~6000 years ago) to lower than ~ 430 mbsl around 8000 years ago [*Bartov et al.*, 2007; *Bookman (Ken-Tor) et al.*, 2004; *Bookman et al.*, 2006; *Migowski et al.*, 2006]. The drop of the current lake level has caused the formation of deep gullies along the retreating shores. These gullies provided an excellent opportunity to study the late Holocene sedimentary sections in detail. The paleoseismic data in the current study was derived from the outcrops of the Ze'elim Gully and the Ein Feshkha Gully. Another site used for comparison, the Ein Gedi core, drilled at the shore of the Ein Gedi spa, was studied by Migowski et al. (2004, 2006). The Dead Sea straddles the strike-slip duplex fault structure [*Woodcock and Fischer*, 1986]. Three transverse faults have been mapped in the Dead Sea basin (Figure 3.1.1): the Kalia fault, the Ein Gedi fault, and the Amatzyahu fault.

The study site of Ein Feshkha Gully (at the Ein Feshkha Nature Reserve) is located at the north-western shore of the Dead Sea, 60 km north of the Ze'elim Gully site (Figure 3.1.1). Ein Feshkha is an oasis of brackish streams and pools. Nearly exclusively lacustrine sediments are exposed in the Ein Feshkha site by a~6.5 m deep gully (as of 2008). The site is close to the Jordan Valley segment of the DST and may be located on the WNW continuation of the Kalia transverse fault mentioned above.

The Ze'elim Gully (site ZA) is dissected into the Ze'elim plain east of the ancient fortress of Massada (Figure 3.1.1). Currently (as of 2009) the ZA Gully is ~11 m deep (approximately at lake level, to slightly above). The gully exposes a stratigraphic sequence of lacustrine, shore-environment, and fluvial sediments.

1.4.2 Cave study sites

The Soreq and Har-Tuv caves, the vicinity of the Avshalom Nature Reserve, in the Judean Hills, are located 15 km west of Jerusalem and 40 km due west of the Dead Sea Transform (Fig. 1.1). They are carbonate caves, small (<5000 m2), shallow (12–50 m below the surface), developed in well-bedded to massive Upper Cenomanian dolomite, and of phreatic origin [*Frumkin et al.*, 1999]. During the past several hundred thousand years abundant speleothems have been growing in the study caves, and their oxygen and carbon stable isotope records provide a climate record of the late Pleistocene–Holocene times [*Bar-Matthews*, 2012a; b] [*Ayalon et al.*, 2002; *Bar-Matthews et al.*, 1997; 2000; *Bar-Matthews et al.*, 2003]. The caves are strewn with an enormous amount of fallen cave deposits (Figures 3.4.1, 3.4.3). The two caves have nearly identical geological and climatic conditions. The Har-Tuv Cave, less than 1 kilometer from the larger and better preserved Soreq Cave, was only recently uncovered by quarrying activities. Research in two caves offers the prospect of correlation. The Har-Tuv Cave is in an active part of the Har-Tuv Quarry, is not in the nature reserve, and is intended for destruction. The Denya Cave, in the Denya neighborhood of the city of Haifa, is a small carbonate cave with abundant speleothems. The paleoseismological history of this cave was investigated by *Braun* [2009] and is used here for comparison with the Holocene portion of the Soreq-Har-Tuv archive.

1.5 *Research aims*

1.5.1 The major aims of the study

1. Establish the chronological framework of the Ze'elim Formation outcrops at the Ein Feshkha Nature Reserve and the Ze'elim Gully. The main tools used for this purpose are Radiocarbon dating and depositional age modeling using Bayesian statistics.
2. Reconstruct the paleoseismic history of the Late Holocene Ze'elim Formation. The comprehensive chronological record together with the detailed field and laboratory descriptions of the seismites is used to reconstruct the paleoseismic history of the Dead Sea basin area for the past three millennia. This is discussed in the context of the historical catalogues and other paleoseismic archives in the vicinity.
3. Establish the accurate and high-resolution chronological and geological framework of the damages to the Soreq and Har-Tuv caves for the past 200 millennia and reconstruct the far off-fault paleoseismic history. The main tool used for this purpose is mapping of the cave damage and dating by Uranium-Thorium (U-Th) disequilibrium series.
4. Investigate fault coupling between the Dead Sea basin, Jordan Valley, and Carmel Fault sectors of the DST. This was done by comparing the Holocene portion of the Soreq-Har-Tuv caves earthquake archive, the Denya Cave earthquake archive, and other paleoseismic archives in the vicinity.
5. Compare and integrate the paleoseismic information from the lake and cave archives.

1.5.2 Structure of the work

The methodology used in this study is presented in Chapter 2. The results are presented in four chapters. Chapter 3.1 is "**Intrabasin paleoearthquake and quiescence correlation of the late Holocene Dead Sea" [*Kagan et al.*, 2011].** The section comprises the reconstruction of the paleoseismic history of the Late Holocene Ze'elim Formation at two Dead Sea basin outcrop sites and compare their records to the Ein Gedi core archive and to historical catalogues. Chapter 3.2 is "**Paleoearthquakes as anchor points in Bayesian radiocarbon deposition models: a case study from the Dead Sea" [*Kagan et al.*, 2010].** This study presents the methodology of the Bayesian modeling of the radiocarbon data from two Ze'elim Formation paleoseismic sites. It goes on to test the possibility of including known historic earthquakes as anchor points in the age modeling and concludes that the unanchored model is almost as tighltly constrained and requires less assumptions than the anchored one. The procedure developed here opens the way for establishing high-resolution and accurate chronology for paleoearthquake records. Chapter 3.3 is **Dating speleoseismites near the Dead Sea Transform and the Carmel Fault: Clues to coupling of a plate boundary and its branch [*Braun and Kagan* *(equal contribution)* *et al.*, 2011]:** This work summarizes the study of Holocene paleoseismic records from two cave sites on two separate sectors of the DST fault system (one near the Carmel fault, one in the Judean Hills near the Dead Sea basin) and test the interaction between them. Chapter 3.4 presents: **Reconstructing a long-term earthquake history from speleoseismites: Soreq and Har-Tuv caves.** This chapter aims to reconstruct the chronology of the paleoseismic history of the off-fault DST area in the Judean Hills. In Chapter 4, I summarize and conclude the results outlined in the various chapters.

2. Methodology

"We learn geology the morning after the earthquake"
Ralph Waldo Emerson (1803-1882)

This chapter gives an overview aimed at non-specialists of the methods used in this study. More detailed descriptions are given in the relevant sections of Chapter 3.

2.1 Field work and sample preparation

Field work at the Ein Feshkha and Ze'elim sites in the Holocene Ze'elim Formation at the margins of the Dead Sea (Figure 3.1.1) included preparation of columnar sections, photographing, and detailed description of earthquake markers (disturbed layers) within the sedimentary sections. At Ein Feshkha 58 continuous 10 cm-long blocks of wet sediment were extracted from the modern surface plain down to 40 cm below the autumn 2005 water level of the out-flow of the Ein Feshkha spring. This 5.85 m long profile (Figure 3.1.3) was described and photographed in detail in the field and further examined in the laboratory. Samples were wrapped and kept in cold temperatures to prevent rapid and damaging halite crystallization. At the Ze'elim Gully the 10.5 m-long profile was described in detail in the field and some sediment blocks were retrieved from the various lithological units (Figure 3.1.4). In addition, organic debris specimens (typically short lived leaves or twigs), found in the two outcrops, were sampled for radiocarbon dating. Samples were opened in the laboratory for more detailed reexamination of lithology and seismites and for additional sampling for dating and other analyses.

Field work in the cave environment included mapping and abundant sampling of damage cave deposits (seismites) (Figure 2.1). Speleothem seismite samples were collected in the Soreq and Har-Tuv caves by hammer and by core driller (2 inch diameter) while striving for spatial randomness of sampling sites under the esthetic constraints of Nature preservation. Samples were taken on the basis of field observations of collapses, breakages, and fissures. The drilling positions were chosen to incorporate the paleoseismic contact and both the pre-seismic and post-seismic material. After sawing at the GSI and visual examination, the contact was marked. Sub-samples for dating were drilled adjacent to the contact, using 0.8-4 mm diameter drill bits, at the GSI. The position of the contact in seven seismites was examined under polarizing microscope.

2.2 Petrography

Petrography of speleothems can give insight into growth patterns, hiatuses, soil entry into caves, growth rate, climate [*Ayalon et al.*, 1999; *Bar-Matthews et al.*, 1991; *Boch et al.*, 2009] and earthquakes (this study). Speleothems were sawed parallel to the growth axis in order to expose their growth laminae and paleoseismic contact (contact between pre-damage and post-damage material). Thin sections of some of the speleothem seismites were prepared at the Geological Survey of Israel (GSI). The paleoseismic contact and the laminae on either side of it were studied using a polarizing microscope.

Samples of Holocene lake sediment seismites were dehydrated, hardened, and then mounted onto thin section at GeoForschungsZentrum (GFZ), Potsdam. The thin sections were then studied under a polarizing microscope mainly to investigate the composition of the "homogenite-type" layer and to verify that this observed phenomenon is actually a micro-breccia.

2.3 *Radiocarbon dating and modeling*

The chronologies of the Ein Feshkha and Ze'elim sections were constructed by radiocarbon dating of organic debris (mainly small pieces of wood and twigs) brought to the lake by floods. Nine samples from EFE and twelve samples from ZA2 were prepared for radiocarbon dating at the Radiocarbon laboratory, Weizmann Institute, Rehovot, Israel. The samples were then measured by accelerator mass spectrometry (AMS) or liquid scintillation counting (LSC) at the NSF-radiocarbon facility in Arizona. Four additional organic debris samples from EFE were taken from a core drilled a mere few meters away, on the cliff bounding the gully, and were analyzed at the AMS facility in Kiel. Dating of these additional four samples and core correlation with the outcrop was in conjunction with Markus Schwab at GFZ-Potsdam. Radiocarbon ages are reported in conventional radiocarbon years (before present =1950) in accordance with international convention [*Stuiver and Polach*, 1977]. Calibrated ages (= cal BP) were calculated by applying the INTCAL04 calibration scheme of [*Reimer et al.*, 2004] by means of the OxCal v4.1 program of [*Bronk Ramsey*, 1995; 2001; *Bronk Ramsey*, 2008; *Ramsey*, 2008]. Age-depth models and seismite chronologies were also constructed with the help of OxCal (v4.1) [*Bronk Ramsey*, 1995; 2001; *Bronk Ramsey*, 2008; *Ramsey*, 2008].

2.4 *U-Th dating*

The speleothem calcite was dated by the U-Th disequilibrium technique. Aliquots of calcite powder were obtained in the laboratory from the field samples by precise drilling using a 0.8-4 mm diameter drill. The amount of material needed depends on the uranium concentration. Normally for Soreq Cave speleothems ([U]≈0.5 ppm) ~0.2-1 g was dissolved in 7N HNO_3 and thereafter spiked with a ^{236}U-^{229}Th spike. The U and Th of the carbonate fraction of the speleothems were chemically separated using chromatography and then measured by a Multi-Collector Inductively Coupled Plasma Mass Spectrometer (MC-ICP-MS) Nu Instruments Ltd (UK) equipped with twelve Faraday cups and three ion counters at the Geological Survey of Israel. A standard reference material for U isotope ratio measurements (NBL 112a) was used to test instrument performance. The isotopic mass discrimination of the instrument was corrected for by the use of $^{238}U/^{235}U$ as an internal standard. An in-house standard speleothem powder is prepared and measured every 30-50 samples; the reproducibility is within 500 years for a sample with an age of 56 ka and is always within error. Ages were calculated using an EXCEL^{TM} macro developed for that purpose. Calculations are based on the assumption that no initial ^{230}Th is present in the sample. ^{232}Th is routinely monitored during analysis for detection of detrital U and Th. Samples containing less than an acceptable threshold of $^{230}Th/^{232}Th$ can be identified [*Hellstrom*, 2006]. For Soreq-Har-Tuv there is an assumption of no initial Th in the calcite itself, based on *Bar-Matthews et al.* [1997]. According to *Kaufman et al.* [1998] a sample is considered to have a high detrital content, which requires a correction for the contribution of ^{230}Th by the decay of ^{232}Th, if this ratio is less than ~30, since for larger ratios the correction becomes negligible compared to the analytical uncertainty. *Richards and Dorale* [2003] and *Li et al.* [1989] argued for thresholds of between 100 and

300 for the case of mass spectrometric dating, due to the high-precision analysis of initial Th. 100 was the ratio used here as the threshold for detrital correction. *Kaufman et al.* [1998] determine that the detrital components within Soreq Cave speleothems have a $^{232}Th/^{238}U$ ratio of ~1.8 and this is the value used in the correction calculations here. This entire technique is elaborated upon by *Kuperman* [2005], *Vaks et al.* [2006] and *Bar-Matthews et al.* [2010].

Figure 2.1. Photographs of speleoseismite sampling in Soreq Cave. Corer is 2 inches in diameter.

3. Results

"I used to sleep nude - until the earthquake", Alyssa Milano, actress (b. 1972)

3.1 *Intrabasin paleoearthquake and quiescence correlation of the late Holocene Dead Sea*

3.1.1 Introduction

The Dead Sea Rift zone, extending from the Red Sea in the south to the Taurus Mountains in the north (Figure 3.1.1, inset), has been a major source of historic earthquakes [*Ben-Menahem et al.*, 1976; *Garfunkel*, 1981]. The fault system can potentially cause earthquakes that would affect a large number of people in the adjacent countries. Different types of paleoseismic evidence along the Dead Sea Transform (DST) show that large earthquakes have occurred in the past tens of thousands of years, [*Amit et al.*, 1999; *Ferry et al.*, 2007; *Kagan et al.*, 2005; *Y Klinger et al.*, 2000; *Marco et al.*, 1996; *Matmon et al.*, 2006; *Meghraoui et al.*, 2003; *Niemi et al.*, 2001; *Reches and Hoexter*, 1981; *Shaked et al.*, 2004]. The pioneering works of *El-Isa and Mustafa* [1986] and Marco and co-authors *[Marco, 1996; Marco and Agnon, 1995; Marco et al., 1996]* on the intraclast breccia layers (originally termed "*mixed layers*") in the late Pleistocene Lisan Fm. have set the stage for extensive lacustrine paleoseismic research in the Dead Sea basin. Intraclast breccias are temporally associated with surface faulting in places, strongly suggesting a genetic relationship between brecciation of the laminated lacustrine sediment and surface faulting, attesting to the earthquake origin of the deformation [*Marco and Agnon*, 2005]. Therefore, the intraclast breccia layers were interpreted as seismites. This identification was subsequently supported by the studies of [*Ken-Tor et al.*, 2001]] and [*Migowski et al.*, 2004]] who enabled correlations between dates of historic earthquakes (derived from historical charts) and radiocarbon ages of intraclast breccias and other seismites (e.g. liquefied sands) recovered from the exposures and drillholes of the late Holocene Ze'elim Fm. *Katz et al.* [2009] have reported geochemical anomalies in intraclast breccia layers, carried by micro-crystals of barium-strontium-sulphate. They suggest that precipitation of these micro-crystals from a super-saturated brine was triggered by exposure of gypsum nucleation centers, formed on the bottom sediments and suspended during earthquake shaking.

The presence of seismites in late Quaternary sedimentary sections in the Dead Sea basin allows reconstruction of earthquake recurrence patterns. Establishment of such patterns was attempted by *Marco et al.* [1996] for the Lisan Fm. comprising the sedimentary sequences of Lake Lisan that filled the Dead Sea basin during the last glacial period (~70-14 ka). They determined an average recurrence interval (RI) of 1600 yr with a coefficient of variation larger than unity, expressed as alternation of periods of 10-15 kyr with earthquakes occurring in relatively rapid succession, versus ones with relative quiescence [clustering, see [*Kagan and Jackson*, 1991]]. Subsequently *Ken-Tor et al.* [2001a] and *Migowski et al.* [2004] established the RI for the last ~2000 years (RI=100-300 yr) and ~10,000 years (RI=100-1000 yr, clustered), respectively.

The seismites are probably the result of turbulence in the soft sediment [*Heifetz et al.*, 2005]; the threshold for triggering can be affected by water depth at the site (mass of water above sediment), lithology, sediment compaction, and sedimentation rate. The intensity of shaking

depends on earthquake magnitude, distance from source, and position with respect to basin structure ("basin effects"). None of these factors controlling the intensity and its threshold was evaluated rigorously. Early efforts in quantifying the "basin effect" were conducted by [*Begin et al.*, 2005] who argue that site effects due to basin topography may have caused seismite thickness differences between two Pleistocene lacustrine sections. On the other hand *Ken-Tor et al.* [2001a] and *Migowski et al.* [2004] found no relationship between seismite thickness and historic earthquake intensity. On outcrop scale [*Marco and Agnon*, 2005]] found lateral thickness variations of seismites across faults at the Massada Pleistocene seismite site. This illustrates that seismite thickness can be dictated by the local bathymetry that moderates post-seismic transport. At the Wadi Darga outcrop thickness changes were reported in association with faults, while in some beds internal deformation disappears as a layer thins and reappears when the layer returns to its more characteristic thickness [*Enzel et al.*, 2000]. These authors suggest that bedding or laminae thickness may be one control on seismite formation. *Heifetz et al.* [2005] assert that compaction profile, ground acceleration, and wave period all determine the threshold for onset of deformation. Therefore the thickness of the deformed sequence may be sensitive to the details of the wave train, and not necessarily to the local intensity.

Most of the paleoseismic studies in the Dead Sea basin, as of yet, based the evaluation of the data (e.g. recurrence intervals, RI) on the individual sections. Nevertheless, an important result of the study done by *Migowski et al*. [2004] on the Ein Gedi core, was their comparison with the existing Ze'elim Gully chronology [*Ken-Tor et al.,* 2001], showing that historic earthquakes that lack in the Ze'elim archive occurred during depositional hiatuses, while they do appear in the more continuous Ein Gedi core.

In this paper, we expand the effort to integrate multi-site paleo-seismite information. We analyze and date two new seismite-bearing outcrops: Ein Feshkha Nature Reserve section and an eastern Ze'elim Gully section. We then compare with the patterns of seismite appearance with the previously dated Ein Gedi core and western Ze'elim Gully exposure. This integrated study allows us to compose a picture of the spatial and temporal distribution (e.g. the recurrence intervals = RI) of earthquakes that affected part of or the entire Dead Sea basin (as monitored in the three recording stations). Specific issues dealt with in this study are: sedimentary characterization of the seismites (namely, the dependence of the seismite appearance on the sedimentary facies and environment of deposition), the temporal (RI) and spatial patterns of seismites at the late Holocene Dead Sea basin, and identification of earthquakes that formed seismites along the entire basin.

3.1.2 Geological background and research sites

The Holocene Dead Sea is a terminal lake filling a deep tectonic depression along the boundary between the Sinai sub-plate and the Arabia plate, the Dead Sea Transform (DST). The DST has a total left-lateral offset of about 105 km since about 18 Ma ago [*Freund et al.*, 1968]. Over 1100 km long, it trends from the spreading centre in the Red Sea to the Taurus collision zone in Turkey. The Dead Sea basin is likely the largest pull-apart basin along the DST and one of the largest pull-apart basins on Earth [*Mechie et al.*, 2009]. Recent comprehensive geophysical investigations have illuminated the structure of the lithosphere and crust across pure transform and basinal segments (Wadi Araba and Dead Sea, respectively) [*Mechie et al.*, 2009; *ten Brink et al.*, 2006; *Weber et al.*, 2009]. The Dead Sea

straddles the strike-slip duplex fault structure [*Woodcock and Fischer*, 1986]. Three transverse faults have been mapped in the Dead Sea basin (Figure 3.1.1): the Kalia fault, the Ein Gedi fault, and the Amatzyahu fault. Details of the Dead Sea basin fault system are given in Figure 3.1.1. Two GPS campaigns six years apart at seventeen stations straddling wadi Araba yielded on-going slip rate calculations of 4.9 ± 1.4 mm/yr [*Le Beon et al.*, 2008]. Slip rates calculated by geological and archaeological markers, on varying time scales, yielded slip rates of 1.5-8.5 mm/yr *[Freund et al., 1968; Garfunkel, 1981; Ginat et al., 1998; Gomez et al., 2003; Gomez et al., 2007; Haynes et al., 2006; Klinger et al., 2000; Marco et al., 2005; Meghraoui et al., 2003; Niemi et al., 2001]*.

Frequent seismic activity along the DST has been detected instrumentally in the past century and recorded historically and archaeologically over the past 4000 years [*Ambraseys*, 2009; *Ambraseys et al.*, 1994; *Ben-Menahem*, 1991; *Ellenblum et al.*, 1998; *Guidoboni and Comastri*, 2005; *Guidoboni et al.*, 1994; *Haynes et al.*, 2006; *Marco et al.*, 2006]. Other faults in the region are much less active and distant to the Dead Sea and are therefore less likely candidates for earthquake sources of the sediment deformation at the Dead Sea.

The first major earthquake on the DST to be recorded instrumentally was M6.2 on the 11th of July, 1927 in the northern Dead Sea (Figure 3.1.1) [*Avni*, 1999]. The location of the event is given by an error uncertainty ellipse in Figure 3.1.1 which is based on best estimate of seismological data [*Shapira et al.*, 1993] and our tectonic considerations [cf. *Niemi and Ben-Avraham*, 1994]. On the 11th of February, 2004 a M5.1 earthquake ruptured the northeast corner of the pull-apart, with an aftershock sequence demarcating a transverse fault [*Hofstetter et al.*, 2008; *Lazar et al.*, 2006] (Figure 3.1.1). This fault is termed the Kalia fault [*Lazar et al.,* 2006].

The sediments of the Holocene Dead Sea comprise the Ze'elim Fm. of the Dead Sea Group. The sediments represent various depositional environments: fluvial, fan deltas, shores, and lacustrine [see detailed description in [*Bookman (Ken-Tor) et al.*, 2004]. The current (2009) lake level is 422 meters below sea level (mbsl), reflecting mainly anthropogenic diversion of freshwater inflow, while during the Holocene the natural (climate related) level varied from ~370 mbsl (e.g. ~6000 years ago) to lower than ~ 430 mbsl around 8000 years ago [*Bartov et al.*, 2007; *Bookman (Ken-Tor) et al.*, 2004; *Bookman et al.*, 2006; *Migowski et al.*, 2006]. The drop of the current lake level [12 m from 1980 to 2000; *Bookman (Ken-Tor) et al.,* 2004] has caused the formation of deep gullies along the retreating shores. These gullies provided an excellent opportunity to study the late Holocene sedimentary sections in detail. The paleoseismic data in the current study was derived from the outcrops of the Ze'elim Gully and the Ein Feshkha Gully. Another site used for comparison, the Ein Gedi core site, was studied by *Migowski et al.* [2004].

The study site of Ein Feshkha Gully (at the Ein Feshkha Nature Reserve) is located at the north-western shore of the Dead Sea, 60 km north of the Ze'elim Gully (Figure 3.1.1). Ein Feshkha is an oasis of brackish streams and pools. Nearly exclusively lacustrine sediments are exposed in the Ein Feshkha site by a ~6.5 m deep gully (as of 2008). The site is close to the Jordan Valley

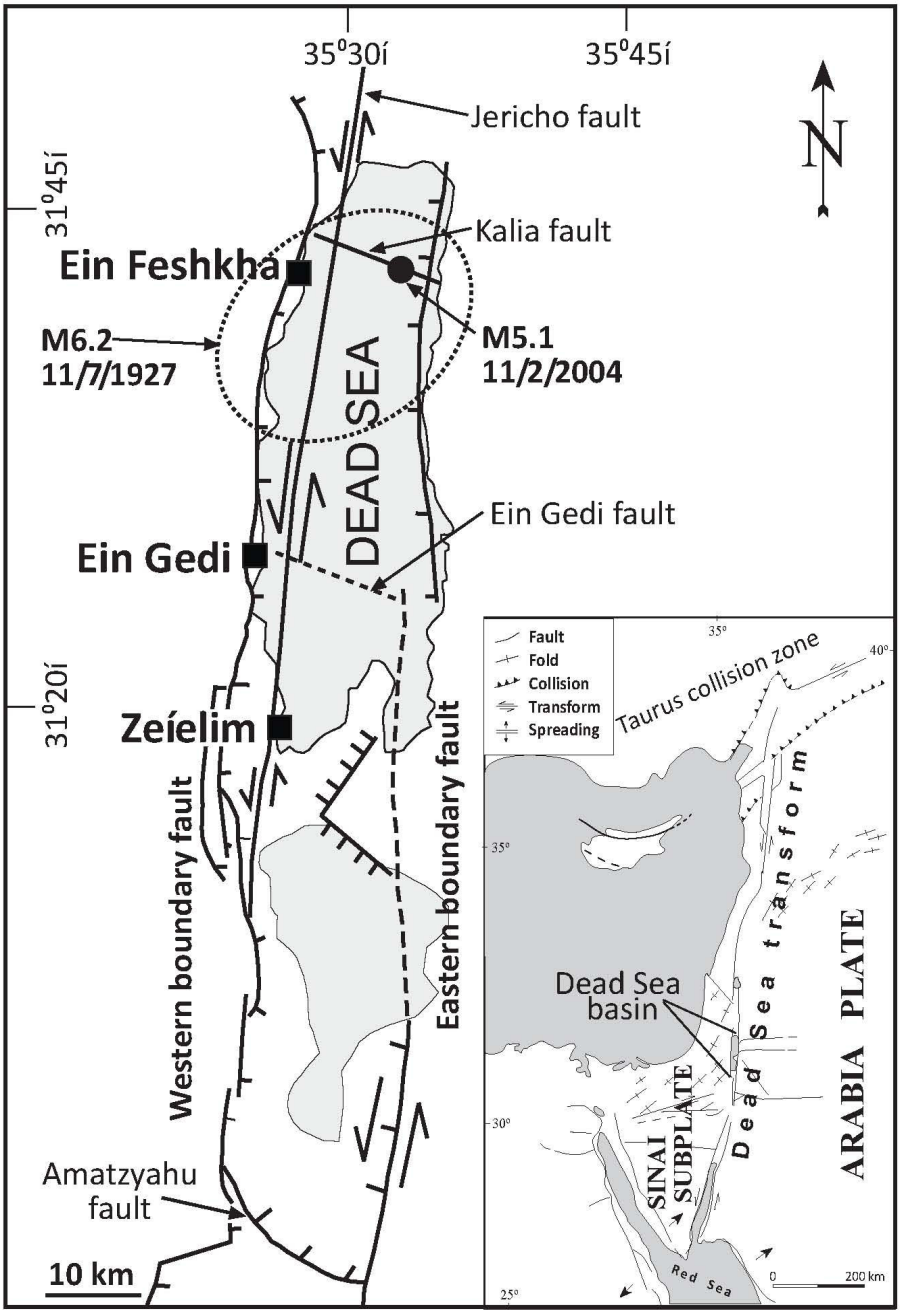

Figure 3.1.1. Map depicting location of study sites (Ein Feshkha and Ze'elim), a 3rd site for comparison (Ein Gedi), and main active tectonic features in the area. Modified after [*Bartov and Sagy*, 2004]; *Bartov et al.*, 2007]. Faults (solid lines) and suspected fault traces (dashed lines) are marked. The epicenter of a M5.1 earthquake (Feb. 11, 2004) is indicated and a left lateral fault delineated by its aftershocks (the Kalia fault) is marked [*Lazar et al.,* 2006 - Figure 9], [*Hofstetter et al.*, 2008]. The uncertainty ellipse of the M6.2 1927 earthquake is based on an continuation of the best estimate of [*Shapira et al.*, 1993] and on the possible interpretation of the Kalia fault discussed above as the source fault. The Ein Gedi transverse fault was mapped by *Neev and Hall* [1979]. Dark areas are currently underwater (as of 2009). Inset displays the regional tectonics after *Garfunkel* [1981].

segment of the DST and may be located on the WNW continuation of the Kalia transverse fault mentioned above. The Ze'elim gullies (site ZA) are dissected into the Ze'elim Plain east of the ancient fortress of Massada (Figure 3.1.1). Currently (as of 2009) the ZA Gully is ~11 m deep (approximately at lake level, to slightly above). The gully exposes a stratigraphic sequence of lacustrine, shore-environment, and fluvial sediments. The ZA site is closer to the Arava segment of the DST, about 50 km away, than to the Jericho fault. The active eastern boundary normal fault of the DST is at a similar distance to all sites, less than 5 km away (Figure 3.1.1).

3.1.3 Seismite description

El Isa and Mustafa [1986] used intraformational folds to generate an earthquake archive. Subsequent studies presented more complete archives recognizing that folds might present the weakest events. "Mixed layers" were renamed "intraclast breccia layers" [*Agnon et al.*, 2006].

Agnon et al. [2006] define field criteria for the recognition of intraclast breccias, focusing on features diagnostic of a seismic origin. The field criteria reflect the mechanisms of breccia formation, which include ground acceleration, shearing, liquefaction, water escape, fluidization, and resuspension of the originally laminated mud.

In the current study we recognize deformed structures such as intraclast breccias, liquefied sands, folded laminae, and small faults (centimeter scale). Figure 3.2.2 displays photographs and photo tracings of seismites from the study sites. In addition we recognize another type of deformation termed micro-breccia or homogenite. This type of mid-grey color sedimentary layer ranges in thickness from a few mm to 1-2 cm and appears homogenous in the field. Thin-section investigation under a polarizing microscope shows that these are actually brecciated laminae, and include a mixture of detritus, aragonite, and in places gypsum fragments.

In the more fluvial Ze'elim section there are instances of seismites with a combination of lacustrine breccia and sand liquefaction. For example (see Figure 3.1.2c) ZA seismite III is the product of the deformation of a lower sandy layer and an upper laminated marl layer, resulting in brecciated marl laminae (grey and white) with injection of sand fingers (orange) from below.

3.1.4 Fieldwork

Fieldwork included the detailed description and sampling of sub-vertical to vertical outcrops in the Ein Feshkha and Ze'elim Gullies. Columnar sections were prepared with emphasis on measurement and description of the deformations. Adjacent outcrops were examined in order to describe spatial variations in lithology and seismites. Sediment blocks (~10x10x10 cm in size) were collected for further analysis in the lab. At Ein Feshkha 58 continuous blocks of wet sediment were retrieved from the gully wall at the columnar section site, from the surface plain down to 40 cm below the autumn 2005 water level of the spring outflow [see our previous paper [*Neumann et al.*, 2007]. At the Ze'elim Gully sediment blocks were retrieved from the various lithological units. In addition, organic debris (typically short lived leaves or twigs), found in the two outcrops, were sampled for radiocarbon dating.

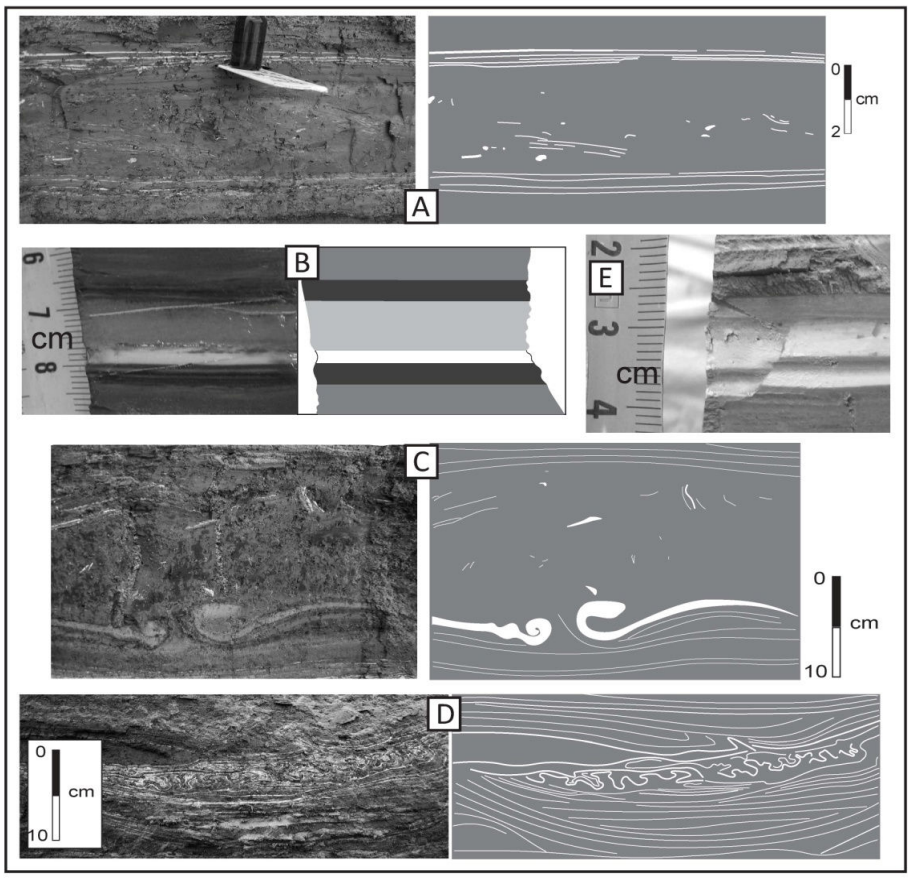

Figure 3.1.2. Photographs and line tracings of five types of lake seismites from EFE and ZA study sites, details in Table 3.1.1. A: Intraclast breccia layer, note fragmented aragonite laminae (white) in matrix (grey). B: Micro-breccia (see text). C: Liquefied sand layer within brecciated clay and aragonite. D: Folded laminae. E: Small fault, mm-scale throw.

Table 3.1.1: Types of seismites at the study sites

A	Intraclast breccia: Previously often termed “mixed layers”. Light and dark laminae "floating” in a dark matrix. See *Agnon et al.* [2006] for criteria.
B	Micro-breccia: A light grey layer, seemingly homogenous to the naked eye, of intermediate color somewhere between the dark brown/grey detrital laminae and the white/beige evaporitic laminae. Petrography shows this to be a mixture of the evaporitic and the detrital material.
C	Liquefied sand
D	Fold: Small-scale folds, where the amplitude is on the order of millimeters to a few centimeters.
E	Fault: Tiny faults, millimeter to centimeter scale throw.

3.1.5 Stratigraphic sections

Ein Feshkha (EFE)

The Ein Feshkha section was documented in an outcrop in the gully incising into the near-shore surface of elevation 413 mbsl. The stratigraphic section of Ein Feshkha, down to a depth of 5.9 m below plain surface, is given in Figure 3.1.3. The section spans approximately 3000 years. The sediments are mainly laminated lacustrine calcitic silts and clays and sequences of laminated primary aragonite and fine detritus. Fifty-two layers in this laminated sequence display disturbed sedimentary features. Organic debris, mainly twigs, are common and are often found within breccia layers. The base of the outcrop is characterized by 5–50 cm thick domelike structures consisting of aragonite crusts, marl, and commonly driftwood encrusted with concentric hard gypsum [*Neumann et al.*, 2007]. The occurrence of dome-structures is a localized phenomenon, which is known from the near-shore fan-delta surface (1400 AD or younger). These structures probably represent lake lowstands.

Ze'elim Gully (ZA)

We investigate a 10.75 m deep section in the Ze'elim A Gully, which shows both lacustrine and fluvial fan delta sediments (Figure 3.1.4). The section (ZA2) spans approximately 6500 years and consists mainly of laminated calcitic marls with some aragonite laminae, gypsum, silt, sand, and pebbles. Sediment features include beach ridges, cross-bedded carbonatic sands, aragonite crusts, brecciated marls, and liquefied sand [see *Bookman (Ken-Tor) et al.,* 2004]. The laminae are interrupted by deformed sedimentary structures (Figure 3.1.4). A prominent beach ridge that was dated to ~ 1200 BC appears at a section depth of 8-9 m. The beach ridge marks a significant drop in lake level that was, associated with abrupt aridity in the Dead Sea drainage region [*Kushnir and Stein*, 2010]. A two meter thick section below this beach ridge shows several deformed layers, including breccias and "ball and flame" sand liquefaction structures. They laterally change their thickness, their appearance, and their position relative to the beach ridge. There are many on-laps, angular and erosional unconformities, and facies changes in this unit below the beach ridge and therefore a detailed study of the seismites there is not attempted. This ZA2 section is a few tens of meters east (lakeward) of the section studied by *Ken-Tor et al. [2001]* (termed here ZA1).

3.1.6 Radiocarbon dating: method and results

The chronologies of the Ein Feshkha and Ze'elim sections were constructed by radiocarbon dating of terrestrial organic debris (mainly small pieces of wood and twigs). All the recovered wood in Dead Sea sections can be considered driftwood, however their transport time is relatively short. We made an effort, where possible, to date only short-lived organic debris. Nine samples from EFE and twelve samples from ZA2 were prepared for radiocarbon dating at the Radiocarbon laboratory, Weizmann Institute, Rehovot, Israel. The samples were then measured by accelerator mass spectrometry (AMS) or liquid scintillation counting (LSC) at the NSF-radiocarbon facility in Arizona. Eight additional organic debris samples from EFE were taken from a core drilled a mere few meters away, on the cliff bounding the gully, and were analyzed at the AMS facility in Kiel. The core was correlated with the outcrop by Marcus Schwab at GFZ-Potsdam. Radiocarbon ages are reported (Table 3.1.2) in conventional radiocarbon years (before present =1950) in accordance with international convention [*Stuiver and Polach*, 1977].

Table 3.1.2 Results of radiocarbon dating and OxCal modeling of organic debris samples

Sample number	Lab number	*Depth [cm]	C^{14} yr (BP)	†Calibrated age range (68% probability)	†Calibrated age range (95% probability)	††Modeled age range (68% probability)	††Modeled age range (95% probability)
Ein Feshkha							
Boundary (surface)		0				1300-1344 AD	1280-1422 AD
EFW-009	RTT5174	9	700±40	1268-1382 AD	1243-1392 AD	1271-1303 AD	1255-1383 AD
DSF-B1-18	KIA32721	26.5	1189±27	783-882 AD	729-940 AD	outlier	
EFW-029	RTT5175	29	780±40	1223-1271 AD	1178-1285 AD	1194-1236 AD	1172-1261 AD
DSF-B1-31	KIA32722	46.5	933±36	1038-1154 AD	1022-1182 AD	1124-1160 AD	1098-1179 AD
EFW-80	RTT5176	80	1015±40	980-1117 AD	898-1154 AD	991-1026 AD	960-1045 AD
EFW-120	RTT5177	120	1310±40	661-767 AD	647-779 AD	820-879 AD	752-886 AD
EFW-169	RTT5178	169	1750±40	237-344 AD	140-399 AD	outlier	
DSF B3-28	KIA11641	218.5	1541±68	432-576 AD	391-646 AD	415-507 AD	340-575 AD
	Boundary	230				363-479 AD	286-541 AD
DSF-B5-43	KIA11642	412	2143±27	346-115 BC	353-60 BC	201-166 BC	233-130 BC
DSF-B5-58	KIA32723	426.5	2215±29	361-208 BC	377-202 BC	247-207 BC	296-188 BC
EFW-430	RTT5180	430	2150±45	352-111 BC	360-54 BC	260-217 BC	307-199 BC
DSF-B5-65	KIA32724	430.5	2662±36	840-796 BC	896-792 BC	outlier	
DSF-B5-76	KIA32725	448	2036±31	90 BC-17 AD	160 BC-51 AD	outlier	
EFW-492	RTT5181	492	2380±40	511-397 BC	743-386 BC	478-400 BC	523-391 BC
	Boundary	500				508-423 BC	556-410 BC
EFW-518	RTT5182	518	3005±50	1372-1133 BC	1407-1090 BC	outlier	
EFW-530	RT5183	530	2850±65	1116-926 BC	1254-845 BC	1041-905 BC	1115-839 BC
DSF-B6o-73	KIA32726	537	2873±88	1193-926 BC	1308-838 BC	1166-983 BC	1261-912 BC
	Boundary	537				1166-983 BC	1261-912 BC

Ze'elim							
ZA 37	RTT5184	132	825±40	1185-1259 AD	1056-1276 AD	1049-1226 AD	1041-1265 AD
ZA 35	RTT5185	234	1295±40	668-770 AD	651-853 AD	729-875 AD	706-884 AD
ZA 33	RTT 5186	346	1685±40	264-412 AD	246-431 AD	375-507 AD	355-530 AD
ZA 25	RTT5187	467	1840±50	94-238 AD	63-325 AD	23-101 AD	18 BC-142 AD
ZA 20	RTT5188	632	2345±40	505-380 BC	725-257 BC	521-465 BC	553-399 BC
ZA 18	RTT5189	742	2820±40	1015-914 BC	1114-851 BC	944-840 BC	985-825 BC
ZA 871	na	871	3175±30	1491-1420 BC	1503-1402 BC		
ZA 50	RTT5190	872	3730±45	2196-2039 BC	2284-1979 BC		
ZA 51	RT5191	897	3500±75	1921-1738 BC	2024-1634 BC		
ZA 5	RTT5192	967	3540±45	1941-1775 BC	2015-1745 BC		
ZA 10	RTT5193	1022	3475±45	1877-1744 BC	1913-1686 BC		
ZA 16	RTT5194	1067	5860±50	4794-4623 BC	4843-4583 BC		

Note:

*Gully depth below fan delta surface

†Calibration by OxCal 4.1 [*Bronk Ramsey*, 1995, 2009] using the IntCal 04 atmospheric calibration curve [*Reimer et al.*, 2004].

††Model ages from OxCal P_Sequence (k factor=1) deposition model (see text for details).

EFW samples are from the Ein Feshkha outcrop, DSF samples from the Ein Feshkha core, ZA samples from the Ze'elim ZA2 outcrop

In the ZA2 section only the top 8 m were included in the age-depth Bayesian model, model boundaries are the top and bottom radiocarbon sample depths.

Calibrated ages (= cal BP) were calculated by applying the INTCAL04 calibration scheme [*Reimer et al.*, 2004] by means of the OxCal v4.1 program [*Bronk Ramsey*, 1995; 2001; *Bronk Ramsey*, 2008; *Ramsey*, 2008]. Age-depth models (Figures 3.1.3 and 3.1.4) and seismite chronologies (Table 3.1.3) were also created with OxCal (v4.1) [*Bronk Ramsey*, 1995; 2001; *Bronk Ramsey*, 2008; *Ramsey*, 2008].

Radiocarbon data are listed in Table 3.1.2. The table presents the measured ages, calibrated ages, and deposition model ages applying the Bayesian statistics of the OxCal v4.1 program. The depositional model ages were used to establish an age-depth chronological model for the seismites. The fundamental assumption in Bayesian modeling of stratigraphic sequences is that age increases with depth. This requires use of a function usually termed *Boundaries* in OxCal. The boundaries separate different sedimentary units that may have different sedimentation rates, grain sizes, and facies. They are also placed on the top and bottom of the entire series to constrain the model to a specific time interval. With no other information, this would be treated by what is usually termed the *Sequence* model by OxCal. A uniform sedimentation rate would be treated with the *U_Sequence* type model. Depth and other dating information can be included in a less rigid way using Poisson distribution priors, termed *P_Sequence* models, where the time gap between deposition of grains varies, and the events are basically random but deposition is given approximate proportionality to depth. This requires the estimation of the uniformity of the deposition (given as the *k parameter*), which signifies the increment size (conceptually the grain size, or size of deposition events) and indicates the relation between the events and the stratigraphic process [*Bronk Ramsey,* 2008].

In this study a *P_sequence* (Poisson distribution) Bayesian depositional model was used, with a k factor value of 1 [see [*Ramsey*, 2008]] and [*Kagan et al.*, 2010]] for details of Bayesian factors used (Figure 3.1.3, Table 3.1.2). In *Kagan et al.,* [2010] the main objective was to test the Bayesian model with and without historic earthquake anchor points. The conclusion of the work was that the "known-earthquake-anchors" do not significantly improve the age-model. For that reason, and due to the complexity in choosing definite historical anchors, in this study no anchors are used and the models are based solely on radiocarbon data, stratigraphic data, and the P_sequence and k-factor constraints discussed above and in *Kagan et al.* [2010].

Ein Feshkha (EFE) chronology: For the EFE section the chronological model is based on the treatment of seventeen radiocarbon ages of which five were excluded as outliers (Table 3.1.2). In the last 2500 years, the period with historic earthquake correlations and implications, there were only two outliers, both of which were too old and probably represent long-lived organic debris from the shores. One of these two outlier samples also appeared in *Neumann et al.* [2007] (169 cm depth) and was considered an outlier. One interval, from 230 to 390 cm, is slightly anomalous: the sediment is much darker than the rest of the section and has less aragonite layers. Within this interval, between 230 and 330 cm, we did not recognize any deformed layers (Table 3.1.3). No organic debris was found from 220-410 cm depth (Table 3.1.2, Figure 3.1.3).

Several different models were run: 1) No internal boundaries from 0-500 m depth; 500 cm to base modeled separately, 2) Two internal boundaries in the 0-537 cm interval, at 230 and at 500 cm depth, which allow, but do not force, the model to have sediment rate changes, 3) The 0-230

Table 3.1.3. Ze'elim and Ein Feshkha seismites with model ages and historic event correlation

no.	Depth (cm) *	Type ¥	Thickness (cm)	†Modeled calendar age (68%, ~1 σ)	†Modeled calendar age (95%, ~2 σ)	Historic Earthquake correlation	‡Fit	¥¥ All possible events (within 2σ range, 1σ in bold)
Ze'elim seismites								
I	32	A	10	[a]~1400-1650 AD		**1456 AD**		1408, 1456,1481, 1546 AD
II	242	A	2	699-848 AD	682-859 AD	**748±1 AD**	**1σ**	**748±1,757, 835, 847, 853**, 859
III	315	A&C	17	467-606 AD	452-627 AD	**551 AD**	**1σ**	**502,551 AD**
IV	342	A	5	386-519 AD	370-541 AD	**419 AD**	**1σ**	**419,502 AD**
V	445	A	5	86-164 AD	55-210 AD	**115 AD**	**1σ**	**112,115,117 AD**
VI	470	A	4	12-91 AD	20 BC-131	**33 AD**	**1σ**	**33,76 AD**
VII	486	A	6	40 BC-35 AD	77 BC-74 AD	**31 BC**	**1σ**	**31 BC,33 AD**
VII	516	A	8	140-66 BC	178-28 BC	**Mid II century**	**1σ**	**92, 64 BC**
IX	552	A	8	260-190 BC	300-150 BC	**199 BC**	**1σ**	**199 BC**
X	700	A&C	variable	781-700 BC	824-667 BC	**Mid VIII cent.**	**1σ**	**Mid VIII cent. BC**
XI	710	A&C	variable	819-734 BC	861-705 BC	**Mid VIII cent.**	**1σ**	**Mid VIII cent. BC**
XII	919	A	variable	[b]~ 2020-1635 BC				
Ein Feshkha seismites								
1	0.0	A	10	1300-1343 AD	1279-1421 AD	**1312 AD**	**1σ**	1293, **1303,1312**, 1401-8
2	12.0	A	7	1260-1293 AD	1239-1367 AD	**1293 AD**	**1σ**	**1293**,1303,1312
3	28.0	A	2	1199-1240 AD	1176-1267 AD	**1202/1212 AD**	**1σ**	1170, **1202,1212**
4	40.0	A	6	1150-1190 AD	1125-1210 AD	**1170 AD**	**1σ**	1138/9,1150,1156/7,1170,1202, 1212
5	48.0	A	2	1118-1155 AD	1091-1174 AD	**1117/1138 AD**	**1σ**	**1113/4,1114,1115,1117,1138/9 ,1150,1156**/7, 1170
6	66.0	A	1	1044-1084 AD	1017-1105 AD	**1068 AD**	**1σ**	1032,1033**,1042,1063,1068a,10 68b**
7	70.0	Q	1	1028-1067 AD	1002-1088 AD	**1063 AD**	**1σ**	991,**1032,1033,1042,1063,1068 a,1068b**
8	74.0	A	1.5	1013-1051 AD	986-1071 AD	**1033 AD**	**1σ**	991,**1032,1033,1042**,1063,1068 a,1068b
9	80.0	A	1.5	991-1026 AD	962-1045 AD	**991 AD**	**1σ**	952,956,**991,1032,1033**,1042
10	86.0	A	4	963-1005 AD	929-1023 AD	**956 AD, LS**	**1σ**	952,**956,991**,1032
11	104.0	D	6	885-939 AD	833-954 AD	**873 AD, LS**	**2σ**	835,847,853/4,859,873,952,956
12	110.5	Q	1.5	859-915 AD	801-926 AD	**859 AD, LS**	**1σ**	835,847,**853/4,859,873**
13	113.0	A	3	849-905 AD	788-915	**847 AD, LS**	**1σ**	835,**847,853/4,859,873**
14	125.0	A	1	801-861 AD	733-870 AD	**757 AD**	**2σ**	747/9,757,**835,847,853/4,859**,8 73
15	126.5	A	2.5	795-856 AD	729-865 AD	**748±1 AD**	**2σ**	747/9,757**,835,847,853/4,859**, 873
16	157.0	B	3	666-747 AD	599-773 AD	**660 AD**	**1σ**	634,**660,747/9,757**
17	172.0	D	1	603-692 AD	538-727 AD	**634 AD**	**1σ**	500/502,551,**634,660**
18	186.5	Q	1	543-638 AD	476-681 AD	**551 AD**††	**1σ**	500/502,**551,634**,660
19	210.0	A	2	448-551 AD	376-605 AD	**419 AD**	**2σ**	419,**500/502,551**
20	212.5	Q	1	439-542 AD	365-595 AD			419,**500/502,551**
21	220.0	B	2	408-515 AD	334-570 AD	**363 AD**	**2σ**	349,362/3,**419,500/502**,551
22	228.0	A	1	372-487 AD	296-548 AD	**349 AD**	**2σ**	303,349,**363,419,**500/502,551
23	338.0	B	1	25-100	20BC-142 AD	**33 AD**	**1σ**	**33,37,76,110**
24	364.0	B	1	57 BC-7 AD	94 BC-46 AD	**31 BC**	**1σ**	92BC,**64BC,31BC**,33,37

no.	Depth (cm) *	Type ¥	Thickness (cm)	†Modeled calendar age (68%, ~1 σ)	†Modeled calendar age (95%, ~2 σ)	Historic Earthquake correlation	‡Fit	¥¥ All possible events (within 2σ range, 1σ in bold)
25	377.0	B	<1	96-41 BC	131-2 BC	**64 BC**	**1σ**	**92BC,64BC,31BC**
26	377.8	B	<1	101-42 BC	133-6 BC			**92BC,64BC**,31BC
27	387.0	B	1	126-76 BC	160-39 BC	**92 BC**	**1σ**	**92BC**,64BC,31BC
28	393.0	B	1	146-96 BC	177-61 BC	**mid-2nd century**	**1σ**	**92BC**,64BC, mid-2nd century BC
29	402.0	B	1.5	172-130 BC	204-95 BC	**mid-2nd century**	**1σ**	199BC, **mid-2nd century BC x 2**,92BC
30	425.0	B	2	243-202 BC	288-183 BC	**199**	**1σ**	**199BC**
31	428.0	D	2	252-212 BC	301-192 BC			199BC
32	438.0	A&E	2	286-240 BC	336-222 BC			331BC
33	447.0	B	2	321-267 BC	366-249 BC	**331 BC ****	**1σ**	**331BC**
34	473.0	A	1	412-346 BC	458-328 BC			331BC
35	478.5	Q	1	433-361 BC	477-346 BC			
36	483.0	A&E	1	447-375 BC	492-361 BC			
37	487.0	A&B	7.5	461-386 BC	507-373 BC			
38	495.0	A	5	489-408 BC	537-398 BC	**525 BC****	**2σ**	525BC
39	513.0	B	1.5	749-630 BC	817-577 BC			**Mid-8th century BC x 2**
40	515.0	B&E	2	784-661 BC	854-607 BC	**Mid-8th century BC**	**1σ**	**Mid-8th century BC x 2**
41	521.0	B	3	886-756 BC	963-699 BC	**mid-8th century BC**	**1σ**	**Mid-8th century BC x 2**
42	527.5	A	1.5	1002-862 BC	1076-801 BC			~1050BC
43	531.0	A	>9	1059-915 BC	1136-846 BC	**~1050 BC****	**1σ**	**~1050BC**
44	543.0	A	3-6	unmodeled				
45	547.0	B	1					
46	558.0	Q	0.7					
47	561.0	A	6					
48	572.0	B	1.5.					
49	574.5	A	0.5					
50	576.0	D	1					
51	578.0	A	0.6					
52	579.0	D	1					

Notes:

* Gully depth below fan delta surface

† Model ages of seismites extrapolated from deposition model (see text for details);

¥ Seismite type: A-Intraclast breccia layer, B-Microbreccia ("homogenite" to the naked eye), C-liquefied sand; D-Folded laminae; E-Small offsets; Q-Questionable as seismite. See Table 3.1.1, Fig. 3.1.2;

‡ Fit of historical earthquake dates within 1s or 2s calibrated age ranges of seismites. Although model ages are tabulated here with 1 year precision for convenience, event fit considers the realistic precision of 10 years (see text);

[a] Outside model range, extrapolated from model (Figure 3.1.4).

[b] Outside model range, estimated based on below and above radiocarbon ages (Figure 3.1.4).

** Events could have been caused by seismites below or above the one marked.

¥¥ All other possible events within the age probability range (1σ or 2 σ range) of the designated earthquake.

LS=local source, moderate earthquake, not appearing in the historical catalogues, may have produced these seismites.

††The seismites correlated to the 551 A.D. historic earthquake could also be accorded to the 597/598 A.D. earthquake discussed by *Rucker and Niemi* [2012] and noted by *Ambraseys* [2009].

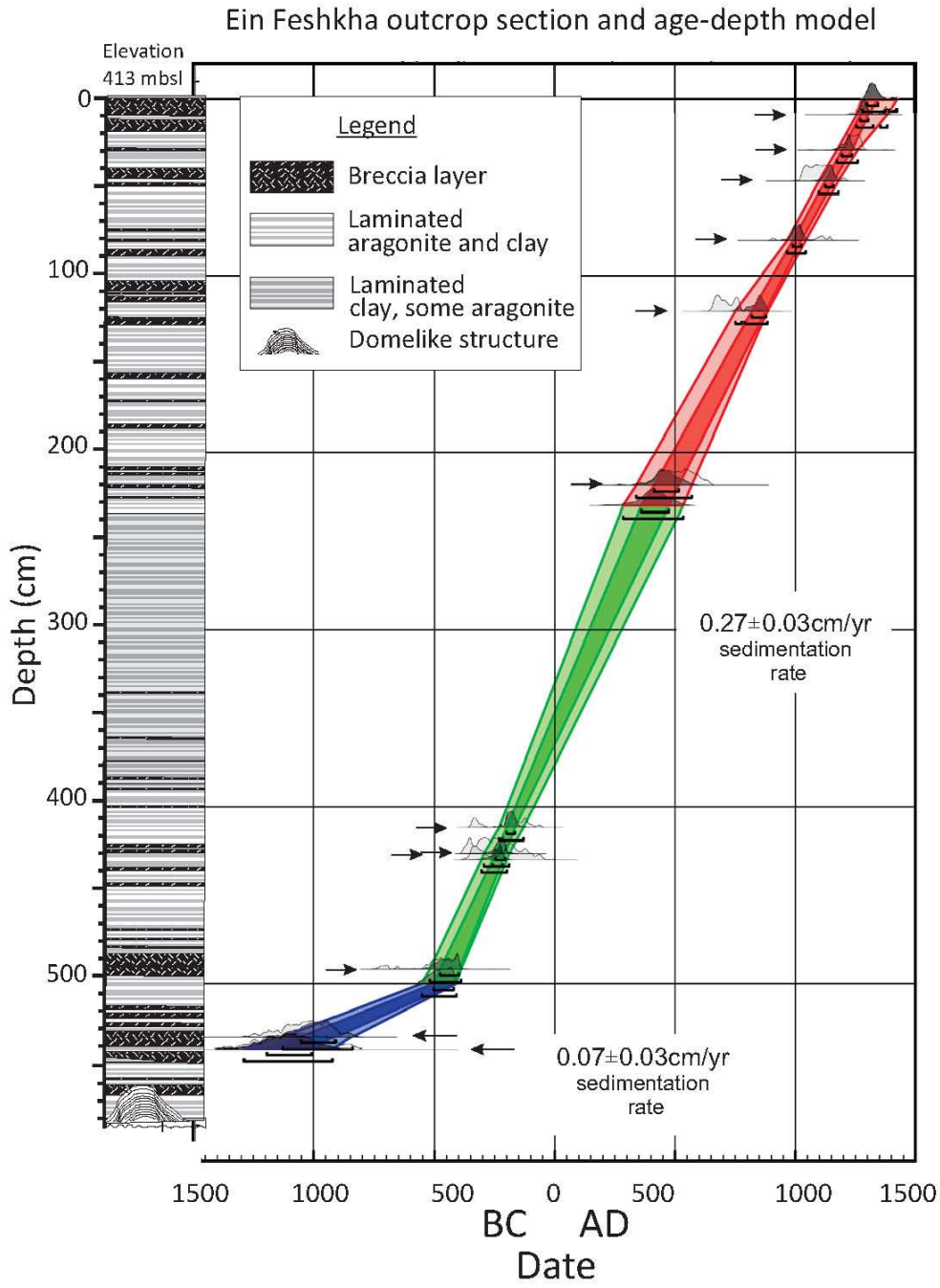

Figure 3.1.3. Stratigraphic section of Ein Feshkha outcrop (left) and age-depth deposition model derived by OxCal 4.1. Breccias are marked in section by hatched black layers. Probability density functions (histograms) on the graph give model ages for radiocarbon calibrated ages (marked with arrows) and model boundaries (details in Table 3.1.3). The histograms give the distributions for the single calibrated dates while the darker center part of each histogram take into account the stratigraphic information (see text and [2008] for model specifics). The depth model curves are envelopes for the 95% (outer, lighter, approximately 2σ) and 68% (inner, darker, approximately 1σ) highest probability density ranges. Color of model age curve changes at boundaries.

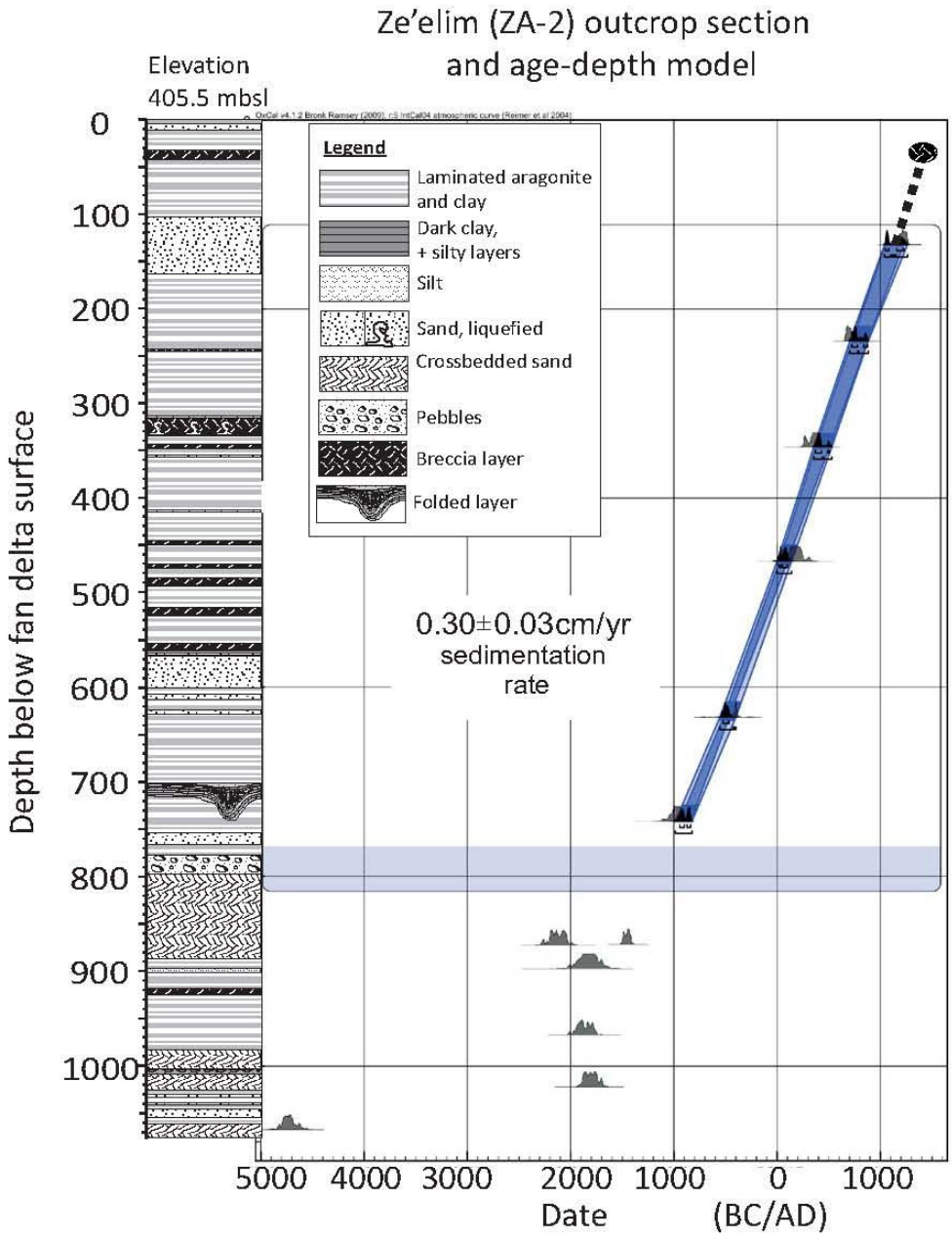

Figure 3.1.4. Stratigraphic section (left) of Ze'elim (ZA2) and age-depth deposition model derived by OxCal 4.1. The top 7.5 meters are modeled, while the bottom of the section is presented as single calibrated dates. Probability density functions (histograms) on the graph give model ages for radiocarbon samples (details in Table 3.1.3). The histograms give the distributions for the single calibrated dates while the darker center part of each histogram take into account the stratigraphic information (see [2008] for model specifics). The depth model curves are envelopes for the 95% (outer, lighter, approximately 2σ) and 68% (inner, darker, approximately 1σ) highest probability density ranges. The dashed line near the top is the extrapolation of the model upwards, while the ellipse represents the uppermost seismite.

cm and 390-500 cm deep segments run separately, 4) Various other options with different boundaries and various outliers.

We choose option #2 from the above list (Figure 3.1.3). This curve yields the best "agreement indexes" for the Bayesian model, only one index value under 60% (at 17%) while the other models have lower agreement indexes. Alternative models give seismite ages from at least the 5th century BC and on that are very similar to the chosen model and do not change the paleoseismic conclusions (for an example see option #1 in Figure 3.1.12). The slight facies change at 230 cm depth is allowed a degree of freedom to coincide with sedimentation rate change, but the resulting model shows no significant rate change.

The chronology of the top 537 cm of the section is Bayesian-modeled as one space with two internal boundaries at 230 cm and 500 cm, implying continuous sedimentation and allowing, but not forcing, sedimentation rate change at these boundaries. Agreement values are found to be well above 60% at most depths of the model. The resulting model ages of the section indicate a maximum range of 1261 BC to 1383 AD, but more likely from ~1100 BC to 1312 AD (Table 3.1.2, Figure 3.1.3). The top unit, from 0 cm (surface) to 500 cm, shows ages that range from the 5th century BC to the 14th century AD, with a 0.27 ± 0.03 cm/yr sedimentation rate (based on 2σ age ranges). The age range of the lower unit (500 to 537 cm) is from approximately 11th -5th century BC (0.07 ± 0.03 cm/yr sedimentation). The base of the seismite-bearing investigated section is at 590 cm, however in the bottom 53 cm no organic matter was found and therefore the age was not modeled. The sedimentation rate of the top 500 cm calculated here (0.27 cm/yr) is approximately constant, in comparison to that stated for the same section in *Neumann et al.* [2007] (0.14, 0.51, and 0.11 cm/yr for three stratigraphic units within the same depth interval). The rates presented here, based on the new Bayesian model, are more similar to rates published elsewhere (e.g. *Migowski et al.* [2004] ~0.15 cm/yr for the entire Holocene Ein Gedi core) and more congruous with homogeneous pollen concentrations [*Neumann et al.*, 2007], which are normally closely linked to sedimentation rate [*Horowitz*, 1992].

The truncation of the last six centuries from the studied EFE section eliminates recording the key instrumental earthquake M6.2 11/7/1927, the source zone of which spans the site (Figure 3.1.1). Macroseismic evidence for the 1927 AD instrumentally recorded earthquake was reported along the Jordan River [*Hough and Avni*, 2011]. *Niemi and Ben-Avraham* [1994] interpreted large submarine slumps in the northern Dead Sea basin to have been caused by this earthquake. For the purpose of the discussion below this event will be considered recorded in the northern Dead Sea basin.

Ze'elim Gully (ZA2) chronology: Twelve organic debris samples from the 10.7 m deep Ze'elim (ZA2) outcrop were measured. Their calibrated radiocarbon ages range from 1056-1276 AD to 4843-4583 BC (95% probability). A deposition model is calculated for the top 8 m of this section. Model ages of samples are given in Table 3.1.2. The more western ZA1 section (~100 m away) was dated by *Ken-Tor et al.* [2001] and revised by *Agnon et al.* [2006]. In the Ze'elim Gully previous studies infer the sedimentation rate to range between 0.28 to up to~ 1.3 cm/yr [*Agnon et al.*, 2006; *Ken-Tor et al.*, 2001; *Neumann et al.*, 2007] reflecting the additional detrital-clastic sediments that are more abundant in the fan delta environment. The lower sedimentation rate (0.3±0.03 cm/yr) at the ZA2 section of Ze'elim (current study) reflects the proximity of this section to the lacustrine environment. The ZA2 outcrop (this study) is interpreted to show continuous deposition according to the age-depth

model (Figure 3.1.4), as opposed to the numerous unconformities at the more landward ZA1 outcrop. However, at ZA2 there is the possibility of short hiatuses compensated by additional sediments at sandy facies which therefore are not manifested in the age-depth diagram.

3.1.7 Discussion

3.1.7.1 Seismite chronology and historic earthquakes

Ages of seismites (Table 3.1.3) are interpolated from the radiocarbon age-depth data using Bayesian stratigraphic constraints. The ages and their uncertainties are interpolated using the OxCal program and take into consideration the asymmetrical probability distribution of radiocarbon ages. Each seismite is assigned a probability distribution histogram with a 68% (~1σ) and 95 % (~2σ) probability age range (Figures 3.1.3 and 3.1.4). Model ages are presented (Table 3.1.3) with a nominal precision of a single year, however due to the Bayesian statistical modeling each model run produces slightly different age ranges and therefore ages could be rounded off by 10 years. Although the annual dates are shown they are dealt with as if rounded off, for example when giving the historical "fit" in Table 3.1.3, the age ranges are considered in decades.

Seismite ages have been compared to historical catalogues as a major component in the assessment of the validity of the interpretation of the breccia layers as seismites [e.g. *Ken-Tor et al*., 2001a; *Migowski et al*., 2004]. At the same time seismites can be used for the corroboration of individual earthquakes in the historical record. *Ken-Tor et al.* [2001a,b] used the radiocarbon ages of the individual breccia layers or liquefied sands for direct comparison with the historical records, and noted that notorious historic earthquakes unrepresented in the geological record lie within sedimentary hiatuses in the western Ze'elim Gully section (termed here ZA1). *Migowski et al.* [2004] positively identified these "missing" earthquakes in the continuous lacustrine section of the Ein Gedi core, supporting the hiatus-hypothesis. Moreover, by counting the laminae in the intervals between seismites they were able to correlate almost the entire historical and Ein Gedi core records.

Table 3.1.5 presents the historic earthquakes in the region with information regarding damage, casualties, sources of historical data, and, in the footnotes selected archaeological and paleoseismic data. This table is based on earthquake catalogues, whereas the information in the catalogues is derived from historical sources. The table is reliable mostly during the past two millennia (from the Roman period and onwards), but less information is available for the time interval 750-1100 AD (when the Muslim empire center moved from Damascus to Baghdad). The historical accounts in the pre-Christian era are rare and if they do exist tend to be vague [*Karcz*, 2004]. A mid-8th century event and its paleoseismological and historical implications are discussed in detail in a note at the end of this chapter. Local source moderate earthquakes are probably missing in the historical catalogues. For seismite ages where only very distant correlative historic earthquakes exist, we propose small local source events as *possible* sources of seismite genesis (marked LS on Table 3.1.3). A map of historical locations is given in Figure 3.1.11.

For the past two millennia we correlated almost all of the seismites, in the Ze'elim and Ein Feshkha records, to historic earthquakes (details in Tables 3.1.3 and 3.1.4). All historic earthquake dates that correspond to the 95% probability range of each seismite age are given in Table 3.1.3 (right column). Those that correspond to the 68% probability range are in bold.

The protocol for assigning a particular historic earthquake to a seismite in the sedimentary section is the following: (1) We consider all known earthquakes within a time segment of the age-depth model pertaining to the seismite depth (segment= within 1-2σ uncertainty of the radiocarbon-model age). This step is given in column titled "all possible events" in Table 3.1.3; (2) Among the earthquakes within this time segment, we select the one that is most consistent with age-depth models of Figures 3.1.3 and 3.1.4 (preserving the sedimentation rate); see the correlation in Figure 3.1.5. We also considered the local intensity for the earthquakes estimated for the study area when deliberating, in certain cases, between the various earthquakes.

Table 3.1.4 and Figure 3.1.5 present the results of the correlation of the paleoseismic evidence (Table 3.1.3) with the historical record (Table 3.1.5) and the comparison of these results from four sections: EFE, EG, ZA1, and ZA2. In Figure 3.1.5 the historical dates of seismites are superimposed on the age-depth models to display the matching of the two models, the deposition model and the historical correlation model.

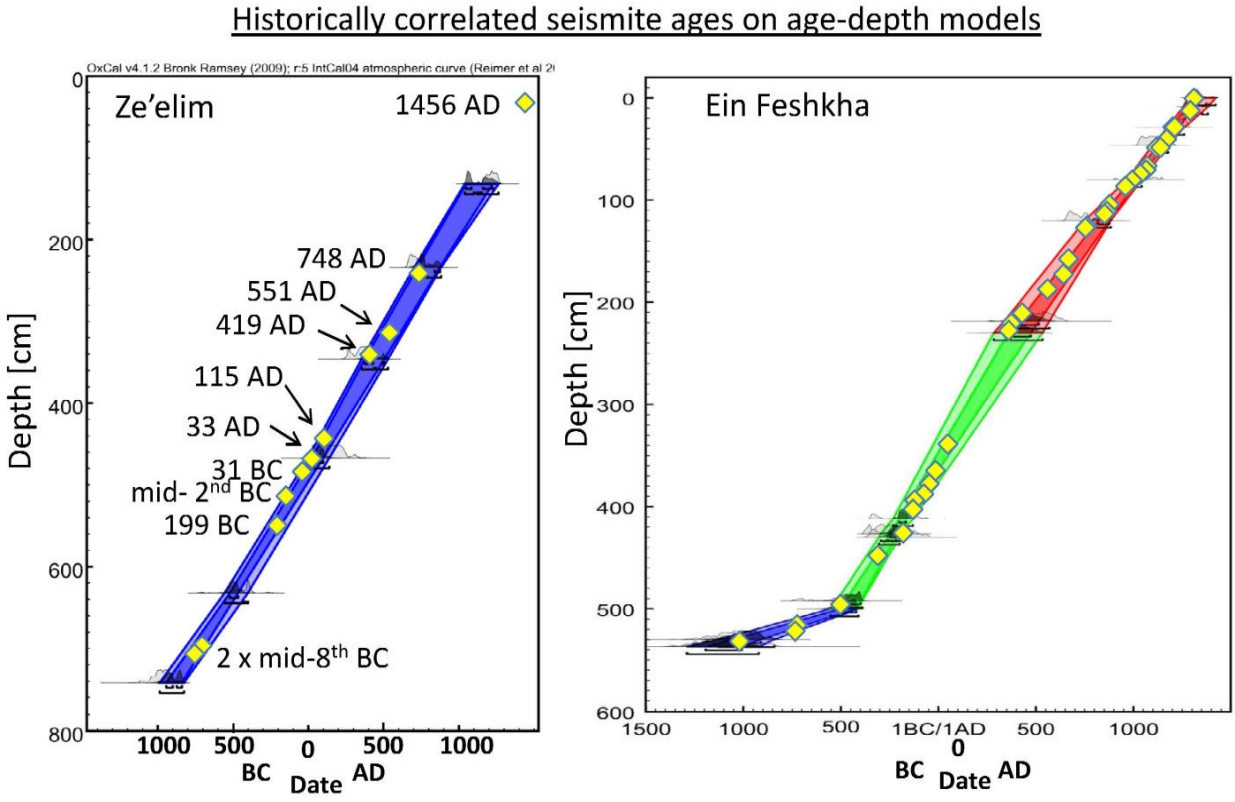

Figure 3.1.5. Correlation of historic earthquakes to age-depth model. Left panel: Ze'elim Gully outcrop. Right panel: Ein Feshkha outcrop. Squares indicate historic earthquake ages correlated to ages of seismites. Some historic earthquake dates are shown.

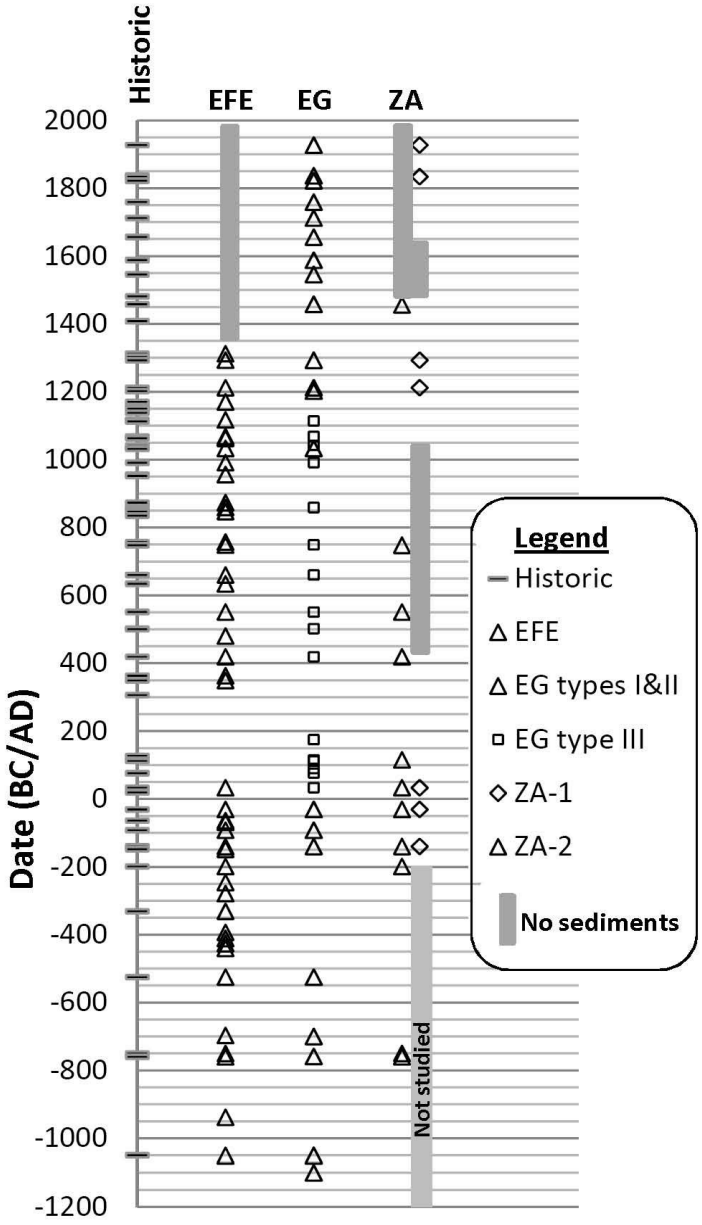

Figure 3.1.6. Comparative diagram showing seismites at Ein Feshkha (EFE), Ein Gedi (EG), and Ze'elim (ZA1 & ZA2) and historically documented earthquakes. EFE and ZA2 data from this study; ZA1 data after *Ken-Tor et al.* [2001a]; EG data from *Migowski et al.* [2004]. Information and references for historic events given in Table 3.1.5. Ages of seismites in diagram are the historical dates correlated to the seismite model ages or the model ages for seismite depths that are uncorrelated to historic events (see Table 3.1.3). The leftmost column displays historic earthquakes in the area (short horizontal lines). Seismites are indicated by triangles or diamonds. Microscopically detected seismites at EG are indicated by small squares. Periods where sediments are not available for study are indicated by grey vertical bars.

There are two possible sources of errors in a comparison between two archives, such as the historic earthquakes and the radiocarbon dated seismites. As noted in Table 3.1.3 the uncertainty in the age-depth model is variable but typically less than 100 years (2σ). This reflects the errors derived from the age-depth Bayesian model. The uncertainty in the "historic ages" of specific seismites reflects the spread of all historic earthquakes that lie within the 2σ model age range of the specific seismite depth (the right-hand column of Table 3.1.3). Thus, the errors on the Bayesian curve are the reasonable estimate of errors in the historical ages-seismite comparison. In other words we say that the maximum error in our comparison is less than 100 years, and as Table 3.1.3 shows typically lower than 50 years.
A special case is the couplet of earthquakes at 1202 and 1212 AD that, with the typical temporal resolution in Dead Sea sediments, are not resolvable. We chose to present them as a pair of events: 1202/1212 AD. The seismite at 28 cm depth at EFE has a 1σ model age of 1199-1240 AD, which includes both optional dates. Both the 1202 AD and 1212 AD are large M>7 earthquakes that ruptured far from the Dead Sea (north of the Sea of Galilee to Lebanon –minimum 130 km [*Marco et al.,* 2005] and south of the Arava – minimum 250 km , respectively). *Agnon et al.* [2006] show two adjacent seismites at this time in the EG core record and interpret these to represent both the 1202 AD and 1212 AD events. Both are candidates for this EFE seismite.

The Ein Gedi core was dated by 20 radiocarbon ages and by laminae-counting of ~1500 years, from 200 BC to 1300 AD [*Migowski*, 2001; *Migowski et al.*, 2004]. The laminae-counted floating chronology of the seismites was matched with the historic earthquake catalogue. The best fit history of *Migowski et al.* [2004] gave ages younger than their radiocarbon ages by 50-200 years, consistent with reworking of organic debris (e.g. wood) in the near-shore environment before settling to the bottom of the dense saline lake. In our analysis, the chronologies of the Ze'elim and Ein Feshkha sections indicate no long reworking time of the organic debris before settling in the sediment. When referring to the seismites from the Ein Gedi (EG) core *only***,** we use the shifted laminae-counted chronology of *Migowski et al.* [2004] for the EG section.

Note in Table 3.1.3 that the type B seismites, "homogenites", clearly correlate with important historic earthquakes, which supports their interpretation as seismites.

The recording of earthquakes by seismites, as well as by historical documents, requires intensity above respective thresholds. In this study our data suggest that these two thresholds are similar. Quiescence intervals are more robust than specific earthquakes, because they are less sensitive to individual date correlation. Specifically there is a quiescence interval in the seismite archive of the three sites from the end of the 2nd to the beginning of the 4th century AD (Figure 3.1.7). This correlates to an historic earthquake quiescence period noted without a single historically documented earthquake in the region from 127-306 AD (Table 3.1.5).

3.1.7.2 Summary of multi-site seismite distribution

Here we summarize the occurrence of seismites at the three sites presented above and in Table 3.1.4: Ein Feshkha (EFE), this study; Ein Gedi (EG core; after *Migowski et al.* [2004]); and the two Ze'elim Gully subsites: ZA1 (western, landward; after *Ken-Tor et al.* [2001] and *Agnon et al.* [2006]) and ZA2 (eastern, lakeward; this study), considered here forth as one site. We limit the comparison to the historical period starting at the 2nd century BC.

1) Seismites that appear in all three sites (termed here intra-basin seismites, IBS): **Mid-2nd century BC, 31 BC, 33 AD, 419 AD, 551 AD, 749 AD, 1202/1212 AD, 1293 AD, 1927 AD.**
2) Seismites that appear only in Ein Gedi: 76, 90, 112, 500/502, 1042, 1546, 1588, 1656, 1712, 1759, 1822 AD.
3) Seismites that appear only in Ein Feshkha: 64 BC, 349, 363, 634, 847, 859, 956, 1063, 1170, 1312 AD, and numerous older pre-historic seismites.
4) Seismites that appear in Ein Gedi and Ein Feshkha but not in Ze'elim: 92 BC, 660, 757, 873, 991*, 1033*, 1114/7*, 1068*. Stars indicate dates at which time there is no archive at Ze'elim.
5) There is one quiescence interval at ZA and EG ~ 500-150 BC and another at all three sites from the end of the 2nd to the middle of the 4th century AD

The new chronologies of the seismites in the Ze'elim (ZA) and Ein Feshkha (EFE) sedimentary sections are integrated with the high-resolution seismite chronology of the Ein Gedi (EG) core to produce a comprehensive archive of late Holocene paleoseismic earthquakes from the entire Dead Sea basin. The paleoseismic archives also provide an opportunity to re-evaluate a number of earthquake histories with timing and patterns (e.g. single or several episodes) that were not well established.

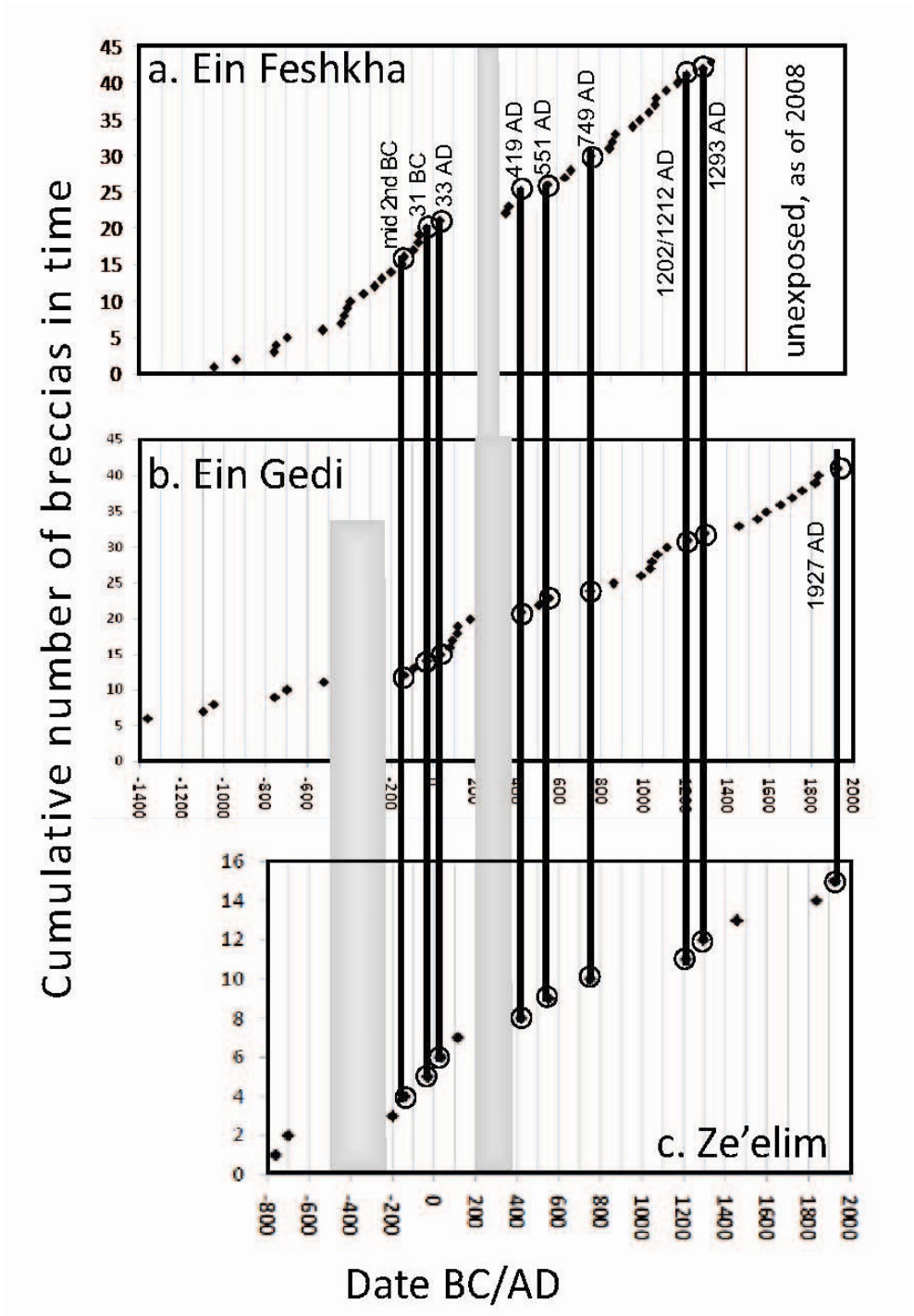

Figure 3.1.7. Recurrence intervals and cumulative number of breccias in time. a. Ein Feshkha (EFE), b. Ein Gedi (EG), c. Ze'elim (ZA1 & ZA2). Diamonds represent breccias, circled diamonds are the IBS (intra-basin seismites). Vertical grey bars indicate periods of seismic quiescence, the earlier (left) period is recorded at EG and ZA, the younger quiescence period (right) is recorded at all three sites. Vertical lines connect IBS events at the three sites.

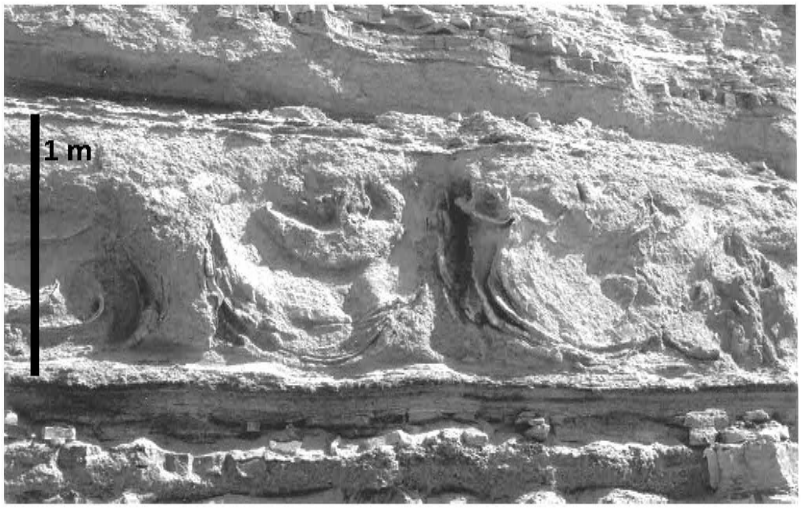

Figure 3.1.8. Photograph of liquefaction structure >1 m thick at Ze'elim Gully, correlative to the 1927 earthquake at the northern Dead Sea.

3.1.7.3 Site comparison

The chronologies that were established for the Ein Feshkha and Ze'elim sections combined with that of the Ein Gedi core [*Migowski et al.*, 2004] allow us to compare the recurrence time of the seismites in these sites and to produce an integrated picture for the appearance of seismites in the northern Dead Sea basin (Table 3.1.4, Figure 3.1.6). The number of seismites in the Ze'elim Gully sections is significantly smaller than at Ein Feshkha and Ein Gedi for the same time interval. *Ken Tor et al.* [2001a] and *Agnon et al.* [2006] recognized that the missing seismites at ZA1 (explained above) relate to sedimentary hiatuses in the section. The new section we described at ZA2 yielded an apparently continuous age-depth profile, and the hiatuses in the ZA1 section can be correlated with clastic-sandy sequences in the ZA2 section. One of the missing (sedimentary hiatus) earthquakes (in the landward ZA1 section) does appear in the continuous ZA2 section as liquefaction in a sandy unit (correlative to the historic earthquake of 551 AD). In two instances the situation is reversed, where two seismites, correlated to 1293 and 1212 AD appear in the more landward ZA1 outcrop, and do not appear in the more lakeward ZA2 section. This specific period is characterized by a sandy facies at ZA2 (Figure 3.1.4) and detailed detection is also inhibited by difficult access at this part of the section.

The EFE section has 52 seismites, while for the same time period the EG section shows 30 seismites. A quiescence period at EFE at around mid-1st to 3rd century AD is concurrent to a period in EG with microscopic seismites [Type III of *Migowski et al.,* 2004]. This could reflect the higher detection resolution of the Ein Gedi study. Despite this resolution difference, the situation is reversed in the pre-2nd century BC period where EFE has 25

seismites (<1cm to >9 cm) compared to 7 at EG. The recurrence of earthquakes in each one of these sections is illustrated as a cumulative function in Figure 3.1.7.

A quiescence at ZA and EG during a period of enhanced seismicity in the north (EFE) at ~ 500-150 BC (Figure 3.1.7) may suggest a period of moderate earthquakes concentrated north of the Dead Sea (i.e. Kalia fault). Additionally, there is a quiescence interval in the seismite archive of the three sites from the end of the 2nd to the middle of the 4th century AD, which correlates to an historic earthquake quiescence period 127-306 AD (Table 3.1.5). This is in line with the low seismicity interval during this period along the DST, the high seismicity period on the North Anatolian fault, and the mechanical coupling and alternation of activity of the two faults suggested by *Migowski et al.* [2004] and *Agnon et al.* [2006].

The comparison of EFE versus both EG and ZA clearly suggests higher activity in EFE. This can be explained by a difference in sensitivity between the sites, or the proximity of EFE to the Kalia transverse fault bounding the Dead Sea basin from the north (Figure 3.1.1). The EFE site is located on the continuation of this fault to the WNW, and has likely recorded local earthquakes of magnitude ~5.5 that were too far to affect EG and ZA. Also, several seismites (during the time interval of the historical charts) were recorded *only* at the northern site of Ein Feshkha (e.g. 64 BC, 349, 363, 634, 847, 859, 956, 1063, 1170, 1312 AD). Most of these events have destruction documented mainly in the northern Holy Land or further north (Antioch, Tyre, Turkey, see Table 3.1.5), 1312 AD being the main exception. Since the work of *Russell* [1980], the 363 AD earthquake is often considered as one that ruptured from the north to the Arava. We suggest that this interpretation congeals two earthquakes, one northern and another southern (see Table 3.1.5). The lack of documentation of earthquakes in the south can reflect bias due to population density, the south being more arid. However, the excess of recorded earthquakes at Ein Feshkha may corroborate higher seismic activity in the north. First let us consider the local setting of the Ein Feshkha Nature Reserve site: it is positioned at the edge of both the Jericho fault and the Kalia transverse fault (Figure 3.1.1). Ze'elim Gully, on the other hand, is several tens of kilometers from both Jericho and Arava faults, the likely sources of M>6.5 events. Therefore, earthquakes rupturing the northern part of the Jericho segment will record at Ein Feshkha but not at the southern sites. Likewise, magnitudes 5.5-6 from the Kalia fault may be recorded locally but not at the southern sites.

Our sites are located on the western shore of the lake, close to the western strand of the transform duplex. This observation may suggest an alternative explanation to the excess of earthquakes in the northern site EFE: The site is close to the Jordan (aka Jericho) fault that might act as a wave guide, a property documented for the plate boundary south and north of the Dead Sea [*Haberland et al.*, 2003; *Shtivelman et al.*, 2005]. Guided earthquake waves have been invoked to explain anomalous accelerations and damage in instrumentally recorded Dead Sea events [*Wust-Bloch*, 2002]. The seismite sites in the south (EG, ZA) are farther from the Jordan fault, and disconnected from the Araba/Arava fault. This explanation can be tested by a similar research on the eastern shore: it would predict that the southern sites there will show more frequent events.

Table 3.1.4. Multisite comparison of Holocene seismites from four lacustrine sediment sites along the western Dead Sea basin[a]

Historic[b]	Seismites at Sites			
	EFE	EG[c]	ZA1[d]	ZA2
1927 A.D.	**Macroseismic damage**	**10 cm**	**30 cm (ZB)**	
1834/1837 A.D.	3	cm	25 cm (ZB)	
1822 A.D.	3	cm	Lam	
1759 A.D. (x2)	2	cm	Lam	
1712 A.D.	12	cm	Lam	
1656 A.D.	4.	8 cm		
1588 A.D.	1	cm		
1546 A.D	3	cm		
1456/1458 A.D.	13	cm	10	cm
1312 A.D.	10 cm	Lam	Lam	Lam
1293 A.D.	**7 cm**	**1 cm**	**16 cm**	**sf, da**[e]
1212 A.D.	**2 cm**	**3 cm**[f]	**10.5 cm**	**sf, da**
1202 A.D.	**interchangeable with 1212 A.D.**	**1 cm**[f]	**interchangeable with 1212 A.D.**	**sf, da**
1170 A.D.	6 cm	Lam	sf	, da
1150 A.D.	2 cm	Lam	sf	, da
1114/1117 A.D.	interchangeable with 1150 A.D.	0.8 cm	sf	, da
1068 A.D.	1 cm	0.4 cm	sf	, da
1063 A.D.	1 cm	Lam	sf	, da
1042 A.D.	Lam	0.8 cm	sf	, da
1033 A.D. (x2)	1.5 cm	7.4 cm	sf	, da
991 A.D.	1.5 cm	0.2 cm	sf	, da
956 A.D.?	4 cm	Lam	La	m
873 A.D.?	6 cm	Lam	La	m
859 A.D.?	1.5 cm	0.8 cm	La	m
847 A.D.?	3 cm	Lam	La	m
746/749/757 A.D.	**1 cm**	**0.2 cm**		**2 cm**
746/749/757 A.D.	2.5 cm[g] La	m		Lam
660 A.D. (x2)	3 cm	0.5 cm	La	m
634 A.D.	1 cm	Lam	La	m
551 A.D.	**1 cm**	**0.3 cm**		**17 cm**
500/502 A.D.	Lam 0	.7 cm	La	m

Historic[b]	Seismites at Sites			
	EFE	EG[c]	ZA1[d]	ZA2
418–419 A.D.	**2 cm**	**0.5 cm**	**3 cm**	**5 cm**
MA = 365–595 A.D.	1 cm	Lam	Lam	Lam
363 A.D. x2	2 cm	Lam	Lam	Lam
349 A.D.	1 cm	Lam	Lam	Lam
MA=~175 A.D.	Lam	0.7 cm	Lam	Lam
115 A.D.	Lam	0.2 cm	Lam	5 cm
112 A.D.	Lam	0.5 cm	Lam	Lam
90 A.D.	Lam	0.5 cm	Lam	Lam
76 A.D.	Lam	0.4 cm	Lam	Lam
33 A.D.	**1 cm**	**0.2 cm**	**4.5 cm**	**4 cm**
31 B.C.	**1 cm**	**9 cm**	**20.5 cm**	**6 cm**
64 B.C.	<1 cm	Lam	Lam	
92 B.C.	1 cm	1 cm	Lam	Lam
MA = 133–6 B.C.	<1 cm	Lam	Lam	Lam
Mid-2nd century B.C.	**1 cm**	**1 cm**	**15 cm**	**8 cm**
Mid-2nd century B.C.	1.5 cm[g] La	m		Lam
199 B.C.	2 cm	Lam	8	cm
MA = 301–192 B.C.	2 cm	Lam	La	m
MA = 336–222 B.C.	2 cm	Lam	La	m
331 B.C.[h]	2 cm	Lam	La	m
MA = 458–328 B.C.	1 cm	Lam	La	m
MA = 477–346 B.C.	1 cm	Lam	La	m
MA = 492–361 B.C.	1 cm	Lam	La	m
MA = 507–373 B.C.	7.5 cm	Lam	La	m
525 B.C.[h]	5 cm	1 cm	La	m
MA = 817–577 B.C.	1.5 cm	Lam	La	m
Mid-8th century B.C.	**2 cm**	**2 cm**		**seismite**
Mid-8th century B.C.	**3 cm**	**5 cm**		**seismite**
MA = 1076–801 B.C.	1.5 cm	Lam		
~1050 B.C.[h]	>9 cm	5 cm		

[a]Bolded rows indicate the earthquakes observed at all three areas (EFE, EG, ZA): 1927, 1293, 1202/1212, 749, 551, 419, and 33 A.D. and 31 and mid-2nd century B.C. The four right columns exhibit either the seismite thickness (cm) correlated to that date, Lam (undeformed laminated sediments), missing section (hiatuses) (shown by empty column entry), or irregular bedding and discontinuous deformities which are difficult to define ages for (bottom two rows of ZA2 column). At depths where no historical earthquake can be correlated, model ages (MA) of the seismites are given (from Table 3 for EFE and from *Migowski et al*. [2004] for EG).

[b]Historic earthquakes based on catalogs and sources discussed in Appendix A.

[c]Data from Table 2 of *Migowski et al*. [2004], correlation of earthquakes to seismites from Ein Gedi core.

[d]*Ken-Tor et al.* [2001a], revised by *Agnon et al.* [2006]. ZB indicates seismites from the adjacent ZB Gully (termed Gully B by *Ken-Tor et al*. [2001a]).

[e]sf, sandy facies; da, difficult access.

[f]The 1202 A.D. earthquake shown to not be masked by the 1212 A.D. event, but to be apparent in Ein Gedi core [*Agnon et al.*, 2006]. The 1212 A.D. seismite thickness corrected in light of observation of laminae separating the 1212 A.D. event from the 1202 A.D. event.

[g]This adjacent seismite could be the one correlative to the IBS in the row above.

[h]The correlation to the historic earthquake could be valid instead for the seismites above and below the one indicated.

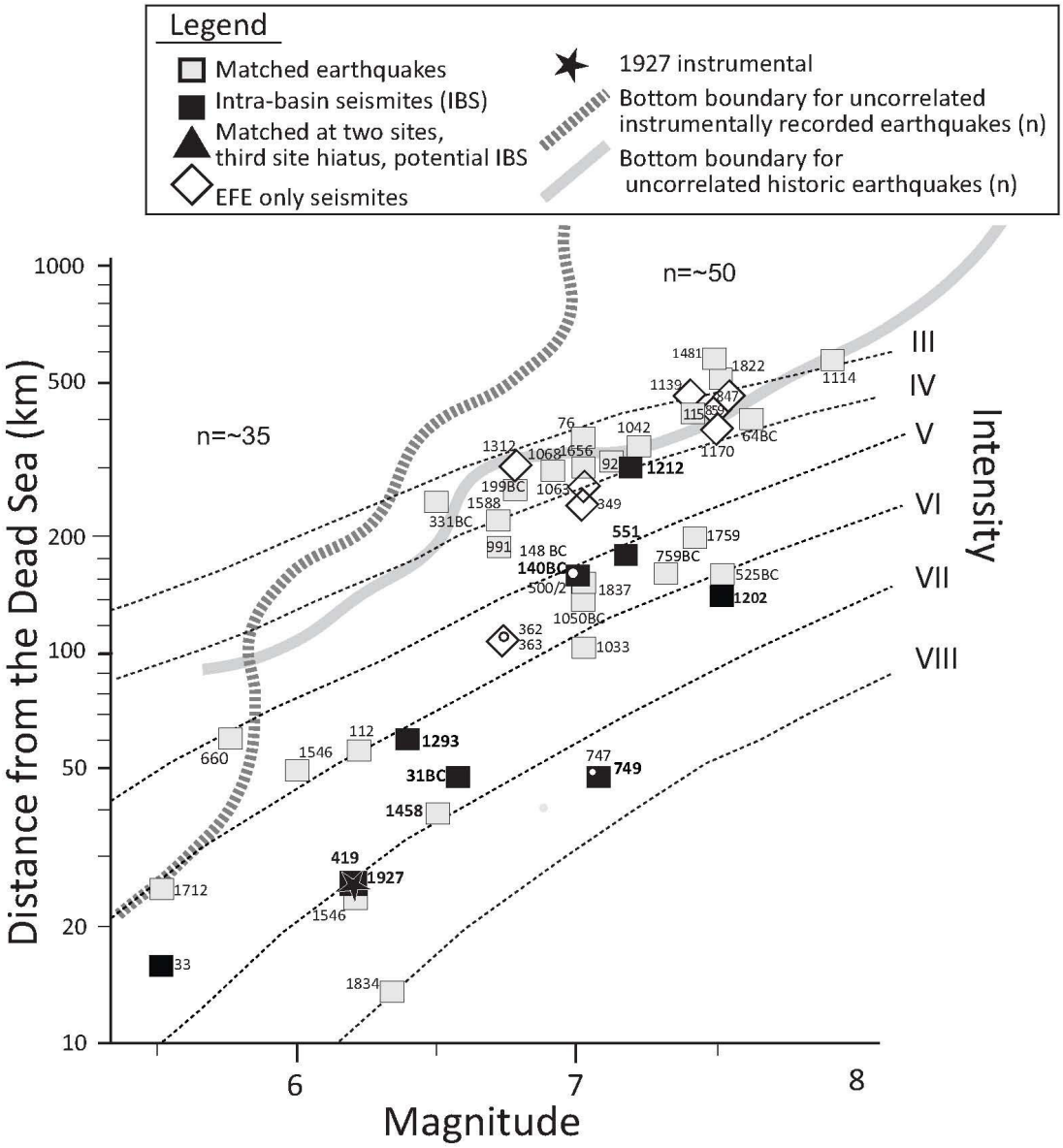

Figure 3.1.9. Magnitude-distance field showing regional and local earthquakes that could have affected the Dead Sea area. Each symbol represents a historic earthquake documented in the region and matched to a seismite (open squares). Some are matched to seismites at all three sites in the study (intra-basin seismites - IBS, solid squares). Distances are from the Ein Gedi site (Figure 3.1.1), for consistency with previous publications [*Migowski et al*., 2004; *Agnon et al.,* 2006]. A field corresponding to earthquakes (number of these earthquakes indicated by *n*) not matched to seismites is demarcated by the thick grey curves (above solid grey curve: earthquakes from historical catalogs, above dashed grey curve: instrumentally recorded events). Modifications made to the published diagrams are explained in the text and appendices. Also, second earthquakes were added at ~mid 2nd century BC, at 362/3 AD, and at 747/9 AD (see Table 3.1.5). The location and magnitude of these added events are difficult to estimate and are therefore not indicated by a separate symbol but are marked by a dot within the pair's symbol. Also, symbols were added for 331 BC, 199 BC, 835, and 847 AD, earthquakes, which are matched to seismites in this study but do not appear in the abovementioned previous works. For 847 AD the magnitude is taken from *Sbeinati et al.* [2005], while for the other added events magnitudes and isoseismal curves were calculated using the attenuation relationship of *Ambraseys and Jackson* [1998] (see text). Dashed lines are intensity lines plotted according to the equation (eq. 2) established by *Ambraseys and Jackson* [1998]. Where not indicated the date refers to AD.

3.1.7.4 Basin distribution

In this section we discuss the temporal distribution of seismites that are recorded at all of our sites (intra-basin seismites=IBS). Eight seismic events are recorded in all three sections, north, center, and south. In addition we add to this list the 1927 AD instrumentally recorded event that formed seismites at the EG and ZA1 sites for which macroseismic evidence was found along the Jordan River [1999] and caused slumping under the Dead Sea waters (interpreted by *Niemi and Ben-Avraham* [1994]) near the EFE site. The 1927 AD event also produced the most pronounced sedimentary structure (in the ZA Gully) with sand liquefaction reaching >1 meter in thickness (Figure 3.1.8). In addition, two seismites that were recovered from the Ze'elim and Ein Gedi sections and correlated to the 1458 and 1834/7 AD historical events are not represented in Ein Feshkha since this part of the section is missing. However we predict that processing of the upper part of the section preserved east of our EFE study site will recover these events. Note that the age of the seismite at ZA2 correlated to 1458 AD is above the dated and modeled part of the section and its age is extrapolated from the deposition model (see Figures 3.1.4 and 3.1.5). Part of this IBS group of seismites (mid 2nd century and 31 BC; 33, 419, 1212 and 1293 AD) appears in sedimentary sequences of the lacustrine facies indicating clearly offshore conditions of at least 10-20 meters of water above the sediment. Other IBS seismites (551, 749, and 1927 AD) were at near shore conditions (hiatus at ZA1, sand and lacustrine sediments at ZA2, lacustrine sediments at EFE and EG). Thus, we see no clear correlation between lacustrine conditions and the three-site seismite appearance. This observation is corroborated by the lack of seismites in intervals of the lacustrine section at Ze'elim while they appear in Ein Feshkha and Ein Gedi (e.g. between 830-1200 AD, see Table 3.1.4).

The conclusion that we can draw from these observations is that the temporal and spatial appearance of the seismites does not depend strongly on the limnological–sedimentological conditions. Seismites appear in both sandy facies and clay-evaporite (marly) sequences. The Ze'elim sections contain prominent sand layers that were clearly affected by earthquakes, producing liquefied structures. Significant earthquakes, such as 1927, do appear in all lithological units. This does not imply that low magnitude or remote earthquakes have no effect on sandy layers. The topic clearly requires more investigation. If sediments were deposited in the lake, they are affected by the earthquakes whether they comprise sands or marls. Figure 3.1.10 indicates that soil liquefaction and lacustrine brecciation have apparently similar thresholds. Hence, the archives we documented provide a reasonable picture of the earthquake activity and its effects in the lake basin, not filtered by the lacustrine environment. This conclusion opens the way for using the seismite spatial and temporal distribution to evaluate basin effects and recurrence patterns.

All seismites in the Dead Sea basin are marked on an epicentral distance versus magnitude diagram along with the field of instrumental earthquake data (Figure 3.1.9). This diagram highlights domains of intensity, which is a function of magnitude and distance of epicenter from the recording site. In Figure 3.1.9 the intensity lines are plotted according to the equation proposed by [*Ambraseys and Jackson*, 1998] (here termed *A&J*):

eq. 1 $$Ms=-1.54+0.65\,(I_i)+0.0029\,(R_i)+2.14\,\log(R_i)+0.32p$$

where $R_i=(r_i^2+9.7^2)^{0.5}$, r_i, in kilometers, is the mean isoseismal radius of intensity I, and p is zero for mean values and one for 84 percentile values [*Ambraseys* 1992; *Ambraseys and Jackson*, 1998]. This attenuation relationship is based on 123 instrumentally recorded shallow (depth<26 km) earthquakes from the Eastern Mediterranean from a period of 85 years and ~9000 intensity points. Different coefficients may be more appropriate for the magnitude-distance field of the earthquakes associated specifically with Dead Sea rift seismicity. The earthquakes plotted are mainly after the similar diagram in *Migowski et al.* [2004] and *Agnon et al.* [2006], where modified input data are explained below and in Table 3.1.5. Each symbol represents a historic earthquake documented in the region, matched to seismites (open squares), and some matched to seismites at all three sites in the study, the intra-basin seismites (IBS, solid squares). Distances are from the Ein Gedi site, for consistency with previous publications. A field corresponding to earthquakes not matched to seismites is demarcated by the thick grey curves (above solid grey curve: earthquakes from historical catalogs; above dashed grey curve: instrumentally recorded events). The magnitude-distance data for each historic earthquake has significant uncertainties (for examples see Figure 3.1.10); however this type of diagram has been shown to be useful [*Migowski et al.,* 2004] for portraying a pattern in the presence of a large sample, barring any systematic bias. Figure 3.1.10 depicts only the IBS with estimated uncertainties. Each earthquake shows as a rectangle. We were especially cautious when estimating the upper-left corner for each IBS rectangle. This corner, minimum magnitude and maximum distance, corresponds to the minimum intensity at the seismite site, which may be a threshold for intra-basin seismites. The considerations we applied when defining the IBS positions and uncertainties in Figure 3.1.10 are given here:

Mid-2nd century BC: *Guidoboni et al.* [1994] cite one event or more recorded at Antioch (for a summary of historica earthquakes in the region see Table 3.1.5; for locations of historical cities and towns see Figure 3.1.11). The only traceable historical record for an earthquake comes from the cultural and political center at Antioch, where buildings were reportedly damaged, and *Sbeinati et al.* [2005] assign local intensity I=VII. For comparison, the 1202 AD event was only *felt* in Antioch, no damage reported [*Ambraseys and Melville*, 1988; *Ambraseys*, 2009; *Guidoboni and Comastri*, 2005]. Therefore if the magnitude of the mid-2nd century BC event is smaller than M7.5 assigned for 1202 AD, then the source was closer to Antioch and farther from the Dead Sea. Hence for the mid-2nd century BC event we assign an uncertainty rectangle constrained by a bottom-left corner coinciding with the 1202 AD position. The rectangle represents a range of local intensities spanning V-VII at Antioch, where the distance is calculated to the closer end of the respective rupture (consistent with the magnitude) along the DST. For this specific earthquake we cannot, at present, constrain the top left corner.

31 BC: The magnitudes of 31 BC and 749 AD are set at 7.2 assuming similarity in rupture length, both reported to have ruptured the 110 km-long Jordan Valley segment [*Reches and Hoexter*, 1981]; the sites of damage attributed to the 31 BC event demarcate that segment. *[Ambraseys, 2009]* points out that 3.5 m dip-slip displacement reported by *Reches and Hoexter* [1981] would correspond to an earthquake too large comparing with the historical reports. However, the displacement is measured locally on unconsolidated sediments. *Reches and Hoexter* [1981] explicitly avoid rejecting the possibility that a part of the slip occurred during several centuries following the event. Moreover they are aware of local complications in the strike of the fault that amplify dip-slip. Hence we tentatively adopt the identification of the surface rupture with the 31 BC event. [*Gardosh et al.*, 1990] reevaluated the trench data in light of a newer geomorphic surface faulting study in the Dead Sea area. They conclude that

slip accumulation reaches 1.2 m for two events in the past 2000 years on the trench strand. The uncertainty range of the magnitude of this event (Figure 3.1.10) is projected from a minimum given by *Karcz* [2004] and a maximum given by the rupture length discussed here.

419 AD: Damage from this event was reported for Jerusalem and "many cities and towns" and "all great cities" [sources in *Russell*, 1985 and *Guidoboni et al.,* 1994]. Archaeological damage from Antipatris (central Holy Land) has been attributed to this earthquake [*Karcz and Kafri*, 1978] suggesting a Jordan Valley rupture. We think that it is feasible that the source of this event was similar to that of 1927 AD earthquake (see below). We assume a $6 \leq M \leq 6.5$, with a maximum distance of 50 km.

551 AD: The event was updated to a larger magnitude off-shore Lebanon earthquake, as is more widely accepted in the literature (Table 3.1.5). Magnitude estimation is based on sonar imaging of seafloor morphology [*Elias et al.*, 2007] and historical account compilation [*Sbeinati et al.,* 2005].

749 AD: The historical sources are consistent with a rupture event or two in the Jordan Valley (between the Dead Sea and Sea of Galilee). The range of magnitude (M6.6-7.7) in Figure 3.1.10 reflects either a single event or a double event with a cumulative rupture of that 110 km-long segment (calculated using [*Karcz*, 2004; *Marco et al.*, 2003; *Wells and Coppersmith*, 1994], Table 3.1.5).

1202/1212 AD: A single event brecciated the sediments in the EFE section in the early 13th century. Two events are recorded in the EG core. ZA recorded one or two events. Therefore only one of them is an IBS and the dating cannot rule which.

For the **1202** event we use M7.4-7.6 based on historical analysis of *Ambraseys and Melville* [1988] and *Ellenblum et al.* [1998]. Paleoseismic and archaeoseismic trenching corroborate these assessments [*Daeron et al.*, 2007; *Ellenblum et al.*, 1998; *Marco et al.*, 2005; *Nemer et al.*, 2008]. The distance of the rupture edge from the farthest seismite site is 165±10 km, based on rupture uncovered in trenching at the northern shore of the Sea of Galilee [*Marco et al.,* 2005].

For the **1212** event *Ambraseys et al.* [1994] suggest a rupture south of the Dead Sea or in the Gulf of Eilat (Red Sea). In severity of damage and aftershock occurrence it is seemingly similar to the 1995 modern event [*Hofstetter*, 2003], or could have been closer to the Dead Sea, according to the high level of damage at Aila and Karak. This similarity prompts us to give a best estimate of 7.2 magnitude and 300 km distance.

1293 AD: Based on evidence at an archeological site built on the Arava segment of the DST, the northern Arava did not rupture during this event [*Haynes et al.*, 2006]. We consider the 12 km-long Amatzyahu fault (Figure 3.1.1) as the source for this event. This rupture length is consistent with a 6.2-6.7 magnitude earthquake. The maximum intensity recorded for this event was recorded at Karak (eastern Dead Sea), 45 km from the Amatzaya fault [*N N Ambraseys et al.*, 1994], *Guidoboni and Comastri*, 2005] consistent with a magnitude of 6.7 according to the *A&J* equation (eq. 1). Taking into account poor construction and site effects this intensity could be achieved at a somewhat lower magnitude.

1927 AD: This event was recorded instrumentally [*Shapira et al.*, 1993] (M 6.2) and its distance uncertainty range is based on the distance from the ZA site to the Kalia transverse

fault in the northern Dead Sea (Figure 3.1.1). It is also a possible scenario that the main fault of the DST ruptured along a limited length causing the 1927 earthquake.

In addition to the above, other modifications (Figure 3.1.9) made to the published magnitude-distance diagrams are explained here. Regarding the 363 AD event, our review of the evidence indicates two or more separate earthquakes from ~362 and 363 AD, with damage in geographically disparate regions (see Table 3.1.5). Also, symbols were added (in Figure 3.1.9) for 331 BC, 199 BC, 835 AD, and 847 AD historic earthquakes, which are matched to seismites in this study, but not in previous studies at the Dead Sea basin. For the 331 BC event *[Sbeinati et al., 2005]* give intensity VI in the general region of "Syria". For this ancient and not well-covered event only a rough calculation is possible. An isoseismal distance of 70 km is consistent with a M6.5 earthquake using the attenuation relation of *A&J*. This is a relatively ancient event, population density was low, and a distance of ~70 km from seismic source to historic source is reasonable. For the 199 BC event, assuming the intensities documented are from the same event (VII and VIII in "Syria" – probably Damascus – and Sidon respectively, [*M. R. Sbeinati et al.*, 2005]), the magnitude is estimated in the same way to Ms=6.8. For 847 AD the magnitude is taken from the analysis of *Sbeinati et al.* [2005]. The 873 and 956 AD events [*Ambraseys et al.,* 1994, *Guidoboni et al*., 1994], matched to seismites in this study, are not on the distance-magnitude diagram for lack of sufficient information.

Second earthquakes were added at ~mid 2nd century BC, at 362/3 AD, and at 747/9 AD. The location and magnitude of these added events are not known, each appearing in the diagram as a small circle on the symbol of the previously published single event.

The intra-basin seismites that were recorded in all three sites (EFE, EG, ZA) define a well constrained field in the magnitude-distance diagram, which cuts the *A&*J intensity lines plotted (Figures 3.1.9 and 3.1.10).

We have excluded the **33 AD** IBS event from Figure 3.1.10 for lack of reliable historical evidence [see *Ambraseys*, 2009].

Of the earthquakes matched to seismites on this diagram 60% occupy the field of intensities larger or equal to IV. 89% of the IBS seismites occupy the field of intensities larger or equal to V (or 100% if 1202 is chosen over 1212 AD, see above discussion), as opposed to 46% of all seismites.

Figures 3.1.9 and 3.1.10 suggest that farther and stronger earthquakes require lower local intensities for being recorded in the entire basin (IBS). If we accept that 1212 AD is the IBS (as opposed to 1202) at the beginning of the 13th century then it is the farthest (300 km) with M7 and I=IV. Otherwise the 551 AD earthquake and the mid-second century BC earthquake are the farthest. The intensity threshold for magnitude 6.2 seems to be VII (419 and 1927 AD). A possible explanation for this observation is sensitivity to long period waves. The frequency content of the wave train is biased to long periods in earthquakes from large and remote sources. A M_s6 earthquake shows a corner frequency f_c~0.1 Hz (period ~10 s), whereas M_s7 shows f_c~0.04 (period 25 sec) [e.g. *Geller*, 1976]. Attenuation of the wave during travel, where the waves are damped according to the number of cycles between the source and the site in question, results in further bias toward lower frequencies.

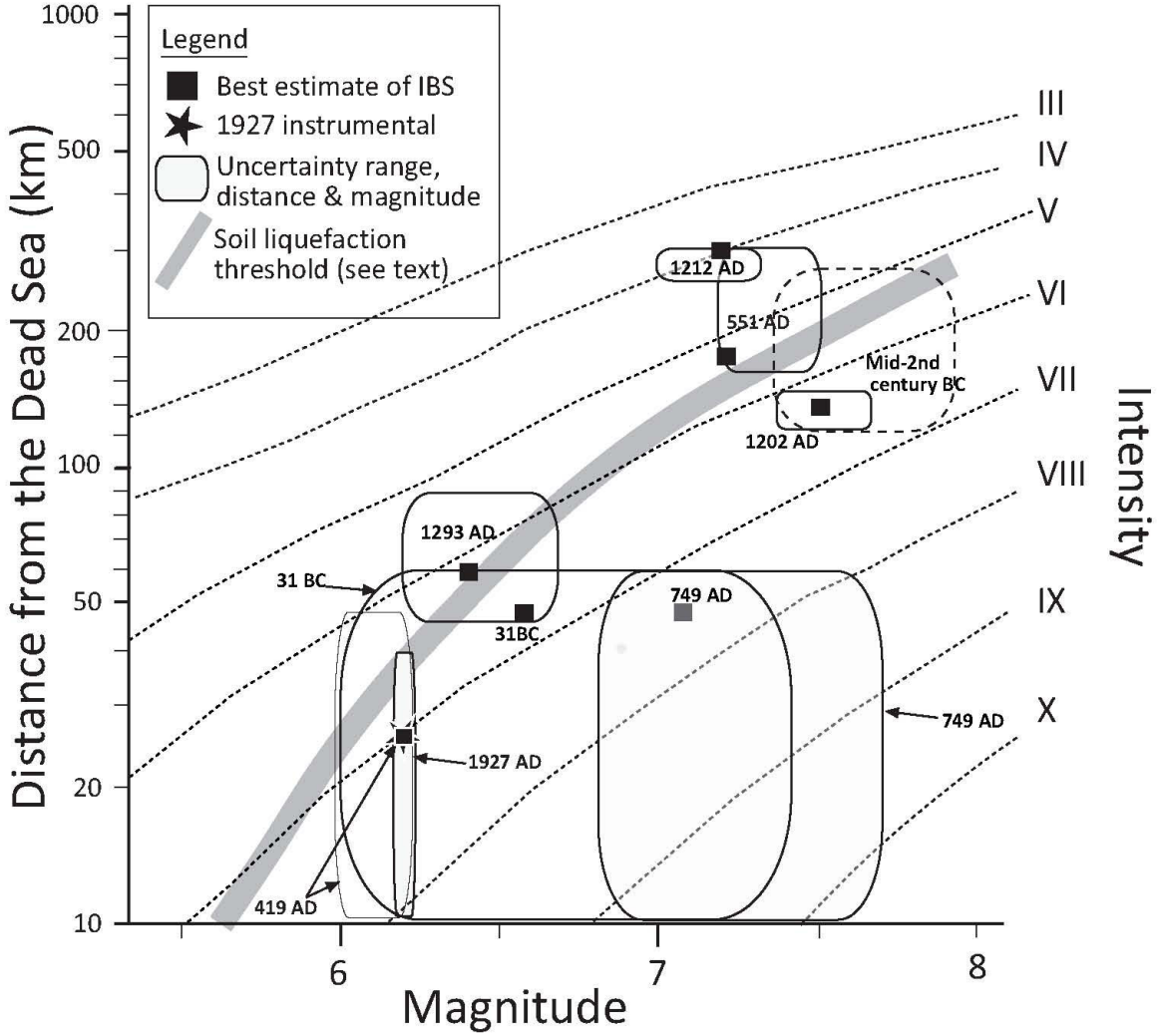

Figure 3.1.10. Intra-basin seismites (IBS) on distance–magnitude diagram. The width of each envelope includes the range of distance to the three seismite sites (maximum distance from furthest seismite site, and minimum distance from closest seismite site) and the estimated uncertainty based on historical, paleoseismic and tectonic considerations. The black squares represent the best estimate magnitude, and distance from Ein Gedi site (as in Figure 3.1.9). The thick grey curve represents the farthest epicentral distance of liquefaction of soil caused by modern earthquakes in the Aegean region [*Papathanassiou et al.*]. See text for detailed discussion. Dashed lines are intensities calculated using the attenuation relationship of *Ambraseys and Jackson* [1998].

The sensitivity to low frequency may indicate that the critical condition for brecciation may depend on ground velocity rather than ground acceleration, where the frequency equals the ratio of the latter to the former. *Heifetz et al.* [2005] and *Wetzler et al.* [2010] suggest a Kelvin-Helmholtz instability mechanism for the disturbances in the sediments (intraformational folding leading ultimately to brecciation). In this scenario the sediment bed is considered to have a gradient in the horizontal velocity (due to a density decrement). If the duration of the wave cycle is sufficiently long (or the frequency sufficiently low), a

disturbance can be sustained: the growth rate of a disturbance must be larger than the driving frequency.

The thick grey curve on Figure 3.1.10 represents the farthest epicentral distance of liquefaction of soil caused by modern earthquakes in the Aegean region [*Papathanassiou et al.*]. Note that if 1202 AD is the date of the early 13th century IBS (as opposed to 1212 AD) then the threshold for intra-basin seismite genesis is very similar to this soil liquefaction curve.

The average recurrence time of IBS is ~200 years, which is significantly longer than the ~50-95 yr based on all seismites in the Ein Gedi core during the past 1600 years [*Migowski et al.,* 2004] or ~50 yr at EFE since 525 BC. The possibility to establish a high-resolution comparison between distinct sedimentary sections located in different sites of the Dead Sea basin opens the way to further explore the response of the lacustrine system to various sources of seismic activity and thus extends the paleoseismic study to older sections such as those of the last glacial Lake Lisan. Such a comparison is currently under investigation.

Mid-8th century BC earthquakes revisited

An earthquake at this time has been linked historically to the prophecy by Amos of Teko'a and is mentioned numerous times in the bible (e.g. Amos 1:1, dated to 760 BC). In the rigorous historical work by [*Guidoboni et al.*, 1994] this event is considered the "only Biblical earthquake with sound and direct historical evidence". Previous discussions in the literature regarding the occurrence of one or two earthquakes [*Austin et al.*, 2000] can now be resolved by the paleoseismic evidence here. The Ein Feshkha (EFE), Ein Gedi (EG), and Ze'elim (ZA2) seismite records show two seismites at around this time. At EG the two seismites are separated by 4 cm while at ZA2 by 10 cm, and at EFE by 6 cm, which is comparable to a few decades.

The apparent southward decrease in extent of damage at archaeological sites in the region led *Austin et al.* [2000] to suggest an epicenter in Lebanon with local magnitude estimated at about 8. They argued that the recurrence interval of earthquakes during historical times was around a century and merged all damage observed in 8th century BC sites to one event. This argument has no basis in fact since there is a plentitude of evidence for couplets of earthquakes, for example the 1202 and 1212 AD [*Amiran et al.*, 1995; *Guidoboni and Comastri*, 2005; *Guidoboni et al.*, 1994]. Paleoseismological as well as historical evidence summarized by *Agnon et al.* [2006, Figure 3.1.13] points to recurrence intervals of 50-73 years for the period of 1000-1800 AD. Archaeological evidence of events is abundant throughout the area (see Figure 3.1.1 map of *Austin et al.* [2000]). Additional support of two events includes studies at Megiddo archaeological site [*Marco et al.*, 2006], which also show two deformation events, one post-dating 800 BC and the other postdating 700 BC. The archaeological dating of the strongest evidence for shaking has a resolution of approximately 100 years, so it could correlate with the Dead Sea seismites. Paleoseismic trenches at the Tel Rehov archaeological site near Bet She'an revealed a fault scarp created by two seismic events, one in the 7th and 6th century BC [*Ezra Zilberman et al.*, 2004]. Our results, in addition to those of other paleoseismological and archaeological studies, support two earthquakes during the mid-8th century BC.

3.1.8 Conclusions

1. This study established for the first time an integrated chronology of spatially distributed paleoearthquakes (seismites) in the late Holocene Dead Sea basin. Radiocarbon chronologies based on Bayesian statistics were constructed for two new stratigraphic sections at the northern and southern parts the basin (at the Ein Feshkha Nature Reserve and at the Ze'elim Gully, respectively). The ages of the seismites were compared with the paleoseismic chronology proposed for the Ein Gedi core [*Migowski et al*., 2004] located at the central part of the basin and with catalogues of historic earthquakes during the past 2000 years.

2. Temporal and spatial appearance of the seismites shows no strong dependency on the limnological–sedimentological conditions in the specific sections (representing lake conditions of up to several tens of meters depth). Sediments of various sedimentary facies were affected simultaneously by the earthquake's activity (e.g. liquefied sands and disturbed lacustrine marly sequences). Thus, the documented records provide a reasonable picture of the earthquake activity in the vicinity of the Dead Sea basin without being filtered by the sedimentary environment.

3. Several seismites (1927 AD, 1293 AD, 1202/1212 AD, 749 AD, 551 AD, 419 AD, 33 AD, 31 BC, and mid-2nd century BC were recorded in all three stratigraphic sections (termed IBS). The recurrence interval of the IBS during the period of continuous deposition is ~200 yr. Compiling the IBS record filters the shorter recurrence intervals of the individual records.

4. Several seismites (during the time interval of the historical catalogues) were recorded only at the northern site of Ein Feshkha (64 BC, 349, 363, 634, 847, 859, 956, 1063, 1170, 1312 AD) This may be due to the northern source of these events or to wave guiding along the main plate boundary.

5. Quiescence intervals in seismite appearance are apparent at ~ 500-150 BC at the two southern sites and from the end of the 2nd to the beginning of the 4th century AD at all three seismite sites. These are correlative to historic earthquake quiescence periods and suggest similar intensity thresholds for both types of data sets in this region.

6. The IBS define a steep diagonal array in the magnitude-distance diagram that lies in the sector of high intensity lines that were established by [*Ambraseys and Jackson*, 1998]. This is similar to the soil liquefaction threshold calculated for modern earthquakes in the Aegean region. Thus, the IBS provide a pattern of temporal behavior of relatively strong earthquakes that are associated with the Dead Sea transform.

Table 3.1.5. Earthquakes occurring in the region in the last three and a half millennia according to historical reports. Historical documentation is mostly reliable in the last two millennia. Some archaeological and paleoseismic evidence for the events is given in the footnotes. A location map of many of the sites mentioned in this table is given in Figure 3.1.11.

Date of Historic Earthquake	Location, description, discussion	References
1560 BC	BM: Destruction of Jericho. Put in writing by the scribes of the late Kings of Judea (7-th century B.C.E. [1]	BM, NE
1365 BC	Destruction of Ugarit (NW Syria). Tsunami at Syrian coasts. DV: The Amarna letters, written by Abi-milki of Tyre to Akhenaten, describe large-scale destruction to Ugarit, probably as a result of an earthquake. [2]	BM, DV, SB
1050 BC	AM3: Judaea, 1070 BC, spurious. BM: Archaeological evidence only, see footnote [3] BM	, AM3
Mid VIII cent. BC (1)	BM: Great destruction and many casualties in Judea, Samaria, and Galilee. Heavy damage in Sebastia and Jerusalem. Biblical references: Amos 1:1; Zecharia. 14: 3-5; Ezek. 38: 19-22; these refer to the reign of King Uzziah of Judah (~787-736 BC). GB1: This is the "only Biblical earthquake with sound and direct historical evidence". *Austin et al.* [2000] compared the archaeological and biblical information to decipher a single M 7.8-8.2 event based on the spurious assumption that only a single earthquake might hit the region in a century. The spatial extent and the apparent southward decrease in degree of damage at archaeological sites in the Holy Land led *Austin et al.* [2000] to suggest an epicenter in Lebanon.[4]	BM, KZ1, GB1, AU, AM3
Mid VIII cent. BC (2)	[5] Only archaeological evidence. Also see p. 49, this report.	
525 BC	Destruction at Sur, Sidon, felt at Kiklades (Greece). Tsunami at Lebanese coast. Unreliable.	BM,SB
331 BC	Earthquake causing destruction and casualties in Syria	SB
198/199 BC	Earthquake in Phoenicia (Lebanon), two thirds of Sidon collapsed, damage in Syria (after Posidonius, reliable, GB1).	GB1, AM3
Mid II cent. BC	GB1: 148 BC. Antioch destroyed. Due to Malalas' confusing chronology we may decipher two events (BM: 148 BC and 140 BC), see below.	BM,GB1, AM3
Mid II cent. BC	BM: 140 BC. A number of authors refer to elusive reports of one or more earthquakes and a tsunami between Antioch and Acre. Sea wave along Syrian coast.	BM,AM1, KZ2
92 BC	BM cites without a reference: "Big Tsunami hit Levantine coasts. Flooding of Pelusium. Felt in Syria, Egypt and The Holy Land." KZ2: Mentioned in Talmud (Megilat Ta'anit)" and classical sources, chronology and location unclear.	BM,AR, KZ2, SB
64 BC	Earthquake in northern Syria. Damage to Jerusalem, city walls damaged. BM: "Destruction of Antioch. Felt in Cyprus and the Holy Land. Damage to walls of second Temple in Jerusalem during the siege of the city by Horkanus and the Nabatians (A = 500 km). Destruction of Antioch." KZ2 carefully studies the historical evidence and locates the epicenter in the north of Syria based on Justinus (2nd century AD) and states that Talmudic source of information regarding damage to Jerusalem is very vague and may not refer to an earthquake, or only to people feeling the Syrian event, but not damaging anything.	WL,BM,AR, KZ2
31 BC	Josephus Flavius (Book I, chapter IXX):" at the beginning of the spring, the earth was shaken, and destroyed an immense number of cattle, with thirty thousand men; but the army received no harm, because it lay in the open air". KZ2 suggests this was a moderate event, with exaggerated or misinterpreted archaeological evidence.[6]	GB1, AM, AM3 KZ2
33 AD	WL (after Arvanitakis) documents damage to Jerusalem, Judea, Bithynie (Anatolia). New Testament (St. Matthew) mentions earthquake during time of the crucifixion.	BM, AR, WL, AM3

37 AD	After Malalas: An earthquake at Antioch, northern Syria.	GB1
76 AD	BM: "Destruction of Salamis (Famagusta), Kition (Larnaca), and Paphos (all in Cyprus). (Malalas). Felt in Syria.	BM, AM3
110-114 AD	Only archaeological evidence. [7]	AM1,AM3, RU2
115 AD	GB1: Antioch suffered extreme damage (after Dio Cassius). AM1: Tidal wave at Yavne. [8]	GB1, AM1, AM3
127 AD	GB1: Nicopolis (Imwas-Latrun) and Caesarea collapsed (single but reliable report by Eusebius).	GB1, KZ1
303 AD	Destruction at Tyre, Sidon, Gush Halav, damage to Khirbet Shema, Nabratein (near Safed), Jerusalem. Tsunami in Caesarea.	BM, AR, AM3
349 AD	BM: Off-coast earthquake, destruction at Beirut, Syrian coast. AM3: Dates to 347 AD.	BM, GB1, AM3
~362 AD and 363 AD	AR: From Paneas (Banyas) in the north to Petra in the south. GB1 (after various Christian sources): Great loss of life, destruction to Jerusalem, Bet Gubrin, Bet Shean, Sebastia, Nicopolis (Latrun), Lydda (Lod), Asclon (Ashkelon), Antipatris (Tel Afek), Ceasarea, Samaria, Gophna (near Ramallah), Petra, Tiberias, Hamat Gader, Jaffa, Paneas. AR (after Hieronymus): Seiche in southern Dead Sea. RU1 advocates the authenticity of Harvard Syriac 99, seemingly attributed during the 6th century to the contemporary Bishop Cyril of Jerusalem. Reviewing the evidence we are inclined to consider two or more separate earthquakes from ~362 (BM) and 363 AD, with damage in geographically separate regions.[9]	AR, GB1, RU1, AM3
418/419 AD	AR: Severe in Jerusalem. GB1 (after Augustine, Marcellinus, Hydatius): Severe earthquake, affected Jerusalem and other places in the country. AM3 prefers the date of 418 AD for this event.[10]	AR, GB1, AM3
500/502 AD	Destruction of Antioch. Damage to Safed. Felt in Turkey and Greece. AR: "Peripheral effect of severe earthquake in Syria". GB1 (after Joshua the stylite): Reports from Ptolomais (Acre), Tyre, Sidon. AM3: Destruction of Acre, probably off-shore.	AR, BM, AM3, SB
551 AD	Many catalogues (after Antoninus of Piacenza): Severe damage along Lebanese coast, Syria, tsunamis reported. GB1: Arabia, the Holy Land, Mesopotamia affected by aftershocks or secondary effects. Most authors place source offshore Lebanon, including paleoseismic studies[11]. AM1 placed source in Jordan Valley but recently updated this to Lebanon (AM3). SB concludes a 7.2 magnitude event near Tyre.	AM1, AR, BM, GB1, SB, AM3
634 AD	GB1: Earthquake in the Holy Land and a month of tremors, same time as comet and darkness.[12]	GB1
660 x2 AD	GB1, AR: Two events, one in June and one in Sept. 1st event: many collapses around the Holy Land, Jordan Valley, Rehov. 2nd event: deaths and damage to many churches in Jericho.	AR, GB1
746/7 and/or 749/750 and/or 757AD	AR: 749 AD, severe loss of life, damage to Susita, Arbel, Tiberias, Kasrin, Capernaum, Hamat Gader, Jerusalem, Lod, Jericho, Jerash, Philadelphia (Amman), tsunami at Mediterranean coast, seiche in Dead Sea; 756/757AD: Jerusalem, al-Aqsa mosque damaged. GB1: Various versions of exact chronology. KZ2 thoroughly studied the numerous Judaic, Christian, Samaritan, and Arab historical sources to conclude that there were at least two earthquakes, one in ~747 AD with a somewhat southern epicenter, and another one a few years later with much destruction in the central and northern Holy Land, probably damaging structures weakened by the previous event. AM3: Three distinct large earthquakes affecting the Holy Land and surrounding areas: (1) January 746, (2) 749/750, (2) ~March 757. [13]	KZ2, AM1, AM3, GB1, AR, SB
835 AD	Antioch. AM3:Spurious	GB1, SB, AM3
847 AD	Damascus (also felt in Antioch)	GB1, SB
853/4 AD*	Tiberias, landslide, many victims	GB1, SB
859 AD	GB1: Antioch, Mt. Casius (Syria). BM: "Total destruction. Earthquake felt in Mecca and caused damage in Jerusalem". Total destruction of Antioch. Damage in Jerusalem. Felt in Egypt, Turkey, Armenia, Mesopotamia, and Mecca. Tsunami. Other sources do not mention the Holy Land.	GB1, BM, SB
873 AD	Wadi Araba/Arabian Desert. [14]	AM1

952 AD	Aleppo, forty days of tremors causing damage and many casualties	GB1, AM3
956 AD	Egypt and Syria affected by destructive earthquake. Alexandria's lighthouse damaged. Only one historical second hand source given.	GB1, AM3
991 AD	BM: Dead Sea Fault, Bekaa-Syria. Great destruction and many casualties in Baalbek and Damascus. Felt as far as Egypt. GB (after Al-Antaki): Casualties in Damascus, Baalbek. SB: Tsunami. No reports of damage to The Holy Land.	BM, GB1, AM3
1032 AD	BM: Offshore Mediterranean, tsunami. Heavy damage in Gaza. Felt in Jerusalem and Negev. Spurious since other catalogues do not mention this event.	AR, BM
1033 AD	AJ: Surface rupture at Jordan, Holy Land. GB2: Heaviest damage to Ramla, also Nablus, Jericho, Acre (Akko), Balas (location uncertain), as far as Jerusalem. Tsunami at Acre.	AJ, BM, AR, AM1, AM3, GB2
1042 AD	Destruction of Palmyra (Tudmor) and Baalbek. Felt in Lebanon, Tabriz (Iran), and Egypt. No mention of Holy Land.	BM, GB2, AM3
1063 AD	Strong earthquakes struck coast from Turkey to Lebanon. Tripoli, Antioch, Laodicea (Denizli, Turkey), Tyre damaged.	AR, GB2, AM3
1068 AD March	All inhabitants of Aila killed. All structures destroyed. New fissures and springs formed at Aila. New springs also at Tabuk and Taima (NE Saudi Arabia). [15]	AR,BM, GB2, AM3
1068 AD May	All houses in Ramla collapsed. Paneas and Jerusalem damaged. 15 000 victims, Euphrates overflowed. Sea surge on Mediterranean coast with many victims. Previously the two 1068 AD earthquakes were taken to be one event. GB2 analyses and concludes that there were **two** events. Some reports of this and previous earthquake may be indistinguishable. AJ: surface faulting at Hejaz (Saudi Arabia).	GB2, AJ, AM3
1113/1114 AD	After 1st hand account by Fulk of Chartres: July or August, felt in Jerusalem, no details of damage or what happened elsewhere. Later this year another earthquake near Antioch occurred, often confused in catalogues with the August event. AM3: 1113 AD Jerusalem, 1114 AD probably at Sea of Galilee.	GB2, AM3
1114 AD	Severe event. Antioch destroyed, all of Syria affected. Felt in Jerusalem.	AR, GB2
1115 AD	AR: Disastrous in Syria, moderate in Jerusalem. GB2: Southern Turkey	GB2, AR
1117 AD	Many buildings destroyed in Jerusalem. GB2: Scandelion fortress destroyed.	GB2, AR, AM3
1138-1139 AD	Near Syrian-Turkish border. Seismic sequence, destructive, from 1138-1139 for 8 months. Most serious damage to Aleppo, Edessa, as far as Damascus, Mesopotamia.	AM1, GB2
~1150 AD	GB2 (after John Phocas): Between Jericho and Jerusalem, destroyed two monasteries (St. John the Baptist and Mar Elias).	GB2
1156-1157 AD	Numerous destructive earthquakes in Syria. No mention of damage to Holy Land.	GB2, AR, AM3
1170 AD	GB2: Widespread event. Numerous historical sources. Aleppo, Antioch, Tripoli, Bekaa Valley, Bagdad, Basra. Months of aftershocks. No mention of effects in the Holy Land by GB2. On the other hand, AR: hundreds perished in the Holy Land, quotes other catalogues, no original sources. BM: Damage to Jerusalem, source not mentioned. WL: Caesarea thrown down. [16]	GB2,AR, BM,WL,AM1
1202 AD	Very destructive earthquake, affected Lebanon, Syria, the Holy Land coasts and in-land. GB2: Acre and Tyre most severely affected. Paneas, Safed, Nablus seriously damaged. Slight damage in Jerusalem. Landslides in Bekaa Valley. AR: Tsunami near Acre. BM: Great damage and many victims. Monuments and temples in Baalbek collapsed. Destruction in Tripoli, Tyre, Acre, Nablus, and Tiberias. Felt in Mesopotamia, Anatolia, Cyprus, and Egypt. [17]	GB2,AR, BM
1212 AD	Severe damage to Aila, Cairo. AM3: Severe damage to the monastery at St. Catherine (Sinai Peninsula). Karak also damaged. AM1: One year of aftershocks.[18]	AR, AM1, AM3, GB2
1293 AD	GB2: Most serious damage at Karak. Reports from Ramla, Lod, Gaza, Qaqun.[19]	AR, AM1
1303 AD	Egypt, Damascus, Safed, felt and tsunami in Acre. GB2: Maybe 2 events, one in Crete, the other in Egypt. Confusing reports.	AR,GB2, AM1

1312 AD	Destructive earthquake in northern Red Sea area, destruction in Sinai. Other catalogues do not mention this event.	AR
1408 AD	GB2: Western Syria, Cyprus. Rupture "more than a mile long". Tsunami, landslides. Heavy damage also in Antioch and Aleppo. AJ: 20 km rupture at Orontes (Syria).	GB2,BM, AJ
1458 AD*	Southern Holy Land and Jerusalem, destruction and casualties in Karak. GB2 places source near Karak. Destruction at Hebron, Jerusalem, Ramla.	AR, AM1, AM3
1481 AD, March	GB2: Cyprus and Egypt. AM3: Eastern Mediterranean, reports from Rhodes to Cairo.	GB2, AM3
1546 AD	Damage and casualties in Safed, Tiberias, Ramla, Jaffa, Jerusalem, Hebron, Gaza, Karak, and numerous in Nablus. Tsunami in Mediterranean, seiche at Dead Sea. Felt in Damascus. AK: Highly exaggerated, only a medium-size event affecting mainly Jerusalem.[20]	AM3, BM, AR, AK
1588 AD	Aila, southern Sinai, Cairo	AM1, AM3, BM
1656 AD	Destruction at Tripoli (Lebanon), felt in the Holy Land (numerous sources, see SB). AM3: Confused with Tripoli, Libya.	AR, BM, SB, AM3
1712 AD	Shook houses in Jerusalem, some damage. Felt in Ramla, but not in Jaffa. Other catalogues do not mention this event.	AR
1759 AD, Oct.	Affected most of the Holy Land and Syria. Heavy destruction in Safed, Tiberias, Qunaitra (Syria). Tsunami in Sea of Galilee. Followed by series of strong aftershocks. [21]	AR, SB, BM, AM3
1759 AD Nov.	Baalbek temple destroyed. Damascus, Antioch and Jaffa damaged heavily. AM3: Tiberias, already in a parlous state was ruined. (Two events in the same year, may be confusion between reports)	AR, BM, AM3
1822 AD	Destruction at Antioch and Aleppo. Felt in Beirut, Sidon, Jerusalem, Gaza, and Cyprus. Tsunami at Iskanderouna and Beirut.	AM3, AR, BM
1834 AD	Damage in Jerusalem, Bethlehem, Nablus, Gaza, Karak, Madaba (Jordan). Damage to old walls in Jaffa and Caesarea. Asphalt floated on Dead Sea	AM3, AR
1837 AD	Thousands of casualties in the Holy Land and some in Lebanon. Most severe in Safed and Tiberias. Seiche in Sea of Galilee. Damage and casualties in Nazareth, Acre, Haifa, Samaria, Nablus, Karak. Large blocks of bitumen floated on Dead Sea.	AM3, AR, BM
1927 AD	Entire Holy Land suffered great damage. Felt in Syria and Lebanon. Recorded instrumentally to M=6.2. Locally strongest instrumentally recorded earthquake up to date. Maximum intensity in Jordan Valley.[22]	AM1, BM, AR, AV

Notes:

*attributed to proximate year by different sources. The information here is predominantly from historical catalogues, which are based on ancient sources. References: AJ = *Ambraseys and Jackson*, 1998; AK = *Ambraseys and Karcz*, 1992; AM1 = *Ambraseys et al.*, 1994; AM2 = *Ambraseys*, 1962; AM3 = *Ambraseys*, 2009; AR = *Amiran et al.*, 1994; AV = *Avni*, 1999; BM = *Ben-Menahem*, 1991; DV = *Dever*, 1992; GB1 = *Guidoboni et al*., 1994; GB2 = *Guidoboni and Comastri*, 2005; KZ1 = *Karcz and Kafri*, 1978; KZ2 = *Karcz*, 2004; NE = *Neev and Emery*, 1995; NR = *Nur and Ron*, 1997; RU1 = *Russell*, 1980; RU2 = *Russell*, 1985; SB = *Sbeinati et al*., 2005; SC = *Schaeffer*, 1948; WL = *Willis*, 1928. There were various places in history called Antioch, a common name for towns. We assume the present-day Antakya (southern Turkey) to be the Antioch mentioned in the earthquake catalogues.

[1]BM: Recent archaeological excavations at Tel-Dir-Ala have shown that the city was destroyed by an earthquake close to that time. In Jericho and Tel Beit-Mirsim, a layer of ash was found, dated circa 1560 BC, followed by a break of the occupation of these cities for the next 100 years .

[2] SC: Archaeological evidence at Shamra I (Ugarit). NR: ~1400 BC earthquake at Jericho, archaeological evidence. SB: Destruction at Megiddo VIII and Beit Mirsin, Jericho.

[3] BM alludes to unspecified archaeological destruction at the Timna Copper mines. Megiddo - post ca. 1200 BC damage to Late Bronze gate and Chamber f. Archaeological evidence at Dor [*Stewart*, 1993; *Marco et al.*, 2006]

[4]Megiddo damage postdating ca. 800 BC; *Yadin* [1956] has attributed some damage to a mid VIII century earthquake, yet this interpretation needs to be reviewed [*Marco et al.,* 2006)]. See AM3 for exhaustive list of archaeological sites with damage claimed to be from this event.

[5] Megiddo damage postdating ca. 700 BC [*Marco et al.*, 2006].

[6] Slip and deformation along the Jericho Fault [*Reches and Hoexter*, 1981].

[7] Archaeological evidence for destruction at Petra, Massada, Avdat and others [*Amiran et al.,* 1994].

[8] Missyaf fault segment ruptures ancient Roman aqueduct [*Meghraoui et al.*, 2003].

[9] Archaeological evidence for earthquake damage inferred to 363 AD [*Thomas et al.*, 2007].

[10] Archaeological evidence of damage to Khirbet Shema (collapsed synagogue) [*Russell*, 1985].

[11] *Elias et al.* [2007] argue, using geophysical evidence, that the source of this event is rupture of the offshore ~100–150-km-long active, eastdipping Mount Lebanon thrust.

[12] Qasr Tilah rupture [*Haynes et al.*, 2006] in 634 or 660 AD events. Northern Wadi Araba fault.

[13] Paleoseismic and archaeological evidence at Galei Kinneret (Tiberias) indicate a 100-km-long rupture segment between the Sea of Galilee and the Dead Sea pull-apart basins M > 7 [*Marco et al.,* 2003]; paleoseismic evidence of slip and deformation along the Jericho fault and archaeological evidence of the Hisham fault shearing the Hisham Palace in Jericho [*Reches and Hoexter*, 1981]. Archaeological and numismatic evidence at Bet Shean [*Ambraseys*, 2005]. Umm-El-Qanatir archaeological site, ~10 km east of the Sea of Galilee, was damaged by an earthquake-induced landslide and exhibits extensive typical seismogenic damage dated to this historic earthquake [*Wechsler et al.*, 2009]

[14] Qasr Tilah rupture [*Haynes et al.*, 2006], Northern Wadi Araba fault.

[15] Qasr Tilah rupture [*Haynes et al.*, 2006], Northern Wadi Araba fault. Uplift in Avrona Playa (Elat fault zone) and destruction of an irrigation system by surface deformation [*Zilberman et al*., 2005].

[16] Missyaf fault segment ruptures ancient Roman aqueduct [*Meghraoui et al.*, 2003].

[17] Paleoseismic trenching in the Yammoûneh basin yields evidence both for slip on the Yammoûneh fault in the twelfth–thirteenth centuries and for the lack of a posterior event [*Daeron et al.*, 2007]. Vadum Iacob fortress offset by 1.6 m [*Ellenblum et al.*, 1998]. Buried stream channels at Bet-Zayda (northern Sea of Galilee) have been displaced by the Jordan fault are excavated by 3-D trenching and are dated to this event [*Marco et al.*, 2005]

[18] Did not rupture the northern Arava according to *Haynes et al*. [2006]. *Zilberman et al.* [2005] place this event at the eastern fault bounding the Elat depression (between Aqaba and Nuweiba).

[19] Did not rupture the northern Arava according to *Haynes et al*. [2006].

[20] Qasr Tilah rupture [*Haynes et al.*, 2006], Northern Wadi Araba fault.

[21] Vadum Iacob fortress offset by 0.5 m [*Ellenblum et al.*, 1998]. Buried stream channels at Bet-Zayda (northern Sea of Galilee) have been displaced by the Jordan fault are excavated by 3-D trenching and are dated to this event [*Marco et al.*, 2005].

[22] Deformed sediments in Darga river bed attributed to this earthquake [*Enzel et al.*, 2000]. Seismic-reflection data suggest a large submarine slump was caused by this event [*Niemi and Ben-Avraham*, 1994].

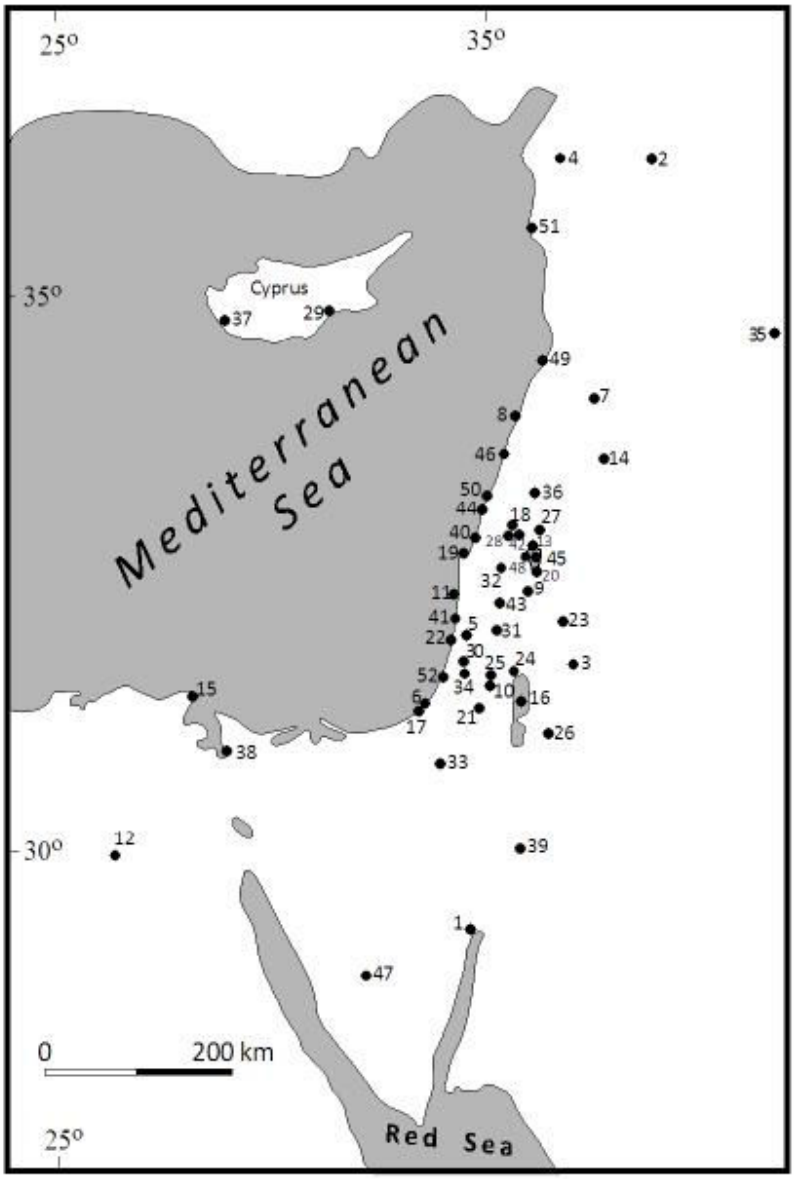

Figure 3.1.11. Map of historical locations mentioned in the manuscript and in Table 3.1.5, based on Google Earth (http://www.google.com/earth/index.html), *Guidoboni and Comastri* [2005], *Guidoboni et al*. [1994], and *Ambraseys* [2009].

Key to map numbers; modern location names are given in parentheses: 1, Aila (Aqaba); 2, Aleppo (Halab); 3, Amman (Philadelphia); 4, Antioch; 5, Antipatris (Tel Afek); 6, Asclon (Ashkelon); 7, Baalbek; 8, Beirut; 9, Bet Shean; 10, Bethlehem; 11, Caesarea; 12, Cairo; 13, Capernaum; 14, Damascus; 15, Damietta; 16, Dead Sea; 17, Gaza; 18, Gush Halav–Jish; 19, Haifa; 20, Hamat Gader; 21, Hebron; 22, Jaffa; 23, Jerash; 24, Jericho; 25, Jerusalem; 26, Karak; 27, Kasrin (Qatzrin); 28, Khirbet Shema; 29, Kition (Larnaca); 30, Lydda (Lod) (Ramla is adjacent to Lydda); 31, Nablus; 32, Nazareth; 33, Nicopolis (Imwas-Latrun); 34, Palmyra (Tudmor); 35, Paneas (Banyias); 36, Paphos; 37, Pelusium; 38, Petra; 39, Ptolemais (Acre-Akka-Akko); 40, Qaqun (Netanya); 41, Safed; 42, Samaria; 43, Scandelion (Iskandarouna); 44, Sea of Galilee; 45, Sidon; 46, St. Catherine monastery (Sinai); 47, Tiberias; 48, Tripoli; 49, Tyre (Sur); 50, Ugarit; 51, Yavne.

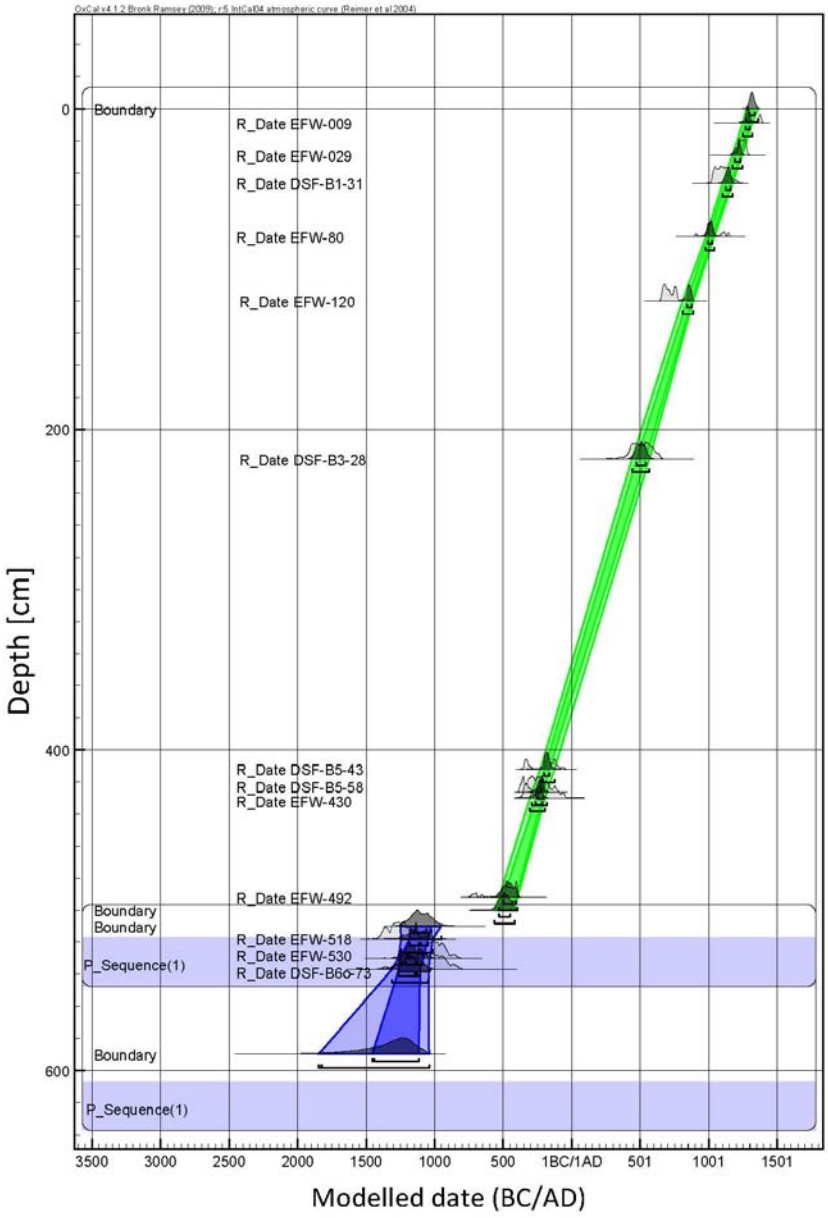

Figure 3.1.12. Example of an alternative age-depth model for the EFE section. Here, the chronology of the section is Bayesian-modeled as two spaces: 0-500 cm depth and 500-590 cm depth. There are no internal boundaries (see manuscript for explanation of terms) within the top 500 cm. The 518 cm depth radiocarbon sample is included in this model, whereas in the chosen model (Figure 3.1.3) this too old sample is considered an outlier and excluded from the model. The inclusion of the 518 cm depth sample forces the model to include a long hiatus at the 500 cm depth of this uninterrupted lacustrine section, which is inconsistent with data from climate and limnology studies. The lack of internal boundaries between 0 and 500 cm causes the model to have a very low agreement index of 4.3 at 120 cm depth, whereas the chosen model (Figure 3.1.3) has an agreement index of 13.7 at this depth, also low, but significantly higher than this model. This alternative model extends to the base of the section at 590 cm depth. The deepest radiocarbon age is at 537 cm depth. The lack of ages below 537 cm causes the model to have a very wide 2-sigma range towards the base of the section, and the model ages of the seismites extracted from this model at these depths are of no use. In the chosen scenario (Figure 3.1.3) the model bottom boundary is at 537 cm depth, the depth of the deepest radiocarbon age. In any case, the top 500 cm of this model gives very similar seismite ages to those from the chosen model and if this model was chosen the paleoseismic conclusions would be very similar.

3.2 *Paleoearthquakes as anchor points in Bayesian radiocarbon deposition models: a case study from the Dead Sea*

3.2.1 Introduction

Radiocarbon dating of terrestrial organic debris (assumed to have formed under atmospheric equilibrium) is a major tool in establishing chronologies of late Pleistocene and Holocene sedimentary sections for paleoseismology studies [*Ken Tor et al.,* 2001; *Migowski et al.,* 2004; *Lienkaemper and Bronk Ramsey,* 2009; and references therein]. With the development of the northern hemisphere radiocarbon calibration curve it is possible to determine accurate ages with a precision of typically *ca.* 100-300 years (95%) for single measurements for Holocene samples. However in many cases the determination of accurate chronology of a sedimentary sequence is hampered by lack of material for dating, recycling of the organic debris, diagenesis, hiatuses and other factors [examples from the Dead Sea basin: *Ken-Tor et al.,* 2001; *Migowski et al.,* 2004; *Neumann et al.,* 2007]. These problems are partly eliminated by the construction of age-depth models that apply uniform sedimentation rates (linear regressions) for the studied sections. For more complex sedimentation patterns and to incorporate typical radiocarbon asymmetrical uncertainties Bayesian techniques are useful which also integrate prior information within the age-depth models [e.g. *Bronk Ramsey,* 2008]. Prior information could comprise known ages of specific stratigraphic horizons in the studied section, textural composition of the sediments, changes in sedimentary facies, depositional boundaries and others (see section below). Here we present a case study from the Dead Sea basin (Figure 3.2.1) where we use historic earthquakes correlated to disturbed layers as prior information-anchors in an age-depth deposition model to improve and better constrain the regression age model. This model will be used to retrieve a high-resolution paleoseismic record of the seismically active Dead Sea Transform area.

3.2.2 Bayesian age-depth modeling

The mathematical details of Bayesian modeling are explained in detail in the literature [e.g. *Buck et al.,* 1991; *D'Agostini,* 2003; *Bronk Ramsey*, 2008]. The approach taken in this paper and the explanations in this paragraph are based mainly on that laid out in Bronk Ramsey [2008] and *Blockley et al.* [2008]. The age models for the Ein Feshkha site were built using the radiocarbon calibration software OxCal 4.1, and key terms will be explained here. Bayesian analysis uses prior information and suppositions when generating a model from any data set. This incorporation is usually termed the *Prior*. The fundamental assumption in Bayesian modeling of stratigraphic sequences is that age increases with depth. This prior requires use of a function termed usually as *Boundaries*. These boundaries separate different sedimentary units that may have different sedimentation rates, grain sizes, facies, and are also placed on the top and bottom of the entire series to constrain the model to a specific time frame. With no other information this would be treated by what is usually termed the *Sequence* model. A uniform sedimentation rate would be treated with the *U_Sequence* type model. Depth and other dating information can be included in a less rigid way using Poisson distribution priors, termed *P_Sequence* models, where the time gap between deposition of grains varies, and the events are basically random, however deposition is given approximate proportionality to depth. This entails the estimation of the uniformity of the deposition (given as the *k parameter*), which indicates the increment size (conceptually the grain size, or size of

deposition events) and signifies the relationship between the events and the stratigraphic process.

All events in the sequence and therefore in the model are related to stratigraphic depths

The stages of modeling are as follows:

- Evaluate the sedimentary sequence, noting any depths where deposition characteristics clearly change (in this case the top of the section under consideration is at 0cm, the bottom at 500cm and there is a facies change from darker to lighter sediments at 348cm).

- Identify the depths at which there are any obvious signs of earthquake activity in the sequence (appearance of seismites).

- Radiocarbon date samples through the sequence at specific depths. This provides constraints on the timing of deposition.

- Evaluate the expected uniformity of deposition. For example, if there is a 100 cm thickness of sediment and the dates of the top and bottom of this sequence are known, with what uncertainty can you say that the point half way down this was deposited at the midpoint in time between the top and bottom? In this case, for a 5% uncertainty in this (approximately Normally distributed) we choose a k value of $1cm^{-1}$ which corresponds to a nominal event size of 1 cm.

- Construct an age depth model with *Boundaries* at the top, bottom and at any depths where there is likely to have been a major deposition change.

- Decide at what resolution you need to interpolate the age-depth model. For an interpolation rate of 1 every 10cm (or 0.1/cm) we use an interpolation parameter of 0.1, so in this case the model is set up with the P_Sequence command:

```
P_Sequence("",1,0.1);
```

- Run the age-depth model with the radiocarbon dating information as the only time control.

- Interpolate between the radiocarbon dated points using the model, to determine a first estimate for the dates of each of the identified horizons.

- Decide whether any of the observed seismites can be confidently assigned to historically documented and dated earthquakes. If so, this information can be added to the model as *anchors*, and the model run again including this additional information.

- Interpolate between the ages and boundaries defined in the model to get final date probability distributions and ranges for all earthquake depths in the sequence.

As with any Bayesian model, the results of the analysis are dependent on the data that has been included and on all of the prior information supplied and assumptions that have been made. A comparison of the unanchored and anchored distributions (as shown in Figure 3.2.5) shows the degree to which the prior knowledge of the historic earthquake impacts on the

model output (or posterior). It is also important to remember that the rigidity of the deposition model (as defined above and shown clearly in the interpolation between points in the right panel of Figure 3.2.5), is defined by the model and not by the data.

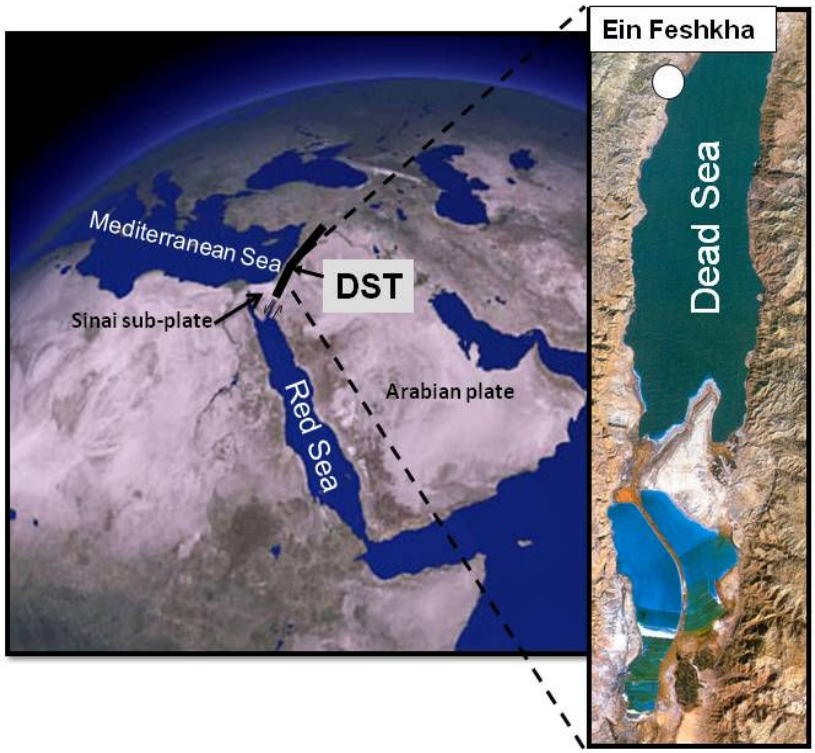

Figure 3.2.1. Satellite image of Dead Sea Transform (DST) (red line) with zoom in (right) to the Dead Sea. White circle indicates Ein Feshkha Gully site.

3.2.3 The Ein Feshkha section at the northern Dead Sea basin and its paleoseismic record

The sediments of the Holocene Dead Sea compose the Ze'elim Formation of the Dead Sea Group. This sedimentary sequence has been deposited within the Dead Sea pull-apart basin that formed by slip along the Dead Sea Transform, an active tectonic boundary between the Arabian plate and the Sinai sub-plate (Figure 3.2.1). Destructive earthquakes occurring in the area during the past four millennia have been documented in catalogues [i.e. *Ben-Menahem,* 1991; *Ambraseys et al.,* 1994; *Amiran et al*., 1994; *Guidoboni et al.*, 1994; *Guidobini and Comastri*, 2005]. The sediments represent various depositional environments: fluvial, fan deltas, shores, and lacustrine (see detailed description in [*Bookman (Ken-Tor) et al.*, 2004]. The mainly anthropogenic drop of the current lake level (~100 cm/a) has triggered deep incision along the retreating shores. These incised gullies have provided excellent opportunities to study the late Holocene sedimentary sections in details. At the Ein Feshkha nature reserve (Figure 3.2.1) new gullies were formed recently exposing the late Holocene section (spanning between ~ 4000 to 600 y BP [*Neumann et al.*, 2007]). The outcrop exposes

the laminated lacustrine marls (mainly calcitic silts and clays) and sequences of laminated primary aragonite and fine detritus. Fifty-two layers in this normally laminated sequence display disturbed sedimentary features (Figure 3.2.2) (details of the seismite sedimentary features is given in Kagan et al. submitted). Based on previous studies of similar disturbed layers [*Marco et al.* 1996; *Ken-Tor et al.* 2001; *Migowski et al.* 2004] it was proposed that the disturbed layers represent earthquake markers and are termed seismites. The appearance of multiple types of seismites in the sedimentary section as well as the availability of numerous radiocarbon-datable organic debris open the opportunity to retrieve a high- resolution paleoseismic record of this seismically active area. This record can be integrated with the chronology of historic earthquakes available for this region. At the same time the best known historic earthquakes can be used as anchors in Bayesian models to improve the radiocarbon chronology of the studied section.

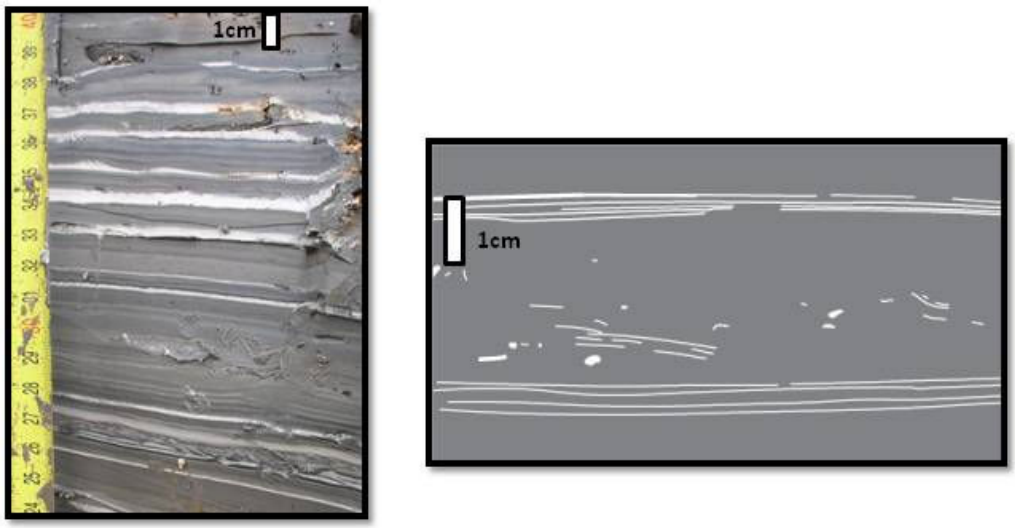

Figure 3.2.2. Left: Ein Feshkha Gully wall outcrop showing sequences of laminated primary aragonite and fine detritus. Right: Schematic diagram of brecciated laminae. Fragmented laminae are "floating" in dark matrix.

3.2.4 Radiocarbon dating of the section and the introduction of Bayesian modeling

The chronology of the Ein Feshkha (EFE) section is constructed by radiocarbon dating of terrestrial organic debris (mainly small pieces of wood and twigs). Six samples from the outcrop were prepared for radiocarbon dating at the Radiocarbon laboratory, Weizmann Institute, Rehovot, Israel [see *Neumann et al.* 2007]. The samples were then measured by accelerator mass spectrometry (AMS) at the NSF-radiocarbon facility in Arizona. Four additional organic debris samples were taken from a correlated drilled-core located on the cliff bounding the gully (a mere few meters away) and were analyzed at the AMS facility in Kiel. The core was correlated with the outcrop by Marcus Schwab at GFZ-Potsdam based on high-resolution stratigraphic correlation of sedimentary markers, which included unusually thick aragonite laminae, aragonite-clay laminated sequences, and deformed layers, and was aided by the unmodeled calibrated radiocarbon dates. Radiocarbon ages are reported (Table 3.2.1) in conventional radiocarbon years (before present =1950) in accordance with international convention [*Stuiver and Polach*, 1977]. Calibrated ages (= cal BP) were calculated by applying the INTCAL04 calibration scheme of [*Reimer et al.*, 2004] by means

of the OxCal v. 4.1 program [*Bronk Ramsey*, 1995; 2001; *Bronk Ramsey*, 2008] (Figure 3.2.4).

The age–depth models that incorporate Bayesian modeling are constructed in several steps that are illustrated schematically in the flow chart of Figure 3.2.3. The radiocarbon ages (listed in Table 3.2.1) are treated by a simple Bayesian P_Sequence deposition model. The model applies a k factor of 1 [which implies for the mid-point of a 1m section a 5% uncertainty in interpolation, see *Bronk Ramsey*, 2008, equation 17A] (Figure 3.2.5, left panel). The next step embodies the interpolation of seismite ages using the OxCal (v4.1) program and the Bayesian model. This results in a model age range for each seismite depth (not shown). Then we correlate the historically documented earthquake dates with the seismite model age ranges. This procedure is analogous to floating chronology matching, where the entire sequence of historic earthquakes is matched to the sequence of model ages of seismites from the section [e.g. *Migowski et al*., 2004]. However, in this case both data sets are time constrained, the historical record has negligible uncertainty in the ages of the earthquakes in the past two millennia, and the seismite age uncertainties are given by the model age ranges. Relative historically documented intensities, interseismic intervals, and other seismicity parameters are taken into consideration when various historic earthquakes can be fit to the same seismites. Then prominent earthquakes in the historical record were selected as anchor points (see below). These anchors were inserted into the OxCal v4.1 model code as specific calendar ages (function termed *C_Date*). We then reiterate the model using the anchors (Figure 3.2.5, right panel). In the final step we reinterpolate all seismite depths from the new anchored model to extract high resolution model ages for all seismites (results in a future paper).

Table 3.2.1. Radiocarbon dates of organic debris from the Ein Feshkha lacustrine outcrop and core. Depths of prominent earthquakes used as anchors are shown in italics along with the historical dates of these events.

Sample nr	Lab nr	Depth below surface (cm)	^{14}C yr (BP)	Calibrated age range (1 σ)	Calibrated age range (2 σ)
EFW-009	RTT5174	9	700 ± 40	AD 1269–1382	AD 1243–1392
Anchor		*28*		*AD 1212*	
EFW-029	RTT5175	29	780 ± 40	AD 1223–1271	AD 1179–1285
DSF-B1-31	KIA32722	46.5	933 ± 36	AD 1039–1155	AD 1022–1183
EFW-80	RTT5176	80	1015 ± 40	AD 980–1117	AD 899–1155
EFW-120	RTT5177	120	1310 ± 40	AD 661–768	AD 648–779
Anchor		*125*		*AD 757*	
Anchor		*210*		*AD 419*	
DSF B3-28	KIA11641	218.5	1541 ± 68	AD 432–576	AD 392–646
Anchor		*338*		*31 BC*	
DSF-B5-43	KIA11642	412	2143 ± 27	345–113 BC	351–59 BC
DSF-B5-58	KIA32723	426.5	2215 ± 29	359–207 BC	376–201 BC
EFW-430	RTT5180	430	2150 ± 45	350–110 BC	359–52 BC
EFW-492	RTT5181	492	2380 ± 40	510–396 BC	741–385 BC

3.2.5 Incorporation of earthquake anchors to the Bayesian model

Fifty-two ages of seismite horizons were interpolated from the non-anchored Bayesian model of the Ein Feshkha outcrop that is presented in Figure 3.2.5, left panel. The calendar age of each seismite is limited by the model age range interpolated from the non-anchored model. The chronology of historic earthquakes [i.e. *Ben-Menahem*, 1991; *Ambraseys et al.,* 1994; *Amiran*, 1994; *Guidoboni et al.*, 1994; *Guidobini and Comastri*, 2005] was then matched to the non-anchored Bayesian model of the Ein Feshkha section.

Four seismite ages were then selected according to the following criteria: I- their historical match represents prominent earthquakes in the historical catalogues, II-they are identified in other sections of the Dead Sea basin [*Ken-Tor et al.,* 2001b; *Migowski et al.,* 2004], III- they are very close to radiocarbon age samples, IV- the matched historic earthquake falls well inside the model age range and does not fall into any of the other possible model ages for such events. The anchors chosen are: 1212 AD, 757 AD, 419 AD, 31 BC. These anchors were inserted into the OxCal model code as calendar ages (C_Date). We then ran the OxCal model again using the anchors (Figure 3.2.5, right panel). The code for the OxCal model with anchors is given in Figure 3.2.6.

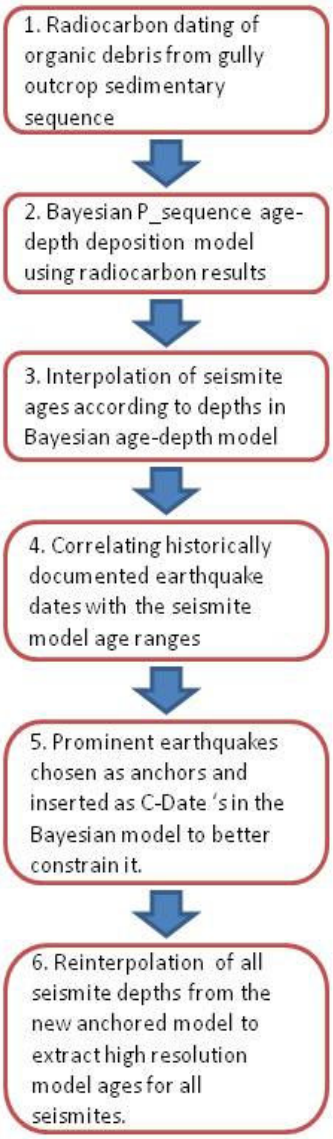

Figure 3.2.3. Flow chart describing steps in Bayesian age-depth modeling of paleoseismic record with earthquake anchors.

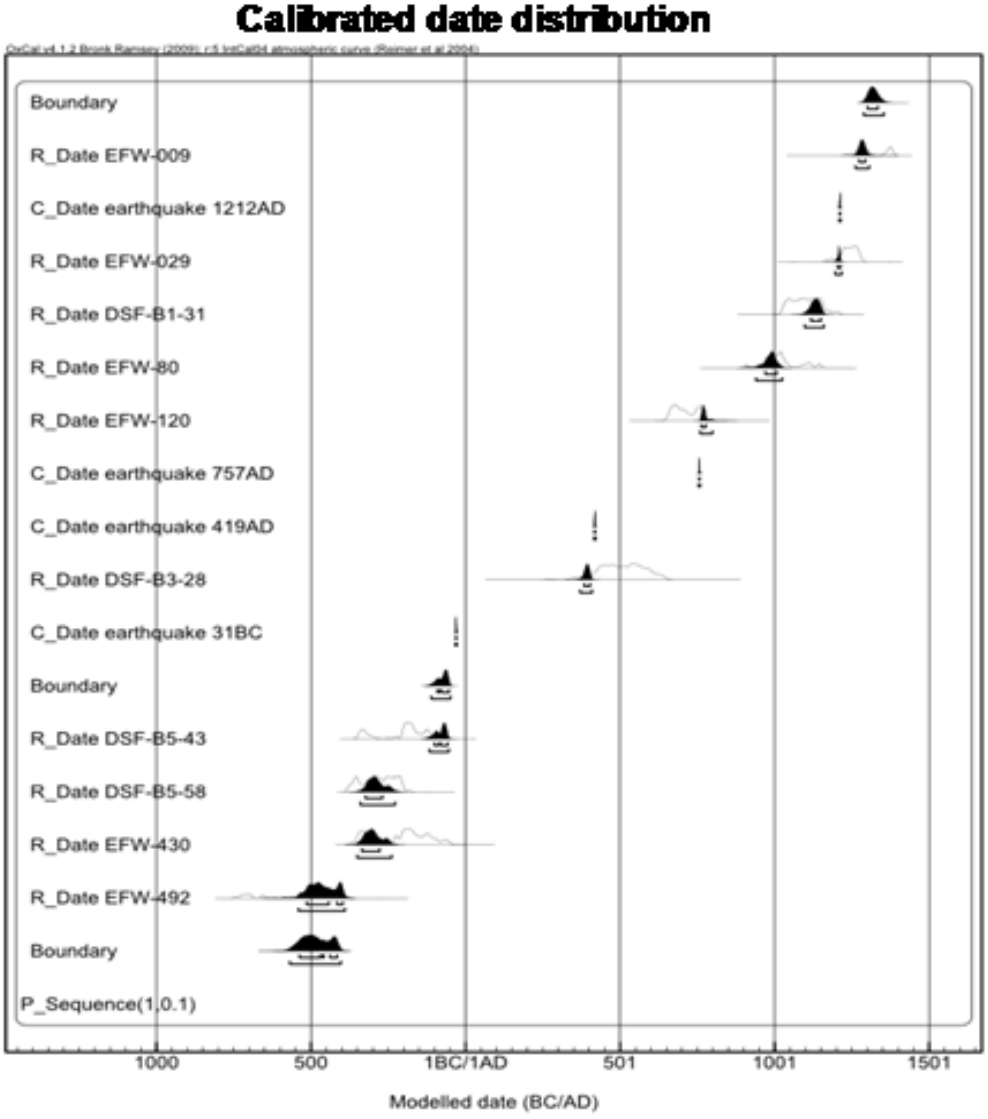

Figure 3.2.4. Date distribution of calibrated radiocarbon ages.

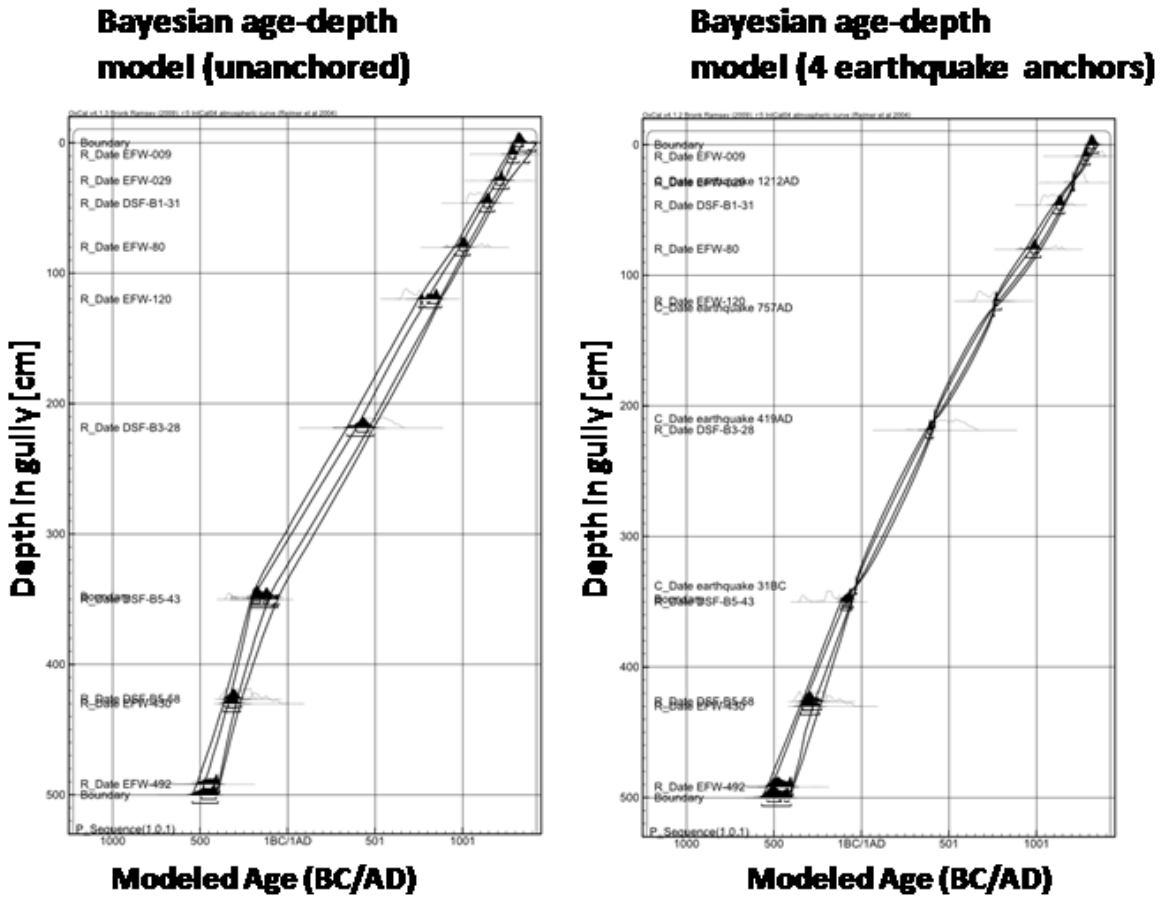

Figure 3.2.5. Bayesian P_sequence age-depth models for the top 5 m of the Ein Feshkha Gully exposure. The two parts in each model are joined by a model boundary stemming from a change in deposition rate and sedimentary features. Left: OxCal age-depth model using 10 radiocarbon ages (R_Date). Right: age-depth model using 10 radiocarbon ages (R_Date) and 4 historic earthquake dates used as anchors (C_Date).

```
Plot()
{
 P_Sequence("",1,0.1)
 {
  Boundary(){ z=500; };
  R_Date("EFW-492",2380,40) { z=492; };
  R_Date("EFW-430",2150,45) { z=430; };
  R_Date("DSF-B5-58",2215,29) { z=426.5; };
  R_Date("DSF-B5-43",2143,27) { z=350; };
  Boundary() { z=348; };
  C_Date("earthquake 31BC", BC(31), 1) { z=338; };
  R_Date("DSF-B3-28",1541,68) { z=218.5; };
  C_Date("earthquake 419AD", AD(419), 1) { z=210; };
  C_Date("earthquake 757AD", AD(757), 1) { z=125; };
  R_Date("EFW-120",1310,40) { z=120; };
  R_Date("EFW-80",1015,40) { z=80; };
  R_Date("DSF-B1-31",933,36) { z=46.5; };
  R_Date("EFW-029",780,40) { z=29; };
  C_Date("earthquake 1212AD", AD(1212), 1) { z=28; };
  R_Date("EFW-009",700,40) { z=9; };
  Boundary() { z=0; };
 };
};
```

Figure 3.2.6. Code for the *anchored* age-depth OxCal 4.1 Bayesian deposition model (the unanchored model code is virtually the same but without the *C_Date* entries).

3.2.6 Conclusions

1. The Bayesian statistical method of the OxCal (v4.1) program is used to construct an age-depth model for a set of AMS radiocarbon ages of organic debris collected from a late Holocene Dead Sea stratigraphic section (the Ein Feshkha Nature Reserve). The paper tests the benefits of constraining the model to prior historic earthquake information; in this case, ages of several prominent historic earthquakes that occurred in the studied area.

2. The anchor-based model provided a tightly constrained age-depth regression. However, the "non-anchored" model as well produces a seismite/historical-earthquake correlation where all of the 68% or 95% age ranges of the seismites can be correlated to historic earthquakes.

3. The procedure developed here opens the way for establishing a high-resolution and accurate chronology for the paleo-earthquake records of the Dead Sea basin, and possibly other locations where prior and independent (paleoseismic) information can be incorporated with the radiocarbon dating of the sedimentary section.

3.3 *Dating speleoseismites near the Dead Sea Transform and the Carmel fault: clues to coupling of a plate boundary and its branch*

3.3.1 Introduction

The N-S left lateral Dead Sea transform (DST) fault system dominates the tectonic regime throughout the Levant (Figure 3.3.1). Historical, archeological, and paleoseismic information derived from this fault system, as well as recent earthquakes, have shown the potential for earthquakes of M7.5, [*Ambraseys and Jackson*, 1998; *Ellenblum et al*., 1998; *Baer et al*., 1999], and perhaps M7.8 and higher [*Hough and Avni*, 2011; *Kagan et al*., 2005]. Earthquakes of, or close to, these proportions are known to have affected the area of the Judean Hills in historic times, causing damage in Jerusalem and other communities of the region (Figure 3.3.1) [e.g. *Hough and Avni*, 2009/2010; *Ambraseys*, 2009]. The first major earthquake on the DST to be recorded instrumentally was M6.2 on the 11th of July, 1927 in the northern Dead Sea (Figure 3.3.1) [*Avni*, 1999]. The location of the event is given by an error uncertainty ellipse in Figure 3.3.1, which is based on best estimate of seismological data [*Shapira et al*., 1993] and tectonic considerations [*Kagan et al*., 2011].

The Carmel fault (CF) branches off the DST in the area of Beth-She'an in a NW-SE direction (Figure 3.3.1). The CF includes a wide seismogenic zone, bounded to the by the Gilboa fault (GF), and continuing NW into the continental shelf in the Mediterranean Sea [*Ben-Avraham and Hall*, 1977; *Ben-Gai and Ben-Avraham*, 1995; *Rybakov et al*., 2000]. Small earthquakes along the CF have been monitored systematically since the 1980's [*Hofstetter et al*., 1996; *Nof et al.,* 2007]. In 1984 a M_L=5.3 earthquake was recorded along this fault system and minor damage was reported to structures in Haifa and adjacent towns [*Hofstetter et al*., 1996; *Rotstein et al*., 2004]. However, it is still not clear whether this fault can generate earthquakes of higher magnitude and intensities.

Recent studies have focused on the neotectonics of the CF at the archaeological site of Megiddo [*Marco et al.,* 2006] and analysis of a shutter ridge along the Yagur segment of the CF [*Zilberman et al*., 2008]. These studies join a wider body of research on paleoseismology of the DST [e.g. *Amit et al*., 2002; *Agnon et al*., 2006; *Daeron et al*., 2007; *Haynes et al*., 2006; *Elias et al*., 2007; *Nemer et al*., 2008; *Katz et al*., 2011; *Shaked et al*., 2011]. The southern DST extends south of the Levant restraining bend (LRB) and is divided into the following sectors (north to south): Jordan Valley (JV), Dead Sea basin (DSB), Arava Valley (AV), and the Gulf of Aqaba (Figures 3.3.1, 3.3.2). For the purpose of the present study, we refer to the area where the CF splays off the DST as the transition between the JV and the DSB.

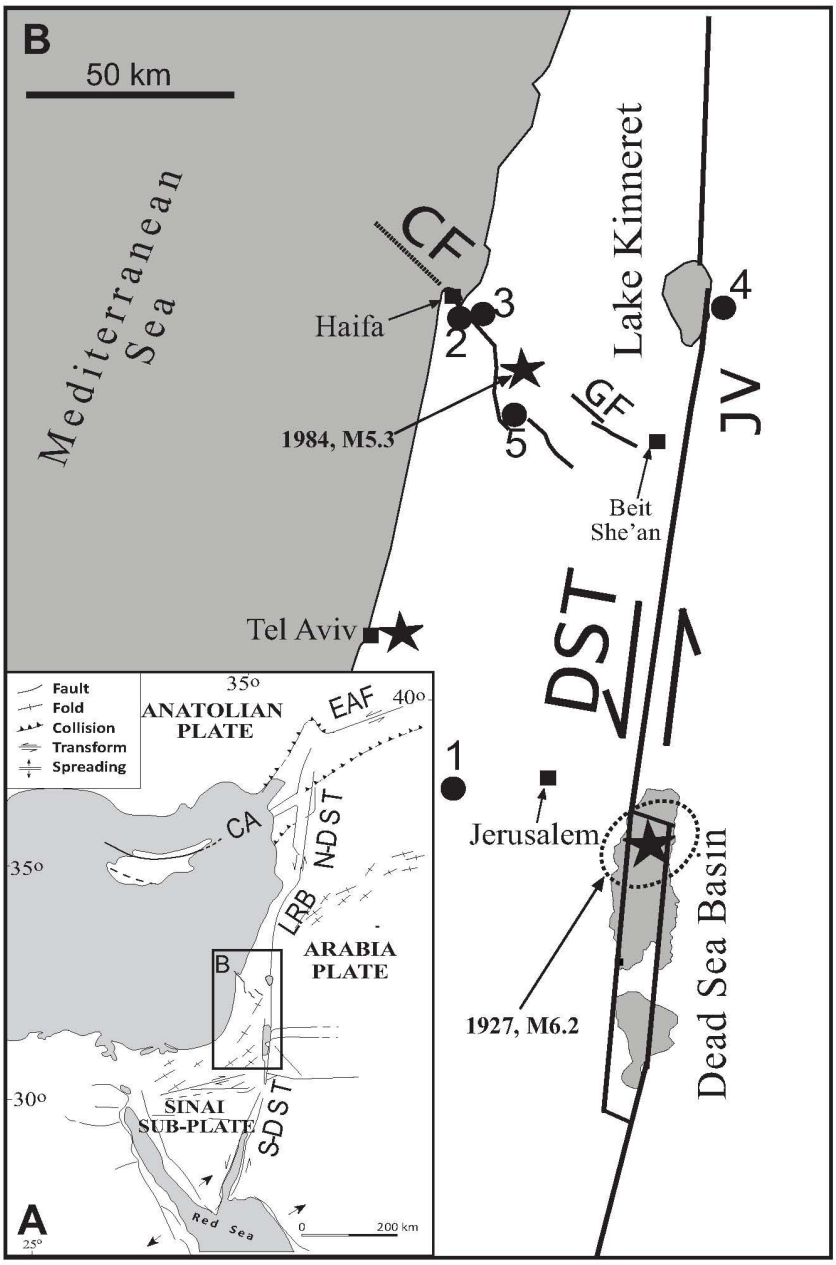

Figure 3.3.1. A: Regional tectonic map of the studied area [after *Garfunkel*, 1981]. B: Location and tectonic map. CF= Carmel Fault (dashed indicates off-shore), DST=Dead Sea transform, S and N = southern and northern sections of DST, respectively, CA-Cypriot Arc, EAF=East Anatolian fault, LRB= Levant Restraining Bend, GF=Gilboa fault. Study sites: 1-Soreq and Har-Tuv caves, 2-Denya Cave, 3- Shutter ridge on Yagur segment of CF [*Zilberman et al*., 2008], 4- Jordan Valley trenches on east shore of Lake Kinneret (Sea of Galillee) [*Katz et al*., 2011], 5-Megiddo archaeological site [*Marco et al.,* 2006]. Faults based on *Bartov and Sagy* [2004], *Marco et al.* [2006], *Bartov et al.* [2007]. The star indicates the estimated location of the 1984 M_L=5.5 earthquake. The location of the 1927 earthquake is given by an error uncertainty ellipse in Figure 3.3.1 which is based on a best estimate of seismological data [*Shapira et al.,* 1993] and our tectonic considerations [*Kagan et al*., 2011].

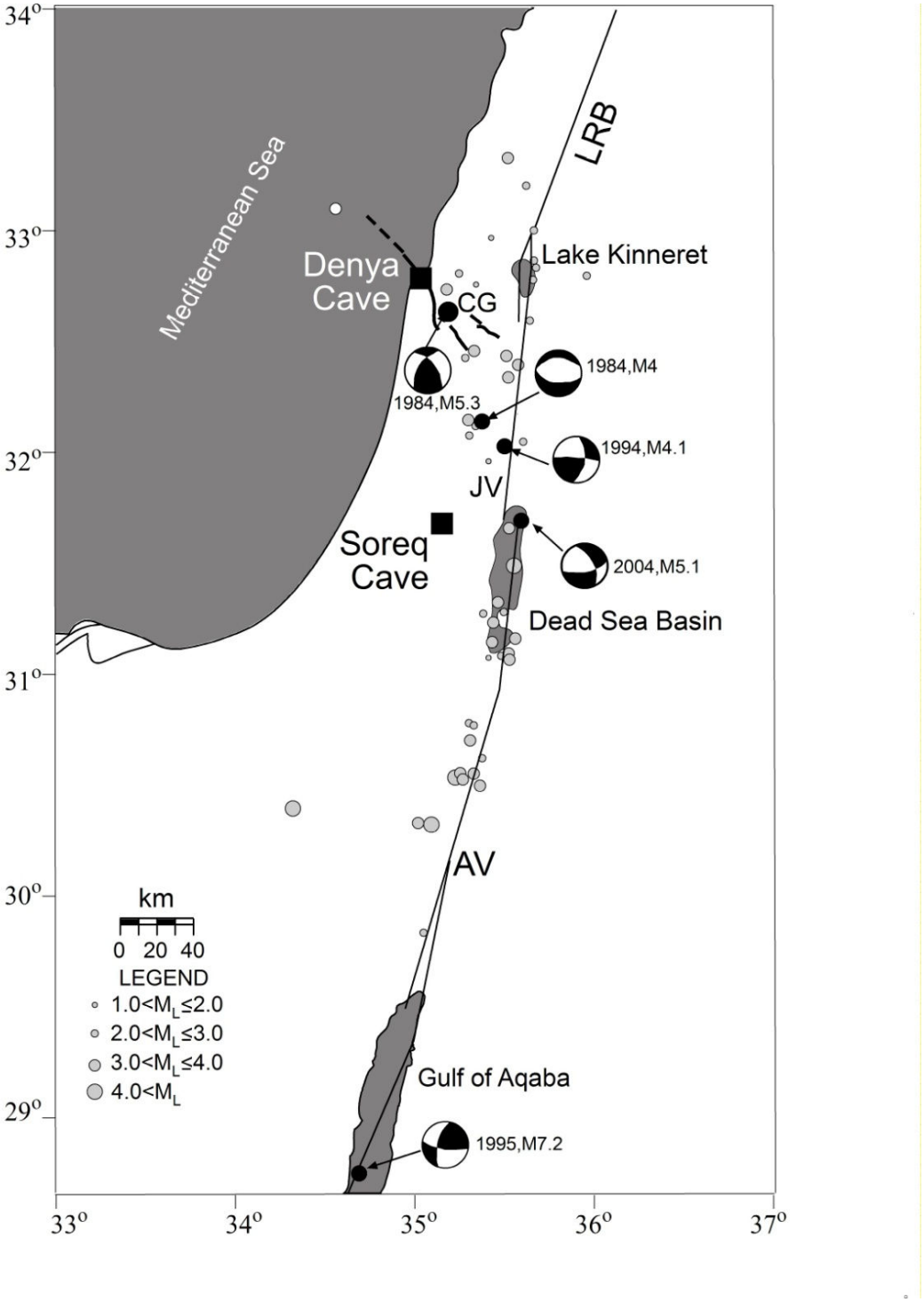

Figure 3.3.2. Seventy-eight relocated earthquakes from 1987-1996 [after *Hofstetter et al.,* 2007] (open circles). The threshold magnitude is approximately ML=2. Composite focal mechanisms of the five largest events from 1984-1994 in the Carmel area are shown, black circles mark locations [see Table 3.3.1 and Figure 3.3.1 of *Hofstetter et al*., 1996, and *Hofstetter et al*., 2007 for the 1994 event location]. The main active tectonic structures are indicated by black lines, LRB=Levant restraining bend CG=Carmel-Gilboa, JV=Jordan Valley, DSB=Dead Sea basin, AV=Arava, (schematic fault traces from the original map).

An earthquake record covering the past 185,000 years was reconstructed based on speleothem damage at two caves in the Judean Hills [*Kagan et al.,* 2005]. Radiometric dating of the time at which speleothems collapsed in these caves (Soreq and Har-Tuv) (Figure 3.3.1) showed repetitive collapse ages. Comparisons with known historical evidence and paleoseismic studies of lacustrine sediments in the DSB reveals that much of the damage to speleothems in the Judean Hills caves was caused by strong earthquakes along the DST (situated over 40km to the east) [*Kagan et al.,* 2005]. That study defined the damaged speleothems to be speleoseismites that can serve as proxies for timing large seismic events. This evidence brought to light a nascent potential proxy for paleoseismic studies, which can contribute to a better understanding of earthquake patterns and recurrence rates of large seismic events for the DST [for studies on earthquake patterns see *Ambraseys*, 1970, *Migowski*, 2004, *Agnon et al*., 2006, *Dolan et al.,* 2007, *Yeats et al.,* 2007, *Wen et al*., 2008, *Kagan Y et al*., 2010; *Scholz et al*., 2010].

The Denya Cave on Mt. Carmel (Figure 3.3.1) also exhibits structural damage to speleothems [*Braun*, 2009]. This cave, situated at approximately the same distance from the JV as the Judean Hills caves are from the DSB (Figure 3.3.1), may therefore have been affected by large earthquakes generated from that region. Alternatively, collapsed speleothem structures in the Denya Cave might be caused by more modest earthquakes, originating from the much closer CF [*Braun*, 2009].

In this study we compare revised results of a published speleoseismic study from the Judean Hills [*Kagan et al.*, 2005] with new results from Mt. Carmel during the Holocene [*Braun*, 2009], and with other paleoseismic studies in the area. Both cave sites are considered off-fault paleoseismic proxy archives potentially affected by the same fault system. However, the two sites may also record separate events along the different segments of the DST or its CF branch. Our goal here is to shed some light on two open issues: (1) Was the Denya Cave damaged by CF earthquakes? (2) Are the CF and DST (JV+DSB) mutually triggered? A long-term temporal comparison between earthquake sequences from on-fault studies along these faults and the respective off-fault paleoseismic archives can contribute to our understanding of regional seismogenic processes.

We present here a case study for the Holocene that can be applied to much longer time periods, up to the U-Th dating method limit (~0.5 My), and to other regions where multiple paleoseismic proxies are available.

In this paper we refer to coupling between fault zones on a phenomenological level, based on empirical correlations of timing. Two fault zones would be considered coupled if their respective seismic events exhibit similar ages. In a special section below we explore the relationships between earthquake timing and coupling of a branch with the segments of the main fault. We also attempt to clarify the effect of temporal resolution on apparent coincidence and clustering of seismic events.

3.3.2 Geological Setting

3.3.2.1 The Dead Sea transform system

The DST extends from the Red Sea spreading center in the south to the East Anatolian fault in the north, forming there a triple junction with the Cypriot Arc (CA) (Figure 3.3.1) [*Garfunkel*, 1981; *Garfunkel and Ben-Avraham*, 1996; *Garfunkel*, 1998]. The DST is a mainly N-S striking left-lateral transform fault with a minor component of normal faulting. Details of the DSB segment of the fault system are given in Figure 3.3.1b based on works by *Ben-Avraham and Lazar* [2006] and *Bartov et al.* [2007].

GPS campaign surveys yield modern slip rates of 4.9 ± 1.4 mm/yr [*Le Beon et al.,* 2008] for the southern DST, consistent with 4–5 mm/yr for the LRB and the northern continuation of the DST [*Gomez et al.,* 2007]. Slip rates calculated by geological and archaeological evidence of offset, on varying time scales, yielded slip rates of 1.5-8.5 mm/yr [e.g. *Freund et al.*, 1968; *Garfunkel,* 1981; *Ginat et al.,* 1998; *Gomez et al.,* 2003; *Makovsky et al*., 2008; *Marco et al*., 2005; *Meghraoui et al*., 2003; *Weinberger et al,* 2011; *Garfunkel,* 2011].

Frequent seismic activity along the DST has been detected during the past century [*Salamon et al.,* 2003] and recorded historically and archaeologically over the past 4000 yrs [e.g. *Ben-Menahem*, 1991; *Ambraseys et al*., 1994; *Guidoboni et al.*, 1994; *Guidoboni and Comastri*, 2005; *Ambraseys*, 2009].

Earthquake recurrence intervals are estimated by a number of paleoseismic studies for various parts of the Dead Sea transform: a) *Marco et al*. [1996]: ~1600 yrs for $M_L \geq 5.5$, recorded in Last Glacial Lisan Formation that spans 50 kyrs. b) *Reches and Hoexter* [1981]: 779 yrs for Jericho fault (interval between two historical events). c) *Salamon et al.* [1996]: DST: 385 yrs M=7; 1250 yrs M=7.5; 3330 yrs M=8. d) *Ken-Tor et al*. [2001]: ~100-300 yrs for M>5.5 on different faults in Dead Sea area. e) *Kagan et al.* [2005]: 10-14 kyr for very large events (M>7.5) documented at the Judean Hills caves.

3.3.2.2 The Carmel fault system

Geophysical evidence suggests that the continental margin west of the DST is divided into two major provinces, the boundary between which is the CF system and its postulated continuation offshore [*Garfunkel and Almagor*, 1984; *Hofstetter et al.,* 1991]. The CF is the northern part of this fault system, which includes the Gilboa fault (GF) and was termed the Carmel-Tirza fault by *Hoffstetter et al*. [1996]. The CF branches from the DST at the Beth-She'an area and extends into the continental shelf of the eastern Mediterranean (Figure 3.3.1) [*Ben-Avraham and Hall*, 1977; *Ben-Gai and Ben-Avraham*, 1995; *Rybakov et al.,* 2000; *Schattner,* 2006]. *Freund et al*. [1970] found a connection between the DST and young faulting trends in the Eastern Galilee and in Lebanon, and concluded that this intense faulting trend is caused by curved segments along the DST.

The CF, which follows a general NW to SE direction (Figure 3.3.2), comprises many small fault strands and has distinct tectonic and morphological expressions [*Hofstetter et al.*, 1996]. Recent activity of the CF is evident in its steep cliffs, displaced stream channels [*Ashkar et al*., 2005], and frequent micro-earthquakes [Figure 3.3.2; and *Hofstetter et al*., 1996]. *Ashkar et al.* [2005] list some surface phenomenon documenting activity along the CF. *Shamir* [2007]

analyzed earthquake data (1.0<M<8.0) using seismic networks from Israel and Jordan between the years 1984 and 2006 and defined the Carmel-Gilboa (CG) fault system as the most seismically active area in the north of Israel. Based on earthquake epicenters, the fault system border in the NE runs along the GF and its continuation to NW, and its SW border runs along the Jezreel Valley (Figure 3.3.2). *Shamir* [2007] stated that the degree of seismic hazard from the Carmel and Gilboa fault systems depends largely on their interaction with large earthquakes along the DST.

3.3.3 Speleoseismology

Caves create an environment protected from most erosive activity. The calcite and detrital deposits within caves have laminar growth patterns preserving delicate evidence including structural damage from earthquakes. Speleothems can be dated with radiometric methods, making it possible to study the temporal patterns of seismic events [e.g. *Kagan et al*., 2005; *Panno et al.*, 2009: *Plan et al*., 2010].

The mechanical relation between earthquakes and the breaking of speleothem structures is not clear. Various aspects of the relation have been investigated in past studies, including investigation of the ground acceleration needed to damage different speleothems, the types of speleothems sensitive to breaking under certain conditions, and predicted modes of failure [e.g. *Cadorin et al.*, 2001; *Lacave et al*., 2000, 2004; *Becker et al.,* 2006]. Yet speleothems are heterogeneous by nature [*Gilli et al*., 1999; *Lacave et al*., 2000] owing to their internal structure, composition, growth rates, and location within a cave. Furthermore, considering site effects and cave depths, shapes and sizes, we are not yet able to precisely predict the effects of earthquakes on speleothems. These considerations make it difficult to evaluate clear intensity values=of speleothem damage for intensity scales such as the Environmental Intensity Scale 2007 [ESI07- *Reicherter et al.,* 2009]. Modern observations and detailed investigation immediately following earthquakes need to be carried out for calibration of the past events to quantitative parameters.

Nevertheless, observations of broken speleothems due to modern earthquakes have been documented in caves from around the world [e.g. *Gilli et al*., 1999; *Aydan*, 2008; *Perez-Lopez et al*., 2009]. Dated damaged speleothem samples were reported to have yielded ages of known historical and pre-historic earthquakes in various studies [e.g. *Postpischl et al*., 1991; *Morinaga et al*., 1994; *Lemeille et al.,* 1999; *Kagan et al.,* 2005].

Effects of earthquakes on caves and speleothems can come in different forms (Figure 3.3.3). These may include cracks and fissures, severed stalagmites, collapsed and broken speleothems, collapsed ceilings and rockslides, changes in growth axes due to tilting [e.g. *Postpischl et al*., 1991; *Morinaga et al.*, 1994; *Forti,* 1998; *Gilli et al*., 1999; *Lemeille et al.,* 1999]. Another form of earthquake induced damage is the closing or opening of cracks, depending upon their locations in relation to stress fields [*Muirwood and King*, 1993].

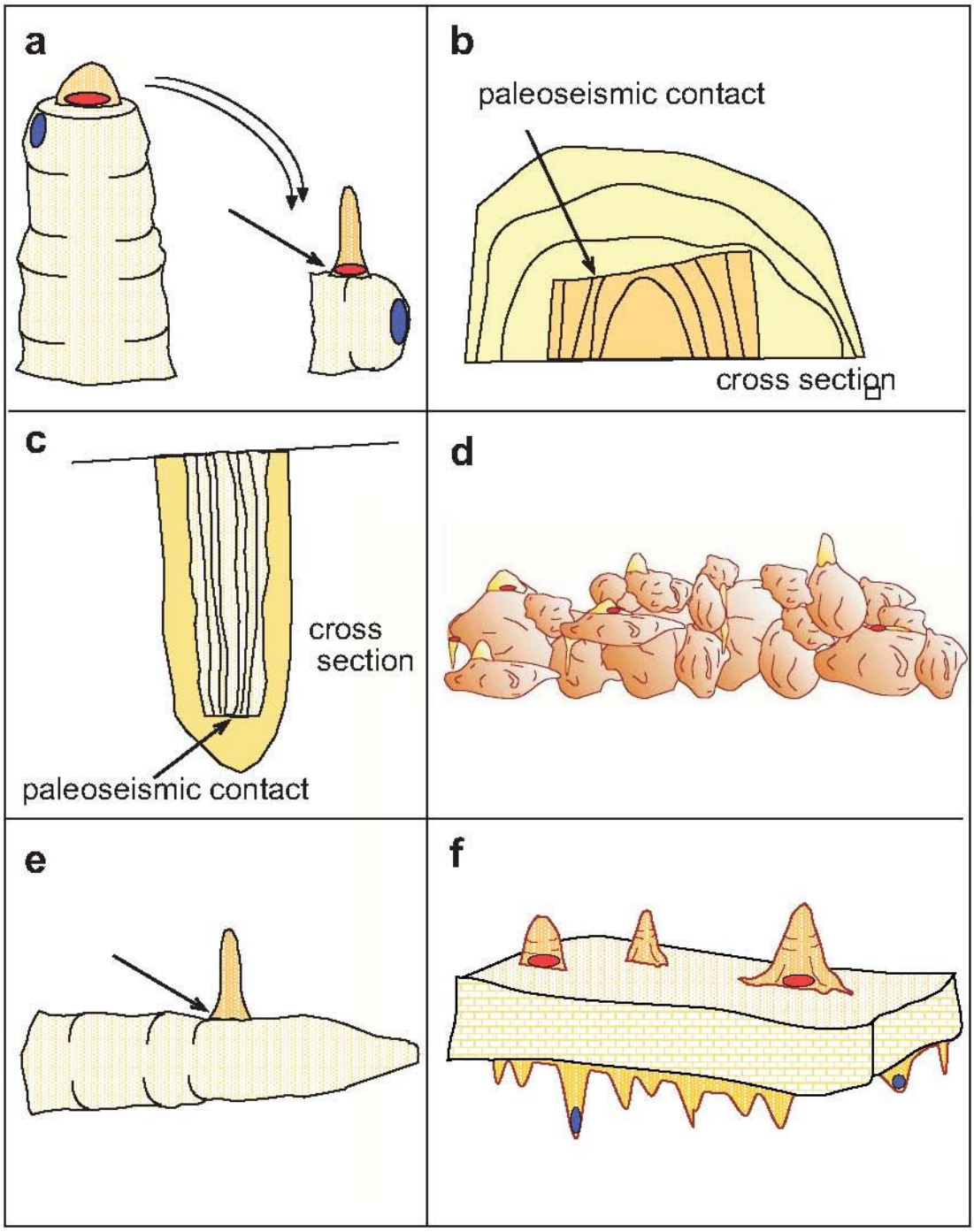

Figure 3.3.3. Schematic diagram depicting speleoseismites found in the study caves. Single arrows point to the paleoseismic contact between the pre-seismic laminae and post-seismic re-growth. a: Stalagmite with top severed, re-growth apparent on both the collapsed top and the standing and broken base, b: cross-section of broken stalagmite embedded in younger stalagmite re-growth, c: cross-section of broken stalactite covered by post-event stalactite re-growth, d: collapsed ceiling rubble with post collapse stalagmite re-growth, e: collapsed stalactite with stalagmite re-growth, f: whole fallen ceiling slab with pre collapse stalactites and post collapse stalagmites. In a, d, and f red ellipses indicate post-seismic growth, while blue ellipses indicate pre-seismic growth.

Most paleoseismological and speleoseismological studies seek to date phenomena which occurred almost instantaneously by earthquakes. When a similar age is obtained by a few different speleothem samples from different parts of a cave, it is suggestive that these were not spontaneous separate collapses, but indicative of an earthquake [*Kagan et al.,* 2005; *Braun*, 2009]. Dating such events can only give an age range due to analytical and geological uncertainties, as in most geological scenarios. These uncertainties can prevent differentiation of closely timed seismic events, but quiescent intervals, as well as periods of clustering, can be identified clearly.

3.3.4 Study sites

In this study we compare the ages of damaged speleothems from two cave sites, the Soreq and Har-Tuv caves near Jerusalem and the Denya Cave in a neighborhood of Haifa, with other paleoseismic studies from the CF and JV (Figure 3.3.1B).

3.3.4.1 Soreq and Har-Tuv caves in the Judean Hills

The Soreq and Har-Tuv caves, located 15 km west of Jerusalem (Figure 3.3.1), offer an excellent opportunity for speleoseismic investigation [*Kagan et al*., 2005]. The two caves have developed under nearly identical geological and climatic conditions. Research in two nearby caves offered the prospect of correlation with most of the 185-ky archive of *Kagan et al*. [2005]. The Soreq Cave has been studied intensively and shows continuous growth of speleothems for the last 185 ky [*Bar-Matthews et al*., 2000; *Ayalon et al*., 2002] and probably the past 350 ky [*Bar-Matthews and Ayalon* pers. comm.] The Har-Tuv Cave is in an active part of the Har-Tuv Quarry and is intended for destruction. Therefore, sampling in this cave was not limited by considerations for preservation.

Soreq Cave is elongated in the NW-SE direction with an average length of 80 m and an average width of 60 m [*Asaf*, 1975]. The floor consists of flowstone, stalagmites, fallen speleothems, and locally some mud. There are abundant fractures on the ceiling of the cave, some of them filled with reddish sediments and probably connect the cave to the ground surface. Curtain-type stalactites grow underneath ceiling fractures and form walls that divide the cave into spaces known as rooms, or halls. This cave contains a large amount of fallen cave deposits, of all types and sizes, which provide information on the seismic history of the region. This history is given mainly by dating seismic events, with additional information on local intensity and other physical data pertaining to underground earthquake damage. Mapping showed preferential orientation of collapses and, together with dating clusters, indicated non-random, non-spontaneous collapses. U-series dating of damaged speleothems and of deposits that have grown on them accurately places the causative events into the regional seismic chronological record.

The Har-Tuv Cave was only recently uncovered during quarrying activities. It is part of the same system of karstic caves described above. At the entrance to the cave there is a fault that dips 75/035, showing slickensides orienting 125^0, whose age is unknown. It is a small cave, fairly horizontal, about 20 m long and maximum 7 m wide. There are many standing speleothem pillars and some broken ones. There is an abundance of ceiling collapses, mostly

covered with stalagmite-stalactite growth. There is also an area covered by a thick layer of flowstone.

The entire Soreq-Har-Tuv Judean Hills archive covers ~185 ky and includes dating of more than 60 speleoseismites. Damages in these caves have been shown to stem from 13-18 earthquakes with a mean recurrence interval of 10–14 ky [*Kagan et al*., 2005]. This archive shows correlation between numerous events at the Soreq and Har-Tuv caves. However, the Holocene portion of this archive, presented in this paper, shows dissimilar dates of collapses in the two caves (Tables 3.3.1, 3.3.2).

3.3.4.2 Denya Cave, Haifa, Mt. Carmel

The Denya neighborhood, hosting the Denya Cave, is within the city of Haifa (Figure 3.3.1) and is situated on a spur sloping down from the summit of Mt. Carmel in a westward direction.

The Denya Cave shows continuous growth of speleothems during the entire Holocene [*Bar-Matthews et al*., pers. comm.]. It is ~ 50m^2 in area and throughout the cave there is evidence of collapses, as seen in broken speleothems, fallen rocks and a tumbled segment of a cave wall. Cracks in the cave ceilings and walls show oblique displacement of a few centimeters with speleothems growing down from some of the cracks in the ceilings. Thirty-two speleoseismites were sampled and dated. Nine age clusters indicating nine seismic events were determined over the last 200 ky using the isochron method discussed below [*Braun*, 2009]. In this section we present the Holocene events.

3.3.5 Methods

3.3.5.1 Paleoseismic research using speleothems

Following a procedure of cave investigation and mapping [*Kagan et al*., 2005; *Braun,* 2009], samples were documented with their settings and extracted from those deposits deemed most likely to have recorded ancient earthquakes. Polished saw-cut surfaces were examined for irregularities in the laminar stratigraphy. Unconformities, the boundaries between damaged speleothems and post-damage re-growth, were identified as seismic contacts. Laminae in such broken or deformed speleothems were then sampled for dating as close as possible to their seismic contacts (see arrows in Figure 3.3.3). Ages of these laminae, either pre-seismic or post-seismic, were determined using the ^{230}Th/U dating method, to constrain ages of damaging events. These procedures, as well as the dating of the samples (see below), were carried out by the authors in previous studies [*Kagan et al*., 2005; *Braun,* 2009].

3.3.5.2 Elimination of non-seismic causes for speleothem damage

Becker et al. [2006] outlined non-seismic causes for damage found in caves. These processes, which have caused damage in other caves in the world, can be ruled out for both the Denya and Soreq-Har-Tuv caves. The caves in this study were closed to the environment up until the last few decades when they were discovered by construction work; damage can be distinguished from less recent seismic events by morphological assessment [*Crispim*, 1999] and predominantly by dating. Glacial movements or ice creep are not considered in these

studies since cave temperatures in this part of the Levant were above freezing during the period investigated [*Frumkin et al*., 1999; *Bar-Matthews et al*., 2000; *Ayalon et al.,* 2002]. Finally, no evidence was found for soil creep, flooding, debris flow, or incation (structural damage to the cave due to loading).

3.3.5.3 Dating methods

In this study we generate ^{230}Th/U dates using a Multiple Collector Inductively Coupled Plasma Mass Spectrometer (MC-ICP-MS). The MC-ICP-MS produces high analytical precision and enables work on small samples (~0.1 g) that give ages at a high resolution due to the ability to sample individual laminae [*Vaks et al.,* 2006; *Bar-Matthews et al.,* 2010]. Ages determined using this method commonly have an analytical error margin of ~ 1% or less. Geological error stemming from distance of a sample from paleoseismic contact, slow sedimentation rate, and other caveats may be larger in some samples or negligible in others [see *Kagan*, 2002; *Kagan et al*., 2005; *Braun*, 2009].

We determine absolute ages for speleoseismite samples in Soreq-Har-Tuv caves for each sample after each single age was corrected for the detrital component using as a correction factor the detrital molar ratio of ^{232}Th/^{238}U=1.8±0.25. This correction factor was calculated by *Kaufman et al*. [1998] for speleothems from Soreq Cave located within the carbonate terrain of the Judean Hills. In the Denya Cave we were unable to use single sample ages since no such correction factor could be determined. The Th component in the carbonate speleothems in the Denya Cave was found to be incorporated in both the calcite lattice and in the detrital component. To overcome this, sub-samples from the same growth lamina of a speleothem yielding different uncorrected ages due to different concentrations and distributions of Th within the detritus and the carbonate, were regarded as having the same age and were plotted along a 3D isochron calculated using *Isoplot3.7* [*Ludwig*, 2008]. Other speleoseismites, which yielded similar ages, were added to the isochron plots under the working assumption that they might have been damaged at the same time. This assumption was tested and deemed correct only when the samples plotted along the isochron line (see isochron ages in Table 3.3.1) [see *Braun*, 2009, for detailed isochron description and analysis]. Isochron ages of the Denya cave speleoseismites were calculated using *Isoplot3.7* (Ludwig, 2008), where the ratio ^{230}Th/^{238}U is used according to the equation suggested by *Broecker* [1963] (Table 3.3.1). Single sample dates of the Judean Hills caves speleothem samples were calculated using the age equation introduced by *Broecker and Kaufman* [1965], in which the ratio ^{230}Th/^{234}U is used (Table 3.3.1).

3.3.6 Results

Dates of nine damaged speleothems found at the Denya Cave suggest two Holocene events, at 4.8±0.8 ka and 10.4±0.7 ka (Table 3.3.2). Dating results of samples in Denya Cave younger than ~1 ka were discarded, since they did not plot along an isochron and as single samples their age could not be corrected and therefore accurately determined. For the entire Holocene at Soreq-Har-Tuv caves, eight speleoseismites were identified. During the prehistoric Holocene, the time period for which we can compare the Soreq-Har-Tuv and Denya caves, six speleoseismites were found. These speleoseismites were dated previously by alpha counting and oxygen wiggle-matching [*Kagan et al*., 2005]. In this work we present the new MC-ICP-MS dating of six speleoseismites from 12 ka to present (Tables 3.3.1, 3.3.2). Some of the

samples dated by the MC-ICP-MS method (this study) yield ages different from the alpha-wiggle-matching results [*Kagan et al.,* 2005] due to significant improvement in dating precision and significantly smaller sample size requirements [*Vaks et al*., 2006; *Bar-Matthews et al*., 2010]. These single sample ages of the Soreq-Har-Tuv speleoseismites cluster to approximately four events (0.186 ka, 0.25 ka, ~5 ka, 8.6 ka).

Modern earthquakes, such as the Carmel event (M5.3, 1984) mentioned above or the Dead Sea earthquake (M5.1, 2004) might or might not have been recorded in the study caves. However, dating techniques cannot differentiate between these dates and dates of possible damage due to blasting at the quarrying or construction sites. In Soreq-Har-Tuv caves, no 20th century damage was dated. In addition, at the Denya Cave only events older than ~1 ka, as discussed above, were considered.

3.3.7 Discussion

3.3.7.1 Implications of speleothem chronometric uncertainties

One difference in the two speleoseismicity studies discussed above is in the number of samples which establish the corrected age of an event. This distinction means that while a single sample from the Judean Hills caves yields the age of an event, more than four samples from Denya Cave are needed in order to create a viable isochron, which in turn yields their combined corrected age. An inherent aspect of the isochron method developed in *Braun* [2009] is the assumption that these separate samples were precipitated closely before or after the same seismic event (within the resulting age uncertainty). The resulting isochron establishes that an event occurred throughout the cave, lending statistical viability to the findings.

It might be argued that the different ages represent separate but close in time events since earthquakes tend to occur in sequences [e.g. *Scholz*, 2002 earlier references – e.g., *Richter*, 1958]. In fact, there is no way to determine how many events occurred during the range of the age uncertainty due to lack of traditional stratigraphy in the cave environment. Notwithstanding, earthquake clusters and quiescent intervals, significant for earthquake mechanics and seismic hazard assessments, can be identified clearly. For example, even if one "event" represents a number of separate earthquakes followed by an inter-seismic interval, this is still significant for recognition of earthquake patterns: the close-in-time earthquakes can be considered a seismotectonic "event" (for instrumentally recorded earthquake examples see *Toksoz et al*. [1979] for the North Anatolian fault and *King et al*. [1994] for California).

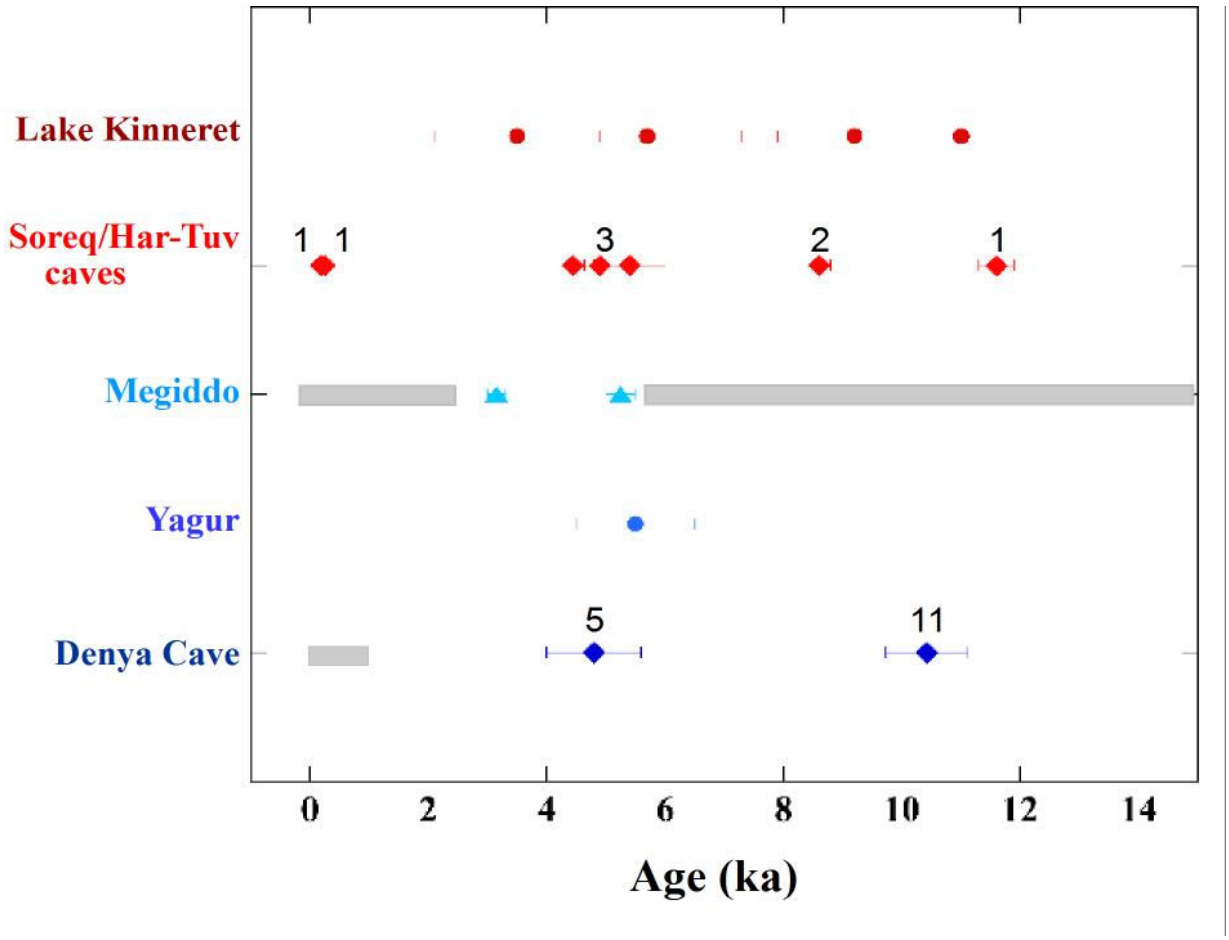

Figure 3.3.4. Comparison of event age results of the different paleoseismic studies (Table 3.3.2). CF studies: Denya Cave [*Braun*, 2009], Yagur shutter ridge [*Zilberman et al*., 2008], Megiddo archaeo-seismic evidence [*Marco et al.,* 2006]. DSB sites: Soreq-Har-Tuv [*Kagan*, 2005 and this study]. JV site: Lake Kinneret (Sea of Galillee) trenches [*Katz et al*., 2011]. Numbers above cave events indicate number of speleoseismites dated to this age. Note: Soreq/Har-Tuv ages are separate single sample ages dated to the same event; while Denya ages are isochron ages [see text and *Braun*, 2009, for details]. Horizontal bars represent "no information" time windows.

3.3.7.2 Independent archives

Table 3.3.2 and Figure 3.3.4 list the ages of seismic events obtained from the two speleoseismic sites and from other paleoseismic studies in the region. Two of the additional studies are from the Carmel fault area: the archeological site of Megiddo and a shutter ridge along the Yagur segment of the CF (see Figure 3.3.1). The Megiddo (biblical Armageddon) site is located on the CF, but similarly to the Denya Cave, may be an off-fault proxy, i.e. damage there may be attributed to CF earthquakes or large earthquakes originating from the DST [*Marco et al*., 2006]. Earthquake damage at Megiddo [*Marco et al.,* 2006] has been attributed to the end of the 4th millennium BCE (~5 ka) and the 9th century BCE (~2.8 ka) and possibly to mid 8th century BCE (~2.75 ka) (Table 3.3.2, Figure 3.3.4). At the Yagur segment of the CF (Figure 3.3.1), tentative evidence suggests increased tectonic activity around 5.5 ka (OSL ages of sediments accumulated behind the shutter ridge) [*Zilberman et al*., 2008].

Table 3.3.1. U-Th results (concentration, activity ratios and age es timates) for dating s peleoseismites in the Judean Hills and De nya caves, measured by MC-ICP-MS. A: Speleo thems from Denya Cave, near Haifa, with isochron ages calculated for proposed synchrono us co llapses. Isochron ages of t he Denya c ave speleoseismites were calculated using *Isoplot3.7* [*Ludwig*, 2008], where the $^{230}Th/^{238}U$ ratio is used according to the equation suggested by *Broecker* [1963]. B: Speleothems from Soreq and Har-Tuv caves (Judean Hills) with corrected (when necessary) and uncorrected single sample ages, based on the ratio $^{230}Th/^{234}U$, used for the a ge equation suggested by *Broecker and Kaufman* [1965]. $^{232}Th/^{238}U$ detrital molar ratio of 1.8 was used fo r detritus co rrection, calcu lated b y *Kaufman et al.* [1998] for speleothems from Soreq Cave located within the carbonate terrain of the Judean Hills.

A. DENYA (HAIFA)

Sample	**$_{238}U$ conc. (ppm)**	**±2σ**	**$(_{230}Th/_{238}U)_A$**	**±2σ**	**$(_{232}Th/_{238}U)A$**	**±2σ**	**$(_{234}U/_{238}U)A$**	**±2σ**	**$(_{230}Th/_{232}Th)_A$**	**±2σ**	**$(_{230}Th/_{234}U)_A$**	**±2σ**	**Isochron age**	**±2σ**
DN-51 pre III	0.2029	0.0002	0.0459	0.0012	0.0049	0.0000	1.0446	0.0011	10.2	0.3	0.0439	0.0012		
DN-2-3 0.	1492	0.0001	0.0497	0.0023	0.00290	0.0000	1.0459	0.0024	22.5	1.1	0.0475	0.0022		
DN-2-4	0.1432	0.0001	0.0588	0.0021	0.0041 0.	0000 1	.0459	0.0015	16.9	0.6	0.0562	0.0020	**4.8**	**0.8**
DN-66c pre III	0.1845	0.0001	0.0840	0.0019	0.038891	0.0002	1.0566	0.0010	1.9	0.1	0.0795	0.0018		
DN-17 post	0.2866	0.0002	0.0957	0.0011	0.0544 0.	0001 1	.0540	0.0014	1.8	0.0	0.0908	0.0011		
DN-7-46bpost 0.	2490	0.0002	0.0845	0.0017	0.0035 0.	0000 1	.0437	0.0021	27.2	0.6	0.0810 0.	0017		
DN-7-47 0.	2070	0.0002	0.0971	0.0014	0.0028 0.	0000 1	.0579	0.0011	38.3	0.6	0.0918 0.	0013		
DN-7post B	0.2542	0.0002	0.1008	0.0007	0.0084 0.	0000 1	.0424	0.0011	12.6	0.1	0.0967 0.	0007		
DN-9b post	0.2590	0.0001	0.1024	0.0030	0.0117 0.	0001 1	.0487	0.0010	9.4	0.3	0.0976 0.	0029		
DN-9b pre	0.1882	0.0001	0.1095	0.0046	0.0092 0.	0001 1	.0399	0.0014	12.8	0.4	0.1053 0.	0044		
DN-51 pre IV	0.2478	0.0005	0.1095	0.0015	0.0250 0.	0001 1	.0319	0.0027	4.5	0.1	0.1061 0.	0014		
DN-7post 0.	3141	0.0002	0.1109	0.0013	0.0085 0.	0000 1	.0436	0.0011	13.6	0.2	0.1062 0.	0012	**10.4**	**0.7**
DN-7-46 0.	2801	0.0002	0.1122	0.0014	0.0052 0.	0000 1	.0562	0.0015	22.4	0.3	0.1063	0.0013		
DN-17 pre	0.2621	0.0002	0.1131	0.0056	0.0187 0.	0001 1	.0399	0.0038	6.7	0.3	0.1088	0.0053		
DN-2-2 0.	1880	0.0001	0.1259	0.0031	0.0137 0.	0001 1	.0555	0.0023	10.4	0.3	0.1193	0.0029		
DN-45 post	0.3754	0.0003	0.2046	0.0021	0.1275 0.	0004 1	.0332	0.0013	1.6	0.0	0.1980	0.0020		

B. SOREQ-HAR-TUV (JUDEAN HILLS) 232/238 detrital molar ratio=1.8

Sample	$_{238}U$ conc.	±2σ	$(_{234}U/_{238}U)A$	±2σ	$(_{230}Th/_{232}Th)_A$	±2σ	$(_{230}Th/_{234}U)_A$	±2σ	Age 2σ (ka)		+2σ
									uncorrected	**corrected**	
SO-38 C1	1.0552 0.	0009	1.0293	0.0008	13.8	0.4	0.0022	0.0001	**0.24**	**0.19**	0.01
SO-32 B1	0.5280 0.	0003	1.0898	0.0009	7.0	0	0.0036	0.0001	**0.39**	**0.25**	0.01
HT-11 A	0.3882	0.0001	1.1054 0.	0012	50.5	1.2	0.0416	0.0009	**4.62**	**4.44**	0.22
HT-12 A	0.2520	0.0001	1.1249	0.0009	112.0 2.	8	0.0714	0.0006	**8.0**		0.1
HT-10 A	0.3707 0.	0001	1.0869	0.0013	190.2 3.	6	0.0765	0.0009	**8.6**		0.2
HT-14 A	0.1795	0.0001	1.0988	0.0017	106.3	1.4 0	.1015	0.0013	**11.6**		0.3

Table 3.3.2. Comparison of paleoseismic results from the Judean hills [*Kagan et al.*, 2005], Denya Cave on Mt. Carmel [*Braun,* 2009], paleoseismic trenches at the Eastern Lake Kinneret (Sea of Galilee) [*Katz et al.,* 2011; OSL ages; TEG indicates trench sample names], a paleoseismic study of a shutter ridge along the Yagur segment of the CF [*Zilberman et al.*, 2008; OSL ages], and archaeoseismic findings in structures at the archeological site of Megiddo [*Marco et al.*, 2006]. Speleoseismite samples from Judean Hills caves Soreq (SO) and Har-Tuv (HT) and Mt. Carmel Denya cave (DN) speleoseismite samples were dated using the U-Th dating method using a MC-ICP-MS, except for two samples [*Kagan et al.*, 2005, indicated by WM] with wiggle matching age results. Ages for Judean Hills caves speleoseismites are single sample ages. Ages for speleoseismites from the Denya cave are presented as the respective isochron ages for speleoseismite groups. Speleoseismite types: broken stalagmite (BS), broken stalactite

Soreq-Har-Tuv caves			**Denya Cave**			**Lake Kinneret trenches**		**Yagur shutter ridge**		**Megiddo archeological site**	
Seismite sample	**Type**	**MC-ages (2σ error)**	**Seismite sample**	**Types**	**MC-Isochron ages (2σ error)**	**Displaced unit**	**OSL ages**	**Back barrier terrace unit**	**OSL ages**	**Observed damage**	**Archeological age**
SO-38 C1	BS-post	**0.186±0.014 ka**									**8th century BCE**
SO-32 B1	BS-post	**0.25±0.01 ka**								Damaged buildings	**~2.75 ka**
			DN-51 pre III	BSt-pre		TEG-1	**3.2±1.4 ka**				
			DN-2-3	BS-post						Tilted pillars	**9th century BCE**
HT-11 A	CC-post	**4.44±0.22 ka**	DN-2-4	BS-post	**4.8±0.8 ka**					& buildings	**~2.8 ka**
HT-15 A	CC-post	**4.9±0.6 ka (WM)**	DN-66c pre III	BSt-pre		TEG-3	**5.0±0.3 ka**	8m depth	**5.5±1 ka**		
HT-13 A	CC-post	**5.4±0.6 ka (WM)**	DN-17 post	BS-post						Fractured temple walls	**4th millenium BCE ~5 ka**
HT-12 A	CC-post	**8.0±0.1 ka**									
HT-10 A	CC-post	**8.6±0.2 ka**				TEG-44	**9.2±1.9 ka**				
			DN-7-46	BS-post		TEG-26	**10±0.8 ka**				
			DN-7-46b	BS-post							
			DN-7-47	BS-post							
			DN-7 post	BS-post							
			DN-7post B	BS-post							
HT-14 A	CC-post	**11.6±0.3 ka**	DN-9b BS-pre		**10.42±0.69 ka**						
			DN-9b pre	BS-pre							
			DN-17 pre	BS-pre							
			DN-2-2	BS-pre							
			DN-45 post	BS-post							

A source for comparison of pre-historic earthquakes along the JV, presented in Table 3.3.2, is an on-fault paleoseismic study along the eastern side of Lake Kinneret (Sea of Galilee) [*Katz et al*., 2011], off the plate boundary. In this study three paleoseismic trenches were excavated perpendicular to normal fault planes that bound the transform basin. Depositional unconformities were dated using the OSL method, indicating the occurrence of two to three seismic events during the Holocene (10 ka, 5 ka, and <5 ka). *Katz at al*. [2011] deduced Mw<7 for historic earthquake in the Sea of Galilee segment based on slope stability analysis. As *Katz et al*. [2011] point out, this magnitude estimate based on scarp height is a minimum estimate due to possible erosion. Moreover, possible strike-slip components might add to the actual magnitude.

3.3.7.3 Correlations

As Table 3.3.2 demonstrates, the Denya cave speleoseismites record two major earthquake events in the Holocene, at ~5ka and ~10.5 ka. The Soreq-Har-Tuv caves record four events: two possible historic earthquakes (younger than the Denya archive and therefore not discussed here further; to be discussed in a future paper), a ~5ka event, and a ~8.6 ka event. In addition, one post-contact sample was dated to 11.6±0.3 ka at Har-Tuv Cave; this poorly constrained collapse event might have occurred prior to this post-contact age.

Three speleoseismite samples from the Har-Tuv Cave cluster to ~5 ka (Table 3.3.2). Considering the error of ages and the sampling process, we suggest that the ages of the three samples may indicate a single event. This event might very well be the same event documented by four fallen speleothems from Denya Cave giving an isochron age of 4.8±0.8 ka.

When comparing this event age (~5 ka) to the results of other paleoseismic studies, complexities arise since this age appears both along the CF, as well as in the JV at all sites discussed here. The shutter ridge sediment along the Yagur section of the CF [*Zilberman et al*., 2008] indicates a time of increased tectonic movements along the CF at ~5 ka, while an event which occurred at ~5ka displaces the slope seen in the paleoseismic trench on the shores of Lake Kinneret, JV [*Katz et al.,* 2011]. Furthermore, fractured Early Bronze temple walls at Megiddo [*Marco et al.*, 2006] show damage interpreted to be earthquake induced and are dated to ~5 ka. *Ferry et al.* [*2011*] also discuss archaeoseismic evidence at ~5 ka (2900±50 BC) from the JV which correlates to this event. Cosmogenic (^{36}Cl) dating of an exposed limestone scarp has inferred a rapid and significant displacement in the lower Galilee around this period (between 4 and 6.5 ka) [*Mitchell et al.*, 2001]. This fault, a part of the E-W Galilee fault system north-west-west of Lake Kinneret, may be related to the regional seismic events indicated in the other sites.

A collapse event recorded in the Har-Tuv Cave speleothems indicates a seismic event along the DSB at ~8.6 ka. As of yet, this is the only location where earthquake evidence has been found for this time interval. However, the extensive and detailed early Holocene paleoseismic archive of the Dead Sea sediments is yet to be investigated [*Kagan et al.,* 2011; *Migowski et al*., 2004].

The inferred seismic event in the early Holocene (~10.5 ka) seems to have had a significant effect on speleothems in the Denya Cave (five speleothem collapses sampled, see Table

3.3.2). No evidence for a seismic event during this time has yet been found elsewhere along the CF. At the JV Lake Kinneret paleoseismic site, one trench exposed a post-faulting unit that yielded an OSL age range of 10±0.8 ka, while another trench exposed a post-faulting unit with an age range of 9.2±1.9 ka [*Katz et al.,* 2011]. This could be the same event, recorded at both the CF cave and the JV trenches (Figure 3.3.4).

The one sample with only a post-contact age of 11.6±0.3 ka found at Soreq-Har-Tuv is not a well-constrained event and the collapse may have occurred before this post-contact age. Unfortunately, this is a period when Dead Sea lacustrine seismites are not available at present due to a climatically driven lake level drop [*Yechieli et al*., 1993; *Stein et al.,* 2010]. Even if this seismite represents a significantly earlier earthquake, then future drill cores in Dead Sea lacustrine sections from this period will not show seismites, as suggested by the results of *Kagan et al.* [2005], for periods with documented lacustrine Dead Sea sediments. The ~10.5 ka event that caused extensive damage at Denya may have been limited to the JV source, since there is no evidence of an event from on-fault CF studies to date, nor from the DSB. Alternatively, this may be a CF event, for which additional evidence is yet to be uncovered. Different interpretations for potential sources of these events are discussed below using a simplified model that represents the DSB-JV-CF fault system and considering its different paleoseismic proxies.

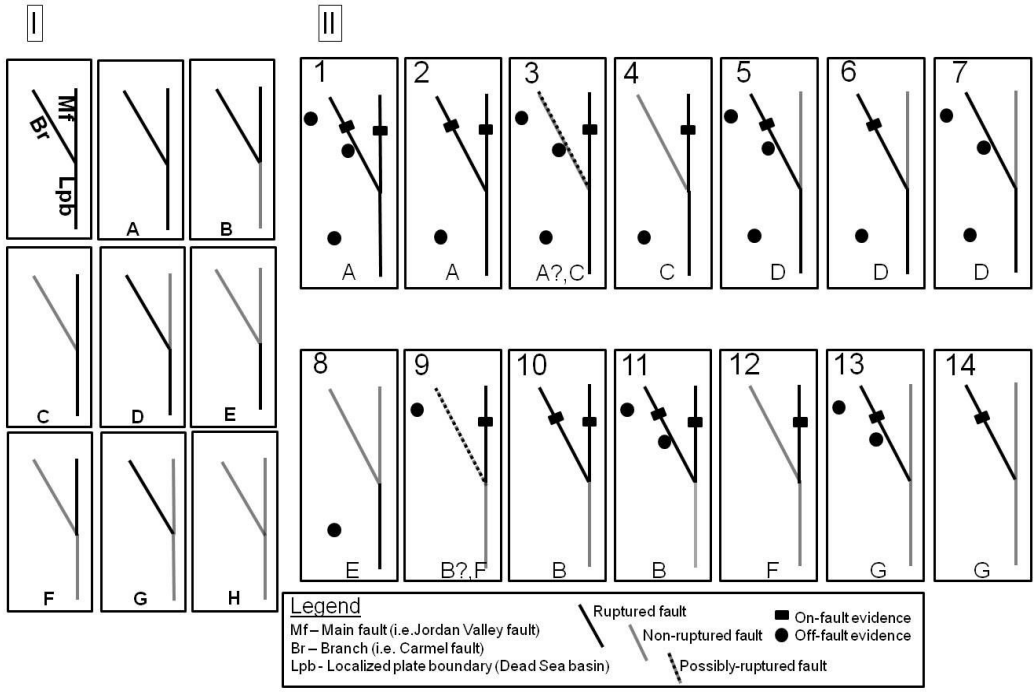

Figure 3.3.5. A schematic representation of possible seismic event scenarios in a simplified model of a Y shaped fault system. Panel I: Rupture scenarios - in this simplified system there is a localized plate boundary (Lpb, i.e. Dead Sea transform) that splays into a main fault (Mf, i.e. Jordan Valley fault) and a secondary branch (Br, i.e. Carmel fault). The schematic drawings represent possible rupture events on the different segments of such a fault system (RS A-H), with the black lines rupturing and the grey lines not rupturing. Panel II: Record Combinations - demonstrates the different types of data set scenarios available, i.e. Record Combinations (1-12) in this study for likely rupture scenarios (A-H), based on Table 3.3.3. Off-fault archives are marked as dots and on-fault archives are marked as rectangles, marking locations of the five archives discussed in this study. Note that RC 14 likely has a smaller magnitude than 13.

Table 3.3.3. Logic table: an evaluation of logical seismic event scenarios based on data available from the different paleoseismic on- and off-fault archives represented in this study. This table considers a simplified Y shaped fault system model, where a localized plate boundary (Lpb) splays into a main fault (Mf) and a secondary branch (Br). Schematic drawings of the different possible rupture scenarios (RS) are presented in Figure 3.3.5-II. This table represents a simplified analysis of the degree of coupling of the fault system segments for each theoretical temporal data set, i.e. *record combination (RC)*.

Record combination (RC)	Localized plate boundary (lpb)	Main Fault (Mf)	Branch (Br)		Coupling (rupture scenario, RS)	Notes
	Off-fault	On-fault	On-fault	Off-fault		
1	yes	yes	yes	yes	A	All faults rupture
2	yes	yes	yes	no	A	All faults rupture, small Br earthquake.
3	yes	yes	no	yes	A?,C	Lpb and Mf rupture/ large Mf earthquake
4	yes	yes	no	no	C	Lpb and Mf rupture/ large Mf earthquake
5	yes	no	yes	yes	D	Lpb and Br rupture/large Br earthquake- not likely
6	yes	no	yes	no	D	Lpb and Br rupture, small Br earthquake /large Br earthquake-not likely
7	yes	no	no	yes	D	Lpb rupture, causing a large earthquake/ large Br earthquake-not likely
8	yes	no	no	no	E	Lpb rupture, causing a large earthquake
9	no	yes	no	yes	B?,F	Mf and Br rupture
10	no	yes	yes	no	B	Mf and Br rupture, small Br earthquake
11	no	yes	yes	yes	F	Mf rupture, Br rupture
12	no	yes	no	no	F	Mf rupture
13	no	no	yes	yes	G	Br rupture, causing a large earthquake
14	no	no	yes	no	G	Br rupture
15	no	no	no	yes	G	Br rupture
16	no	no	no	no	H	No rupture

3.3.7.4 Potential earthquake sources for Denya cave

In a micro-seismicity study of the Carmel-Gilboa (CG) fault systems, *Shamir* [2007] showed a strong connection between this system and the main DST plate boundary. He argues that strong earthquakes along the JV might induce seismic activity in different parts of the CF, depending on the location, depth, and magnitude of the event. This suggests that what is viewed as one seismic event along the DST that caused damage in the Soreq-Har-Tuv caves might have triggered an event along the CF that was recorded in Denya Cave. It remains plausible, however, that strong seismic events along the DST dated to similar ages at Soreq-Har-Tuv and at Denya, affected both cave systems. Alternatively, earthquakes affecting the Denya cave might originate from the CF, for which the potential maximal magnitude is still not clear, but is situated much closer to the cave and has caused structural damage [*Hofstetter et al*., 1996; *Rotstein et al.*, 2004] in the towns in its vicinity (i.e. the M_L=5.3 earthquake of 1984 shown in Figure 3.3.2).

3.3.7.5 Spatio-temporal seismite distributions: possible clues to coupling, clustering, and quiescence

To clarify the implications of our study for fault zone coupling we consider possible event scenarios (Figure 3.3.5). Table 3.3.3 provides a basis for data analysis according to archive locations (see below), off- as well as on-fault, with regard to fault systems and the correlation between the different data sets from the different study sites. This type of analysis assumes complete archives and simplifies the complex relations between faults.

Two adjacent fault zones would be considered coupled if timing of events correlates in proxy archives representing both zones. This definition may hold for instrumental seismicity as well as historical seismicity and paleoseismology, each methodology with its respective time scales and uncertainties. To clarify the concept of coupling we lay out all possible rupture scenarios (RS) on the respective elements of a simple branched fault system (Figure 3.3.5-I, dark lines indicate ruptured element, light lines indicate non-ruptured elements). The examples given are for a simplified DSB-JV-CF system, but a similar model can be applied to other systems elsewhere. In this simplified system, there is a localized plate boundary (Lpb, i.e. Dead Sea transform, central Israel) that splays into a main fault (Mf, i.e. Jordan Valley fault) and a secondary branch (Br, i.e. Carmel fault). All elements of a fully coupled system would rupture simultaneously (Figure 3.3.5-I, RS A). None of the elements of a non coupled system would rupture on each element at the same time (Figure 3.3.5-I, RS: E,F,G). Figure 3.3.5-I shows rupture scenarios of the fault systems with various intermediate coupling states.

Figure 3.3.5-II considers all possible scenarios of earthquake records in the five archives considered for the DSB–JV–CF coupling. The Denya Cave and Megiddo archives are situated close to the secondary branch (Br) for which *Zilberman et al.* (2008) provide an on-fault archive (Figure 3.3.5-II, Table 3.3.2). If all three show simultaneous activity in what is a quiescence period for all the other archives, then the CF ruptured without any coupling (Figure 3.3.5-II; RS G). We define a record combination (RC) for each combination of records of a given event in all available archives. Table 3.3.3 and Figure 3.3.5-II present all possible RCs in archives available to date from DST–CF systems, together with the inferred seismic event scenarios. For example, the abovementioned scenario corresponds to RC 13, interpreted to a specific rupture scenario (RS G) (Table 3.3.3). Record Combination 15, in which events are recorded in both Denya Cave and Megiddo archives and are missing in all

the the other archives, might stem from the limited coverage of the on-fault sites on the CF. However, such a hypothetical RC contradicts our underlying assumptions for this analysis. It may also represent a Mediterranean Sea event (an option not accounted for in our simplified source system).

Our results and compilation for the Holocene correspond to RC 1–RS A (~5 ka), RC 8–RS E (~9 ka), and RC 9–RS B (10.5 ka) (Figure 3.3.5-II, Table 3.3.3).

3.3.8 Summary

We studied two speleoseismic sites, in the Judean Hills and Haifa, each providing individual archives of earthquake shaking in their respective vicinity. Both have been shown to be reliable off-fault cave proxies [*Kagan et al*., 2005; *Braun*, 2009]. Complex as dating speleoseismic events may be, each system shows distinct collapse age groupings. Moreover, when compared with one another, and with independent paleoseismic archives from the JV sector, some coupling is suggested for the CF and JV-DSB fault systems. Specifically, an event at ~5 ka is well-recorded at both the CF and Judean Hills caves, as well as in the Lake Kinneret-JV trenches, the CF-Yagur shutter ridge, and at the archaeological site at Megiddo. The study east of the Sea of Galilee reveals surface rupture and sediment deposition at ~5 ka. The study in the Carmel reveals accumulated sediments behind a shutter ridge at about the same age. Probably the DSB, JV, and the CF faults had to slip to account for these pieces of evidence (RC 1- RS A, complete system coupling). The age bracket of the penultimate Denya Cave event at ~10.5 ka is included in the uncertainty range of dated slip evens in the Lake Kinneret trench archive [*Katz et al*., 2011]. If, as noted above, we assume a complete record from all archives, this could signify a large JV event (Figure 3.3.5-II, Table 3.3.3; RC 9- RS F). Acknowledging that the on-fault record presented by *Zilberman et al.* [2008]'s is incomplete, RC-9 might indicate coupling between the two branches (RS-B) without coupling to the localized plate boundary. This northern event predates the closest event in the Judean Hills archive by two centuries or more. Uncertainties due to differing dating methods and the lack of a Dead Sea lake seismite archive for that period prevent ruling out a correlation. However, quiescent intervals, which are significant for seismic hazard assessment, can be identified clearly, for example the period between ~10 ka and ~5 ka in the cave in Haifa. Within the framework of the uncertainties of each one of the studies discussed, there are contemporaneous seismic ages that may represent alternatively (a) large earthquakes leaving their mark throughout the region, (b) periods of concurrent seismic activity on the CF and JV and/or DSB, or (c) seismic activity on the JV and/or DSB which triggers activity along the CF or vice versa (Figure 3.3.5-II, Table 3.3.3). Potential for additional data can be realized by more extensive sampling for dating seismites at caves in the region and likewise, from additional on-fault and off-fault paleoseismic studies. This type of multi archive analysis provides a clearer view of regional implications of complex fault activity. Using the model presented here, any further paleoseismic data can be analyzed in the context of the regional setting of this fault system and further enhance our understanding of its workings.

3.4 *Reconstruction of a long-term earthquake history from speleoseismites: Soreq and Har-Tuv caves*

3.4.1 Introduction and methods

The Soreq Cave, and to a limited extent the nearby Har-Tuv Cave, provide a long-term, dateable, and preserved paleoseismic archive. Collapsed stalactites, severed or toppled stalagmites, fractured walls, floor, and speleothems, collapses ceiling slabs, macaroni stalactites and other particles embedded in flowstone are some of the various earthquake induced types of damage. The dating of this archive provides a paleoseismic history of large earthquakes in the region. The investigation of the small-scale details of the paleoseismic contacts can potentially provide information on the mechanism of breakage. The subjects presented in this results chapter are: the chronology for the speleothem paleoseismic archive, the distribution in time of the cave damage, and the petrography of the speleoseismites.
The methods used here are 1) Field observations and sampling; 2) Dating of speleothems by applying the U-series method and analysis by MC-ICP-MS mass spectrometry; 3) Thin section investigation under polarizing microscope.

The background and methods for this chapter are described in more detail in the Introduction (1) and Methodology (2) chapters of this work.

3.4.2 Speleoseismite sampling and mapping results

Kagan [2002] mapped all collapses and other earthquake markers in the study caves (Figures 3.4.1 and 3.4.3) and found a general N-S and E-W preferential orientation (Fig. 3.1.3e). Samples taken for dating and petrography are marked on a map in Figures 3.4.2 and 3.4.3. Field sampling techniques are described in Chapter 2.1. Examples of damaged speleothems and other cave deposits in-situ are shown in Figure 3.4.4. Earthquakes are dated by first identifying speleothem seismites within collapsed or otherwise damaged cave deposits. The seismic contact, between pre-damage and post-damage material (speleothem calcite, and sometimes dolomite bedrock) is marked and subsamples are separated from both sides of the contact.

3.4.3 Dating results and discussion

3.4.3.1 Age bracketing

In dating of many geological events there is some discrepancy between the exact time of the event, and the deposition time of the dated material; for example dated colluvium at the base of a fault scarp, where the colluvium is younger than the faulting. In order to best determine the age of the actual event, in this case earthquakes, it is preferable to obtain maximum *and* minimum ages (ages of samples deposited before and after the event), a method termed *bracketing* by *McCalpin* [1996]. In the case of speleothem seismites, obtaining both minimum and maximum ages is a challenge. In order to obtain the minimum and maximum ages of the event in as close a time frame as possible, the damaged speleothem must have been growing continuously until the time of damage, and a post-collapse regrowth must have begun to grow immediately following damage. This ideal scenario is difficult to find. In many cases there is no post-damage regrowth because the speleothem did not fall beneath a dripping fracture and

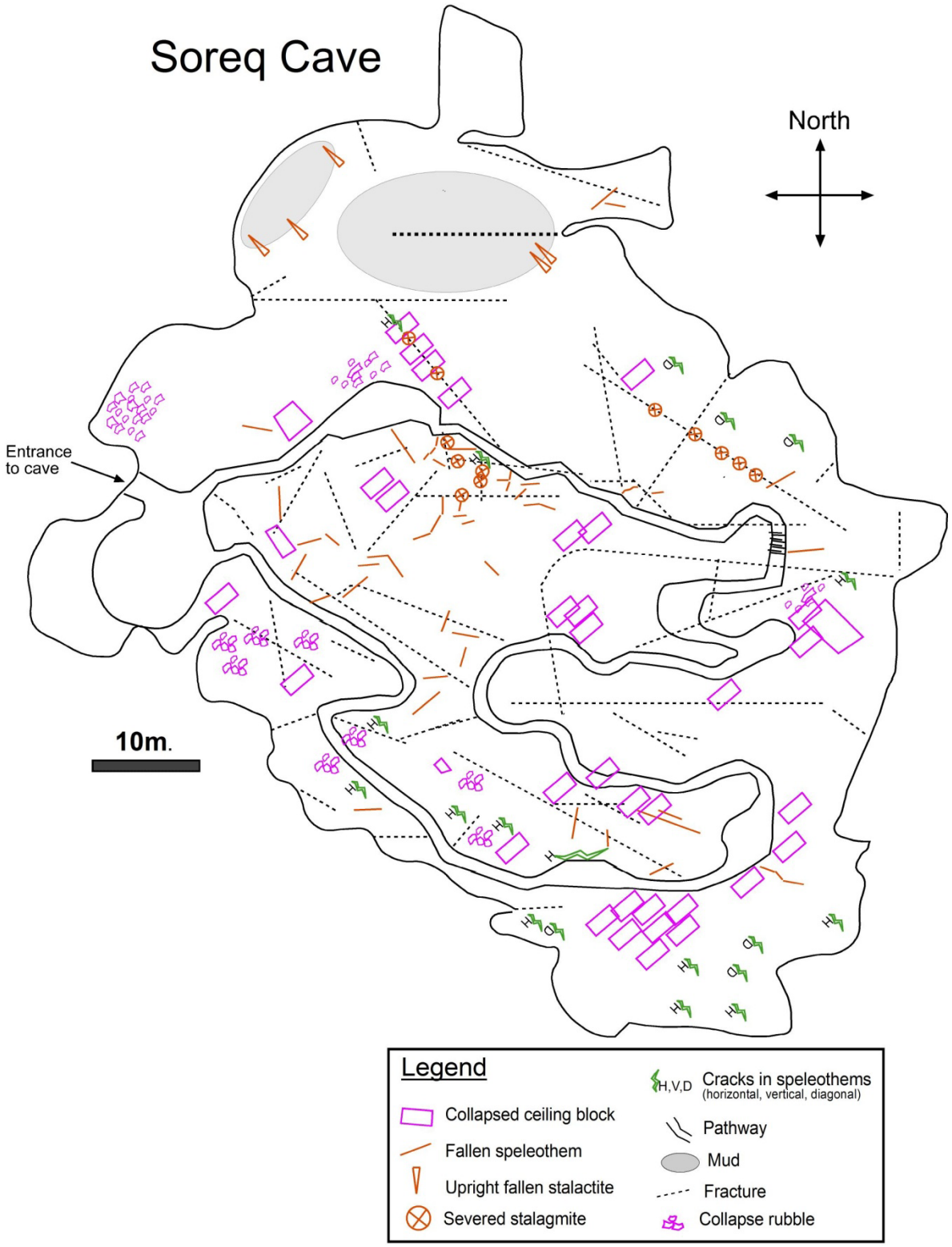

Figure 3.4.1. Map of Soreq Cave indicating the location of collapsed speleothems and ceiling blocks, severed stalagmites, cracks in speleothems, and ceiling fractures.

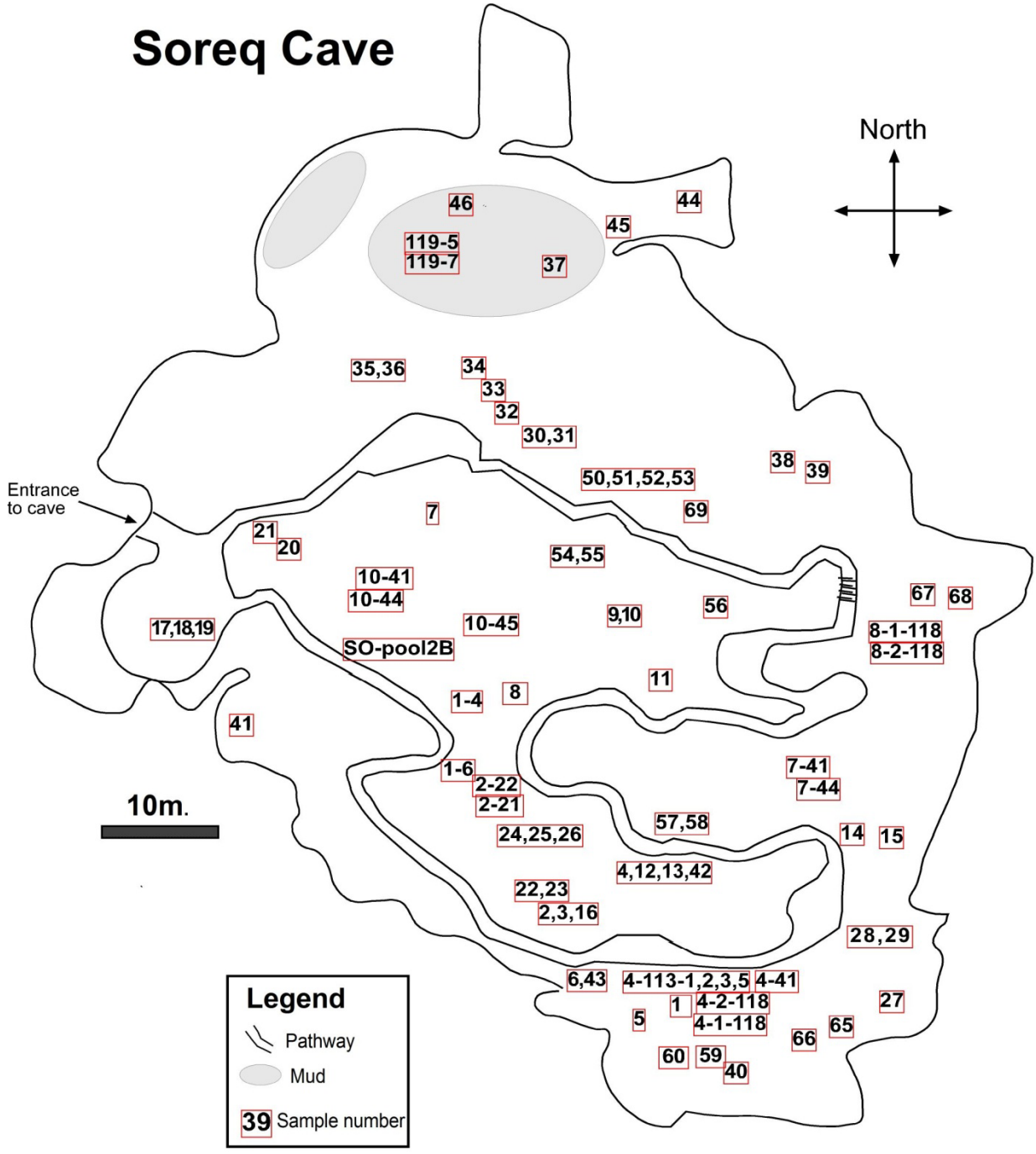

Figure 3.4.2. Map of Soreq Cave with sample locations. Red squares are for visual clarity only and groupings within them have no relevance.

only the outermost (youngest) lamina of the fallen speleothem was dated, yielding a maximum age. In other cases the damaged speleothem gave an age older than the method limit and thus only a minimum age was obtained of the post-damage regrowth. Collapsed ceiling blocks provide only minimum ages (post-collapse regrowth), since the ceiling itself is ancient bedrock whose age is not related to the time of collapse. When only a minimum *or* maximum age is available, one must attempt to understand how much time has passed since the earthquake event. There is no direct assessment technique available for this in the karstic environment. However, it is known that speleothem growth in the entire Soreq Cave is very active and has effectively been continuous, with only lateral dripping (and therefore growth) migrations. In the present study all ages are denoted as minimum, maximum, or constrained by both minimum ("post") and maximum ("pre") ages.

A *seismite* here is used in the sense of earthquake-induced phenomena: damaged speleothem, such as a severed stalagmite, a fallen stalactite, a collapsed ceiling, a fractured speleothem, or a horizon with collapsed debris within flowstone. This can usually be interchangeable with the term *collapse*, however at times the damage is a fracture and not a collapse. Most samples expose one damage occurrence or seismite; however flowstone cores often expose various seismites (collapses on distinct horizons), and sometimes, upon sawing open a stalagmite various generations of damage can be uncovered. The age of a seismite may be constrained by one dated lamina – a single bracket age (either minimum - "post", or maximum - "pre") - or ideally by two dated laminae (both minimum and maximum). An *event* is an earthquake, defined by one seismite or a group of seismites with similar ages, assumed here to have taken place due to the same earthquake event, or earthquake cluster. For those seismites where the pre and post are not close in time, the post age was used to define the age of damage. Theoretically the age of the earthquake can be any time within the pre to post age range, however since earthquakes are known to both open and close cracks [*Muirwood and King*, 1993] through which cave water drips, when pre and post ages are different, they probably each define a tectonic event.

3.4.3.2 U-Th dating results

Uranium-Thorium data for all dated speleothem seismites is presented in Table 3.4.1 and 3.4.2. Isotope ratios are given with 1 sigma uncertainties, while the ages are presented with 2 sigma uncertainties. U-Th dating methodology used here is presented in Chapter 2. Ages are given as uncorrected and corrected. Ages are corrected when $^{230}Th/^{232}Th<100$. Appendix A presents photographs of some sawed and exposed samples with laminae labels. Labeling is the same as in the tables.

More than 130 U-Th MC-ICP-MS ages were measured on forty-four Soreq-Har-Tuv field samples, the majority of which provided ages within the method limit (Table 3.4.1). The ages range from 385±60 ka to 0.19±.01 ka[*]. Four samples yielded ages beyond the method limit. The forty-four samples actually date more than fifty five seismites since many of the drilled cores penetrated flowstone which embedded numerous collapse horizons (for example seismite SO-57 shows four collapse horizons, Appendix A.vi, Table 3.4.2). There are ~7 seismites with only pre-damage ages and ~18 seismites with only post-damage ages, while ~35 seismites have a double-bracketed age (both pre and post) (Tables 3.4.2, 3.4.3). For the

[*] About half of the samples were dated previously by alpha-counting [*Kagan et al.*, 2005], and those which gave alpha-counting ages beyond 200 ka were not re-dated in this study.

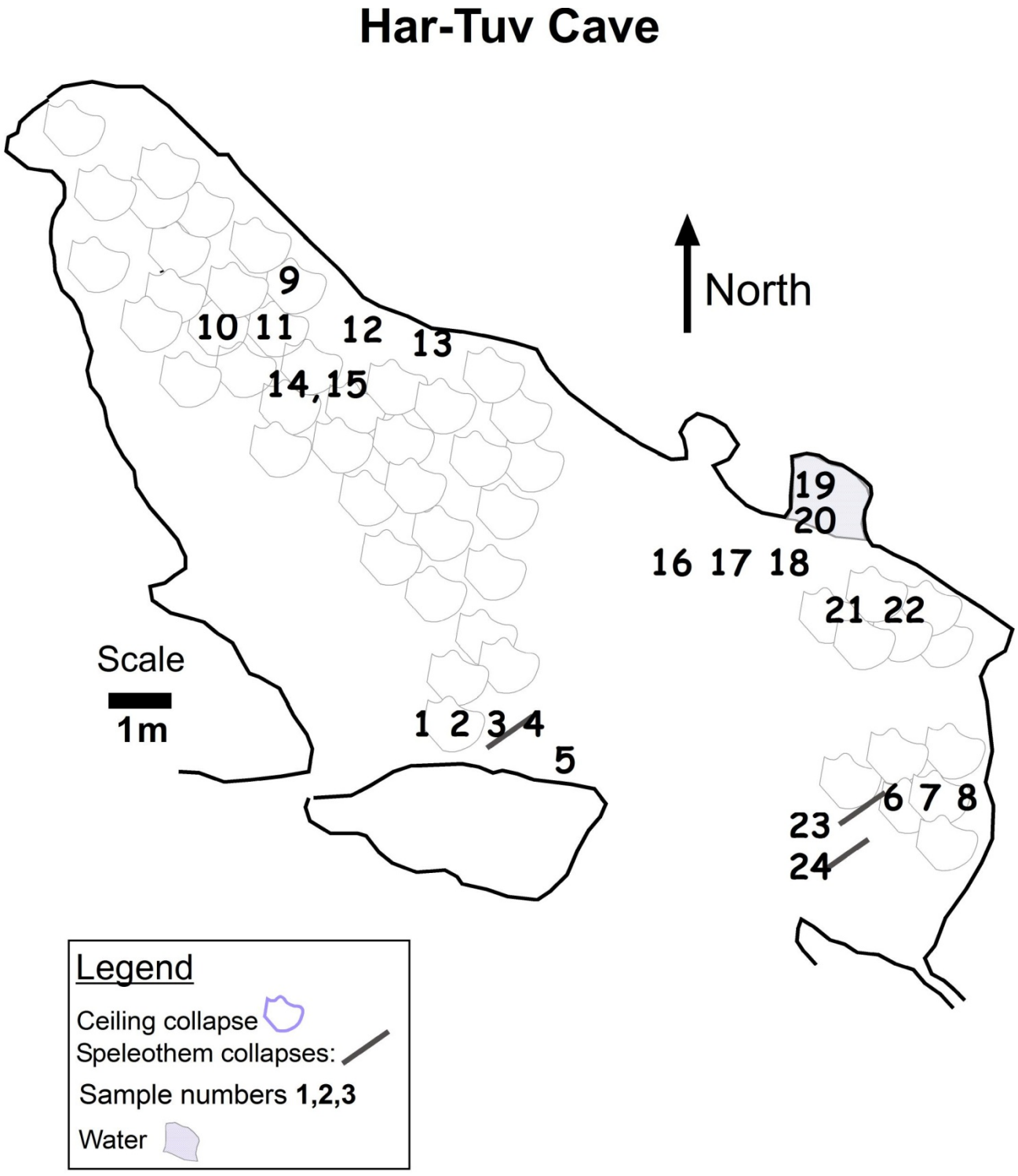

Figure 3.4.3. Map of Har-Tuv Cave with speleothem and ceiling collapses, fractures, pools, and sample numbers.

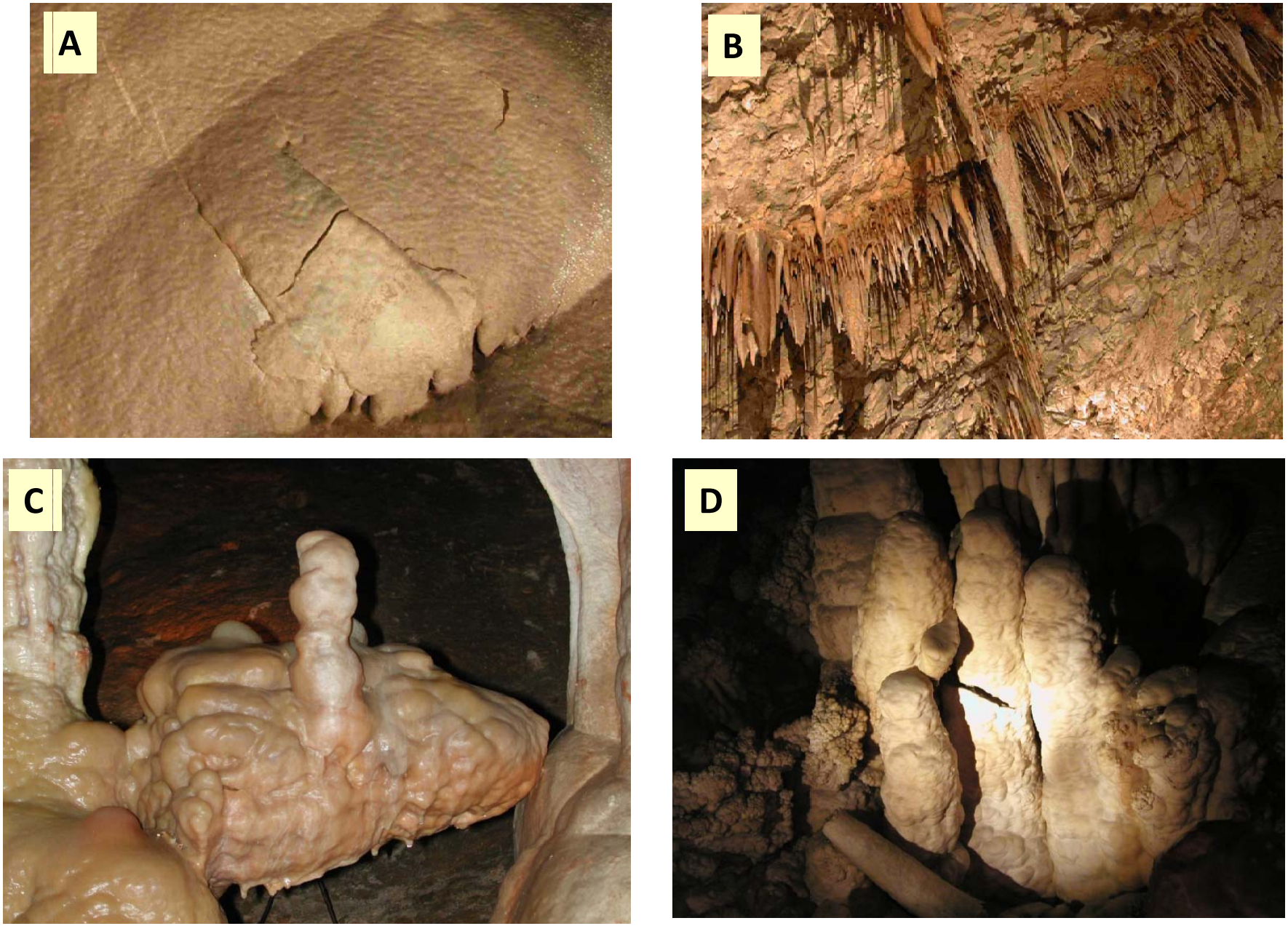

Figure. 3.4.4. Photographs of speleoseismites in Soreq Cave. A. En-echelon style cracks in flowstone; B. Fractures on cave ceiling with stalactite growth below them; C. Collapsed speleothem with post-collapse stalagmite regrowth, suspended between two pillars; D. Horizontal break in stalagmites.

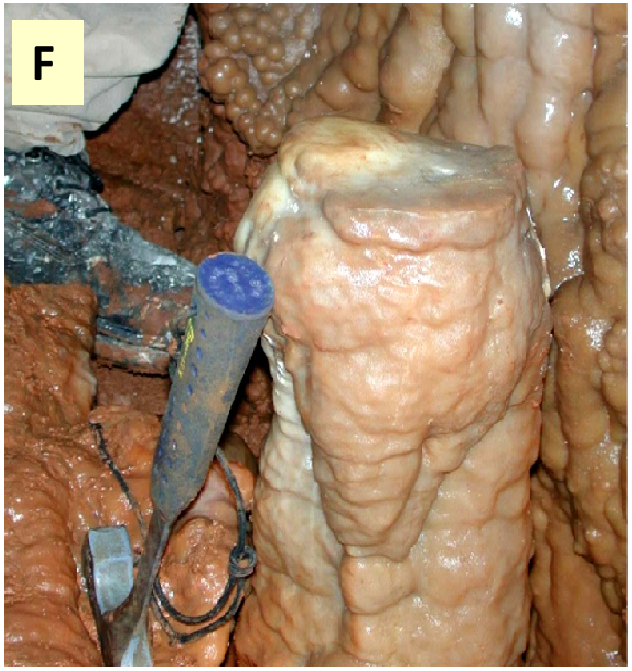

Figure 3.4.4. Continued. E. Collapsed ceiling slab, note pre-collapse broken stalactites below ceiling and post-collapse stalagmite regrowth on top of ceiling; F. Severed stalagmite top with post-damage regrowth (sample SO-32); G. Collapsed soda-straw (macaroni) stalactites embedded in flowstone cave floor; H. Collapsed ceiling blocks with post-collapse stalagmites growing below ceiling fracture.

past 200 millennia these seismites are grouped into 26 *events*, interpreted to be earthquakes (Table 3.4.3). Of these, 1 event is defined by 5 seismites, 1 event is defined by 4 seismites, 5 events by 3 seismites, 5 events by 2 seismites, and 14 events by a single seismite. Five of these events are defined by only a single date. Of the 26, there are 21 seismite events that are defined by more than one seismite or by both pre and post ages. Seismite ages can be seen in their in-situ context in Figures 3.4.12 and 3.4.13, where the minimum ages of seismites are superimposed on maps of Soreq and Har-Tuv caves. Due to potential sampling biases (discussed below) and larger age errors at older ages, only the history of the past 200 millennia is discussed.

3.4.3.3 Potential sampling and dating caveats

An in-depth discussion on caveats in the fields of speleoseismology and paleoseismology in given by *Kagan* [2002]. Older seismites are eventually buried by younger collapses and regrowth. This could ultimately lead to sampling biases. However, the dating results imply that this is not the case on the time scale of this study, and there is no trend towards younger ages. It is also possible that very young damage occurred and was not sampled, since seismites with sufficient post-damage regrowth were preferred in order to procure material to date the pre and post event. The high resolution dating in this study and the small required sample size rectified this caveat; however the post-damage age of seismites with no regrowth could not be generated. Approximately half of the samples in this study were previously dated by the alpha-counting technique, the earlier dating method before mass spectrometric techniques were available to us [see Table 3.4.2 and *Kagan*, 2002]. The samples yielding alpha-counting ages older than ~200 ka were not dated by the MS-ICP-MS and were not included in this study. There are also numerous samples that were not previously dated, and some of these are older than 200 ka. This leads to a bias towards events younger than 200 ka (Table 3.4.3). Only the past 200 millennia are included in the earthquake pattern interpretations (i.e. recurrence interval statistics below).

Younger ages have smaller uncertainties than older ages (usually ~±1-2% of age). Since this leads to higher resolution of the younger ages, they can be grouped into more definite event groups. For example, the 37 ka and 40 ka events (Table 3.4.3) can be distinct due to the small non overlapping errors. On the other hand, the ~128 ka event has seismites with ages separated by up to 3 ky since their errors overlap. Above 200 ka this is especially true, but this time period is not included in the recurrence interpretation.

3.4.3.4 Distribution in time and space

The ages of the seismites, both pre and post damage sub-samples, are presented as distributed over time in Figure 3.4.14a. The age range between the pre and post ages are seen by the green horizontal lines. The ideal scenario, where the pre and post sub-samples of a specific seismite are very close in age, is indicated by green arrows. Quiescence intervals as well as damage events are depicted in Figure 3.4.13.b. Note that age ranges between pre and post dates are not marked here, assuming that either the pre, post or both pre and post ages are indicative of a tectonic event. Seven quiescence intervals are discernible, with no pre or post damage ages during that time. When looking at only post or only pre ages, additional quiescence periods are perceptible. Arrows point to damage events listed in Table 3.4.3, while more specifically, green arrows point to events defined by more than one seismite.

Do different earthquakes or earthquake clusters caused specific types of damage in the study caves? The types observed in the cave are collapsed ceilings (CC), severed and/or toppled stalagmites (BS), fallen stalactites (FS), collapsed macaroni (soda-straw) thin stalactites (mac), and particles in flowstone (PF) –which can be any kind of collapse debris, often unclassifiable without magnification; in the case where the debris is recognized as a macaroni stalactite, it is included in the "mac" classification. Within the PF group are two samples of cracked flowstone, with the fractured laminae and the fracture-fill being dated (samples SO-52, SO-53, Appendix A-viii). Both cracks and fill are older than 300 ka. Figure 3.4.15 portrays the distribution in time of the seismites, classified by damage type. Ellipses encompass groups of close seismite ages for each type of damage. The particles in flowstone and mac types are distributed throughout the 200 ka time period discussed. Ceiling blocks fell distinctly during two periods (~4.4-13.5 ka) and (65-76 ka). Stalactites appear to have fallen almost only during the period of 36-70 ka. Severed and/or toppled stalagmites are limited to the past 70 millennia, with an additional seismite with both pre and post age at ~140 ka. The larger types of damaged material, BS, FS, and CC, occurred almost entirely since 70 ka. Further research is needed to elucidate this. As can be seen here, the types of damage are not random in time. These observations strengthen the argument presented above (section 3.4.3.1) that pre and post ages are applicable to earthquake ages, without having to consider the entire age range between them. Also, specific earthquake sources or frequency patterns could be responsible for different types of damage.

The spatial distribution of the seismite ages can be seen in Figures 3.4.12 and 3.4.13 where they are superimposed on maps of Soreq and Har-Tuv caves. Synchronous damage has occurred throughout the cave, without preference for specific areas (i.e. seismite ages appear to be spatially distributed randomly throughout the cave). Local crack opening or gravity-triggered collapse would produce synchronous ages in the same area of the cave, while an earthquake produces synchronous seismite ages throughout the cave. The randomness in spatial distribution and lack of randomness in temporal distribution of the seismites supports a seismogenic origin for the cave damage.

Table 3.4.1. Raw U-Th data and ages for speleoseismite samples measured by MC-ICP-MS.

Notes: bml= beyond method limit. The errors are calculated for the uncorrected ages. Corrected ages are given when the $^{230/232}$Th ratio is less than 100.

Sample	^{238}U conc. (ppm)	±1σ	$(^{234}U/^{238}U)_A$	±1σ	$(^{230}Th/^{232}Th)_A$	±1σ	$(^{230}Th/^{234}U)_A$	±1σ	Age 2σ Ka)		±2σ
									uncorrected	corrected (when necessary)	
Soreq Cave											
SO-14-AA	0.5156	0.0002	1.1153	0.0015	706.3	3.1	0.4567	0.0018	**65.52**		0.7
SO-32A	0.2802	0.0002	1.1145	0.0012	56.2	0.3	0.1911	0.0012	**23.0**	**22.3**	0.3
SO-32B1	0.5285	0.0003	1.0898	0.0009	7.0	0.1	0.0036	0.0001	**0.39**	**0.25**	0.01
SO-32-B2	0.6237	0.0005	1.0929	0.0018	13.3	0.8	0.0026	0.0002	**0.28**	**0.22**	0.04
SO-32-B3	0.6702	0.0004	1.0859	0.0008	8.7	1.0	0.0017	0.0002	**0.19**	**0.12**	0.04
SO-33-R	0.3461	0.0002	1.0737	0.0015	3.0	0.0	0.3817	0.0022	**52.0**	**24.8**	0.8
SO-33Q	0.3312	0.0002	1.0643	0.0020	4.5	0.0	0.4140	0.0020	**57.8**	**38.5**	0.7
SO-38-C2	1.0383	0.0005	1.0256	0.0008	15.1	0.7	0.0010	0.0000	**0.11**	**0.08**	0.01
SO-38-C1	1.0552	0.0009	1.0293	0.0008	13.8	0.4	0.0022	0.0001	**0.24**	**0.19**	0.01
SO39-Y2	43.8684	0.0221	1.0640	0.0011	350.4	2.1	0.4022	0.0022	**55.6**		0.8
SO-44A	0.3890	0.0003	1.0868	0.0017	1698.1	12.1	0.5096	0.0019	**76.6**		0.9
SO-51-top	0.1750	0.0001	1.0312	0.0019	1.9	0.1	0.4869	0.0132	**72.3**	**too detrital**	5.7
SO-51Y	0.1486	0.0002	1.0487	0.0039	14.4	0.1	0.1491	0.0016	**17.5**	**15.4**	0.4
SO 51-M6	0.3950	0.0002	1.0639	0.0022	22.9	0.2	0.5441	0.0054	**84.5**	**79.9**	2.6
SO 51-M5	0.3798	0.0003	1.0677	0.0021	49.7	0.6	0.4683	0.0059	**68.2**	**66.3**	2.4
SO-52 W	0.1678	0.0002	1.0080	0.0036	161.0	0.8	0.9908	0.0058	**478.7**		184.6
SO-52X	0.1238	0.0001	1.0122	0.0028	28.7	0.1	0.9487	0.0048	**315.4**	**309.0**	22.9
SO-54-W	0.1363	0.0001	1.0361	0.0024	47.3	0.5	0.7104	0.0073	**133.2**	**130.3**	5.6
SO-54-X	0.2731	0.0001	1.0580	0.0010	165.1	1.5	0.6352	0.0054	**108.2**		3.2
SO-54y	0.6236	0.0003	1.0631	0.0010	30.5	0.1	0.5118	0.0019	**77.3**	**74.1**	0.7

SO55-U2	0.3494	0.0002	1.0393	0.0018	441.4	2.1	0.7526	0.0031	**149.6**		2.8
SO-55-V	0.2945	0.0001	1.0487	0.0010	238.3	2.2	0.7514	0.0053	**148.6**		4.6
SO-55-W	0.2877	0.0001	1.0593	0.0015	120.3	1.1	0.6979	0.0062	**127.9**		4.4
SO-55X'	0.2925	0.0002	1.0535	0.0014	210.3	1.1	0.6417	0.0031	**110.0**		2.4
SO-55X''	0.2433	0.0002	1.0407	0.0017	877.3	3.1	0.5617	0.0021	**89.1**		1.1
SO-55-Y	0.5837	0.0003	1.0568	0.00087	22.3	0.1	0.4121	0.0012	**57.4**	**53.9**	0.4
SO-55-4	0.4939	0.0002	1.0546	0.0023	131.0	1.7	0.6280	0.0079	**106.2**		4.5
SO 55-3	0.5555	0.0006	1.0359	0.0011	478.6	8.9	0.6403	0.0112	**110.2**		6.8
SO-56W(upper)	0.3323	0.0005	1.0475	0.0022	1128.8	3.5	0.7132	0.0024	**133.8**		1.9
SO-56-V	0.5746	0.0009	1.0544	0.0028	2783.4	13.1	0.7737	0.0033	**157.9**		3.3
SO-56-U(center)	0.2204	0.0004	1.0292	0.0039	879.0	4.7	0.7991	0.0050	**172.0**		5.9
SO-56-T	0.3779	0.0005	1.0474	0.0033	1549.9	4.9	0.8305	0.0034	**187.8**		4.8
SO-56-S	0.2282	0.0001	1.0212	0.0011	176.3	0.7	0.8599	0.0036	**210.4**		5.8
SO-56 R1	0.2233	0.0001	1.0122	0.0009	424.4	1.6	0.8610	0.0031	**212.6**		5.0
SO-56 Q1	0.2035	0.0001	1.0177	0.0008	533.0	1.8	0.8985	0.0030	**244.3**		6.5
SO 57M	0.3546	0.0002	1.0228	0.0020	16.1	0.2	0.1385	0.0015	**16.2**	**14.5**	0.4
SO-57N	0.2225	0.0001	1.0213	0.0016	8.9	0.1	0.9125	0.0064	**258.5**	**237.4**	16.3
SO-57S	0.2423	0.0002	1.0271	0.0014	28.0	0.2	0.7113	0.0039	**134.0**	**129.0**	2.8
SO-57T	0.3726	0.0002	1.0618	0.0022	19.9	0.1	0.6565	0.0027	**114.5**	**108.1**	1.8
SO-57 U1	0.2403	0.0002	1.0318	0.0025	14.3	0.1	0.5650	0.0030	**90.0**	**82.3**	1.6
SO-57X	0.4598	0.0004	1.0605	0.0014	18.1	0.2	0.3838	0.0031	**52.4**	**48.3**	1.1
SO57-Y(mm)	0.4083	0.0002	1.0535	0.0010	7.5	0.0	0.4924	0.0017	**73.2**	**60.0**	0.7
SO-57Y(ek)	0.4363	0.0003	1.0628	0.0013	7.1	0.0	0.4594	0.0026	**66.4**	**53.5**	1.0
SO-58X	0.4332	0.0000	1.0641	0.0013	20.1	0.1	0.4251	0.0013	**59.8**	**55.8**	0.5
SO-58Y	0.2184	0.0001	1.0387	0.0017	5.7	0.0	0.4703	0.0015	**68.8**	**51.7**	0.6
SO-58 mac	0.3628	0.0004	1.0679	0.0018	33.8	0.2	0.3068	0.0014	**39.7**	**37.9**	0.5
SO-59-X2	0.7822	0.0004	1.2469	0.0017	367.8	2.5	0.4277	0.0026	**59.4**		1.0
SO-59Y	0.5696	0.0004	1.1896	0.0016	55.3	0.2	0.2200	0.0008	**26.8**	**26.1**	0.2
SO-60S	0.4709	0.0002	1.1083	0.0008	1835.6	12.7	0.7618	0.0039	**150.0**		3.3
SO 60-T1	0.3315	0.0003	1.1264	0.0024	1010.8	5.5	0.6773	0.0035	**119.2**		2.3
SO-60V1	0.3702	0.0002	1.1396	0.0017	1602.2	14.5	0.5736	0.0038	**90.6**		1.9

SO 60-W	0.4615	0.0002	1.1254	0.0009	2548.0	25.3	0.5588	0.0048	**87.2**		2.3
SO60-X1	0.4411	0.0002	1.1598	0.0011	394.2	3.0	0.4816	0.0033	**70.2**		1.4
SO60-X2	0.3474	0.0002	1.1460	0.0012	291.7	1.6	0.4531	0.0020	**64.6**		0.8
SO-60X	0.4265	0.0002	1.1540	0.0010	435.9	1.6	0.4882	0.0016	**71.5**		0.7
SO-60-Y	0.3344	0.0005	1.1374	0.0039	69.4	1.0	0.2236	0.0030	**27.4**	**26.8**	0.8
SO-65A	0.4888	0.0002	1.0992	0.0013	454.3	2.7	0.4814	0.0026	**70.5**		1.1
SO-65B	0.3258	0.0002	1.0919	0.0017	440.4	3.2	0.4577	0.0032	**65.9**		1.3
SO-67a	0.5906	0.0003	1.0561	0.0020	507.1	4.3	0.6496	0.0048	**112.5**		3.0
SO-67b	0.6964	0.0005	1.0674	0.0010	760.2	5.8	0.4481	0.0026	**64.2**		1.0
SO-68-Q	0.5978	0.0004	1.1003	0.0011	48.4	0.7	0.1807	0.0025	**21.6**	**20.9**	0.7
SO-68R	0.1824	0.0001	1.0603	0.0029	7.0	0.1	0.3882	0.0062	**53.2**	**41.8**	2.2
SO68-Q'	0.4502	0.0002	1.1103	0.0011	43.6	0.3	0.1864	0.0010	**22.4**	**21.5**	0.3
SO68-R'	0.1636	0.0001	1.0485	0.0012	3.8	0.1	0.3934	0.0115	**54.1**	**32.1**	4.1
SO-68-a	0.5818	0.0002	1.0986	0.0019	122.1	1.2	0.6688	0.0061	**117.3**		3.9
SO-68-b	0.8622	0.0003	1.0911	0.0012	208.4	2.8	0.3114	0.0041	**40.3**		1.3
SO-68-1-a	0.4694	0.0004	1.1175	0.0016	558.1	7.1	0.5566	0.0065	**86.8**		3.1
SO-69A	0.3468	0.0002	1.0355	0.0011	534.0	2.6	0.9609	0.0039	**291.2**		16.0
SO-69B	0.3221	0.0002	1.0345	0.0015	71.6	0.5	0.9760	0.0063	**326.8**		18.9
SO-69Q	0.2181	0.0002	1.0140	0.0021	245.2	1.5	1.0021	0.0064	**385.8**		58.8
SO-69P	0.3092	0.0002	1.0056	0.0021	6.5	0.3	0.0079	0.0003	**854.5**	**too detrital**	12,928.5
SOpool 2b-a	0.6863	0.0006	1.0663	0.0022	83.5	1.1	0.3390	0.0044	**47.4**	**46.4**	1.0
SOpool 2b-b	0.3846	0.0002	1.0579	0.0012	534.0	2.6	0.9609	0.0039	**44.8**		1.4
1-4-Y	0.4778	0.0002	1.0717	0.0017	44.2	0.2	0.3980	0.0017	**54.8**	**53.1**	0.6
1-4-Z	0.2399	0.0002	1.0355	0.0023	57.7	0.7	0.3616	0.0044	**48.7**	**47.5**	1.5
1-6-A2	0.4256	0.0003	1.0654	0.0009	47.1	0.1	0.2754	0.0005	**34.9**	**33.8**	0.1
1-6-B1	0.5693	0.0003	1.0650	0.0008	18.2	0.0	0.3311	0.0005	**43.5**	**40.1**	0.2
1-6-C1	0.3437	0.0003	1.0565	0.0020	13.2	0.2	0.3455	0.0044	**45.9**	**40.8**	1.5
1-6-C2	0.6503	0.0008	1.0691	0.0022	26.8	0.3	0.3347	0.0033	**44.1**	**41.7**	1.1
7-41 crust	0.3253	0.0003	1.1224	0.0020	61.4	0.5	0.1741	0.0014	**20.7**	**20.2**	0.4
7-41-A	0.6610	0.0004	1.0754	0.0010	474.3	3.0	0.2771	0.0015	**35.1**		0.5
7-44-x	0.5144	0.0002	1.0232	0.0013	556.5	4.7	1.0098	0.0070	**bml**	**bml**	
7-44-y	0.3572	0.0002	1.0541	0.0019	105.5	0.7	0.9547	0.0066	**304.9**		25.4

10-41A	0.7743	0.0003	1.0680	0.0011	383.3	2.3	0.1543	0.0008	**18.2**		0.2
10-41-TOP	0.4696	0.0002	1.0702	0.0009	124.5	1.0	0.1550	0.0012	**18.3**		0.3
10-44-A	0.4491	0.0003	1.0466	0.0019	92.8	1.4	0.1042	0.0015	**12.0**	**11.7**	0.4
10-45-A	0.2647	0.0001	1.0739	0.0021	99.8	1.7	0.2053	0.0034	**24.9**		0.9
10-45-B	0.7068	0.0005	1.0601	0.0011	248.8	1.1	0.2946	0.0012	**37.8**		0.4
10-45-A contact	0.2108	0.0001	1.0713	0.0021	41.6	0.6	0.2722	0.0036	**34.4**	**33.1**	1.1
10-45B contact	0.6979	0.0006	1.0605	0.0011	173.5	1.1	0.3055	0.0018	**39.5**		0.6
10-45-aa	0.6369	0.0004	1.0558	0.0021	123.0	0.9	0.2885	0.0021	**36.9**		0.7
10-45-bb	0.2918	0.0002	1.0702	0.0016	52.8	0.9	0.3005	0.0047	**38.7**	**37.6**	1.5
10-45-bb-crust	0.6181	0.0003	1.0622	0.0012	107.8	1.4	0.2856	0.0035	**36.4**		1.1
2-21 A1	0.2257	0.0002	1.0406	0.0025	5.0	0.1	0.1351	0.0040	**15.8**	**10.3**	1.0
2-21 A2	0.4197	0.0003	1.0708	0.0015	99.8	0.6	0.2220	0.0013	**27.2**	**26.8**	0.4
2-21 A3	0.4666	0.0003	1.0688	0.0016	126.0	0.8	0.2876	0.0018	**36.7**		0.6
2-21 B1	0.4106	0.0005	1.0584	0.0021	132.2	1.0	0.3072	0.0024	**39.8**		0.8
2-22-A1-1	0.4582	0.0003	1.0448	0.0012	409.8	1.2	0.7131	0.0021	**133.8**		1.6
2-22-A1-2	0.4293	0.0005	1.0474	0.0019	236.0	0.8	0.7017	0.0025	**129.7**		1.9
2-22A2	0.5344	0.0004	1.0481	0.0013	715.6	2.6	0.7141	0.0024	**134.1**		1.9
2-22-A3	0.6063	0.0004	1.0589	0.0011	568.8	1.7	0.7157	0.0021	**134.2**		1.6
2-22-A4	0.5869	0.0005	1.0552	0.0017	616.5	2.1	0.7265	0.0025	**138.4**		2.0
2-22B1	0.6832	0.0005	1.0567	0.0018	963.3	4.0	0.7375	0.0029	**142.6**		2.4
2-22B2	0.6545	0.0004	1.0577	0.0011	738.9	3.2	0.7458	0.0030	**145.8**		2.5
2-22-B3(2004)	0.6186	0.0004	1.0546	0.0012	361.2	0.8	0.7462	0.0017	**146.2**		1.5
2-22-b3(2006)	0.6726	0.0006	1.0582	0.0019	2020.7	11.3	0.7604	0.0031	**151.9**		2.8
2-22-B4	0.7654	0.0005	1.0508	0.0016	634.1	23.9	0.7373	0.0228	**142.8**		18.9
4-41-A	0.3473	0.0004	1.0730	0.0017	99.1	0.5	0.6495	0.0031	**112.1**	**110.8**	2.0
4-41-A"	0.6326	0.0006	1.0452	0.0013	147.9	0.5	1.0508	0.0037	**bml**	**bml**	
4-41-B	0.4038	0.0002	1.0156	0.0014	89.3	0.4	1.0656	0.0041	**bml**	**bml**	
4-41-B"	0.4064	0.0002	1.0151	0.0018	63.4	0.3	1.0534	0.0046	**bml**	**bml**	
4-1-118-C1	0.3953	0.0002	1.1032	0.0011	207.9	3.5	0.3480	0.0058	**46.2**		1.9
4-113-3-2	0.6819	0.0005	1.0882	0.0012	293.5	6.9	0.4266	0.0088	**60.0**		3.3
4-113-2-1	0.6139	0.0006	1.0607	0.0012	274.7	2.4	0.4835	0.0035	**71.3**		1.5
4-113-1-1	0.2674	0.0002	1.0327	0.0017	16.8	0.1	0.9511	0.0062	**308.8**	**297.9**	25.2

4-113-1-2	0.9720	0.0009	1.0176	0.0018	584.8	22.1	0.9450	0.0354	**305.6**		189.9
4-113-5-1	0.7637	0.0009	1.0720	0.0013	82.9	0.9	0.1780	0.0017	**21.3**	**20.8**	0.4
8-1-118-A	0.8734	0.0008	1.0811	0.0016	806.8	7.4	0.7811	0.0063	**159.7**		6.0
8-2-118-A	0.5591	0.0003	1.0701	0.0017	285.3	3.1	0.5023	0.0050	**75.2**		2.2
119-5-A	0.3985	0.0003	1.0759	0.0015	104.8	2.2	0.1086	0.0023	**12.5**		0.5
119-7a	0.5870	0.0007	1.0500	0.0018	27.7	0.3	0.2411	0.0028	**29.9**	**28.3**	0.8
119-7E	0.3277	0.0003	1.0529	0.0019	37.9	0.2	0.4941	0.0024	**73.6**	**71.1**	1.1
119-7F	0.3072	0.0003	1.0455	0.0022	69.0	0.3	0.4930	0.0023	**73.4**	**72.1**	1.0
119-7G	0.3420	0.0001	1.0433	0.0022	20.0	0.1	0.5194	0.0022	**79.2**	**74.1**	1.0
Har-Tuv Cave											
HT-9A	0.4782	0.0004	1.1234	0.0012	101.1	0.4	0.1170	0.0004	**13.5**		0.1
HT-9B	0.4373	0.0002	1.1186	0.0011	159.2	1.3	0.0992	0.0008	**11.3**		0.2
HT-10A1	0.3707	0.0001	1.0869	0.0013	190.2	3.6	0.0765	0.0009	**8.6**		0.2
HT-11A	0.3882	0.0001	1.1054	0.0012	50.5	1.2	0.0416	0.0009	**4.6**	**4.4**	0.2
HT-12-A1	0.2520	0.0001	1.1249	0.0009	112.0	2.8	0.0714	0.0006	**8.0**		0.1
HT-14-A1-closer	0.1795	0.0001	1.0988	0.0017	106.3	1.4	0.1015	0.0013	**11.6**		0.3
HT-18E2	0.5868	0.0003	1.1386	0.0013	3711.9	7.9	0.7793	0.0016	**155.8**		1.7
HT-18F1	0.5779	0.0004	1.1388	0.0019	797.6	4.3	0.7056	0.0016	**128.0**		1.2

Table 3.4.2. Dated speleoseismite samples, laminae descriptions, and their U-Th ages. MC-ICP-MS ages from this study. Corrected ages are given when samples showed $^{230}Th/^{232}Th<100$. Errors given are calculated for the uncorrected ages. From previous studies: alpha counting and stable isotope wiggle-matching [after *Kagan*, 2002 and *Kagan et al.*, 2005].

Sample name	sample description	Lamina dated	MC-ICP-MS age (ka)	2σ error ky	corr /unc	description of laminae	alpha (ka) (Kagan, 2002)	wiggle-matching (ka) (Kagan, 2002)
Soreq Cave								
SO-2	regrowth on fallen large stalagmite.	A				Contact not clear	99±9	
SO-3	same as SO-2	A					268±59	
		C					>309	
		D					>138	
		E					231±75	
SO-4	Huge fallen column with regrowth	A					198±31	
		B					>LIM	
		C					107±7	
		D					111±15	
SO-6	collapsed stalagmite with regrowth	A				pre	>LIM	
		C				post	77±3	
		G				later post	8.93±0.7	
SO-7	fallen large speleothem	A				Contact is unclear	46±3	
		C				after laminae a axis direction changes	50±3.5	
		D					41±3.5	46.5 ± 0.6
SO-8	fallen large speleothem (local name: the Bread Loaf formation)	A				pre	133±12	
		B				post	120±10	128 ± 2.5
		C					94±6	
		D					48±3	
SO-9	same collapsed ceiling as SO-10	A				post-collapse	>313	
SO-10	same collapsed ceiling as SO-9	A				post-collapse	>324	
SO-11	collapsed column	A				contact unclear	>LIM	
		B					>LIM	
SO-12	Huge fallen column with regrowth (same as SO-	A				post	84±6	
		B				post	58±7	
		C				post	54±3	
SO-13	Huge fallen column with regrowth (same as SO-4&12)	B				post (oldest of all posts)	132±13	163
SO-14	Collapsed ceiling slab	A					74±3	71.0 ±1.3
		AA	**65.5**	0.7	unc	post		
SO-15	Collapsed ceiling slab	AA					126±44	128±2.5
		A				post	130±10.5	
SO-16	Same fallen column as SO-2 and 3	A					89±6	
		B				contact unclear	87±5	
		C					93±4	
		D					76±4	
SO-17		SO-17AB					40±2.5	
SO-18	Huge collapsed ceiling slab (SO-17,18,19 same)	SO-18A				post	45.9±3	52.5 ± 1.5
SO-21	fallen large speleothem covered in coralitites and flowstone	A				pre	236 +88-44	
		B				post	>LIM	
SO-22	Suspended collapsed stalactite (same as SO-23)	A				pre	>287	
		B				coralitite, probably post	>304	
		C				post	>LIM	
SO-24	Upsidedown stalactites from fallen ceiling	Y				pre	198+31-23	
SO-28	Upsidedown stalactites from fallen ceiling	Y				pre		
		Yi				pre	139±11.5	
		Yii				pre	124±15.5	71.5
SO-31	Post-collapse stalactites below fallen ceiling	B				post	109±11.5	119±2.4
SO-32	Severed stalagmite	B2	**0.22**	0.04	cor	post		
		B1	**0.25**	0.01	cor	post	0.12±0.18	5.2+-0.6
		A	**22.3**	0.3	cor	pre		
SO-33	ceiling piece in flowstone	R	**24.8**	0.8	cor	pre - very high detritus		
		Q	**38.5**	0.7	cor	post - very high detritus		
	flowstone on fallen ceiling	A				post	>217	
SO-34	stalagmite on fallen ceiling	A				post	>LIM	
SO-35	stalagmites on fallen ceiling	SO-35 B				post	>LIM	
SO-36		SO-36 A				pre	>LIM	
		SO-36 B				post	>LIM	
SO-37	Fallen stalactite stuck in mud	Y				last laminae in fallen stalac.	238 +43-30	
SO-38	Severed stalgmite with regrowth	B				pre	72±4	
		C1	**0.19**	0.01	cor	post		5.4+-0.6
		C2	**0.11**	0.08	cor	post	0.072±0.32	
SO-39	Pre-collapse stalactite on fallen ceiling	Y				pre	65±6	
		Y2	**55.6**	0.8	unc	pre		
SO-40	core into flowstone floor, collapse layers	A				pre-collapse	94±5	102 ±2.7
		B				post-collapse	60±3	
SO-42	Same as large fallen SO-13 column.	Y				pre-collapse, rib of column	>LIMIT	
SO-43	Collapsed stalagmite with regrowth (same as SO-6)	A				pre-collapse	>LIMIT	
		B				post-collapse	135±11.5	144 ±3.7
SO-44	Stalagmite on fallen boulder. Base missing.	AB				post boulder collapse	71±5	
		A	**76.6**	0.9	unc			78
SO-45	Fallen stalactite with small post-event stalactites growing below it.	B				post	230 +61-36	
		A				pre		
SO-51	Core in flowstone floor with macaroni cemented on surface, fracture exposed, collapsed ceiling piece at base	top				thin film, not much		
		y	**15.4**	0.4	corr	post		
		X				pre-macaronis	49.86±4	51.0 ± 1.0
		W						
		m6	**79.9**	2.6	corr	post-mac, thin corally-type laminae,		
		m5	**66.3**	2.4	corr	pre-mac; chronol. order not good		
SO-52	Core in flowstone floor, exposes fracture and ceiling collapse	Y				post		
		X	**309.0**	22.9	corr	first lamina filling fracture, post		
		W	**478.7**	184.6	unc	pre-fracture		
		A				post ceiling fall	>310	
SO-53	Core in flowstone floor, exposes fracture with fill and small collapses	B				pre- fracture;	>method limit	
		F				post - fracture & post-mac	>method limit	
SO-54	Core in flowstone floor, exposes embedded pieces	Y	**74.1**	0.7	corr	post- embeds mac		
		X	**108.2**	3.2	unc	pre surface macs.		
		W	**130.3**	5.6	corr	post-embeds debris		
SO-55	Core in flowstone floor, exposes embedded pieces 3 events within v,w,y laminae	y	**53.9**	0.4	cor	surface, embeds a large stalactite, sin		
		X ''	**89.1**	1.1	unc	pre surface	177.5 +52-33	
		X '	**110.0**	2.4	unc			
		w	**127.9**	4.4	unc	embeds debris		
		v	**148.6**	4.6	unc	post embeds macaroni, is pre to w seismite		
		U-2	**149.6**	2.8	unc	pre macaroni		
	Macaroni stalactites embedded between laminae X&Y	4	**106.2**	4.5	unc	inner laminae in collapsed mac		
		3	**110.2**	6.8	unc	pre-outer laminae in collapsed mac		

Sample name	sample description	Lamina dated	MC-ICP-MS age (ka)	2σ error ky	corr /unc	description of laminae	alpha (ka) (Kagan, 2002)	wiggle-matching (ka) (Kagan, 2002)
SO-56		AB				post-collapsed ceiling	>201	
		Q1	244.3	6.5	unc	post - embeds ceiling pieces		
		R1	212.6	5.0	unc	not seismite		
		S	210.4	5.8	unc	not seismite		
	Core in flowstone floor, exposes embedded pieces, 5 seismites	T-top	187.8	4.8	unc	pre , top of lamina	179.7±16.5	
		U-center	172.0	5.9	unc	post		177 ±7
		V-center	157.9	3.3	unc	post and pre	173±29	150.9±3
		W-upper	133.8	1.9	unc	post-embeds mac	118+ - 13.5	
		X				pre-collapse		155-151??
		Y				surface, full of fallen macaroni stalactites		
SO-57		Z				surface, post of macaronis		
		Y(ek)	53.5	1.0	corr	post - embeds mac, same lamina		47.5 ± 1.0
		Y(mm)	60.0	0.7	corr	post - embeds mac, same lamina (duplicate)		
		X	48.3	1.1	corr	pre (x and y in wrong chronol order)	51.2±3	
		W				not seismite	51.12±4.3	
	Core in flowstone floor, exposes embedded pieces. 3 seismite events	V				not seismite	79±10.5	
		U1	82.3	1.6	corr	embeds ceiling piece		
		T	108.1	1.8	corr	post. and pre to U1	159.5±34	119
		S	129.0	2.8	corr	pre macs	157 +44-30	
		N	237.4	16.3	corr	post		
		M	14.5	0.4	corr	problem with age		
SO-58		mac	37.9	0.5	corr	pre. collapsed macaronis		
		Y	51.7	0.6	corr	post, thin laminae covering macs		45.7+-1
	Core in flowstone floor, exposes embedded pieces. 3 seismite events	X	55.8	0.5	corr	pre	44.7±5	
		W				post&pre of 2 events		103+-2.7
		V				pre-collapse	130±23	
		U				post, bottom embeds macaronis		106+-2.7
SO-59		X				pre-surface macaronis	70±5.5	71.5 ± 1.3
	Core in flowstone floor, exposes embedded	X2	59.4	1.0	unc	pre-surface macaronis		
		y	26.1	0.2	cor	post		
SO-60		y	26.8	0.8	corr	post; surface layer, +cemented macs		
		x2	64.6	0.8	unc	pre & post		
		x1	70.2	1.4	unc	pre		
		X	71.5	0.7	unc	encompasses x1 & x2		46.5 ± 1.0
		W	87.2	2.3	unc	post, embeds macs etc..		
	Core in flowstone floor, exposes embedded pieces, 4 or 5 seismites	V1	90.6	1.9	unc	pre	83±7	
		U				may embed collapses		
		T1	119.2	2.3	unc	post		
		T				post		154±3.5
		S	150.0	3.3	unc	pre collapse	121.3+34.2 -	
SO-65	Fallen ceiling with pre-collapse stalactites	A	70.5	1.1	unc	pre (broken stalactite)		
		B	65.9	1.3	unc	post (regrowth)		
SO-67	Core in flowstone floor, exposes embedded speleothems	a	112.5	3.0	unc	pre		
		b	64.2	1.0	unc	post		
		a	117.3	3.9	unc	pre, broken stalactite		
		1-a	86.8	3.1	unc	pre,broken stalactite		
		b	40.3	1.3	unc	post, regrowth on broken stalactite		
SO-68	Fallen ceiling with pre-collapse stalactites and post-collapse stalagmites	q	20.9	0.7	cor	pre - not in chrono. order		
		r	41.8	2.2	cor	post - not in chrono.order		
		Q'	21.5	0.3	cor	pre - duplicate, also not in chrono. order		
		R'	32.1	4.1	cor	post - duplicate, also not in chrono. order		
SO-69		A	291.2	16.0	unc	pre - wrong order		
	Two large fallen speleothems embedded in flowstone	B	326.8	18.9	unc	post - wrong order		
		Q	385.8	58.8	unc	post		
		P	beyond limit		unc	pre		
1-4	Fallen stalagmite with top severed, with regrowth	Z	47.5	1.5	corr	post break		
		Y	53.1	0.6	corr	pre-break		
		A2	33.8	0.1	corr	younger than post broken speleothem		
1-6	Fallen stalagmite with top severed with regrowth	B1	40.1	0.2	corr	post broken stalact(stalagmite?)	31.53±3	36.0 ± 0.4
		C1	40.8	1.5	corr	pre broken stalact(stalagmite?)	44.77±3	39.5 ± 1.0
		C2	41.7	1.1	corr			
2-21		A1	10.3	1.0	corr	younger than post contact		
	Fallen stalagmite with top severed with regrowth	A2	26.8	0.4	corr	younger than post contact		
		A3	36.7	0.6	unc	post, first after broken speleothem	30.95±2	34.5 ± 0.4
		B1	39.8	0.8	unc	pre of broken speleothem	46.11±3.81	39.0 ± 1.0
2-22	Fallen stalagmite with top severed	a4	138.4	2.0	unc	post		
		b1	142.6	2.4	unc	pre		
7-41	Fallen stalagmite with top severed	crust	20.2	0.4	cor	post		
		A	35.1	0.5	unc	pre		
7-44	Fallen stalagmite with top severed, with regrowth	x	beyond limit			pre		
		y	304.9	25.4	unc	post		
4-1-118	stalactite below collapsed ceiling	C1	46.2	1.9	unc	pre; broken stalactite		
4-113-1	Fallen stalagmite with top severed, with regrowth	1	297.9	25.2	corr	post		
		2	305.6	189.6	unc	pre		
4-113-2	collapsed stalagmite	1	71.3	1.5	unc	pre		
4-113-3	collapsed stalagmite	2	60.0	3.3	unc	pre		
4-113-5	collapsed stalagmite	1	20.8	0.4	corr	pre		
8-1-118	stalactite below ceiling	8-1-118-A	159.7	6.0	unc	pre-collapse stalactite		
8-2-118	stalagmite on ceiling	8-2-118-A	75.2	2.2	unc	post-collapse		
119-5	stalagmite on mud pile	A	12.5	0.5	unc	post-collapse		
119-7	stalagmite fallen with mud pile	EFG	71-74			soil collapse events within laminae		
		A	28.3	0.8	corr	pre; collapsed stalactite		
10-41	severed stalagmite	a	18.2	0.2	unc	pre		
		top	18.3	0.3	unc	post		
10-44	collapsed stalagmite	a	11.7	0.2	corr	pre		
		a	24.9	0.9	unc	post		
		a-contact	33.1	1.1	corr	post		
10-45	collapsed stalagmite	aa	36.9	0.7	unc	post-closest to contact		
		b	37.8	0.7	unc	pre		
		b-contact	39.5	0.6	unc	pre		
		bb-crust	36.4	1.1	unc	pre-closest to contact		
		bb	37.6	1.5	cor	pre		
SO-pool-2E	Fallen and embedded stalactite	a	46.4	1.0	corr	pre		
		b	44.8	1.4	unc	post		
4-41		a	110.8	2.0	corr	post		
	Fallen stalactite	a1	beyond limit			post-closer to contact		
		b and b'	beyond limit			pre		
Har-Tuv Cave								
HT-1	Broken column	A				pre	>LIMIT	
		B				post	230 +59-36	
HT-7	Collapsed ceiling with regrowth	A				post	136±11	151±3.5
HT-9	Collapsed ceiling with regrowth	A	13.5	0.1	unc	post - closest to contact	7.6±0.6	13.5±1
		B	11.3	0.2	unc	post		

Sample name	sample description	Lamina dated	MC-ICP-MS age (ka)	2σ error ky	corr /unc	description of laminae	alpha (ka) (Kagan, 2002)	wiggle-matching (ka) (Kagan, 2002)
HT-10	Collapsed ceiling with regrowth	**A1**	**8.6**	0.2	unc	post	2.8±0.57	5.7±0.6
HT-11	Collapsed ceiling with regrowth	**A**	**4.4**	0.2	cor	post	2.4±0.3	3.9±0.5
HT-12	Collapsed ceiling with regrowth	**A1**	**8.0**	0.1	unc	post	5.3±0.6	5.3
HT-13	Collapsed ceiling with regrowth	**A**				post	2.5±0.3	5.4±0.6
HT-14	Collapsed ceiling with regrowth	**A**	**9.4**	0.1	unc	post	11±0.6	13
		A1	**11.6**	0.3	unc	post - closest to contact		
		B				post	9.8±0.6	
HT-15	Collapsed ceiling with regrowth	**A**				post	0.87±0.46	4.9±0.6
HT-18	Core into flowstone exposes pieces	**A**				embeds macaronis	>LIMIT	
		C				post	243 +61-37	
		E2	**155.8**	1.7	unc	pre	190 +20-16	148±3.7
		F1	**128.0**	1.2	unc	post	145±7	
		H				PRE, I is sin	96±7	97±1.7
HT-19	Collapsed ceiling with regrowth	**A**				post ceiling collapse	54±3	
HT-20	Collapsed ceiling with regrowth	**A**				post ceiling collapse	107±5	144±3.7
HT-21	Collapsed ceiling with regrowth	**AB**				post ceiling collapse	93±5	110± 2
HT-23	Collapsed ceiling with regrowth	**A**				post ceiling collapse	119±6	135± 2.7
HT-24	Collapsed speleothem	**A**					>351	
		B					>LIMIT	
		C					>242	
		D					>LIM	

Table 3.4.3 Speleoseismite events in chronological order. U-Th data is in Tables 3.4.1 and 3.4.2.

Seismite sample	Seismite type*	dated lamina	Relation to event **	Age of dated laminae (ka) and 2σ error	Total age range (ka)	Event age (ka)	# of collapses dated to event
SO-38	BS	c1	post	**0.19±0.01**	0.18 or older		
SO-32	BS	b1	post	**0.25±0.01**	0.24 to 22.6	**mid 18th century**	2
		a	pre	**22.3±0.3**			
HT-11	CC	a	post	**4.4 ±0.2**	4.2 or older	**~4.4**	1
HT-12 CC		a	post	**8.0 ±0.1**	7.9 or older	**~8.5**	2
HT-10	CC	a	post	**8.6 ±0.2**	8.4 or older		
HT-14	CC	a	post	**11.6 ±0.3**	11.3 or older		
10-44	BS	a	pre	**11.7±0.2**	11.9 or younger		3
119-5	collapsed	a	post	**12.5±0.5**	12.0 to 29.5	**~12.5**	
119-7	mud pile	a	pre	**28.3±0.8**			
HT-9 CC		a	post	**13.5±0.1**	13.4 or older	**~13.5**	1
SO-51	mac	y	post	**15.4±0.4**	15.0 or older	**~15.5**	1
10-41	BS	a	pre	**18.2±0.2**	18.0 to 18.6		
		top	post	**18.3±0.3**		**~18**	1
7-41	BS	crust	post	**20.2±0.4**	19.8 to 35.5		
		a	pre	**35.1±0.4**		**~21**	2
4-113-5	BS	1	pre	**20.8±0.4**	21.2 or younger		
SO-33	PF	r	post	**24.8 ±? Hi det**	24.8 to 38.5 ± ??		
		q	pre	**38.5 ±? Hi det**			
SO-59	mac	y	post	**26.1 ±0.2**	25.9 to 60.4	**~27**	
		x2	pre	**59.4±1.0**			3
SO-60	mac	y	post	**26.8 ± 0.8**	26.0 to 65.4		
		x	pre	**64.6±0.8**			
10-45	BS	aa	post	**36.9±0.7**	35.3 to 37.6		
		bb-crust	pre	**36.4±1.1**		**~37**	
2-21	FS	a3	post	**36.7 ± 0.6**	36.1 to 40.6		2
		b1	pre	**39.8 ± 0.8**			
SO-68	FS	b	post	**40.3±1.3**	39.0 to 89.9		
		1-a	pre	**86.8±3.1**		**~40**	2
1-6	BS	b1	post	**40.1 ±0.2**	39.9 to 42.3		
		c1	pre	**40.8 ±1.5**			
SO-pool2B	FS	a	post	**44.8 ±1.4**	43.4 to 47.4		
		b	pre	**46.4 ±1.0**			
1-4	BS	z	post	**47.5 ± 1.5**	46.0 to 53.7	**~47.5**	3
		y	pre	**53.1±0.6**			
4-118	FS below CC	c1	pre	**46.2±1.9**	48.1 or younger		
SO-58	mac	y	post	**51.7 ± 0.6**	51.1 to 56.3		
		x2	pre	**55.8 ± 0.5**			4
SO-55	mac	y	post	**53.9±0.4**	53.5 to 90.2	**~53**	
		x"	pre	**89.1±1.1**			
SO-39	FS	y2	pre	**55.6 ± 0.8**	56.4 or younger		
4-113-3	BS	2	pre	**60.0±3.3**	63.3 or younger		
SO-67	PF	b	post	**64.2±1.0**	63.2 to 115.5		
	PF	a	pre	**112.5±3.0**			
SO-65	FS	b	post	**65.9 ± 1.3**	64.6 to 71.6		5
	FS	a	pre	**70.5±1.1**		**~65**	
SO-60	PF	x2	post	**64.6±0.8**	63.8 to 71.6		
		x1	pre	**70.2±1.4**			
SO-14 CC		aa	post	**65.5 ± 0.7**	64.8 or older		
4-113-2	BS	1	pre	**71.3±1.5**	69.8 or younger		
119-7	soil events	e,f,g		**71 to 74**	71 to 74		
SO-54	mac	y	post	**74.1±0.9**	73.2 to 111.4		3
		x	pre	**108.2±3.2**		**~74**	
8-2-118	CC	a	post	**75.2±2.2**	73.0 to 165.7		
8-1-118	FS below CC	a	pre	**159.7±6.0**			
SO-44 CC		a	post	**76.6±0.9**	75.7 or older	**~76**	1
SO-57 PF		u1	post	**82.3 ± 1.6**	80.7 to 109.9		
		t	pre	**108.1±1.8**		**~82**	1
SO-60 mac		w	post	**87.2±2.3**	84.9 to 92.5	**~87**	
		v1	pre	**90.6±1.9**			1
SO-57 mac		t	post	**108.1±1.8**	106.3 to 131.8	**~108**	
		s	pre	**129.0±2.8**			1
SO-60 PF		t1	post	**119.2 ± 2.4**	116.8 to 153.3	**~119**	
		s	pre	**150.0±3.3**			1
SO-55	PF	w	post	**127.9±4.4**	123.5 to 153.2		
		v	pre	**148.6±4.6**			
SO-54	PF	w	post	**130.3±5.6**	124.7 or older	**~128**	3
HT-18	PF	f	post	**128.0±1.2**	126.8 to 157.5		
		e	pre	**155.8±1.7**			
SO-56	mac	w	post	**133.8±1.9**	131.9 to 161.2	**~134**	1
		v	pre	**157.9±3.3**			
2-22	BS	a4	post	**138.4±2.0**	136.4 to 145.0	**~138**	1
		b1	pre	**142.6±2.4**			
SO-55	PF	v	post	**148.6 ± 4.6**	146.8 to 153.2	**~149**	1
		u-2	pre	**149.6 ± 2.8**			
SO-56	PF	v	post	**157.9±3.3**	154.6 or older	**~158**	1
SO-56	PF	u	post	**172.0±5.9**	166.1 to 192.6	**~172**	
	PF	t	pre	**187.8±4.8**			1
SO-57	PF	n	post	**237.4±16.3**	221.1 or older	**~237**	1
SO-56	PF	q1	post	**244.3±6.5**	237.8 or older	**~244**	1
4-113-1	BS	1	post	**297.9±25.2**	272.7 to 495.2		
		2	pre	**305.6±189.6**			
7-44	BS	y	post	**304.9±25.4**	279.5 or older		
		x	pre	**beyond limit**		**~309**	3*
SO-52	FF	x	post	**309.0 ±22.9**	286.1 or older		
		w	pre	**478.7 ±184.6**			
SO-69	FS q		post	**385.8±58.8**	327.0 or older	**~386**	1
	in flowstone	p	pre	**beyond limit**			
4-41	FS	a1	post	**beyond limit**	beyond limit		
		b	pre	**beyond limit**			

Notes:

Only laminae ages directly relevant to event ages are presented here (i.e. ages from laminae which are not the closest dated laminae to contact are not included here; laminae from same seismite whose ages not in chronological order are also not included here). In cases where there is a large difference between pre and post ages of the seismite, the event age is estimated by the post-damage age, see text for details.
*The number of collapses in this event is due to the larger errors at this time period and therefore inclusion of more collapses in this event age range.
PF=particles in flowstone core; BS=broken stalagmite; FS=fallen stalactite; CC=ceiling collapse (refers to regrowth on CC unless otherwise stated); mac=broken and collapsed macaroni (soda-straw stalactites); mud pile refers to collapsed pile of soil at the northern end of the Soreq Cave. *Soil event* refers to intensive soil inclusion within speleothem laminae which is indicative of soil collapse into cave fissures.

3.4.3.5 Recurrence intervals of speleoseismite recorded earthquakes

Recurrence statistics can be expressed by two parameters: the mean recurrence interval (RI) and an aperiodicity parameter, defined as the standard deviation of the RI divided by RI [*Goes*, 1996]. An aperiodicity value (also known as coefficient of variation) of 1.0 is the threshold for earthquake clustering behavior (aperiodicity>1 represents clustering, aperiodicity<1 represents quasi-periodic behavior) [*Kagan and Jackson*, 1991]. For the study caves, the 26 events from 200 ka to present lead to a mean recurrence interval (RI) of approximately 6.8 ky, or 6.6-6.8 ky, depending on the time period chosen for investigation (Table 3.4.4). The standard deviation of the recurrence interval is 4.4 to 4.7 ky. The aperiodicity value is 0.7, lending to quasi-periodic behavior. If only the 21 seismite events dated by more than one date are used, the RI increases to 7.8-8.6 ky, the standard deviation to 4.3-5.3 ky, and the aperiodicity values change slightly to 0.5-0.6; the quasi-periodic behavior persists. This RI is much longer than that interpreted from the lake archive earthquake history (RI on the order of tens or hundreds of years). This is due to filtering out of the smaller earthquakes in the cave environment and at the somewhat more removed location (40 km from the DST). This produces a paleoseismic catalogue of major earthquakes. The RI is on the scale of the longest of the Lisan Formation quiescence periods and enhanced seismicity periods. Large earthquakes, like the ones recorded in the caves, could trigger periods of high seismicity [*Lyakhovsky et al.*, 2001].

Table 3.4.4. Earthquake recurrence statistics based on cave seismites. Data from Table 3.4.3. Aperiodicity=standard deviation/average recurrence interval. The top three rows are for all twenty-six events since 200 ka, the bottom three rows are for the twenty-one events since 200 ka with more than one date.

	Time period	**Average recurrence interval [ky]**	**Standard deviation [ky]**	**Aperiodicity**
26 events	0-170 ka	6.8	4.4	0.7
	4 ka-150 ka	6.6	4.6	0.7
	10 ka-150 ka	6.8	4.7	0.7
21 events	0-170 ka	8.6	5.3	0.6
	4 ka-150 ka	7.8	4.3	0.6
	10 ka-150 ka	8.0	4.4	0.5

As can be seen from Table 3.4.3, the age bracketing of many samples features a large gap between the pre and post damage ages. This age gap reflects the time of growth cessation. The earthquake most probably occurred at the time of the pre-event age (growth cessation) or at the time of the post-event age (growth renewal), however, any time in between cannot completely be ruled out. This is discussed above in Chapter 3.4.3.1. Many events are dated by only one seismite (although most seismites have more than one date – pre and post). This issue can only be resolved by additional extensive dating of speleoseismites in the Judean Hills.

3.4.4 Petrography of speleoseismites

Previous petrographic investigations of speleoseismites are minimal. *Panno et al.* [2009] found what they interpret as post-earthquake initiated stalagmites to be composed of columnar calcite with their long crystallographic axes normal to the substrate on which the stalagmites were growing. Alternating clear and dark bands are interpreted to be annual growth laminae. The petrography of inactive or pre-earthquake speleothems was not examined. Broken or collapsed speleoseismites have not been previously examined. Detailed petrographic analyses on intact speleothems from the Soreq Cave were carried out by *Bar-Matthews et al*. [1991] and *Ayalon et al.* [1999].

Thin sections of seven speleothems were analyzed under a polarizing microscope. As described in Chapter 2.2, seven samples were analyzed under polarizing microscope. Five are collapsed or severed stalagmites, one is part of a group of collapsed stalactites, and one is a core drilled into flowstone embedding horizons of collapse debris. All have post-damage regrowth. Figures 3.4.5 through 3.4.11 present thin sections under different polarizing microscope enlargements. Petrography of these samples is described here:

1-6 (Figure 3.4.5). This broken stalagmite is dated to 40.8 ±1.5 ka (pre) and 40.1±0.2 ka (post). This sample specifically shows fast growth rate. This implies a negligible time lapse between the earthquake and continuation of dripping and growth.

PRE: The pre contact crystals are more equant-shaped or heterogeneously shaped. The crystals are randomly oriented, small quasi-equant, and disarranged.
POST: The post contact crystals are elongated and large and show wavy extinction.
CONTACT: At the contact is a crack with "dust-fill" or crushing (gauge?), or gauge/dust that was washed away.

10-45 (Figure 3.4.6). This broken stalagmite is dated to 36.4±1.1 ka (pre) and 36.9±0.7 ka (post). This indicates a very fast growth rate and almost no gap between pre and post seismic growth.
Pre and post contact crystals show very different extinctions.
PRE: Pre-contact crystals are porous and heterogeneous with wavy and feathery extinction. Rhombohedra are abundant in the pre-contact area, not all are destroyed, but seem rearranged: the rhombs are "floating" in cavities. Also shows "rope"-like texture (maybe crushing between the "feathers"). The pre-contact shows tiny crystals that are crushed carbonate crystals, with no reason to believe that they formed this way originally.
POST: Post-contact crystals are very organized and elongated
CONTACT: The contact is covered by crypto-crystalline opaque, probably clay-sized, grains. The contact zone appears not to be sharp (see C in figure). Even after the breakage it takes time for the crystals to recover and for the system to become able to form large elongated crystals.

7-44 (Figure 3.4.7). This broken stalagmite is dated to beyond the method limit (>500 ka).
PRE: Small crystals, which get smaller as approaching the contact. 2 cm from contact the pre-event crystals are also elongated with parallel extinction. At contact crystals look crushed. There is a crack in the pre-contact material that reaches the contact and is filled with clay-size carbonate (also seen by eye, very dark black parallel joints). In figure: C: Shattering in pre-event crystals, D: Pre-event crystals, 2 cm away from contact. POST: Large elongated crystals

SO-32 (Figure 3.4.8). This severed stalagmite is dated to 22.3±0.3 ka (pre) and 0.25±0.01 ka (post)
PRE: Crystals are smaller, equant, and less organized (D in figure: deformed pre-event crystals).
POST: Crystals are larger, elongated, with clear orientation, blocky (C in figure: non-deformed crystals, post-event).
CONTACT: Suture is not a straight line

SO-7 (Figure 3.4.9). The collapse of this stalactite was dated to 46.5 ka by the alpha-dating and wiggle-matching techniques [*Kagan et al.*, 2005]. The contact between pre and post was assumed to be where the growth axis makes a sharp change (see Figure 3.4.9A, between lamina c and d). However, under the polarizing microscope no contact is visible, all laminae look like regular growth laminae, some smaller, some larger, but none look damaged. This sample was taken from a large group of connected but fallen and sub-horizontal stalactites, so a collapse event did necessarily occur. However, the petrography here shows that the contact horizon demarking the pre-and post event material, imperative for dating the event, is ambiguous or perhaps was not reached when the seismite was drilled into in the field.

2-21 (Figure 3.4.10). This collapsed stalagmite is dated to 39.8 ±0.8 ka (pre), 36.7±0.6 ka (post)
PRE: Crushed, non laminated, unorganized structure (D in figure).
POST: Small but elongated crystals.

SO-58 (Figure 3.4.11). This collapsed debris embedded in flowstone is dated to 55.8±0.5 ka (pre) and 51.7±0.6 ka (post). Fallen soda-straw type stalactite gave illogical date of 37.9±0.5 (younger than laminae covering it).
PRE: Shattered macaronis (B and C) and other tiny crystals (D) embedded on surface horizon.
POST: Covers the shattered macaronis and undamaged laminae.

Investigation under the polarizing microscope allowed a close look at the crystals within seismite samples. The identification of the paleoseismic contact in the drilled sample was verified. The crystals adjacent to the paleoseismic contact were examined. In all cases the pre-contact crystals were smaller, non-elongated, and disorganized, as opposed to the post-contact crystals being larger, elongated, and oriented perpendicular to contact, or parallel to growth direction. In two cases (Figures 3.4.5 and 3.4.6) the contact was characterized by opaque, crypto-crystalline growth, indicating dust-fill, gouge-fill, or fill that was washed away. Dust-filled air could also be expected after large collapses or intense shaking during an earthquake. Clay-fill would suggest a time elapse from pre to post deposition. In one case, the pre-contact crystals at 2 cm below contact the crystals look like long and large, and become smaller closer to the contact. Additional thin sections of these samples, and others, of these should be investigated at varying distances to the contact in order to better understand the damage to the broken speleothems.

Figure 3.4.5. Speleoseismite sample **SO-1-6.** A. Hand sample, B-C. Photographs under polarizing microscope. See text for details.

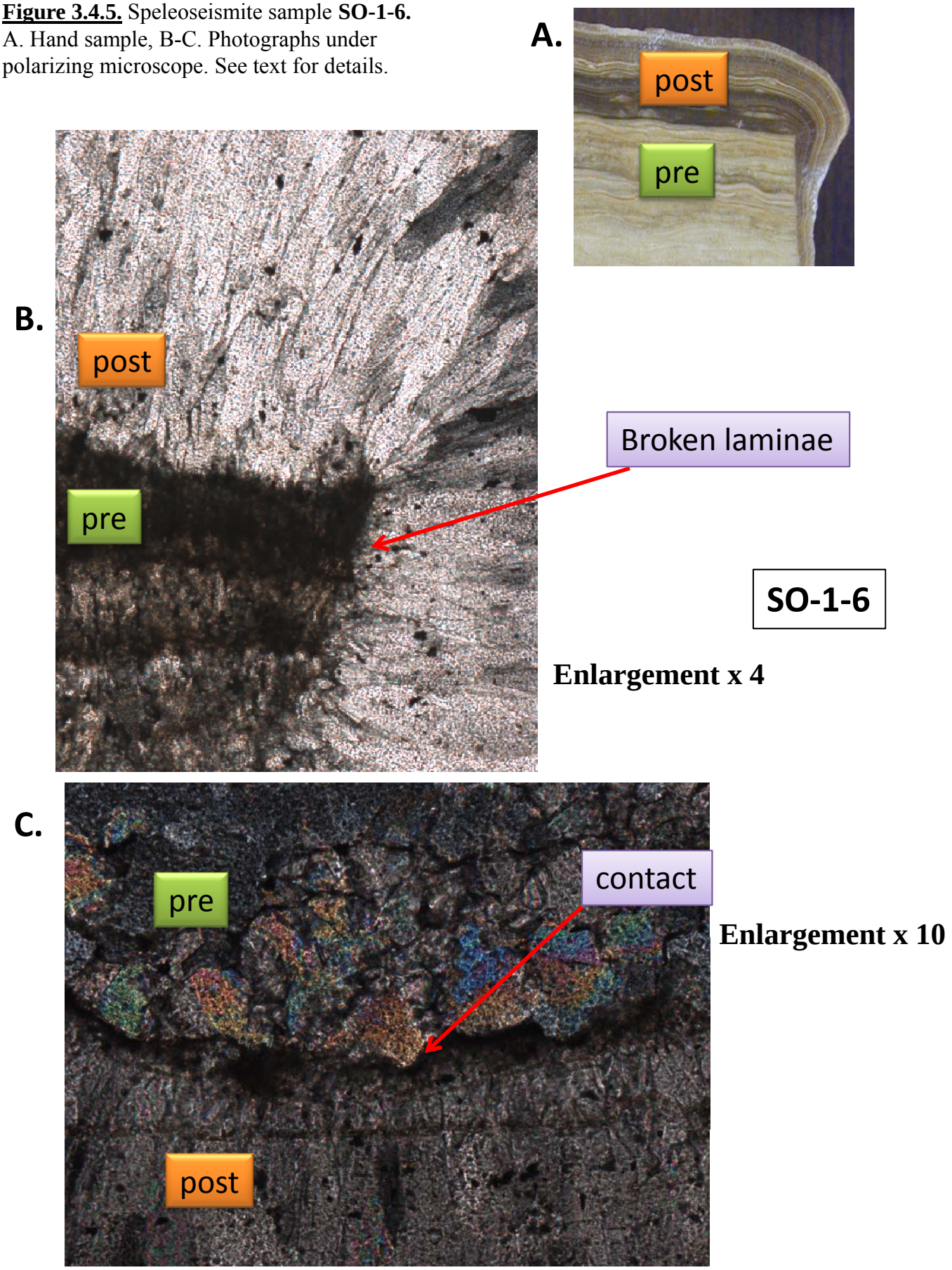

Figure 3.4.6. Speleoseismite sample **SO-10-45**
A. Hand sample, B-C. Photographs under polarizing microscope. See text for details.

A.

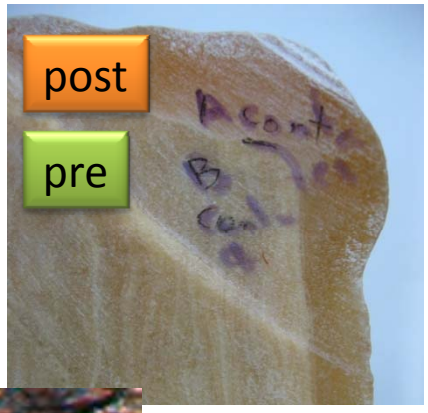

SO-10-45

B.

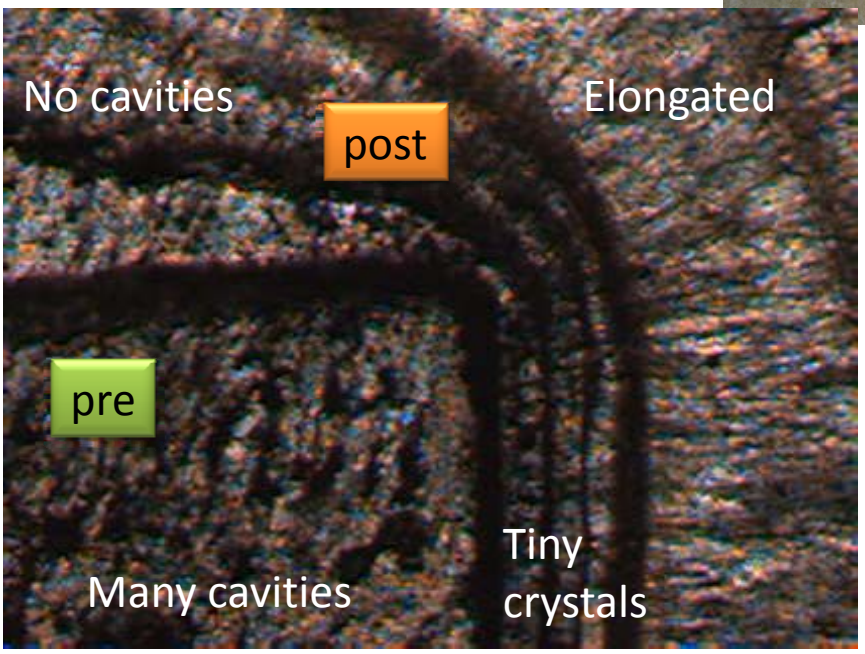

Enlargement x 4

C.

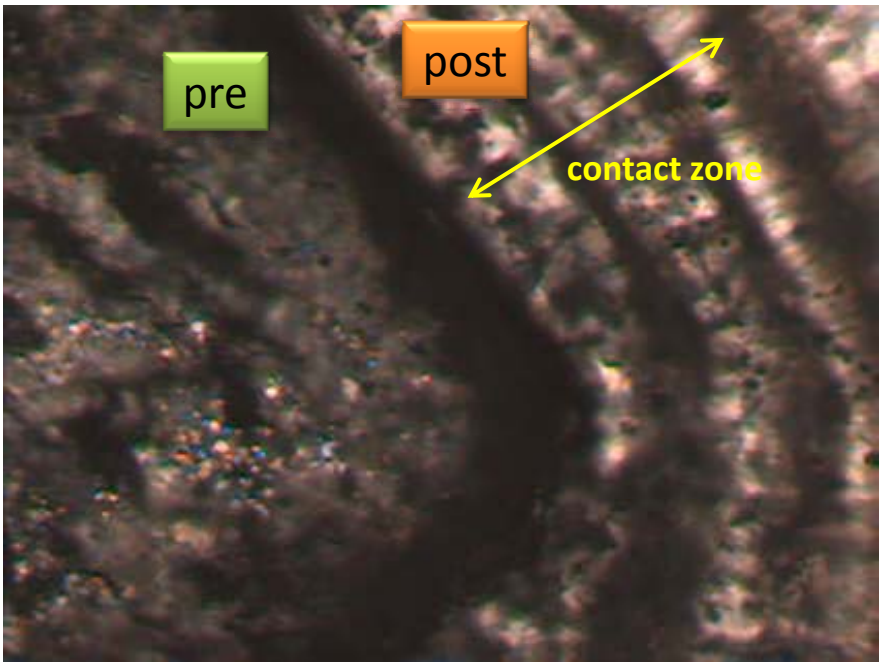

Enlargement x 10

Figure 3.4. 7 Speleoseismite sample **SO-7-44.** A. Hand sample, B-D. Photographs under polarizing microscope. See text for details.

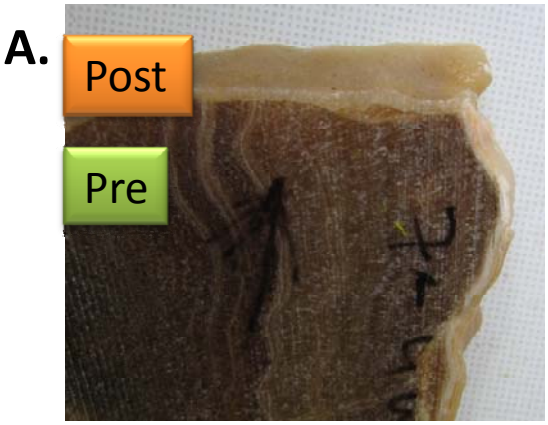

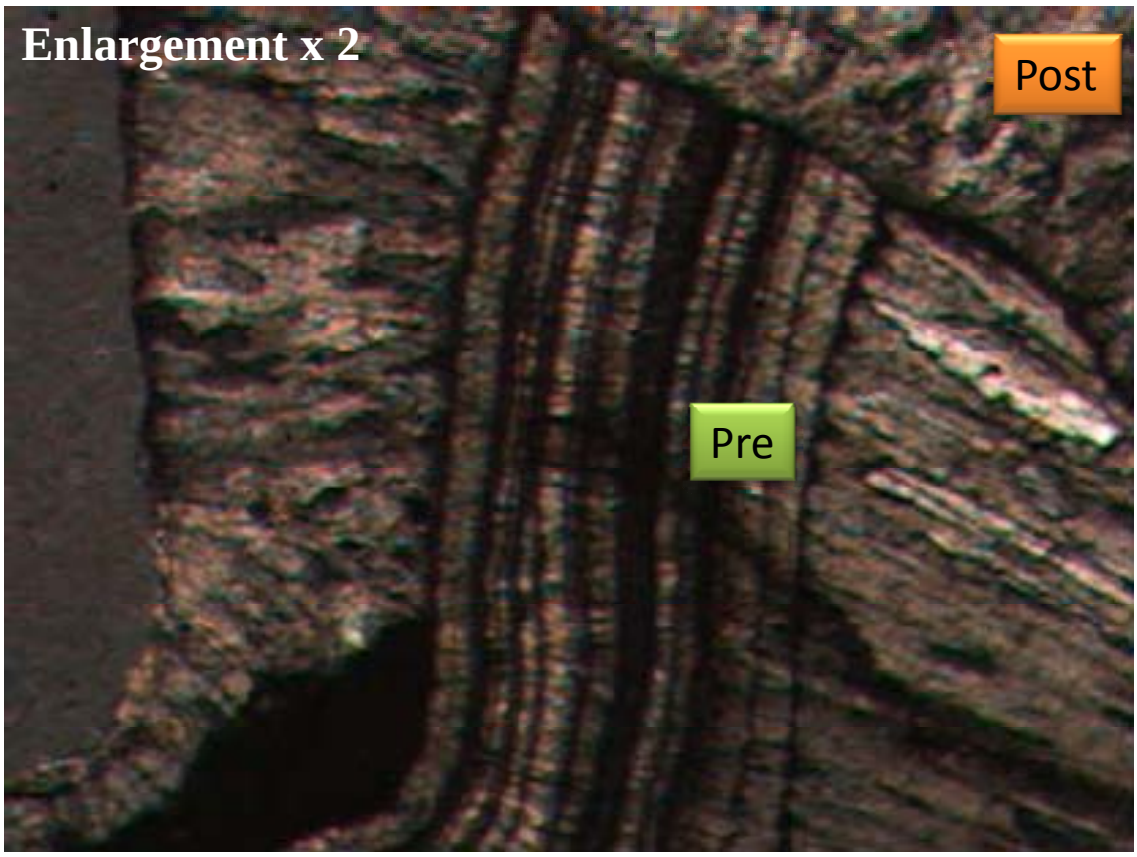

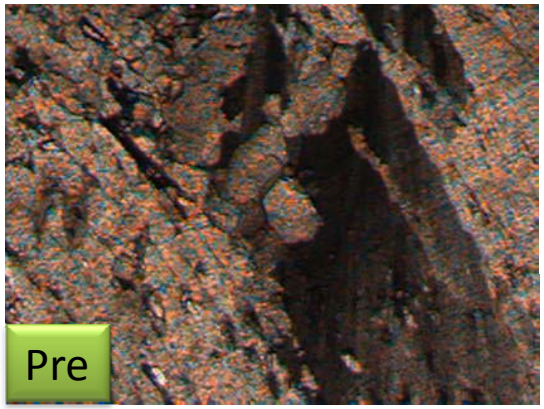

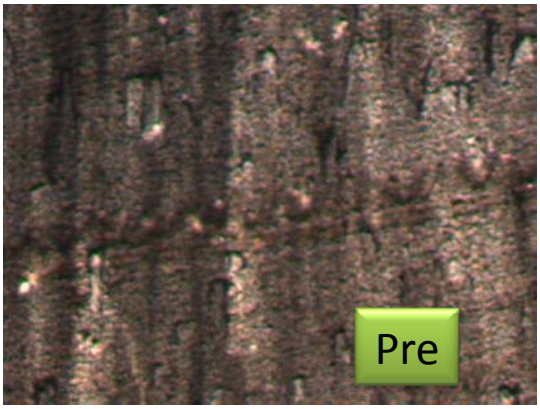

Figure 3.4.8 Speleoseismite sample **SO-32.** A. Hand sample, B-D. Photographs under polarizing microscope. See text for details.

A.

SO-32

B.

Enlargement x 2

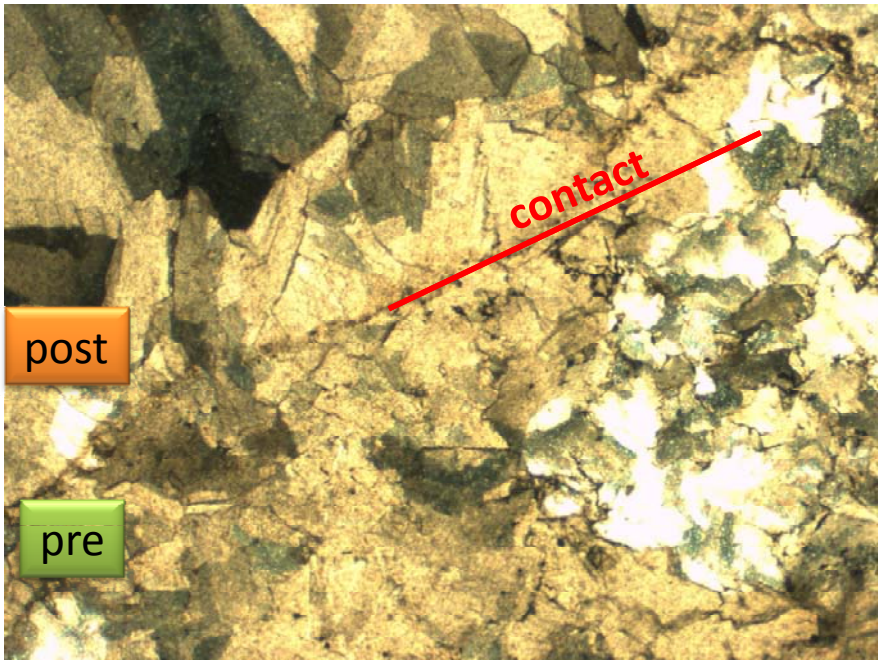

C.

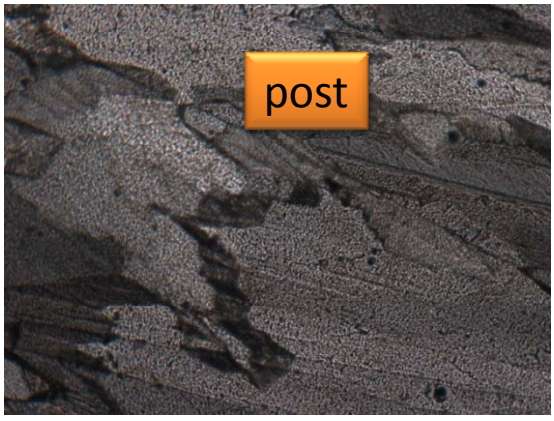

Enlargement x 4

D.

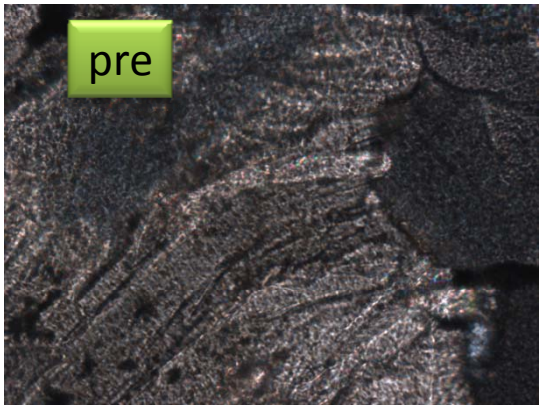

Enlargement x 10

Figure 3.4.9 Speleoseismite sample **SO-7.**
A. Hand sample (core diameter is 2 inches,
B-C. Photographs under polarizing microscope.
See text for details.

SO-7

A.

B.

Enlargement x 4-10

C.

Figure 3.4.10. Speleoseismite sample **SO-2-21.** A. Hand sample, B-D. Photographs under polarizing microscope. See text for details.

SO-2-21

A.

B.

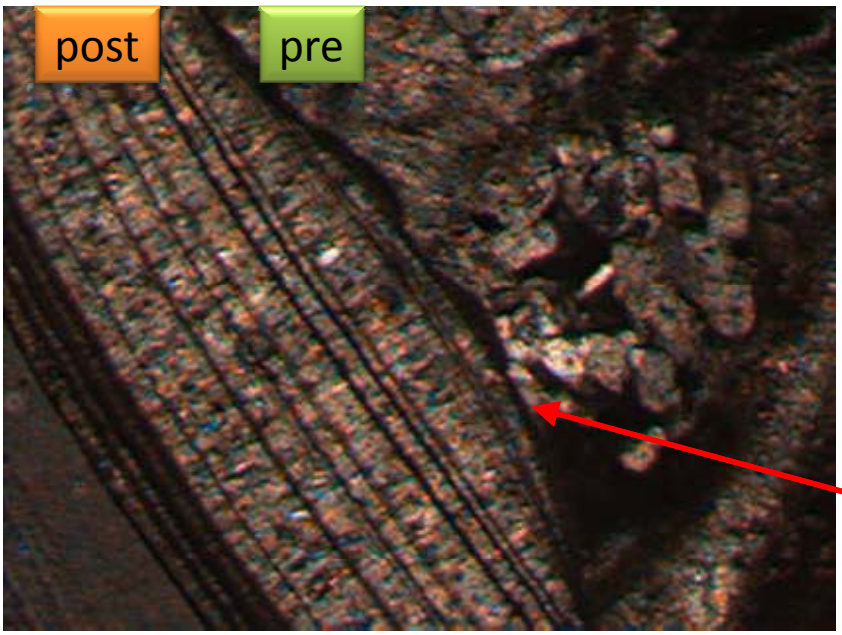

C.

Enlargement x 4-10

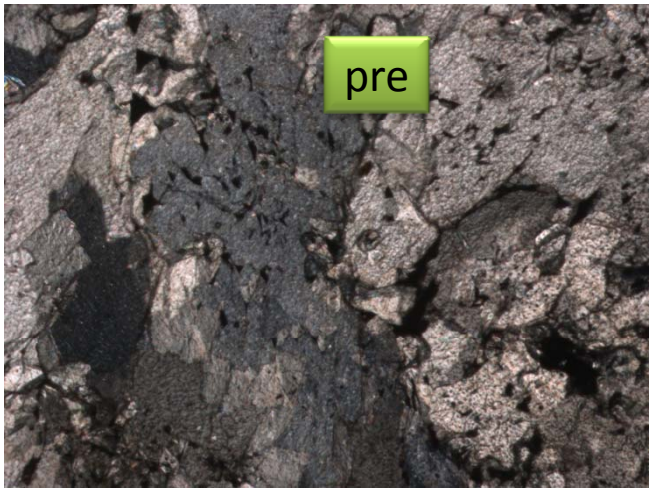

D.

Figure 3.4.11 Speleoseismite sample **SO-58.** A. Hand sample, B-D. Photographs under polarizing microscope. See text for details.

SO-58

A.

B.

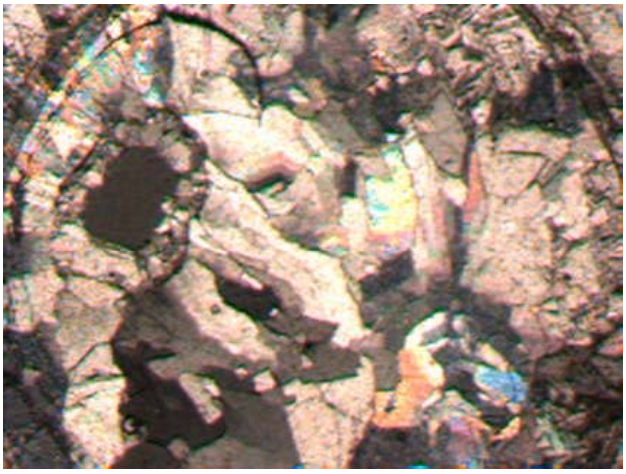

C.

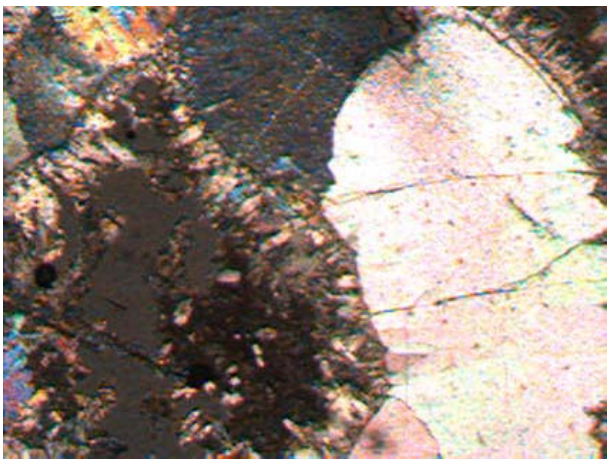

Enlargement x 4-10

D.

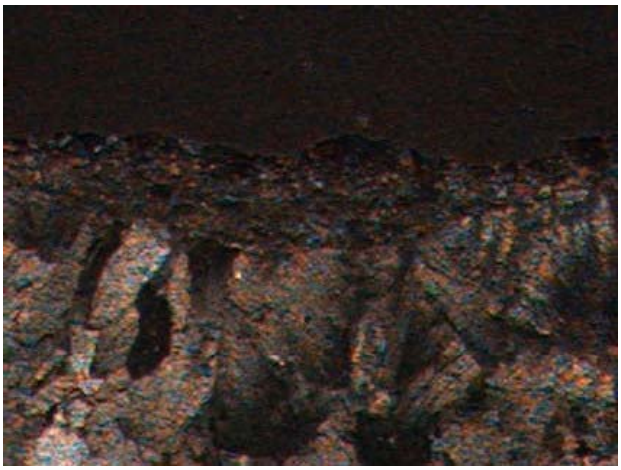

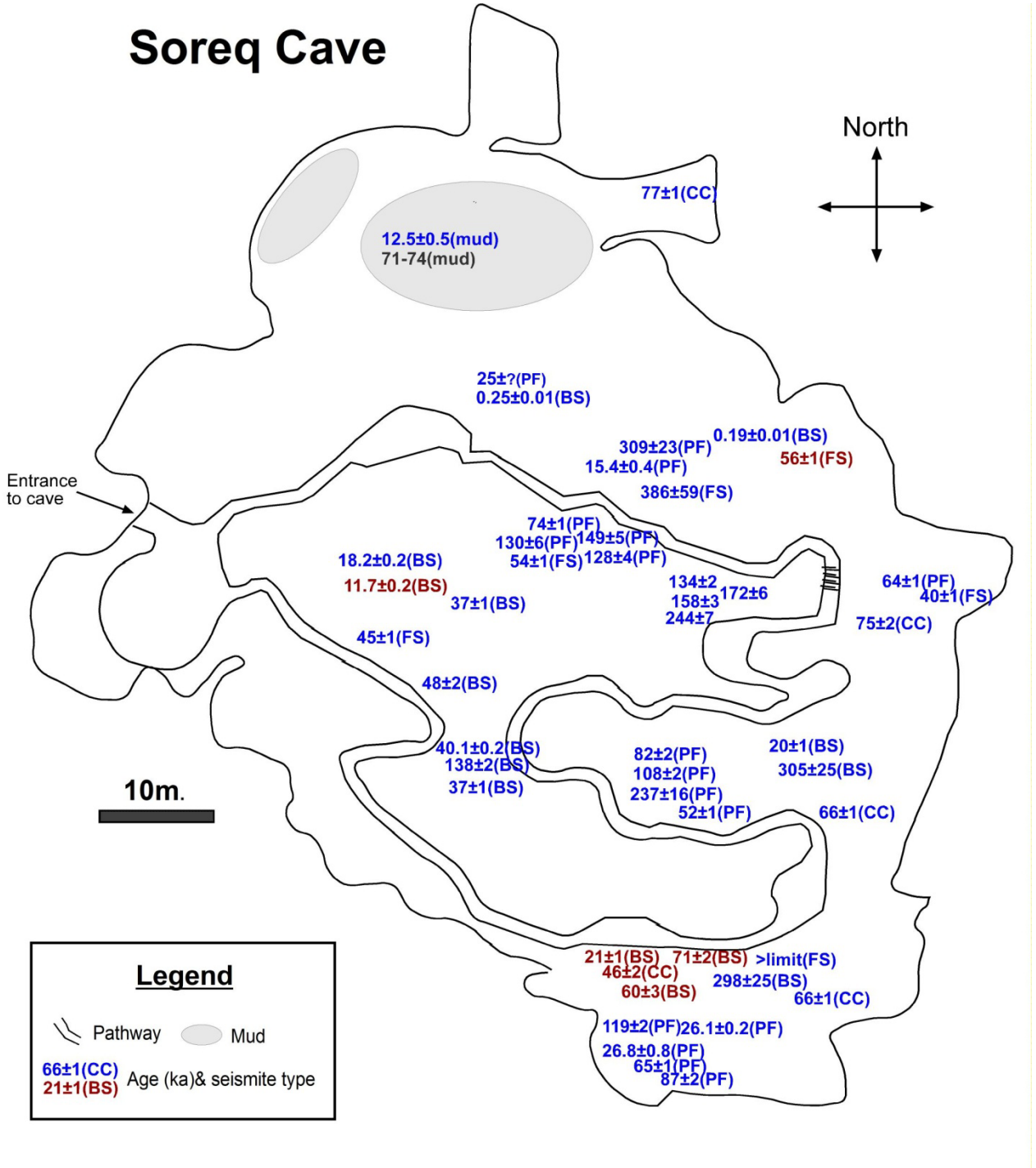

Figure 3.4.12. Map of Soreq Cave with ages of damage (some numbers rounded). Only MC-ICP-MS ages (this study) given. When gap exists between pre and post damage ages, the post ages are given here. Data from Table 3.4.2. Seismite types given in parentheses: BS=broken stalagmite, FS=fallen stalactite, CC=collapsed ceiling, PF=particles in flowstone, mac=macaroni stalactites collapsed, mud=mud entry into cave. Blue ages are post-damage ages of samples, red age given when only pre-damage age available.

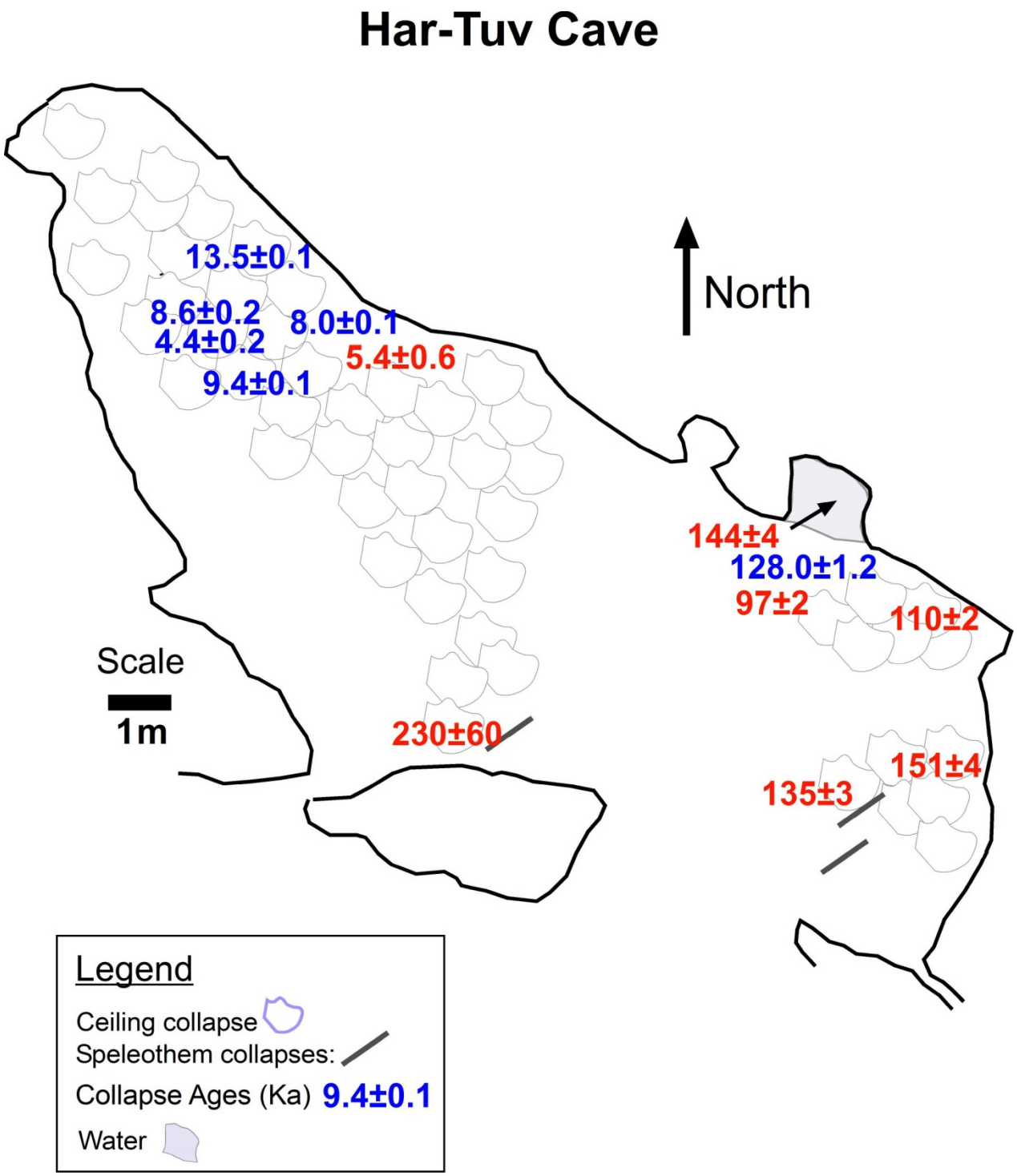

Figure 3.4.13. Map of Har-Tuv Cave with ages of seismites. In blue: MC-ICP-MS ages (ka), data in Tables 3.4.1 to 3.4.3. In red: ages from *Kagan et al.* [2005] for samples with no MC-ICP-MS ages. Ages are given in thousands of years before the present (ka). All samples here have post-damage ages only, except for the 128 ka seismite, which has a 156 ka pre-damage constraint.

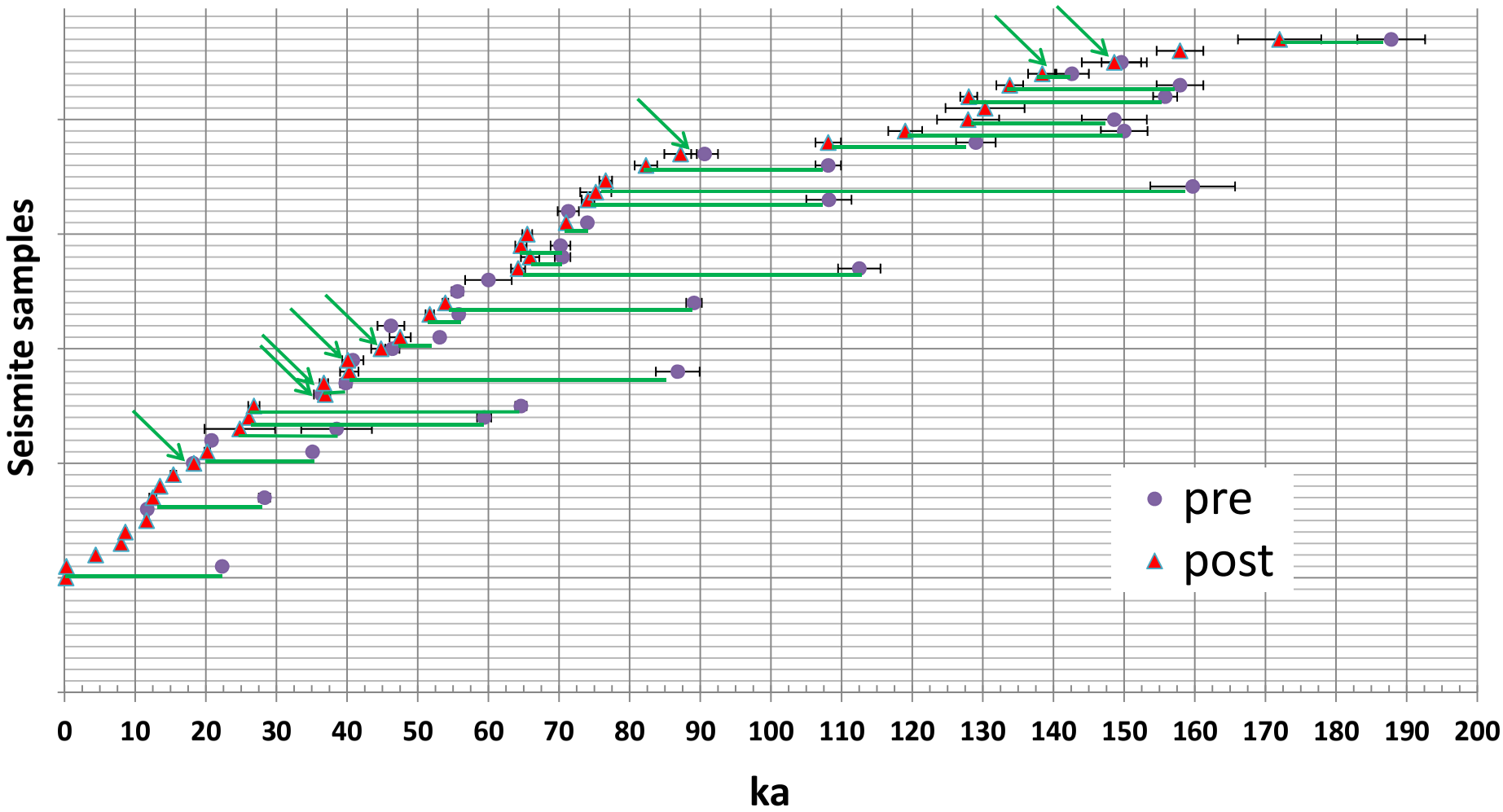

Figure 3.4.14.a. Distribution in time of dated seismite samples. Pre ages (circles) are from the laminae older than the paleoseismic contacts; Post ages (triangles) are from laminae younger than the paleoseismic contacts. The data points are distributed on the y-axis according to seismite sample, in chronological order, thus each sample is on a separate horizontal line. This enables discernment of the range between the pre and post ages of each sample (green horizontal lines). Samples whose pre and post ages are so close in time (ideal situation) that a connecting line is impossible to discern on this diagram are indicated by green arrows. As discussed in the text, some samples have *only* pre or post ages (neither green line nor arrow).

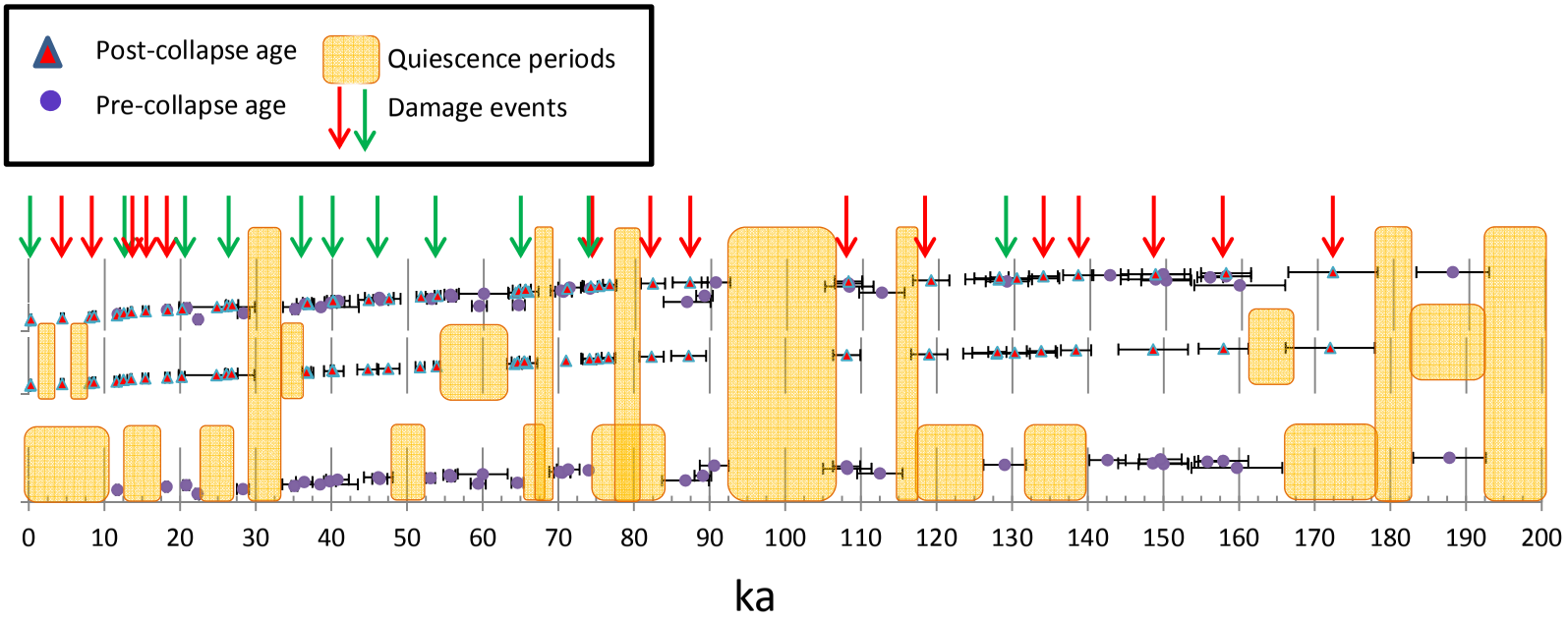

Figure 3.4.14.b. Distribution in time of dated seismite samples. Bottom graph - only pre-damage ages, middle graph - only post-damage ages, top graph - both pre and post damage ages. Seven quiescence intervals are discernible, with neither pre nor post damage ages. When looking at only post or only pre ages, additional quiescence periods are perceptible. Red and green arrows point to *events* (listed in Table 3.4.3, see text for details). Green arrows point to collapsed defined by more than one collapse.

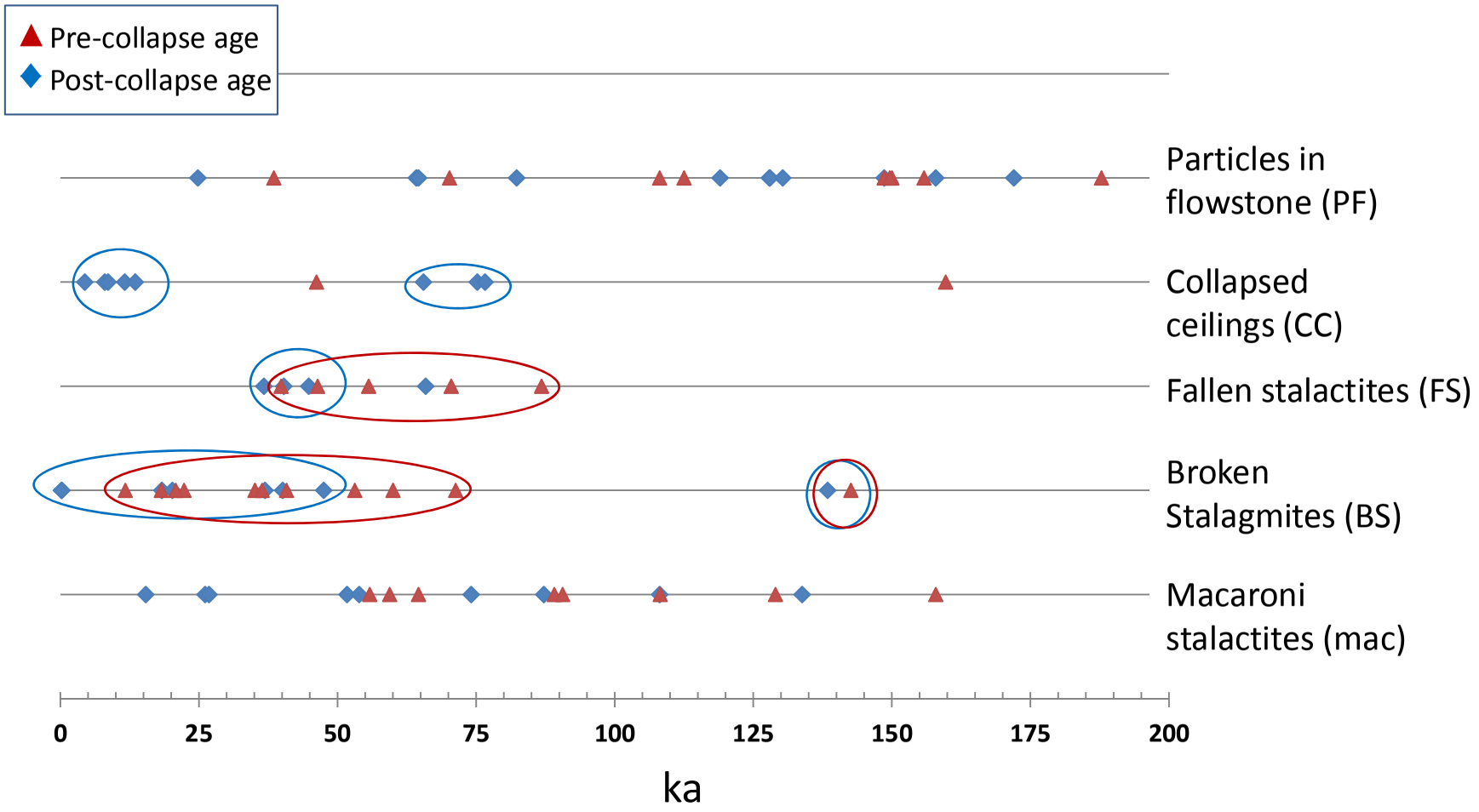

Figure 3.4.15. Distribution in time of seismites, classified by seismite type. Age errors are displayed in Figure 3.4.14 and given in Tables 3.4.1-3.4.3. In parentheses are labels used in Table 3.4.3. Particles in flowstone can be any kind of collapse debris, often unclassifiable without magnification. In the case where the debris is recognized as a macaroni stalactite, it is included in the "mac" classification. Ellipses (blue post, red pre) encompass groups of close damage ages for each type of seismite. The PF and mac types are distributed throughout the time 200 ka time period discussed. Ceiling blocks fell distinctly during two periods (~4.4-13.5 ka) and (65-76 ka). Stalactites appear to have fallen during the period of 36-90 ka. Severed and/or toppled stalagmites are limited to the past 70 ka, with an additional seismite with both pre and post age at ~140 ka.

3.4.5 Summary

The extensive, dateable, and well-preserved cave speleoseismite archive of the Soreq and Har-Tuv caves was mapped, sampled, and dated rigorously. Damaged crystals were observed in the pre-earthquake speleothem calcite by petrographical study of the paleoseismic contacts. An earthquake history reaching back to ~ 400 ka is presented. The archive is dated fairly extensively up to 200 ka. Between twenty-one and twenty-six damaging events are evident since 200 ka. A mean earthquake recurrence interval of ~6.6-8.6 or kyr is calculated, with an aperiodicity vale of 0.5-0.7, suggesting quasi-periodic (non-clustered) behavior. Some types of speleoseismites occurred at specific times in the studied period. Spatial randomness and temporal grouping of seismites both support a seismogenic origin. The rigorous and high-resolution mass spectrometric dating of these seismites is the framework for future comparison with the lake archives.

4. Summary and Conclusions

"An earthquake achieves what the law promises but does not in practice maintain - the equality of all men"

Ignazio Silone (1900 -1978)

This study deals with the paleoseismological history of the Israel region during the Late Quaternary. The present research aims at establishing the chronological framework for the lacustrine and speleothem earthquake archives, determining earthquake recurrence times and spatial patterns, as well as interpreting the control of various media on seismite formation. The paleoseismological history of the area has been studied previously at individual sites. In this study a multi-site approach is taken in order to extract information available through spatial-temporal analysis.

The archives chosen for study of the Holocene earthquake history are two lacustrine Ze'elim Formation sites along the Dead Sea basin (the Ein Feshkha Nature Reserve and the Ze'elim Gully) and the Soreq and Har-Tuv caves speleoseismite archive. The Ein Gedi core archive is used for a detailed comparison with the Holocene lacustrine study, while the Denya Cave is compared to the Holocene portion of the cave study. The Pleistocene paleoseismological study is underway in the Lisan Formation at four sites: Deir Shaman, Bet Ha'Arava, Nahal Mishmar, and Massada along with the Soreq Cave's long-term extensive speleoseismite archive.

4.1 *Lacustrine seismites*

In previous studies, the last glacial Lisan Formation and the Holocene Ze'elim Formation lake archive in Israel has proven to be a sensitive long-term earthquake recorder, has produced a 70 kyr record of earthquakes, and has shown patterns of recurrence. In this study the chronological reconstruction has been improved significantly by extensive dating and expansion to several synchronously deposited lacustrine sediment sites which allow interpretation of complex earthquake behaviour.

Radiocarbon chronologies based on Bayesian statistics were constructed for two new stratigraphic sections at the northern and southern parts the basin (at the Ein Feshkha Nature Reserve and at the Ze'elim Gully, respectively). Various Bayesian deposition models were tested, with and without specific historic earthquake anchors. Best models were chosen according to model agreement-indexes and historic earthquake considerations, but without the use of anchors. The ages of the seismites were compared with catalogues of historic earthquakes during the past 2000 years and with the paleoseismic chronology proposed for the Ein Gedi core [*Migowski et al.*, 2004] located at the central part of the basin. Temporal and spatial appearance of the seismites shows no strong dependency on the limnological–sedimentological conditions in the specific sections (representing lake conditions of up to several tens of meters depth). Sediments of various sedimentary facies were affected simultaneously by earthquake activity (e.g. liquefied sands and disturbed lacustrine marly sequences). Thus, the documented records provide a reasonable picture of the earthquake activity in the vicinity of the Dead Sea basin without being discriminated by the sedimentary environment.

One of the main discoveries in this work was that some earthquakes were recorded at all three sites along the DSB; these seismites are termed Intra Basin Seismites – IBS. These seismites are dated to 1927 AD, 1293 AD, 1202/1212 AD, 749 AD, 551 AD, 419 AD, 33 AD, 31 BC, and mid-2nd century BC. The recurrence interval of the IBS during the period of continuous deposition is ~200 years, about four times longer than the RI at the Ein Feshkha site. Compiling the IBS archive filters the shorter recurrence intervals of the individual records. Another observation that could be made from this multi-site approach is that several seismites (during the time interval of the historical catalogues) were recorded only at the northern site of Ein Feshkha (64 BC, 349, 363, 634, 847, 859, 956, 1063, 1170, 1312 AD). This may be due to the northern source of these events or to wave guiding along the main plate boundary. Quiescence intervals in seismite appearance are apparent at ~ 500-150 BC at the two southern sites and from the end of the 2nd to the beginning of the 4th century AD at all three seismite sites. These are correlated to historic earthquake quiescence periods and suggest similar intensity thresholds for both types of data sets in this region. The IBS define a steep diagonal array in the magnitude-distance diagram that lies in the sector of high intensity lines that were established by [*Ambraseys and Jackson*, 1998]. This is similar to the soil liquefaction threshold calculated for modern earthquakes in the Aegean region. Thus, the IBS provide a pattern of temporal behavior of relatively strong earthquakes that are associated with the Dead Sea Transform.

4.2 *Speleothem seismites*

The nascent field of speleoseismology has allowed the dating of previously under-investigated earthquake-prone areas. Speleoseismites are protected against erosion and can be dated to a high precision by U-Th methods. The speleoseismological archive in Israel is especially promising due to the large amount of karst caves throughout. Speleothem seismites (or speleoseismites) are investigated in this study at the Soreq Cave and the nearby Har-Tuv Cave, in the Jerusalem vicinity. Damaged cave deposits at these caves include collapsed stalactites, fallen stalagmites, standing but severed stalagmites, collapsed bedrock ceilings, cracked speleothems, and a collapsed soil mound. When dripping water and calcite precipitation continue after seismic events, the damaged deposits (pre-event age) are covered by regrowth (post-event age). The pre and post event carbonate is then dated by the U-Th MC-ICP-MS method. This dating method is feasible up to ~ 500 ka. For this study, specific earthquakes can be dated up to approximately 200 ka, since older ages have higher errors which hamper classification of seismites into specific seismic events. However, with additional dating and sampling of older seismites, quiescence periods may become apparent.

The Soreq-Har-Tuv caves provide a 400 ka earthquake history from forty-four speleothems sampled in the field, which documented more than fifty-five seismites. For the past 200 millennia these collapses are grouped into 26 *events*, interpreted to be earthquakes. Of those, there are 21 collapse events that are defined by more than one seismite or by both pre and post ages. Seven quiescence intervals are discernible, with no pre or post damage ages during that time. The 26 events from 200 ka to present lead to a mean recurrence interval of approximately 6.8 ky, or 6.6-6.8 ky, depending on the time period chosen for investigation with an aperiodicity value of 0.7, lending to quasi-periodic behavior. If only the 21 events dated by more than one age are used, the RI increases to 7.8-8.6 ky, and the aperiodicity values change slightly to 0.5-0.6 with the quasi-periodic behavior persisting. This RI is much longer than that interpreted from the lake archive earthquake history due to filtering out of the smaller earthquakes in the cave environment and the somewhat more removed location.

Seismite ages appear to be spatially distributed randomly throughout the cave. Some of the different types of cave damage occurred at specific times in the past 200 millennia. These two observations support seismogenic origin of damage.

The Holocene component of the Soreq-Har-Tuv caves speleothem record is presented and compared here with the Denya Cave archive [an accompanying speleoseismicity study near Haifa; *Braun*, 2009]. Eight speleoseismites from the Soreq-Har-Tuv caves comprise the Holocene portion of this paleoseismic history, six of which are dated by mass spectrometry in the current study and two are included from the *Kagan et al*. [2005] wiggle-matching ages. The eight seismites group into four events (number of seismites per event given in parentheses): 18^{th} – 19^{th} century (2), ~5 ka (3), ~8.5 ka (2), and ~11.6 ka (1)[†]. Nine pre-historical Holocene speleoseismites, interpreted to represent two seismic events (4.8±0.8 ka and 10.4±0.7 ka) are documented at the Denya Cave. These two cave archives constitute the basis for an integrated multi-site analysis that investigates the interaction (coupling) between two sectors of the Dead Sea Transform (DST) and its side branch - the Carmel fault (CF). The two sectors considered are the Dead Sea basin (DSB) and the Jordan Valley (JV). The two archive sites are potentially affected by the same fault system, yet separated by 110 km. A very strong seismo-tectonic event affecting the entire region would give the same ages (to within dating uncertainty) at both archives. Separate, local events from either sector would record separately in either archive. Together with other paleoseismic and archaeoseismic studies from the CF and JV regions, temporal correlation between cave archives implies coupling between the main fault sectors (DSB, JV), and CF branch. Specifically, an event at ~5 ka, is well-recorded at both the Haifa and Judean Hills caves. However, the penultimate Haifa cave event at ~10.5 ka seems to be limited to the northern region, although uncertainties due to differing detrital correction methods, differing event grouping schemes, and the lack of a Dead Sea lake seismite archive for that period prevent ruling out a correlation. The closest in time seismite at Soreq-Har-Tuv is at 11.6±0.3 ka. The ~5 ka event could be a CF rupture or a very large JV-DSB event, or a seismic event on one of the faults followed quickly by an event on one of the others. The quiescence intervals identified for the largest events in the seismic cycle are between ~10 ka and ~5 ka in the cave in Haifa, and from ~5 ka to the historical period in the Judean Hills.

The first petrographic investigation into speleothem earthquake damage is presented here. In all seven thin section samples the *pre-contact* "damaged" crystals were smaller, non-elongated, and disorganized, as opposed to the *post-contact* "undamaged" crystals being larger, elongated, and oriented perpendicular to contact, or parallel to growth direction.

4.3 *The multi-site approach*

The multi-site approach taken in this work benefits from analysis and comparison of paleoseismic archives from various periods, regions, and media. The comparison of three Holocene lacustrine paleoseismic sites allowed interpretation of earthquake sources (and consequently magnitudes for known historic events) for some of the seismites. In addition, the multi-site approach introduced the concept of Intra-Basin Seismites (IBS) developed and provided a recurrence time for these out of the ordinary events. In the cave speleoseismite environment, the Carmel-Soreq comparison is another angle of the multi-site approach. In this

[†] Note that additional dating (Chapter 3.4) since the preparation of Chapter 3.3 produces some differences in the event groupings in Chapter 3.4.

case the two cave systems allowed an analysis of fault coupling. The different media (cave deposits and lake sediments) have thus far only been compared for the Late-Holocene period. During this time period there are two Soreq Cave seismites (both are severed stalagmites; Table 3.4.3) and tens of Ze'elim Formation disturbed layers (Chapter 3.1). This is in accord with the hypothesis here that the lake sediment recorder is more sensitive than the cave sediment recorder to earthquake shaking, and therefore records smaller events.

The ultimate future outcome of this multi-site and diverse-environment study is the comparison of the long-term dated cave and lake paleoseismic archives (Lisan Formation and Soreq-Har-Tuv cave archives). This comparison is currently underway and can resolve mega-earthquakes that affect the entire DSB area and traverse lithological confines. The new Lisan chronologies will allow dating of all Lisan seismites, and this, together with the Soreq-Har-Tuv seismite event chronology, will achieve the multi-archive union.

4.4 *Main contributions*

To conclude, the main contributions of this study are:

1) High-resolution Radiocarbon Bayesian-modeled chronology of the earthquake markers within the Late Holocene Ze'elim Formation at two outcrop sites with correlation to a core site and to historic earthquakes.
2) Temporal and spatial analysis of differential earthquake histories at different sites along the Dead Sea Basin
3) Mean recurrence interval of lacustrine Intra-Basin Seismites calculated to ~200 years
4) Lisan Formation intra-basin chronological and stratigraphical framework for upcoming intra-basin paleoseismological analysis (in progress)
5) Paleoseismic reconstruction of the Soreq-Har-Tuv Cave damage. Recurrence interval of 6.6-8.6 ky (with an aperiodicity value of 0.5-0.7) calculated, lending to quasi-periodic behavior.
6) Specific types of cave damage (ceilings, stalactites, stalagmites) dated to have fallen at different but specific times.
7) Soreq-Har-Tuv and Denya caves' Holocene seismite archives compared. Fault system (Dead Sea - Jordan Valley - Carmel fault) coupling analysis investigated. At a 5 ka event, coupling is apparent. A 10.5 ka event seems to be limited to the north.

4.5 *Topics for consideration and further exploration*

During the course of this work additional research questions were explored. Some were studied intensely and publication is forthcoming:

- The Lisan Formation paleoseismic record of *Marco* [1996] and *Marco et al.* [1996] has now been expanded to four additional and extensively dated Lisan sites (Deir Shaman, Bet HaArava, Nahal Mishmar, and Massada). Publication of the integration of the chronology with the paleoseismological data and the subsequent earthquake pattern interpretation is under preparation.
- Last-Glacial and Holocene lake levels and their relationship with seismicity will be explored. The Lisan paleoseismic history tends to show a longer earthquake recurrence time, and perhaps larger magnitudes than the shorter recurrence time and

smaller magnitudes of the Holocene history. This may be affected by the heavy water load on the Dead Sea basin during the high lake stands of the glacial times, which would inhibit frequent seismicity, as recognized in research into induced seismicity [*Beck et al.*, 1996; *Hampel and Hetzel*, 2006; *Talwani*, 1997]. Dated lake levels [*Bartov et al.*, 2002; *Bookman (Ken-Tor) et al.*, 2004] will be compared with the multi-site seismite archives to explore this issue.

- Asphalt association with brecciated lake sediments was observed during the course of this work (Appendix C-2), in collaboration with Dr. Eli Tennenbaum (*deceased*). The extent of this association and its link to seismicity and petroleum sources will be described in a forthcoming paper.

Others topics were just touched upon, and open questions remain.

- The relationship between earthquake magnitude or intensity and speleothem damage is far from being clear-cut (see Chapter 1.3) and in the future may be better resolved experimentally, by direct observations, and by delicate correlation to other paleoseismic studies.
- The effect of sediment compaction and slope angle on lake-bottom seismite formation will need to be resolved experimentally.

References

Agnon, A., Migowski, C., and Marco, S., 2006, Intraclast breccia layers in laminated sequences: recorders of paleo-earthquakes, *in* Enzel, Y., Agnon, A., and Stein, M., eds., New Frontiers in Dead Sea Paleoenvironmental Research, Geological Society of America Special Paper 401, p. 195-214.

Alsop, G. I., and Marco, S., 2011, Soft-sediment deformation within seismogenic slumps of the Dead Sea Basin: Journal of Structural Geology, v. 33, no. 4, p. 433-457.

Ambraseys, N., and Karcz, I., 1992, The Earthquake of 1546 in the Holy-Land: Terra Nova, v. 4, no. 2, p. 253-262.

Ambraseys, N. N., 1962, Data for the investigation of the seismic sea-waves in the Eastern Mediterranean: Bullletin of Seismological Society of America, v. 52, p. 895-913.

Ambraseys, N. N., 1970, Some characteristic features of the Anatolian fault zone: Tectonophysics, v. 9, no. 2-3, p. 143-165.

Ambraseys, N. N., 2005, The seismic activity in Syria and Palestine during the middle of the 8th century; an amalgamation of historical earthquakes: Journal of Seismology, v. 9, no. 1, p. 115.

Ambraseys, N. N., 2009, Earthquakes in the Mediterranean and Middle East: a multidisciplinary study of seismicity up to 1900, New York, Cambridge University Press, 947 p.

Ambraseys, N. N., and Jackson, J. A., 1998, Faulting associated with historical and recent earthquakes in the Eastern Mediterranean region: Geophysical Journal International, v. 133, no. 2, p. 390-406.

Ambraseys, N. N., and Melville, C. P., 1988, An analysis of the eastern Mediterranean earthquake of 20 May 1202, *in* Lee, W. K. H., et al., ed., History of seismography and earthquakes of the world: San Diego, Academic Press, p. 181-200.

Ambraseys, N. N., Melville, C. P., and Adams, R. D., 1994, The seismicity of Egypt, Arabia and the Red Sea: A Historical Review, New York, Cambridge University Press, v. 5, 181 p.

Amiran, D., Arieh, E., and Turcotte, T., 1994, Earthquakes in Israel and Adjacent Areas - Macroseismic Observations since 100 Bce (Vol 44, Pg 260, 1994): Israel Exploration Journal, v. 45, no. 2-3, p. 201-201.

Amit, R., Zilberman, E., Enzel, Y., and Porat, N., 2002, Paleoseismic evidence for time dependency of seismic response on a fault system in the southern Arava Valley, Dead Sea rift, Israel: Geological Society of America Bulletin, v. 114, no. 2, p. 192-206.

Amit, R., Zilberman, E., Porat, N., and Enzel, Y., 1999, Relief inversion in the Avrona Playa as evidence of large-magnitude historical earthquakes, southern Arava Valley, Dead Sea Rift: Quaternary Research, v. 52, no. 1, p. 76-91.

Asaf, M., 1975, Karstic phenomena in the Soreq Cave (in Hebrew) [M.Sc.: Tel Aviv University, 44 p.

Austin, S. A., Franz, G. W., and Frost, E. G., 2000, Amos's earthquake: An extraordinary Middle East seismic event of 750 BC: International Geology Review, v. 42, no. 7, p. 657-671.

Avni, R., 1999, The 1927 Jericho Earthquake-Comprehensive Macroseismic Analysis Based on Contemporary Sources [Ph.D]: Ben-Gurion University of the Negev, 203 p.

Ayalon, A., Bar-Matthews, M., and Goren, Y., 2004, Authenticity examination of the inscription on the ossuary attributed to James, brother of Jesus: Journal of Archaeological Science, v. 31, no. 8, p. 1185-1189.

Ayalon, A., Bar-Matthews, M., and Kaufman, A., 1999, Petrography, strontium, barium and uranium concentrations, and strontium and uranium isotope ratios in speleothems as palaeoclimatic proxies: Soreq Cave, Israel: Holocene, v. 9, no. 6, p. 715-722.

Ayalon, A., Bar-Matthews, M., and Kaufman, A., 2002, Climatic conditions during marine oxygen isotope stage 6 in the eastern Mediterranean region from the isotopic composition of speleothems of Soreq Cave, Israel: Geology, v. 30, no. 4, p. 303-306.

Aydan, Ö., 2008, Investigation of the seismic damage caused to the Gunung Sitoli (Tögi-Ndrawa) cave by the 2005 Great Nias earthquake: Journal of the Earth Sciences Application and Research Centre of Hacettepe University, v. 29 no. (1), p. 1-15.

Baer, G., Sandwell, D., Williams, S., Bock, Y., and Shamir, G., 1999, Coseismic deformation associated with the November 1995, M-w=7.1 Nuweiba earthquake, Gulf of Elat (Aqaba), detected by synthetic aperture radar interferometry: Journal of Geophysical Research-Solid Earth, v. 104, no. B11, p. 25221-25232.

Bar-Matthews, M., 2012a, Environmental change in the Mediterranean region, *in* A., M. J., ed., The Sage Handbook of Environmental Change, SAGE Publications Ltd.

Bar-Matthews, M, 2012b, Water in the Middle East and Africa, *in* Turekian, K. K., and Holland, H. D., eds., Treatise in Geochemistry, Volume 14.

Bar-Matthews, M., Ayalon, A., Gilmour, M., Matthews, A., and Hawkesworth, C. J., 2003, Sea-land oxygen isotopic relationships from planktonic foraminifera and speleothems in the Eastern Mediterranean region and their implication for paleorainfall during interglacial intervals: Geochimica Et Cosmochimica Acta, v. 67, no. 17, p. 3181-3199.

Bar-Matthews, M., Ayalon, A., and Kaufman, A., 1997, Late Quaternary Paleoclimate in the Eastern Mediterranean Region from Stable Isotope Analysis of Speleothems at Soreq Cave, Israel: Quaternary Research, v. 47, no. 2, p. 155.

Bar-Matthews, M., Ayalon, A., and Kaufman, A., 2000, Timing and hydrological conditions of Sapropel events in the Eastern Mediterranean, as evident from speleothems, Soreq cave, Israel: Chemical Geology, v. 169, no. 1-2, p. 145-156.

Bar-Matthews, M., Marean, C. W., Jacobs, Z., Karkanas, P., Fisher, E. C., Herries, A. I. R., Brown, K., Williams, H. M., Bernatchez, J., Ayalon, A., and Nilssen, P. J., 2010, A high resolution and continuous isotopic speleothem record of paleoclimate and paleoenvironment from 90 to 53 ka from Pinnacle Point on the south coast of South Africa: Quaternary Science Reviews, v. 29, no. 17-18, p. 2131-2145.

Bar-Matthews, M., Matthews, A., and Ayalon, A., 1991, Environmental controls of speleothem mineralogy in a karstic dolomitic terrain (Soreq Cave, Israel): Journal of Geology, v. 99, p. 189-207.

Bard, P. Y., and Tucker, B. E., 1985, Underground And Ridge Site Effects - A Comparison Of Observation And Theory: Bulletin of The Seismological Society of America, v. 75, no. 4, p. 905-922.

Bartov, Y., 2004, Sedimentary fill analysis of a continental basin – The Late Pleistocene Dead Sea [PhD PhD]: Hebrew University of Jerusalem, 114 p.

Bartov, Y., Enzel, Y., Porat, N., and Stein, M., 2007, Evolution of the Late Pleistocene-Holocene Dead Sea basin from sequence stratigraphy of fan deltas and lake-level reconstruction: Journal of Sedimentary Research, v. 77, no. 9-10, p. 680-692.

Bartov, Y., and Sagy, A., 2004, Late Pleistocene extension and strike-slip in the Dead Sea Bas in: Geological Magazine, v. 141, no. 5, p. 565-572.

Bartov, Y., Stein, M., Enzel, Y., Agnon, A., and Reches, Z., 2002, Lake levels and sequence stratigraphy of Lake Lisan, the late Pleistocene precursor of the Dead Sea: Quaternary Research, v. 57, no. 1, p. 9-21.

Beck, C., Manalt, F., Chapron, E., Rensbergen, P. V., and Batist, M. D., 1996, Enhanced seismicity in the early post-glacial period: Evidence from the post-würm sediments of lake annecy, northwestern Alps: Journal of Geodynamics, v. 22, no. 1-2, p. 155-171.

Becker, A., Ferry, M., Monecke, K., Schnellmann, M., and Giardini, D., 2005, Multiarchive paleoseismic record of late Pleistocene and Holocene strong earthquakes in Switzerland: Tectonophysics, v. 400, no. 1-4, p. 153.

Begin, Z. B., Louie, J. N., Marco, S., and Ben-Avraham, Z., 2005a, Prehistoric seismic basin effects in the Dead Sea Pull-apart: Geological Survey of Israel, GSI/04/05.

Begin, Z. B., Steinberg, D. M., Ichinose, G. A., and Marco, S., 2005b, A 40,000 year unchanging seismic regime in the Dead Sea rift: Geology, v. 33, no. 4, p. 257-260.

Ben-Avraham, Z., and Ginzburg, A., 1990, Displaced terranes and crustal evolution of the Levant and the eastern Mediterranean: Tectonics, v. 9, no. 4, p. 613-622.

Ben-Avraham, Z., and Hall, J., 1977, Geophysical survey of Mt. Carmel structure and its extention into the eastern Mediterranean.: Journal of Geophysical Research, v. 82, p. 793-802.

Ben-Avraham, Z., and Lazar, M., 2006, The structure and development of the Dead Sea basin: Recent studies: Special Paper 401: New Frontiers in Dead Sea Paleoenvironmental Research, v. 401, no. 0, p. 1-13.

Ben-Gai, Y., and Ben-Avraham, Z., 1995, Tectonic processes in offshore northern Israel and the evolution of the Carmel structure: Marine and Petroleum Geology, v. 12, no. 5, p. 533-548.

Ben-Menahem, A., 1991, Four thousand years of seismicity along the Dead Sea Rift: Journal of Geophysical Research-Solid Earth, v. 96, no. B12, p. 20195–20216.

Ben-Menahem, A., Nur, A., and Vered, M., 1976, Tectonics, seismicity and structure of the Afro-Eurasian junction -- the breaking of an incoherent plate: Physics of the Earth and Planetary Interiors, v. 12, no. 1, p. 1.

Blockley, S. P. E., Ramsey, C. B., Lane, C. S., and Lotter, A. F., 2008, Improved age modelling approaches as exemplified by the revised chronology for the Central European varved lake Soppensee: Quaternary Science Reviews, v. 27, no. 1-2, p. 61-71.

Boch, R., Spötl, C., and Kramers, J., 2009, High-resolution isotope records of early Holocene rapid climate change from two coeval stalagmites of Katerloch Cave, Austria: Quaternary Science Reviews, v. 28, no. 23-24, p. 2527-2538.

Bookman (Ken-Tor), R., Enzel, Y., Agnon, A., and Stein, M., 2004, Late Holocene lake levels of the Dead Sea: Geol Soc Am Bull, v. 116, no. 5-6, p. 555-571.

Bookman, R., Bartov, Y., Enzel, Y., and Stein, M., 2006, Quaternary Lake Levels in the Dead Sea Basin: Two Centuries of Research, *in* Enzel, Y., Agnon, A., and Stein, M., eds., New Frontiers in Dead Sea Paleoenvironmental Research, GSA, Special Paper 401.

Bowman, D., Banet-Davidovich D, Bruins HJ, and Van der Plicht, J., 2000, Dead Sea shoreline facies with seismically-induced soft-sediment deformation structures, Israel: Israel Journal of Earth Sciences, v. 49:4.

Bowman, D., Bruins, H. J., and van der Plicht, J., 2001, Load structure seismites in the Dead Sea Area, Israel: Chronological benchmarking with C-14 dating: Radiocarbon, v. 43, no. 3, p. 1383-1390.

Braun, Y., 2009, Dating paleo-seismic activity on the Carmel fault using damaged cave deposits from Denya Cave, Mt. Carmel. [M.Sc.]: The Hebrew University of Jerusalem, 87 p.

Braun, Y., Kagan, E., Bar-Matthews, M., Ayalon, A., and Agnon, A., 2011, Dating speleoseismites near the Dead Sea Transform and the Carmel Fault: Clues to coupling of a plate boundary and its branch: Israel Journal of Earth Sciences, v. 58.

Broecker, W. S., 1963, A Preliminary Evaluation of Uranium Series Inequilibrium as a Tool for Absolute Age Measurement on Marine Carbonates: J. Geophys. Res., v. 68, no. 9, p. 2817-2834.

Broecker, W. S., and Kaufman, A., 1965, Radiocarbon Chronology of Lake Lahontan and Lake Bonneville II, Great Basin: Geological Society of America Bulletin, v. 76, no. 5, p. 537-566.

Bronk Ramsey, C., 1995, Radiocarbon calibration and analysis of stratigraphy: The OxCal program: Radiocarbon, v. 37, no. 2, p. 425-430.

Bronk Ramsey, C., 2001, Development of the radiocarbon calibration program: Radiocarbon, v. 43, no. 2A, p. 355-363.

Bronk Ramsey, C., 2008, Deposition models for chronological records: Quaternary Science Reviews, v. 27, no. 1-2, p. 42.

Buck, C. E., Kenworthy, J. B., Litton, C. D., and Smith, A. F. M., 1991, Combining Archaeological and Radiocarbon Information - a Bayesian-Approach to Calibration: Antiquity, v. 65, no. 249, p. 808-821.

Cadorin, J. F., Jongmans, D., Plumier, A., Camelbeeck, T., Delaby, S., and Quinif, Y., 2001, Modelling of speleothems failure in the Hotton cave (Belgium). Is the failure earthquake induced?: Geologie En Mijnbouw-Netherlands Journal Of Geosciences, v. 80, no. 3-4, p. 315-321.

Chapron, E., Beck, C., Pourchet, M., and Deconinck, J. F., 1999, 1822 earthquake-triggered homogenite in Lake Le Bourget (NW Alps): Terra Nova, v. 11, no. 2-3, p. 86-92.

Cita, M. B., Camerlenghi, A., and Rimoldi, B., 1996, Deep-sea tsunami deposits in the eastern Mediterranean: New evidence and depositional models: Sedimentary Geology, v. 104, no. 1-4, p. 155-173.

Crispim, J. A., 1999, Seismotectonic versus man-induced morphological changes in a cave on the Arrabida chain (Portugal): Geodinamica Acta, v. 12, no. 3-4, p. 135.

D'Agostini, G., 2003, Bayesian inference in processing experimental data: principles and basic applications: Reports on Progress in Physics, v. 66, no. 9, p. 1383-1419.

Daeron, M., Klinger, Y., Tapponnier, P., Elias, A., Jacques, E., and Sursock, A., 2007, 12,000-year-long record of 10 to 13 paleoearthquakes on the Yammouneh fault, Levant fault system, Lebanon: Bulletin of the Seismological Society of America, v. 97, no. 3, p. 749-771.

Delaby, S., 2001, Palaeoseismic investigations in Belgian caves: Netherlands Jour. Geosc./Geol. en Mijnbouw, v. 80, p. 323-332.

Dever, W. G., 1992, A Case-Study in Biblical Archaeology: The Earthquake of ca. 760 BCE: Eretz-Israel, v. 23, p. 27-35.

Dolan, J. F., Bowman, D. D., and Sammis, C. G., 2007, Long-range and long-term fault interactions in Southern California: Geology, v. 35, no. 9, p. 855-858.

Edwards, R. L., Taylor, F. W., and Wasserburg, G. J., 1988, Dating earthquakes with high-precision thorium-230 ages of very young corals: Earth and Planetary Science Letters, v. 90, no. 4, p. 371-381.

El-Isa, Z. H., and Mustafa, H., 1986, Earthquake deformations in the Lisan deposits and seismotectonic implications: Geophysical Journal of the Royal Astronomical Society, v. 86, no. 2, p. 413-424.

Elias, A., Tapponnier, P., Singh, S. C., King, G. C. P., Briais, A., Daeron, M., Carton, H., Sursock, A., Jaques, E., Jomaa, R., and Klinger, Y., 2007, Active thrusting offshore mount lebanon: Source of the tsunamigenic AD 551 beirut-tripoli earthquake: Geology, v. 35, p. 755-758.

Ellenblum, R., Marco, S., Agnon, A., Rockwell, T. K., and Boas, A., 1998, Crusader castle torn apart by earthquake at dawn, 20 May 1202: Geology, v. 26, no. 4, p. 303-306.

Enzel, Y., Kadan, G., and Eyal, Y., 2000, Holocene Earthquakes Inferred from a Fan-Delta Sequence in the Dead Sea Graben: Quaternary Research, v. 53, no. 1, p. 34.

Ferry, M., Meghraoui, M., Abou Karaki, N., Al-Taj, M., Amoush, H., Al-Dhaisat, S., and Barjous, M., 2007, A 48-kyr-long slip rate history for the Jordan Valley segment of the Dead Sea Fault: Earth and Planetary Science Letters, v. 260, no. 3-4, p. 394-406.

Ferry, M., Meghraoui, M., Abou Karaki, N., Al-Taj, M., and Khalil, L., 2011, Episodic Behavior of the Jordan Valley Section of the Dead Sea Fault Inferred from a 14-ka-Long Integrated Catalog of Large Earthquakes: Bulletin of the Seismological Society of America, v. 101, no. 1, p. 39-67.

Forti, P., Seismotectonic and paleoseismic studies from speleothems: the state of the art., *in* Proceedings Han 98-Tectonique, Karst et Seismes1998, p. 79-81.

Forti, P., and Postpischl, D., The hypothesis of the induced activity of the faults as a result of a statistical analysis of stalagmites, *in* Proceedings Proc. Europ. Reg. Speleo them. Conf., Sofia, 1980, Volume 1-7, 352.

Forti, P., and Postpischl, D., 1984, Seismotectonic and paleoseismic analyses using karst sediments: Marine Geology, v. 55, p. 145-161.

Freund, R., Garfunke.Z, Zak, I., Goldberg, M., Weissbro.T, and Derin, B., 1970, Shear along Dead-Sea Rift: Philosophical Transactions of the Royal Society of London Series a -Mathematical and Physical Sciences, v. 267, no. 1181, p. 107-130.

Freund, R., Zak, I., and Garfunke.Z, 1968, Age and rate of sinistral movement along Dead Sea Rift: Nature, v. 220, no. 5164, p. 253-255.

Frumkin, A., Ford, D. C., and Schwarcz, H. P., 1999, Continental Oxygen Isotopic Record of the Last 170,000 Years in Jerusalem: Quaternary Research, v. 51, no. 3, p. 317.

Gardosh, M., Reches, Z., and Garfunkel, Z., 1990, Holocene Tectonic Deformation Along The Western Margins Of The Dead-Sea: Tectonophysics, v. 180, no. 1, p. 123-137.

Garfunkel, Z., 1981, Internal structure of the Dead-Sea leaky transform (rift) in relation to plate kinematics: Tectonophysics, v. 80, no. 1-4, p. 81-108.

Garfunkel, Z., 1998, Constrains on the origin and history of the Eastern Mediterranean basin: Tectonophysics, v. 298, no. 1-3, p. 5-35.

Garfunkel, Z., 2011, The long- and short-term lateral slip and seismicity along the Dead Sea Transform: An interim evaluation: Israel Journal of Earth Sciences, v. 58, 217 – 235.

Garfunkel, Z., and Almagor, G., 1984, Geology and structure of the continental margin off northern Israel and the adjacent part of the Levantine Basin: Marine Geology, v. 62, no. 1-2, p. 105-131.

Garfunkel, Z., and Ben-Avraham, Z., 1996, The structure of the Dead Sea basin: Tectonophysics, v. 266, no. 1-4, p. 155-176.

Geller, R. J., 1976, Scaling relations for earthquake source parameters and magnitudes: Bulletin of the Seismological Society of America, v. 66, p. 1501-1523.

Gilli, E., 1999, Evidence of palaeoseismicity in a flowstone of the Observatoire cave (Monaco): Geodinamica Acta, v. 12, no. 3-4, p. 159.

Gilli, E., 2004, Glacial causes of damage and difficulties to use speleothems as palaeoseismic indicators: Geodinamica Acta, v. 17, no. 3, p. 229-240.

Gilli, E., 2005, Review on the use of natural cave speleothems as palaeoseismic or neotectonics indicators: Comptes Rendus Geosciences, v. 337, no. 13, p. 1208.

Gilli, E., Levret, A., Sollogoub, P., and Delange, P., 1999, Research on the February 18, 1996 earthquake in the caves of Saint-Paul-de-Fenouillet area, (eastern Pyrenees, France): Geodinamica Acta, v. 12, no. 3-4, p. 143.

Ginat, H., Enzel, Y., and Avni, Y., 1998, Translocated plio-pleistocene drainage systems along the Arava fault of the Dead Sea transform: Tectonophysics, v. 284, no. 1-2, p. 151-160.

Gluck, D., 2001, The landscape evolution of the southwestern Dead Sea Basin and the paleoseismic record of the southwestern marginal fault of the Dead Sea Basin and of the Carmel Fault during the Late Pleistocene and the Holocene [M.Sc.]: The Hebrew University, 86 p.

Goes, S. D. B., 1996, Irregular recurrence of large earthquakes: An analysis of historic and paleoseismic catalogs: Journal Of Geophysical Research-Solid Earth, v. 101, no. B3, p. 5739-5749.

Gomez, F., Karam, G., Khawlie, M., McClusky, S., Vernant, P., Reilinger, R., Jaafar, R., Tabet, C., Khair, K., and Barazangi, M., 2007, Global Positioning System measurements of strain accumulation and slip transfer through the restraining bend along the Dead Sea fault system in Lebanon: Geophysical Journal International, v. 168, no. 3, p. 1021-1028.

Gomez, F., Meghraoui, M., Darkal, A. N., Hijazi, F., Mouty, M., Suleiman, Y., Sbeinati, R., Darawcheh, R., Al-Ghazzi, R., and Barazangi, M., 2003, Holocene faulting and earthquake recurrence along the Serghaya branch of the Dead Sea fault system in Syria and Lebanon (vol 153, pg 658, 2003): Geophysical Journal International, v. 155, no. 2, p. 749-750.

Goodman-Tchernov, B. N., Dey, H. W., Reinhardt, E. G., McCoy, F., and Mart, Y., 2009, Tsunami waves generated by the Santorini eruption reached Eastern Mediterranean shores: Geology, v. 37, no. 10, p. 943-946.

Grant, L. B., Mueller, K. J., Gath, E. M., Cheng, H., Lawrence Edwards, R., Munro, R., and Kennedy, G. L., 1999, Late Quaternary uplift and earthquake potential of the San Joaquin Hills, southern Los Angeles basin, California: Geology, v. 27, no. 11, p. 1031-1034.

Guidoboni, E., and Comastri, A., 2005, Catalogue of earthquakes and tsunamis in the Mediterranean area from the 11th to the 15th century, Italy: INGV-SGA.

Guidoboni, E., Comastri, A., and Traina, G., 1994, Catalogue of ancient earthquakes in the Mediterranean area up to the 10th century, Italy: INGV-SGA.

Haase-Schramm, A., Goldstein, S. L., and Stein, M., 2004, U-Th dating of Lake Lisan (late Pleistocene Dead Sea) aragonite and implications for glacial East Mediterranean climate change: Geochimica Et Cosmochimica Acta, v. 68, no. 5, p. 985-1005.

Haberland, C., Agnon, A., El-Kelani, R., Maercklin, N., Qabbani, I., Rumpker, G., Ryberg, T., Scherbaum, F., and Weber, M., 2003, Modeling of seismic guided waves at the Dead Sea Transform: Journal of Geophysical Research-Solid Earth, v. 108, no. B7.

Hampel, A., and Hetzel, R., 2006, Response of normal faults to glacial-interglacial fluctuations of ice and water masses on Earth's surface: J. Geophys. Res., v. 111, no. B6, p. B06406.

Haynes, J. M., Niemi, T. M., and Atallah, M., 2006, Evidence for ground-rupturing earthquakes on the Northern Wadi Araba fault at the archaeological site of Qasr Tilah, Dead Sea Transform fault system, Jordan: Journal of Seismology, v. 10, no. 4, p. 415-430.

Heifetz, E., Agnon, A., and Marco, S., 2005, Soft sediment deformation by Kelvin Helmholtz Instability: A case from Dead Sea earthquakes: Earth And Planetary Science Letters, v. 236, no. 1-2, p. 497-504.

Hellstrom, J., 2006, U-Th dating of speleotherns with high initial Th-230 using stratigraphical constraint: Quaternary Geochronology, v. 1, no. 4, p. 289-295.

Hofstetter, A., 2003, Seismic observations of the 22/11/1995 Gulf of Aqaba earthquake sequence: Tectonophysics, v. 369, no. 1-2, p. 21.

Hofstetter, A., Feldman, L., and Rotstein, Y., 1991, Crustal structure of Israel: constraints from teleseismic and gravity data.: Geophys. J. Int, v. 104, p. 371-380.

Hofstetter, A., van Eck, T., and Shapira, A., 1996, Seismic activity along fault branches of the Dead Sea-Jordan Transform System: The Carmel-Tirtza fault system: Tectonophysics, v. 267, no. 1-4, p. 317-330.

Hofstetter, R., Gitterman, Y., Pinsky, V., Kraeva, N., and Feldman, L., 2008, Seismological observations of the northern Dead Sea basin earthquake on 11 February 2004 and its associated activity: Israel Journal of Earth Sciences, v. 57, p. 101–124.

Hofstetter, R., Klinger, Y., Amrat, A. Q., Rivera, L., and Dorbath, L., 2007, Stress tensor and focal mechanisms along the Dead Sea fault and related structural elements based on seismological data: Tectonophysics, v. 429, no. 3-4, p. 165-181.

Horowitz, A., 1992, Palynology of Arid Lands, Amsterdam-London-New York-Tokyo, Elsevier Science.

Hough, S. E., and Avni, R., 2011, The 1170 and 1202 Dead Sea Rift earthquakes and long-term magnitude distribution on the Dead Sea Fault zone: Israel Journal of Earth Sciences.

Juyal, N., Pant, R. K., Basavaiah, N., Yadava, M. G., Saini, N. K., and Singhvi, A. K., 2004, Climate and seismicity in the higher Central Himalaya during 20-10 ka: evidence from the Garbayang basin, Uttaranchal, India: Palaeogeography, Palaeoclimatology, Palaeoecology, v. 213, no. 3-4, p. 315.

Kagan, E., Stein, M., Agnon, A., and Neumann, F., 2011, Intrabasin paleoearthquake and quiescence correlation of the late Holocene Dead Sea: Journal of Geophysical Research-Solid Earth, v. 116.

Kagan, E., Stein, M., Bar-Matthews, M., and Agnon, A., A tale of two cataclysmic earthquakes: 39 and 52 kyr BP, Dead Sea transform, Israel; a multi-archive study, *in* Proceedings AGU Fall Meeting, San Francisco, 2007, Volume Fall Meet. Suppl., 88(52).

Kagan, E. J., 2002, Dating large earthquakes using damaged cave deposits, Soreq and Har-Tuv caves, central Israel [M.Sc.]: Hebrew University of Jerusalem, 93 p.

Kagan, E. J., Agnon, A., Bar-Matthews, M., and Ayalon, A., 2005, Dating large infrequent earthquakes by damaged cave deposits: Geology, v. 33, no. 4, p. 261-264.

Kagan, E. J., Stein, M., Agnon, A., and Bronk Ramsey, C., 2010a, Paleoearthquakes as anchor points in Bayesian radiocarbon deposition models: a case study from the Dead Sea: Radiocarbon, v. 54 (3), p. 1018–1026.

Kagan, Y., Bird, P., and Jackson, D., 2010b, Earthquake Patterns in Diverse Tectonic Zones of the Globe: Pure and Applied Geophysics, v. 167, no. 6, p. 721-741.

Kagan, Y. Y., and Jackson, D. D., 1991, Long-Term Earthquake Clustering: Geophysical Journal International, v. 104, no. 1, p. 117-133.

Kanai, K., Tanaka, T., Yoshizawa, S., Morishita, T., Osada, K., and Suzuki, T., 1966, Comparative studies of earthquake motions on the ground and underground II: Bull. E.R.I, Tokyo, v. 44, p. 609-643.

Karcz, I., 2004, Implications of some early Jewish sources for estimates of earthquake hazard in the Holy Land: Annals of Geophysics, v. 47, no. 2-3, p. 759-792.

Karcz, I., and Kafri, U., 1978, Evaluation of Supposed Archeoseismic Damage in Israel: Journal of Archaeological Science, v. 5, no. 3, p. 237-253.

Kastens, K. A., and Cita, M. B., 1981, Tsunami-Induced Sediment Transport In The Abyssal Mediterranean-Sea: Geological Society of America Bulletin, v. 92, no. 11, p. 845-857.

Katz, A., Agnon, A., and Marco, S., 2009, Earthquake-induced barium anomalies in the Lisan Formation, Dead Sea Rift valley, Israel: Earth and Planetary Science Letters, v. 286, no. 1-2, p. 219-229.

Katz, O., Amit, R., Yagoda-Biran, G., Hatzor, Y. H., Porat, N., and Medvedev, B., 2011, Quaternary earthquakes and landslides in the Sea of Galilee area, the Dead Sea Transform; paleoseismic analysis and evaluation of current hazard: Israel Journal of Earth Sciences, v. 58..

Kaufman, A., Wasserburg, G. J., Porcelli, D., Bar-Matthews, M., Ayalon, A., and Halicz, L., 1998, U-Th isotope systematics from the Soreq cave, Israel and climatic correlations: Earth and Planetary Science Letters, v. 156, no. 3-4, p. 141.

Kempe, S., 2004, Natural speleothem damage in Postojna jama (Slovenia) caused by glacial cave ice? A first assessment: Acta Casologica, v. 33, no. 1, p. 265-289.

Ken-Tor, R., Agnon, A., Enzel, Y., Stein, M., Marco, S., and Negendank, J. F. W., 2001a, High-resolution geological record of historic earthquakes in the Dead Sea basin: Journal of Geophysical Research, v. 106 no. B2, p. 2221-2234.

Ken-Tor, R., Stein, M., Enzel, Y., Agnon, A., Marco, S., and Negendank, J. F. W., 2001b, Precision of calibrated radiocarbon ages of historic earthquakes in the Dead Sea Basin: Radiocarbon, v. 43, no. 3, p. 1371-1382.

King, G. C. P., Stein, R. S., and Lin, J., 1994, Static Stress Changes and the Triggering of Earthquakes: Bulletin of the Seismological Society of America, v. 84, no. 3, p. 935-953.

Klinger, Y., Avouac, J. P., Karaki, N. A., Dorbath, L., Bourles, D., and Reyss, J. L., 2000, Slip rate on the Dead Sea transform fault in northern Araba valley (Jordan): Geophysical Journal International, v. 142, no. 3, p. 755-768.

Kraeva, N., in press, Waveform moment tensor inversion of earthquakes in Israel and adjacent regions: Israel Journal of Earth Sciences, v. 58.

Kuperman, G., 2005, Reconstruction of flood periods by dating speleothems in Nahal Hazera, northern Negev [MSc]: Hebrew University.

Kushnir, Y., and Stein, M., 2010, North Atlantic influence on 19th-20th century rainfall in the Dead Sea watershed, teleconnections with the Sahel, and implication for Holocene climate fluctuations: Quaternary Science Reviews.

Lacave, C., Koller, M. G., and Egozcue, J. J., 2004, What can be concluded about seismic history from broken and unbroken speleothems?: Journal of Earthquake Engineering, v. 8, no. 3, p. 431-455.

Lacave, C., Levret, A., and Koller, M. G., Measurements of natural frequencies and damping of speleothems., *in* Proceedings 12th World Conference on Earthquakes, Auckland, New Zealand, 2000, p. 2118.

Lazar, M., Ben-Avraham, Z., and Schattner, U., 2006, Formation of sequential basins along a strike-slip fault-Geophysical observations from the Dead Sea basin: Tectonophysics, v. 421, no. 1-2, p. 53-69.

Le Beon, M., Klinger, Y., Amrat, A. Q., Agnon, A., Dorbath, L., Baer, G., Ruegg, J. C., Charade, O., and Mayyas, O., 2008, Slip rate and locking depth from GPS profiles across the southern Dead Sea Transform: Journal of Geophysical Research-Solid Earth, v. 113, no. B11.

Lemeille, F., Cushing, M., Carbon, D., Grellet, B., Bitterli, T., Flehoc, C., and Innocent, C., 1999, Co-seismic ruptures and deformations recorded by speleothems in the epicentral zone of the Basel earthquake: Geodinamica Acta, v. 12, no. 3-4, p. 179.

Levi, T., Weinberger, R., Aifa, T., Eyal, Y., and Marco, S., 2006, Earthquake-induced clastic dikes detected by anisotropy of magnetic susceptibility: Geology, v. 34, no. 2, p. 69-72.

Lewan, M.D., Ramini, H., and Tannenbaum, E., 1997, Petroleum formation in Senonian carbonate source rocks of the Dead Sea Basin (abs) : Rocky Mountain Association of Geologists, Outcrop, September, p. 15-16.

Li, W. X., Lundberg, J., Dickin, A. P., Ford, D. C., Schwarcz, H. P., McNutt, R., and Williams, D., 1989, High-precision mass-spectrometric Uranium-series dating of cave deposits and implications for paleoclimate studies: Nature, v. 339, no. 6225, p. 534-536.

Lienkaemper, J. J., and Ramsey, C. B., 2009, Ox Cal: Versatile tool for developing paleoearthquake chronologies-a primer: Seismological Research Letters, v. 80, no. 3, p. 431-434.

Ludwig, K. L., 2008, Isoplot 3.7. A geochronological toolkit for Microsoft Excel: Berkeley Geochronology Center Special Publication, v. 4, p. 77.

Lyakhovsky, V., Ben-Zion, Y., and Agnon, A., 2001, Earthquake cycle, fault zones, and seismicity patterns in a rheologically layered lithosphere: J. Geophys. Res., v. 106, no. B3, p. 4103-4120.

Makovsky, Y., Wunch, A., Ariely, R., Shaked, Y., Rivlin, A., Shemesh, A., Ben Avraham, Z., and Agnon, A., 2008, Quaternary transform kinematics constrained by sequence stratigraphy and submerged coastline features: The Gulf of Aqaba: Earth and Planetary Science Letters, v. 271, no. 1-4, p. 109-122.

Marco, S., 1996, Paleomagnetism and paleoseismology in the Late Pleistocene, Dead Sea Graben [Ph.D.]: Hebrew University, 108 p.

Marco, S., and Agnon, A., 1995, Prehistoric earthquake deformations near Masada, Dead Sea Graben: Geology, v. 23, no. 8, p. 695-698.

Marco, S., and Agnon, A., 2005, High-resolution stratigraphy reveals repeated earthquake faulting in the Masada Fault Zone, Dead Sea Transform: Tectonophysics, v. 408, no. 1-4, p. 101-112.

Marco, S., Agnon, A., Finkelstein, I., and Ussishkin, D., 2006, Megiddo Earthquakes, *in* Finkelstein, I., Ussishkin, D., and Halpern, B., eds., Megiddo IV: The 1998-2002 Seasons, Volume 2: Tel Aviv, The Emery and Claire Yass Publications in Archaeology, p. 568-575.

Marco, S., Hartal, M., Hazan, N., Lev, L., and Stein, M., 2003, Archaeology, history, and geology of the A.D. 749 earthquake, Dead Sea transform: Geology, v. 31, no. 8, p. 665-668.

Marco, S., Rockwell, T. K., Heimann, A., Frieslander, U., and Agnon, A., 2005, Late Holocene activity of the Dead Sea Transform revealed in 3D palaeoseismic trenches on the Jordan Gorge segment: Earth and Planetary Science Letters, v. 234, no. 1-2, p. 189.

Marco, S., Stein, M., Agnon, A., and Ron, H., 1996, Long-term earthquake clustering: A 50,000-year paleoseismic record in the Dead Sea Graben: Journal of Geophysical Research, v. 101, no. B3, p. 6179-6192.

Matmon, A., Shaked, Y., Porat, N., Enzel, Y., Finkel, R., Lifton, N., Boaretto, E., and Agnon, A., 2005, Landscape development in an hyperarid sandstone environment along the margins of the Dead Sea fault: Implications from dated rock falls: Earth and Planetary Science Letters, v. 240, no. 3-4, p. 803-817.

McCalpin, J. P., 1996, Paleoseismology, London, Academic Press, . Int. Geophys. Series, 588 p.

McGarry, S., Bar-Matthews, M., Matthews, A., Vaks, A., Schilman, B., and Ayalon, A., 2004, Constraints on hydrological and paleotemperature variations in the Eastern Mediterranean region in the last 140 ka given by the delta D values of speleothem fluid inclusions: Quaternary Science Reviews, v. 23, no. 7-8, p. 919-934.

Mechie, J., Abu-Ayyash, K., Ben-Avraham, Z., El-Kelani, R., Qabbani, I., Weber, M., and DESIRE-Group, 2009, Crustal structure of the southern Dead Sea basin derived from project DESIRE wide-angle seismic data: Geophysics Journal International, v. 178, p. 457-478.

Meghraoui, M., Gomez, F., Sbeinati, R., Van der Woerd, J., Mouty, M., Darkal, A. N., Radwan, Y., Layyous, I., Al Najjar, H., and Darawcheh, R., 2003, Evidence for 830 years of seismic quiescence from palaeoseismology, archaeoseismology and historical seismicity along the Dead Sea fault in Syria: Earth and Planetary Science Letters, v. 210, no. 1-2, p. 35.

Michetti, A. M., E. Esposito, L. Guerrieri, S. Porfido, L. Serva, R. Tatevossian, E. Vittori, F. Audemard, T. Azuma, J. Clague, V. Comerci, A. Gürpinar, J. Mccalpin, B. Mohammadioun, N.A. Mörner, Y. Ota, E. Roghozin, 2007, Environmental Seismic Intensity Scale 2007 - ESI 2007: Servizio Geologico d'Italia - Dipartimento Difesa del Suolo, APAT.

Migowski, C., 2001, Untersuchungen laminierter holozäner Sedimente aus dem Toten Meer: Rekonstruktion von Paläoklima und -seismizität [PhD: Universität Potsdam, 99 p.

Migowski, C., Agnon, A., Bookman, R., Negendank, J. F. W., and Stein, M., 2004, Recurrence pattern of Holocene earthquakes along the Dead Sea transform revealed by varve-counting and radiocarbon dating of lacustrine sediments: Earth and Planetary Science Letters, v. 222, no. 1, p. 301.

Migowski, C., Stein, M., Prasad, S., Negendank, J. F. W., and Agnon, A., 2006, Holocene climate variability and cultural evolution in the Near East from the Dead Sea sedimentary record: Quaternary Research, v. 66, no. 3, p. 421-431.

Mitchell, S. G., Matmon, A., Bierman, P. R., Enzel, Y., Caffee, M., and Rizzo, D., 2001, Displacement history of a limestone normal fault scarp, northern Israel, from cosmogenic Cl-36: Journal of Geophysical Research-Solid Earth, v. 106, no. B3, p. 4247-4264.

Morinaga, H., Yonezawa, T., Adachi, Y., Inokuchi, H., Goto, H., and Yaskawa, K., 1994, The possibility of inferring paleoseismicity from paleomagnetic dating of speleothems, western Japan: Tectonophysics, v. 230, no. 3-4, p. 241.

Muirwood, R., and King, G. C. P., 1993, Hydrological Signatures Of Earthquake Strain: Journal Of Geophysical Research-Solid Earth, v. 98, no. B12, p. 22035-22068.

Neev, D., and Emery, K. O., 1995, The Destruction of Sodom, Gomorrah, and Jericho. Geological, Climatological, and Archaeological Background, New York, Oxford University Press, 175 p.

Neev, D., and Hall, J. K., 1979, Geophysical investigations in the Dead Sea: Sedimentary Geology, v. 23, no. 1-4, p. 209-238.

Nemer, T., Gomez, F., Al Haddad, S., and Tabet, C., 2008, Coseismic growth of sedimentary basins along the Yammouneh strike-slip fault (Lebanon): Geophysical Journal International, v. 175, no. 3, p. 1023-1039.

Neumann, F. H., Kagan, E. J., Schwab, M. J., and Stein, M., 2007, Palynology, sedimentology and palaeoecology of the late Holocene Dead Sea: Quaternary Science Reviews, v. 26, no. 11-12, p. 1476.

Neumann, F. H., Kagan, E. J., Stein, M., and Agnon, A., 2009, Assessment of the effect of earthquake activity on regional vegetation -- High-resolution pollen study of the Ein Feshka section, Holocene Dead Sea: Review of Palaeobotany and Palynology, v. 155, no. 1-2, p. 42.

Niemi, T. M., and Ben-Avraham, Z., 1994, Evidence for Jericho earthquakes from slumped sediments of the Jordan River delta in the Dead Sea: Geology, v. 22, no. 5, p. 395-398.

Niemi, T. M., Zhang, H., Atallah, M., and Harrison, J. B. J., 2001, Late Pleistocene and Holocene slip rate of the Northern Wadi Araba fault, Dead Sea Transform, Jordan: Journal of Seismology, v. 5, no. 3, p. 449-474.

Nof, R. N., Baer, G., Eyal, Y., and Novali, F., Recent Crustal Movements along the Carmel Fault System, Israel, *in* Proceedings Envisat Symposium, Montreux, Switzerland, 23–27 April 2007.

Nur, A., and Ron, H., 1997, Armageddon's Earthquakes: International Geology Review, v. 39, p. 532-541.

Obermeier, S. F., Olson, S. M., and Green, R. A., 2005, Field occurrences of liquefaction-induced features: a primer for engineering geologic analysis of paleoseismic shaking: Engineering Geology, v. 76, no. 3-4, p. 209-234.

Panno, S. V., Lundstrom, C. C., Hackley, K. C., Curry, B. B., Fouke, B. W., and Zhang, Z., 2009, Major Earthquakes Recorded by Speleothems in Midwestern U.S. Caves: Bulletin of The Seismological Society of America, v. 99, no. 4, p. 2147-2154.

Papathanassiou, G., Pavlides, S., Christaras, B., and Pitilakis, K., 2005, Liquefaction case histories and empirical relations of earthquake magnitude versus distance from the broader Aegean region: Journal of Geodynamics, v. 40, no. 2-3, p. 257-278.

Perez-Lopez, R., Rodriguez-Pascua, M. A., Giner-Robles, J. L., Martinez-Diaz, J. J., Marcos-Nuez, A., Silva, P. G., Bejar, M., and Calvo, J. P., 2009, Speleoseismology and palaeoseismicity of Benis Cave (Murcia, SE Spain): coseismic effects of the 1999 Mula earthquake (mb 4.8): Geological Society, London, Special Publications, v. 316, no. 1, p. 207-216.

Plan, L., Grasemann, B., Spotl, C., Decker, K., Boch, R., and Kramers, J., 2010, Neotectonic extrusion of the Eastern Alps: Constraints from U/Th dating of tectonically damaged speleothems: Geology, v. 38, no. 6, p. 483-486.

Pons-Branchu, E., Hamelin, B., Brulhetet, J., and Bruxelles, L., 2004, Speleothem rupture in karst: tectonic or climatic origin? U-Th dating of rupture events in Salamandre Cave (Gard, southeastern France): Bulletin de la Societe Geologique de France, v. 175, no. 5, p. 473-479.

Postpischl, D., Agostini, S., Forti, P., and Quinif, Y., 1991, Palaeoseismicity from karst sediments: the "Grotta del Cervo" cave case study (Central Italy): Tectonophysics, v. 193, no. 1-3, p. 33.

Prasad, S., Vos, H., Negendank, J. F. W., Waldmann, N., Goldstein, S. L., and Stein, M., 2004, Evidence from Lake Lisan of solar influence on decadal- to centennial-scale climate variability during marine oxygen isotope stage 2: Geology, v. 32, no. 7, p. 581-584.

Ramsey, C. B., 2008, Deposition models for chronological records: Quaternary Science Reviews, v. 27, no. 1-2, p. 42.

Reches, Z., and Hoexter, D. F., 1981, Holocene seismic and tectonic activity in the Dead Sea area: Tectonophysics, v. 80, no. 1-4, p. 235.

Reicherter, K., Michetti, A. M., and Barroso, P. G. S., 2009, Palaeoseismology: historical and prehistorical records of earthquake ground effects for seismic hazard assessment: Geological Society, London, Special Publications, v. 316, no. 1, p. 1-10.

Reimer, P. J., Baillie, M. G. L., Bard, E., Bayliss, A., Beck, J. W., Bertrand, C. J. H., Blackwell, P. G., Buck, C. E., Burr, G. S., Cutler, K. B., Damon, P. E., Edwards, R. L., Fairbanks, R. G., Friedrich, M., Guilderson, T. P., Hogg, A. G., Hughen, K. A., Kromer, B., McCormac, G., Manning, S., Ramsey, C. B., Reimer, R. W., Remmele, S., Southon, J. R., Stuiver, M., Talamo, S., Taylor, F. W., van der Plicht, J., and Weyhenmeyer, C. E., 2004, IntCal04 terrestrial radiocarbon age calibration, 0-26 cal kyr BP: Radiocarbon, v. 46, no. 3, p. 1029-1058.

Reinhardt, E. G., Goodman, B. N., Boyce, J. I., Lopez, G., van Hengstum, P., Rink, W. J., Mart, Y., and Raban, A., 2006, The tsunami of 13 December A.D. 115 and the destruction of Herod the Great's harbor at Caesarea Maritima, Israel: Geology, v. 34, no. 12, p. 1061-1064.

Richards, D. A., and Dorale, J. A., 2003, Uranium-series Chronology and Environmental Applications of Speleothems: Reviews in Mineralogy and Geochemistry, v. 52, no. 1, p. 407-460.

Richter, C. F., 1958, Elementary Seismology, San Francisco, California, Freeman, 578 p.

Rotstein, Y., Shaliv, G., and Rybakov, M., 2004, Active tectonics of the Yizre'el valley, Israel, using high-resolution seismic reflection data: Tectonophysics, v. 382, no. 1-2, p. 31-50.

Rucker, J. D., and Niemi, T. M., 2010, Historical earthquake catalogues and archaeological data: Achieving synthesis without circular reasoning, *in* Sintubin, M., ed., Ancient Earthquakes. Special Paper 471.: Colorado, The Geological Society of America, p. 97-106.

Russell, K., 1980, The earthquake of May 19, A.D. 363: Bulletin of American Schools for Oriental Research, v. 238, p. 47-63.

Russell, K. W., 1985, The earthquake chronology of Palestine and northwest Arabia from the 2nd through the mid-8th century A.D.: Bulletin of American Schools for Oriental Research, v. 260 p. 37- 59.

Rybakov, M., Goldshmidt, V., Fleischer, L., and Ben-Gai, Y., 2000, 3-D gravity and magnetic interpretation for the Haifa Bay area (Israel): Journal of Applied Geophysics, v. 44, no. 4, p. 353-367.

Salamon, A., Hofstetter, A., Garfunkel, Z., and Ron, H., 1996, Seismicity of the eastern Mediterranean region: Perspective from the Sinai subplate: Tectonophysics, v. 263, no. 1-4, p. 293.

Salamon, A., Hofstetter, A., Garfunkel, Z., and Ron, H., 2003, Seismotectonics of the Sinai subplate - the eastern Mediterranean region: Geophysical Journal International, v. 155, no. 1, p. 149-173.

Sbeinati, M. R., Darawcheh, R., and Monty, M., 2005, The historical earthquakes of Syria: an analysis of large and moderate earthquakes from 1365 BC to 1900 AD: Annals of Geophysics, v. 48, no. 3, p. 347-435.

Sbeinati, M. R., Meghraoui, M., Suleyman, G., Gomez, F., Grootes, P., Nadeau, M.-J., Najjar, H. A., and Al-Ghazzi, R., 2010, Timing of earthquake ruptures at the Al Harif Roman aqueduct (Dead Sea fault, Syria) from archaeoseismology and paleoseismology: Geological Society of America Special Papers, v. 471, p. 243-267.

Schaeffer, C. F. A., 1948, Stratigraphie Compare´e et Chronologie de l'Asie Occidentale, London, Oxford University Press.

Schattner, U., Ben-Avraham, Z., Reshef, M., Bar-Am, G., and Lazar, M., 2006, Oligocene-Miocene formation of the Haifa basin: Qishon-Sirhan rifting coeval with the Red Sea-Suez rift system: Tectonophysics, v. 419, no. 1-4, p. 1-12.

Scholz, C. H., 2002, The mechanics of earthquakes and faulting, Cambridge, Cambridge University Press, 473 p.

Scholz, C. H., 2010, Large Earthquake Triggering, Clustering, and the Synchronization of Faults: Bulletin of the Seismological Society of America, v. 100, no. 3, p. 901-909.

Schwarcz, H. P., and Latham, A. G., 1989, Dirty calcites 1. Uranium-series dating of contaminated calcite using leachates alone: Chemical Geology: Isotope Geoscience section, v. 80, no. 1, p. 35-43.

Shaked, Y., Agnon, A., Lazar, B., Marco, S., Avner, U., and Stein, M., 2004, Large earthquakes kill coral reefs at the north-west Gulf of Aqaba: Terra Nova, v. 16, no. 3, p. 133-138.

Shaked, Y., Lazar, B., Marco, S., Stein, M., and Agnon, A., in press, Late Holocene events that shaped the shoreline at the northern Gulf of Aqaba as recorded by a buried reef: Israel Journal of Earth Sciences.

Shamir, G., 2007, Earthquake epicenter distribution and mechanisms in northern Israel: Geological Survey of Israel. Report GSI/16/2007.

Shapira, A., Avni, R., and Nur, A., 1993, A new estimate for the epicenter of the Jericho earthquake of 11 July 1927: Israel Journal of Earth Sciences, v. 42, p. 93-96.

Shtivelman, V., Marco, S., Reshef, M., Agnon, A., and Hamiel, Y., 2005, Using trapped waves for mapping shallow fault zones: Near Surface Geophysics, v. 3, no. 2, p. 95-101.

Siegenthaler, C., Finger, W., Kelts, K., and Wang, S., 1987, Earthquake And Seiche Deposits In Lake Lucerne, Switzerland: Eclogae Geologicae Helvetiae, v. 80, no. 1, p. 241-260.

Stein, M., 2011, Paleo-earthquakes chronometry in the late Quaternary Dead Sea basin Israel Journal of Earth Sciences, v. 58.

Stein, M., Torfstein, A., Gavrieli, I., and Yechieli, Y., 2010, Abrupt aridities and salt deposition in the post-glacial Dead Sea and their North Atlantic connection: Quaternary Science Reviews, v. 29, no. 3-4, p. 567-575.

Stewart, A., 1993, A Death at Dor: British Archaeological Reports, v. 19.2, p. 30-36.

Stuiver, M., and Polach, H. A., 1977, Reporting of C-14 Data - Discussion: Radiocarbon, v. 19, no. 3, p. 355-363.

Talwani, P., 1997, On the Nature of Reservoir-induced Seismicity: Pure and Applied Geophysics, v. 150, no. 3, p. 473-492.

Tannenbaum, E., 1983, Researches in the geochemistry of oils and asphalts in the Dead Sea area, Israel: [PhD], The Hebrew University, Jerusalem.

ten Brink, U. S., Al-Zoubi, A. S., Flores, C. H., Rotstein, Y., Qabbani, I., Harder, S. H., and Keller, G. R., 2006, Seismic imaging of deep low-velocity zone beneath the Dead Sea basin and transform fault: Implications for strain localization and crustal rigidity: Geophysical Research Letters, v. 33, no. 24.

Thomas, R., Niemi, T. M., and Parker, S. T., 2007, Structural Damage from Earthquakes in the Second–Ninth Centuries at the Archaeological Site of Aila in Aqaba, Jordan: Bulletin of the American Schools of Oriental Research, v. 346 p. 59-77.

Toksoz, M. N., Shakal, A. F., and J., M., 1979, Space-Time Migration of Earthquakes Along the North Anatolian Fault Zone and Seismic Gaps: Pageoph, v. 117, p. 1258-1270.

Torfstein, A., Goldstein, S. L., Kagan, E., and Stein, M., in press, An integrated multi-site chronology of last glacial Lake Lisan: Geochimica et Cosmochimica Acta.

Uysal, I. T., Feng, Y., Zhao, J. X., Altunel, E., Weatherley, D., Karabacak, V., Cengiz, O., Golding, S. D., Lawrence, M. G., and Collerson, K. D., 2007, U-series dating and geochemical tracing of late Quaternary travertine in co-seismic fissures: Earth and Planetary Science Letters, v. 257, no. 3-4, p. 450-462.

Weber, M., Abu-Ayyash, K., Abueladas, A., Agnon, A., Alasonati-Tasarova, Z., Al-Zubi, H., Babeyko, A., Bartov, Y., Bauer, K., Becken, M., Bedrosian, P. A., Ben-Avraham, Z., Bock, G., Bohnhoff, M., Bribach, J., Dulski, P., Ebbing, J., El-Kelani, R., Forster, A., Forster, H.-J., Frieslander, U., Garfunkel, Z., Goetze, H. J., Haak, V., Haberland, C., Hassouneh, M., Helwig, S., Hofstetter, A., Hoffmann-Rothe, A., Jackel, K. H., Janssen, C., Jaser, D., Kesten, D., Khatib, M., Kind, R., Koch, O., Koulakov, I., Laske, G., Maercklin, N., Masarweh, R., Masri, A., Matar, A., Mechie, J., Meqbel, N., Plessen, B., Moller, P., Mohsen, A., Oberhansli, R., Oreshin, S., Petrunin, A., Qabbani, I., Rabba, I., Ritter, O., Romer, R. L., Rumpker, G., Rybakov, M., Ryberg, T., Saul, J., Scherbaum, F., Schmidt, S., Schulze, A., Sobolev, S. V., Stiller, M., Stromeyer, D., Tarawneh, K., Trela, C., Weckmann, U., Wetzel, U., and Wylegalla, K., 2009, Anatomy of the Dead Sea Transform from lithospheric to microscopic scale: Rev. Geophys., v. 47, p. no. RG2002.

Wechsler, N., Katz, O., Dray, Y., Gonen, I., and Marco, S., 2009, Estimating location and size of historical earthquake by combining archaeology and geology in Um-El-Qanatir, Dead Sea Transform: Natural Hazards, v. 50, no. 1, p. 27-43.

Wells, D. L., and Coppersmith, K. J., 1994, New Empirical Relationships among Magnitude, Rupture Length, Rupture Width, Rupture Area, and Surface Displacement: Bulletin of the Seismological Society of America, v. 84, no. 4, p. 974-1002.

Wen, X. Z., Ma, S. L., Xu, X. W., and He, Y. N., 2008, Historical pattern and behavior of earthquake ruptures along the eastern boundary of the Sichuan-Yunnan faulted-block, southwestern China: Physics of the Earth and Planetary Interiors, v. 168, no. 1-2, p. 16-36.

Wetzler, N., Marco, S., and Heifetz, E., 2010, Quantitative analysis of seismogenic shear-induced turbulence in lake sediments: Geology, v. 38, no. 4, p. 303-306.

Willis, B., 1928, Earthquakes in the Holy Land: Bulletin of the Seismological Society of America, v. 18, p. 73-103.

Woodcock, N. H., and Fischer, M., 1986, Strike-slip duplexes: Journal of Structural Geology, v. 8, no. 7, p. 725-735.

Wust-Bloch, G. H., 2002, The active Dead Sea Rift fault zone: a seismic wave-guide: EGU Stephan Mueller Special Publication Series, v. 2, p. 11-20.

Yadin, Y., 1956, Excavations at Hazor: The Biblical Archaeologist, v. 19, no. 1, p. 2-11.

Yeats, R. S., 2007, Paleoseismology: Why can't earthquakes keep on schedule?: Geology, v. 35, no. 9, p. 863-864.

Yeats, R. S., Sieh, K., and Allen, C. R., 1997, The geology of earthquakes, New York, Oxford University Press, 568 p.

Yechieli, Y., 1993, The effects of water level changes in closed lakes (Dead Sea) on the surrounding groundwater and country rocks [Ph.D.]: Weizmann Institute of Science, 197 p.

Yechieli, Y., Magaritz, M., Levy, Y., Weber, U., Kafri, U., Woelfli, W., and Bonani, G., 1993, Late Quaternary Geological History of the Dead Sea Area, Israel: Quaternary Research, v. 39, no. 1, p. 59.

Zachariasen, J., Sieh, K., Taylor, F. W., Edwards, R. L., and Hantoro, W. S., 1999, Submergence and uplift associated with the giant 1833 Sumatran subduction earthquake: Evidence from coral microatolls: J. Geophys. Res., v. 104, no. B1, p. 895-919.

Zak, I., 1967, The geology of the Sedom Mountain [Ph.D.]: Hebrew University of Jerusalem, 208 p.

Zilberman, E., Amit, R., Bruner, I., and Nahmias, Y., 2004, Neotectonic and paleoseismic study - Bet She'an Valley: Geological Survey of Israel, GSI/15/04.

Zilberman, E., Amit, R., Porat, N., Enzel, Y., and Avner, U., 2005, Surface ruptures induced by the devastating 1068 AD earthquake in the southern Arava Valley, Dead Sea Rift, Israel: Tectonophysics, v. 408, no. 1-4, p. 79-99.

Zilberman, E., Greenbaum, N., and Ashqar, L., Tour to tectonic sites along the Carmel and Nesher faults, Field Guide, *in* Proceedings Geolgical Society of Israel meeting, Nazareth, 2008.

Appendices

Appendix A

Some speleothem samples sawed with laminae exposed and dated laminae marked. Some hand/field samples shown for clarification. Laminae labels are same as those in Tables 3.1-3.3. Dating data and results can be found in those tables. Cores are 2 inches in diameter.

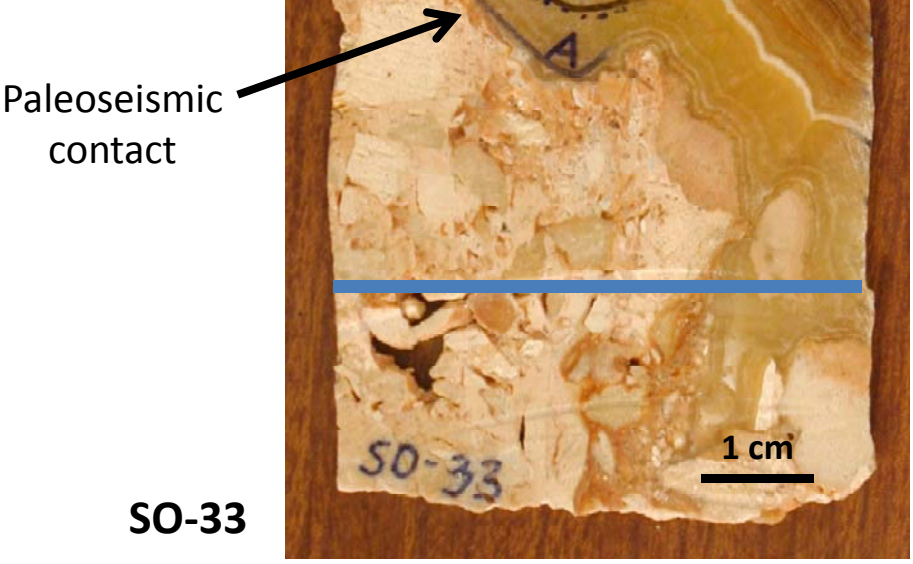

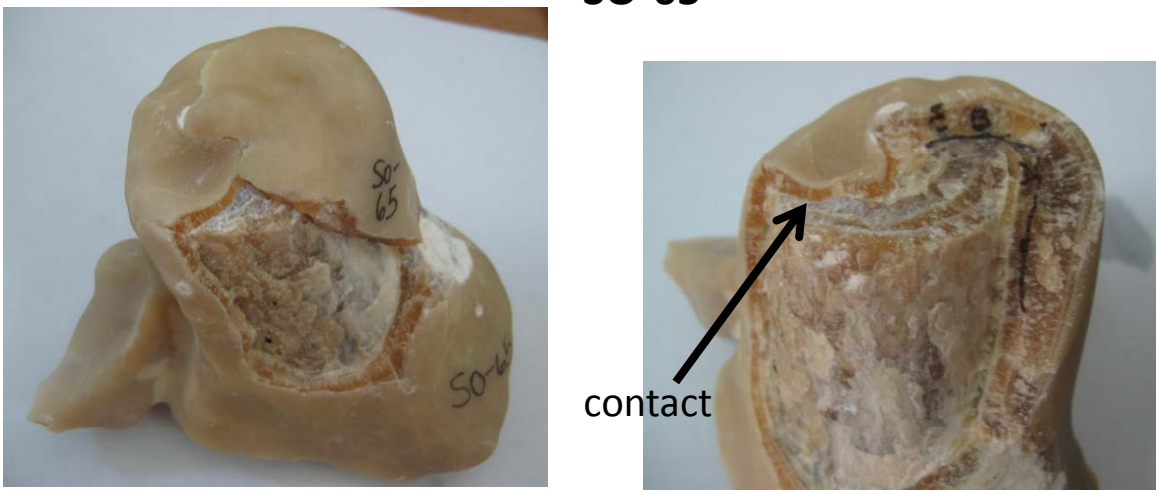

Figure A.i

Appendix A

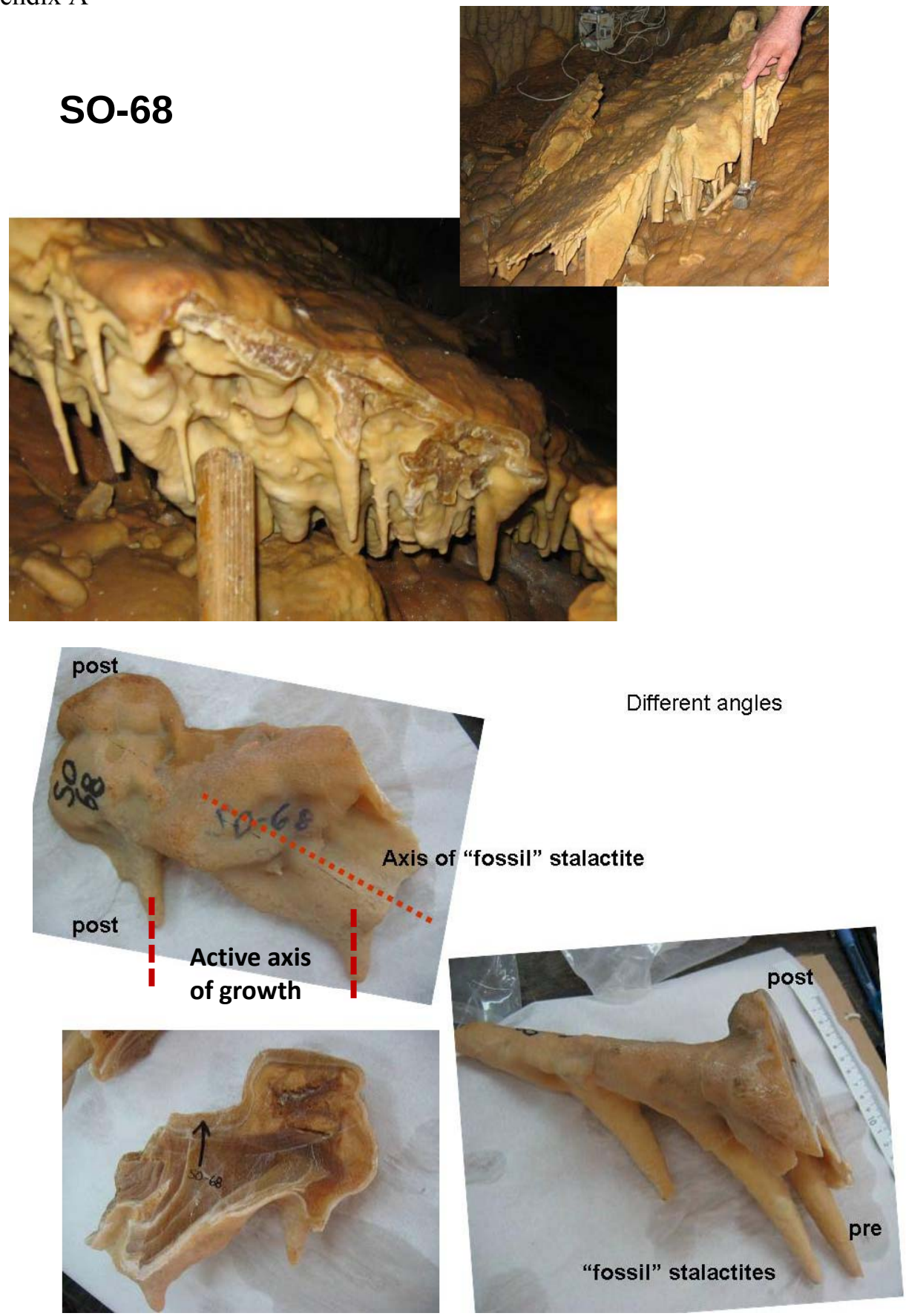

Figure A.ii

Appendix A

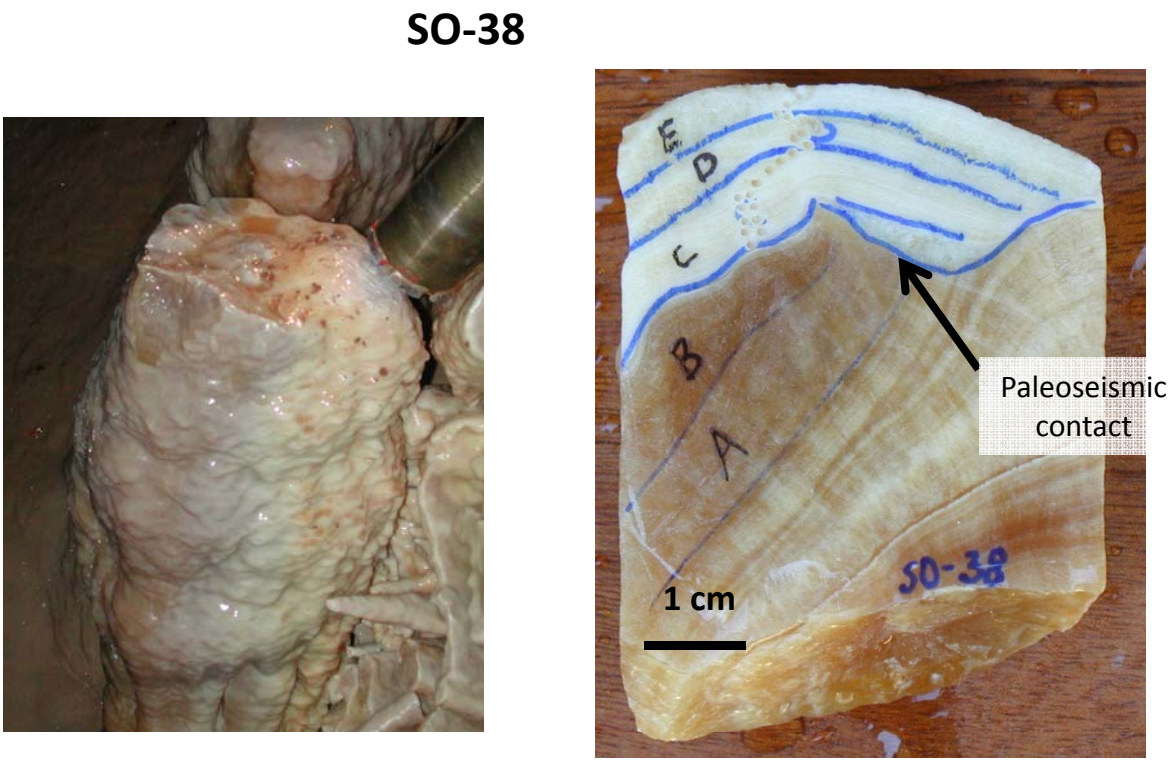

Figure A.iii

Appendix A

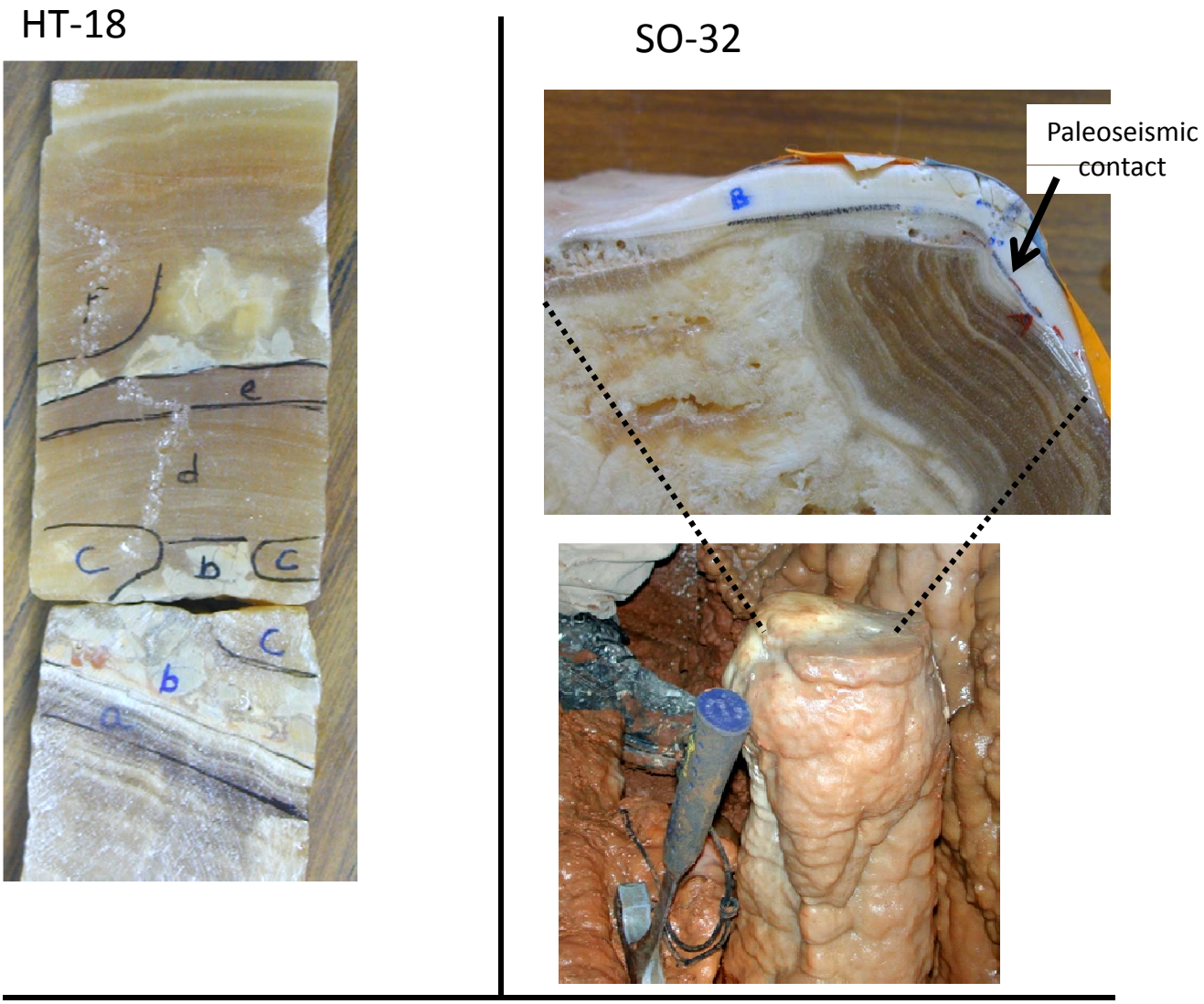

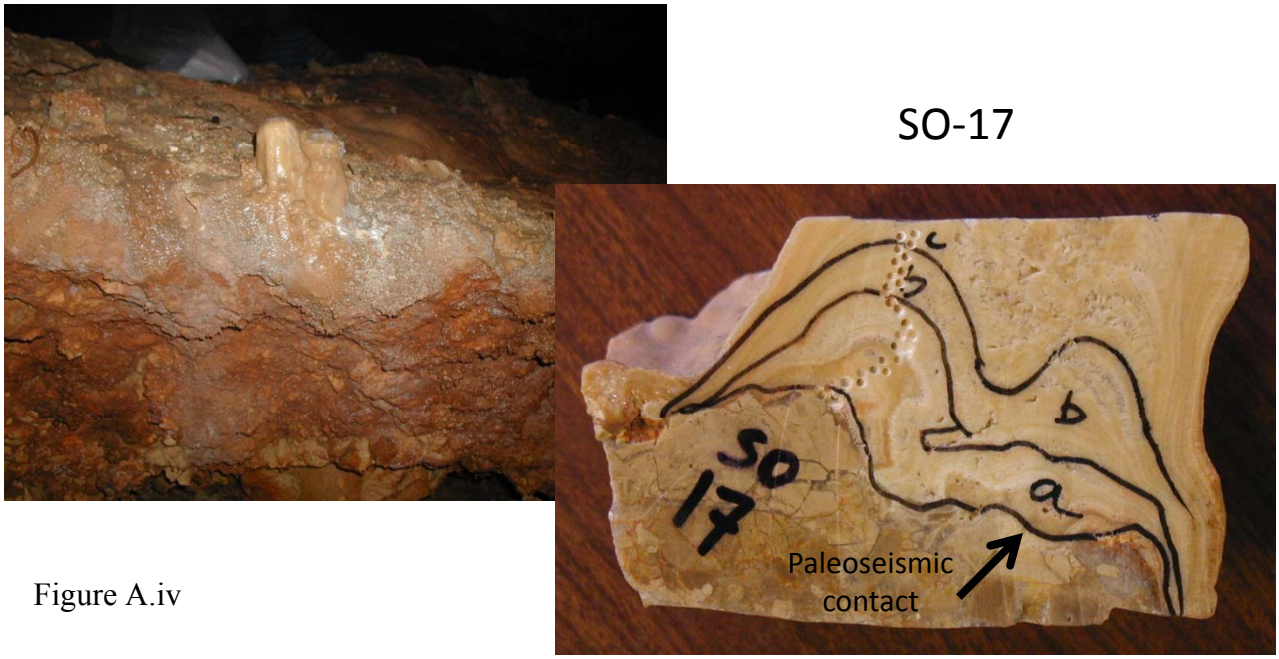

Figure A.iv

Appendix A

SO-55

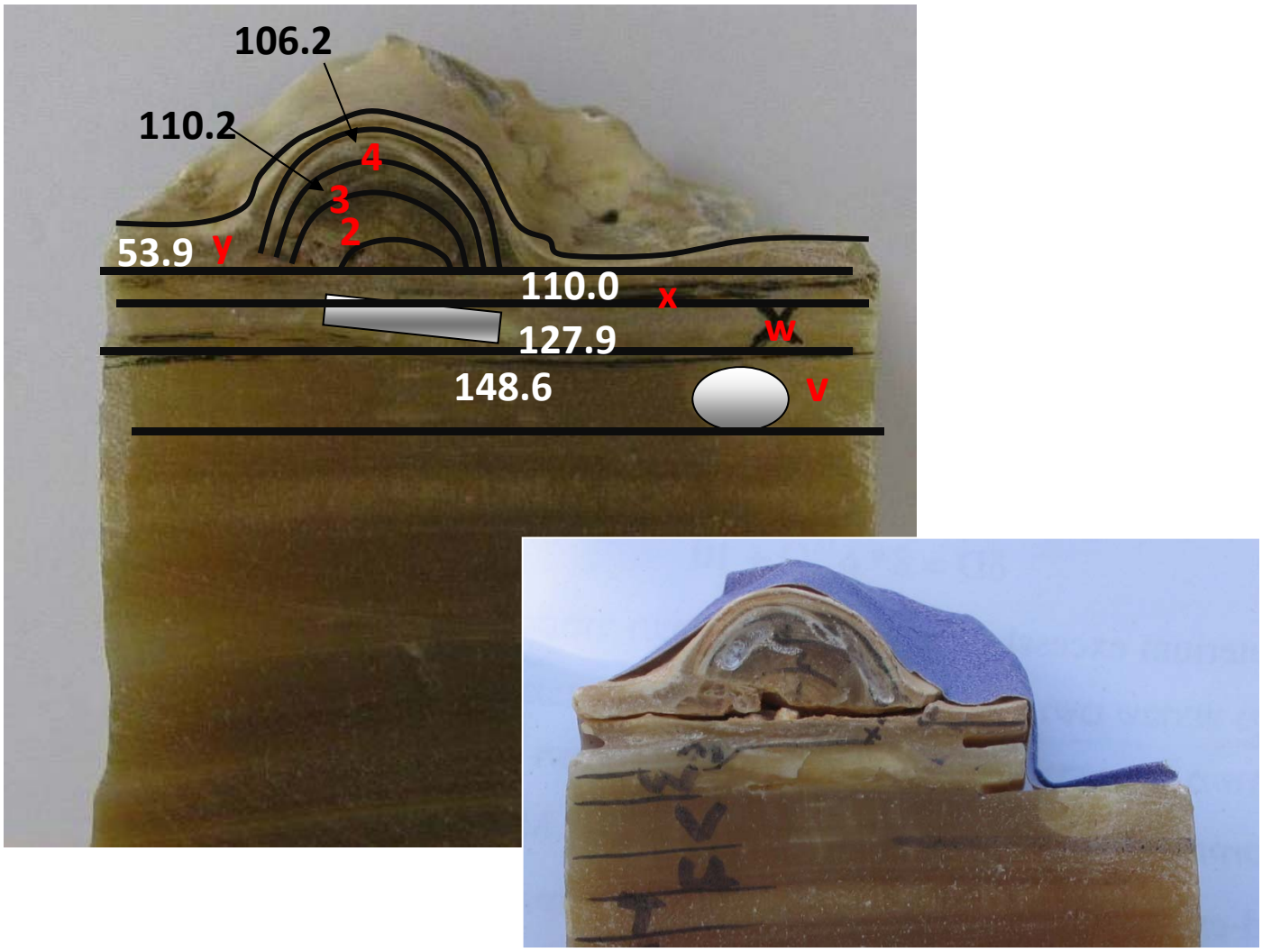

3 damage horizons
1st: fallen macaroni: post: 148.6±4.6 ka
2nd: fallen fragment: pre: 148.6±4.6; post: 127.9±4.4 ka
3rd: broken fallen stalactite: pre: 106.2±4.5; post: 53.9±0.4 ka

Figure A.v

Appendix A

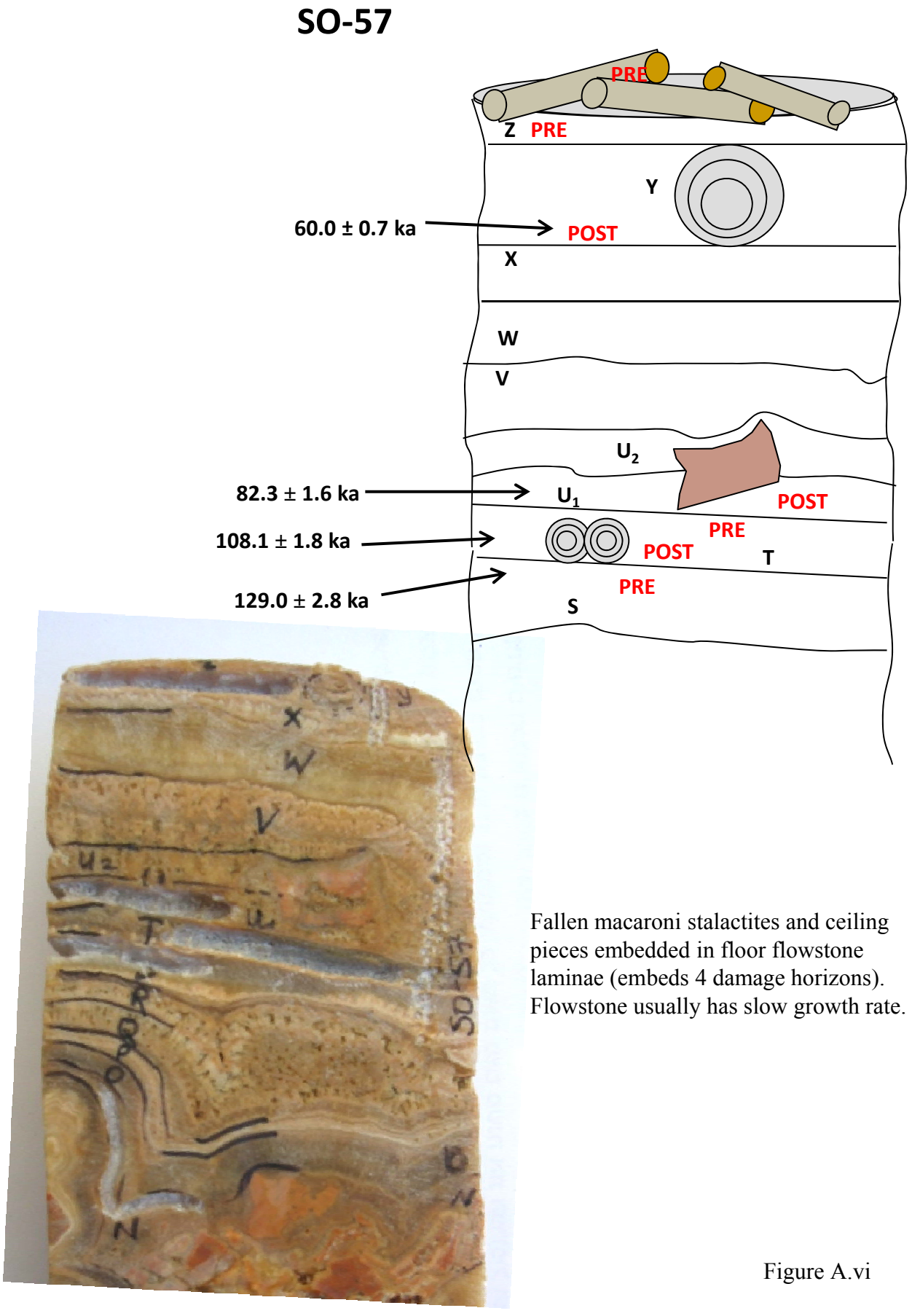

Fallen macaroni stalactites and ceiling pieces embedded in floor flowstone laminae (embeds 4 damage horizons). Flowstone usually has slow growth rate.

Figure A.vi

1-6

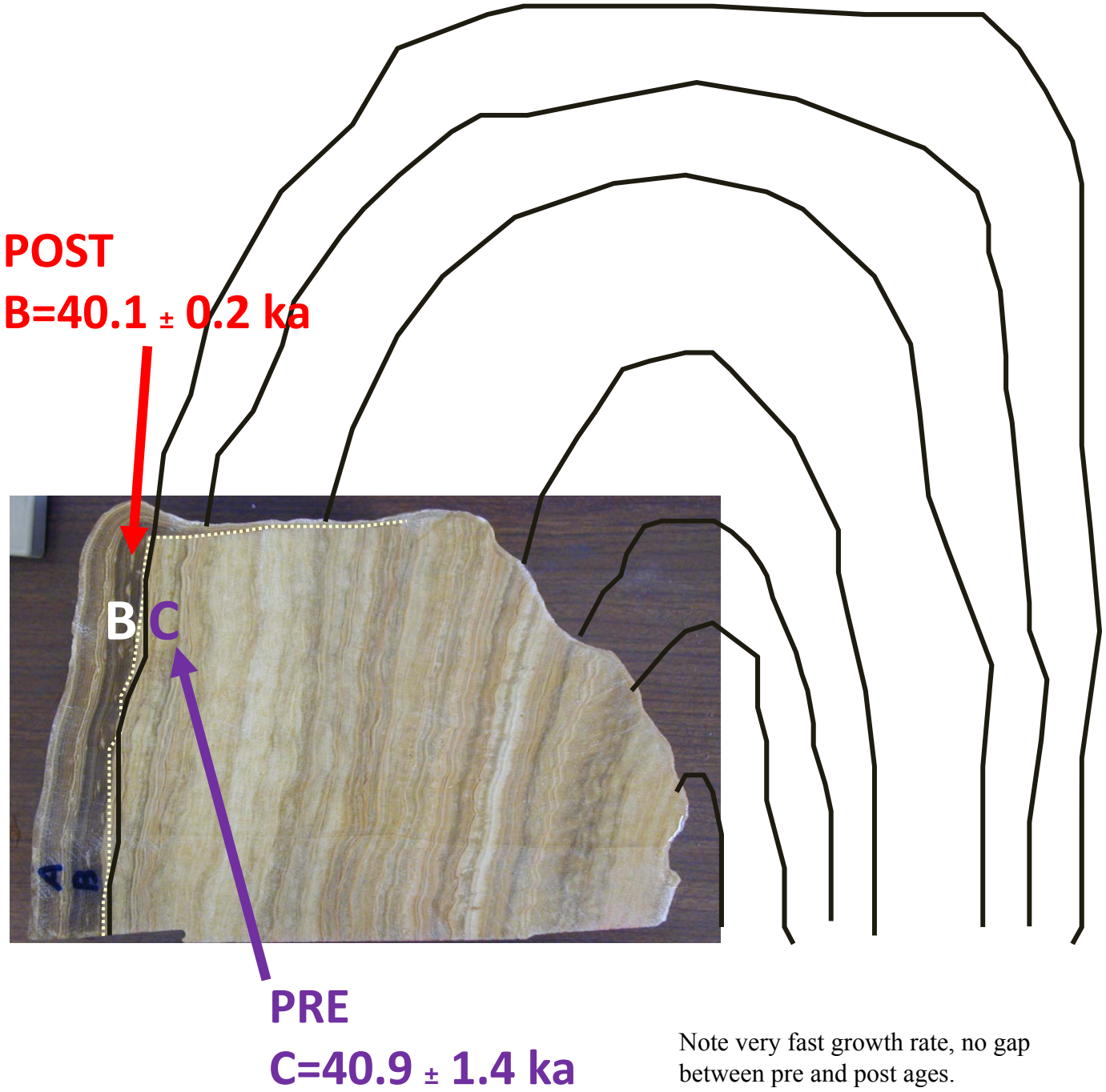

Note very fast growth rate, no gap between pre and post ages.

Figure A.1.vii

Appendix A

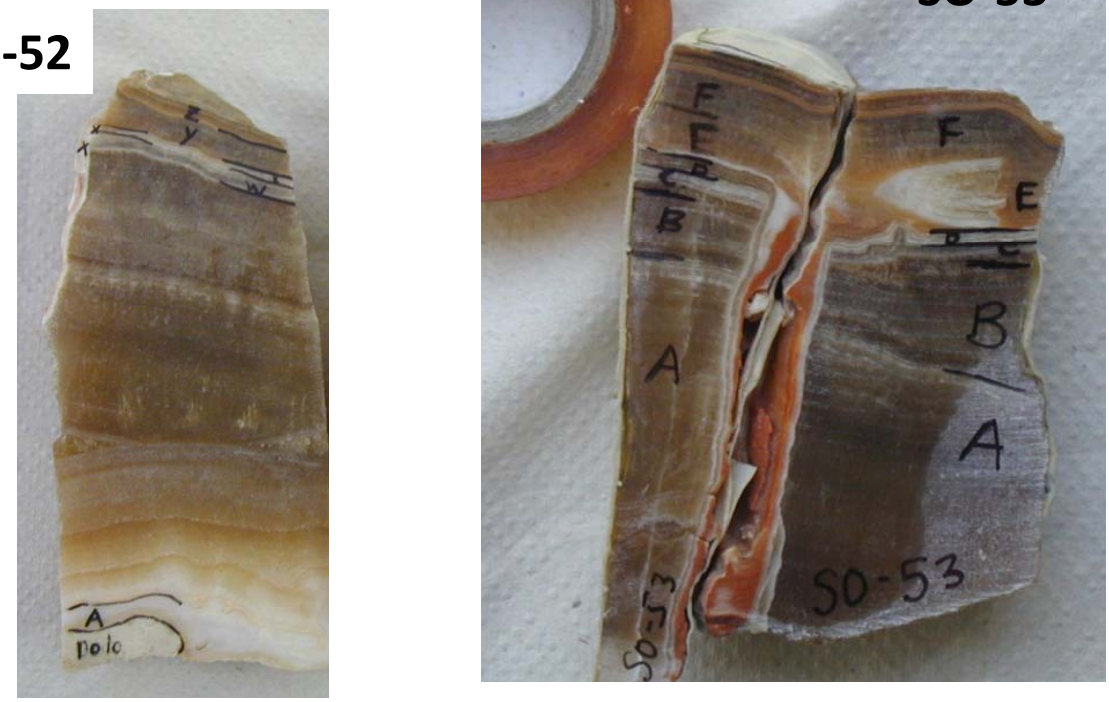

Fractured flowstone and fracture-fill

Figure A.viii

Table B.1. All Holocene lacustrine samples, locations, and C-14 ages.

Sample Name	Lab number	Location	section	Height [cm]	Facies	Description	C-14 age ± 1σ	calibrated age 1σ	calibrated age 2σ
EFW-009	RTT 5174	Ein Feshkha	EFE	9	aad	wood	700±40	1268–1382 A.D.	1243–1392 A.D.
EFW-029	RTT 5175	Ein Feshkha	EFE	29	aad	wood	780±40	1223–1271 A.D	1178–1285 A.D.
EFW-80	RTT 5176	Ein Feshkha	EFE	80	aad	wood	1015±40	980–1117 A.D.	898–1154 A.D
EFW-120	RTT 5177	Ein Feshkha	EFE	120	aad	wood	1310±40	661–767 A.D.	647–779 A.D.
EFW-169	RTT 5178	Ein Feshkha	EFE	169	aad	wood	1750±40	237–344 A.D.	140–399 A.D.
EFW-430	RTT 5180	Ein Feshkha	EFE	430	aad	wood	2150±45	352–111 B.C.	360–54 B.C.
EFW-492	RTT 5181	Ein Feshkha	EFE	492	aad	wood	2380± 40	511–397 B.C.	743–386 B.C.
EFW-518	RTT 5182	Ein Feshkha	EFE	518	aad	wood	300±50	1372–1133 B.C.	1407–1090 B.C.
EFW-530	RTT 5183	Ein Feshkha	EFE	530	aad	wood	2850±65	1116–926 B.C.	1254–845 B.C.
DSF-B1-18	KIA32721	Ein Feshkha	DSF-Core	26.5	aad	wood	1189 ± 27	783–882 A.D.	729–940 A.D.
DSF-B1-31	KIA32722	Ein Feshkha	DSF-Core	46.5	aad	wood	933 ± 36	1038–1154 A.D.	1022–1182 A.D.
DSF B3-28	KIA11641	Ein Feshkha	DSF-Core	218.5	aad	wood	1541 ± 68	432–576 A.D.	391–646 A.D.
DSF-B5-43	KIA11642	Ein Feshkha	DSF-Core	412	aad	wood	2143 ± 27	346–115 B.C.	353–60 B.C
DSF-B5-58	KIA32723	Ein Feshkha	DSF-Core	426.5	aad	wood	2215 ± 29	361–208 B.C.	377–202 B.C.
DSF-B5-65	KIA32724	Ein Feshkha	DSF-Core	430.5	aad	wood	2662 ± 36	840–796 B.C.	896–792 B.C.
DSF-B5-76	KIA32725	Ein Feshkha	DSF-Core	448	aad	wood	2036 ± 31	90 B.C.-17 A.D.	160 B.C. to 51 A.D.
DSF-B6o-73	KIA32726	Ein Feshkha	DSF-Core	537	aad	wood	2873 ± 88	1193–926 B.C.	1308–838 B.C.
ZA 37	RTT 5184	Ze'elim	ZA-2	132	ld	wood	825±40	1185–1259 A.D.	1056–1276 A.D.
ZA 35	RTT 5185	Ze'elim	ZA-2	234	ld	wood	1295±40	668–770 A.D.	651–853 A.D.
ZA 33	RTT 5186	Ze'elim	ZA-2	346	ld	wood	1685± 40	264–412 A.D.	246–431 A.D.
ZA 25	RTT 5187	Ze'elim	ZA-2	467	ld	wood	1840± 50	94–238 A.D.	63–325 A.D.
ZA 20	RTT 5188	Ze'elim	ZA-2	632	ld	wood	2345±40	505–380 B.C.	725–257 B.C.
ZA 18	RTT 5189	Ze'elim	ZA-2	742	ld	wood	2820± 40	1015–914 B.C.	1114–851 B.C.
ZA 50	RTT 5190	Ze'elim	ZA-2	872	ld	wood	3730±45	2196–2039 B.C.	2284–1979 B.C.
ZA 51	RT 5191	Ze'elim	ZA-2	897	ld	wood	3500±75	1921–1738 B.C.	2024–1634 B.C.
ZA 5	RTT 5192	Ze'elim	ZA-2	967	ld	wood	3540±45	1941–1775 B.C.	2015–1745 B.C.
ZA 10	RTT 5193	Ze'elim	ZA-2	1022	ld	wood	3475±45	1877–1744 B.C.	1913–1686 B.C.
ZA 16	RTT 5194	Ze'elim	ZA-2	1067	ld	wood	5860±50	4794–4623 B.C.	4843–4583 B.C.
ZA-100	RT 5531	Ze'elim	ZA-2-BR	800-900	BR	wood	3825±70	2460-2140 B.C.	2480-2040 B.C.
ZA-101	RT 5532	Ze'elim	ZA-2-BR	800-900	BR	wood	4085±110	2870-2490 B.C.	2950-2300 B.C.
ZA-102	RT 5533	Ze'elim	ZA-2-BR	800-900	BR	wood	3545±100	2030-1740 B.C.	2200-1600 B.C.
ZA-103	RT 5534	Ze'elim	ZA-2-BR	800-900	BR	wood	3620±50	2110-1900 B.C.	2140-1870 B.C.
ZA-107	RTT 5535	Ze'elim	ZA-2-BR	800-900	BR	wood	3945±40	2570-2340 B.C.	2570-2290 B.C.
ZA-108	RTT 5536	Ze'elim	ZA-2-BR	800-900	BR	wood	3595±45	2020-1890 B.C.	2130-1770 B.C.
ZA-109	RTT 5537	Ze'elim	ZA-2-BR	800-900	BR	wood	3450±40	1880-1690 B.C.	1890-1660 B.C.

Notes: Abbreviations: aad=alternating aragonite and detritus; ld=laminated detritus; BR=beach ridge; ac=aragonite crust; EFE and ZA heights are given in cm below plain surface. Core heights are in compiled depths (correlated to EFE outcrop). Additional data is given for some of the samples in the published papers in Chapter 3.1 and in Appendix D.
Coordinates of sample sites: EFE and DSF: 31.708796N/35.455021E, ZA: 31.334046N/35.406216E.

Appendix Table B.2

Ze'elim and Ein Feshkha seismites with model ages and historic event correlation

no.	Depth (cm) *	Type ¥	Thickness (cm)	†Modeled calendar age (68%, ~1 σ)	†Modeled calendar age (95%, ~2 σ)	Historic Earthquake correlation	‡Fit	¥¥ All possible events (within 2σ range, 1σ in bold)
Ze'elim seismites								
I	32	A	10	[a]~1400-1650 AD		**1456 AD**		1408, 1456,1481, 1546 AD
II	242	A	2	699-848 AD	682-859 AD	**748±1 AD**	**1σ**	**748±1,757, 835, 847, 853**, 859
III	315	A&C	17	467-606 AD	452-627 AD	**551 AD**	**1σ**	**502,551 AD**
IV	342	A	5	386-519 AD	370-541 AD	**419 AD**	**1σ**	**419,502 AD**
V	445	A	5	86-164 AD	55-210 AD	**115 AD**	**1σ**	**112,115,117 AD**
VI	470	A	4	12-91 AD	20 BC-131	**33 AD**	**1σ**	**33,76 AD**
VII	486	A	6	40 BC-35 AD	77 BC-74 AD	**31 BC**	**1σ**	**31 BC,33 AD**
VII	516	A	8	140-66 BC	178-28 BC	**Mid II century**	**1σ**	**92, 64 BC**
IX	552	A	8	260-190 BC	300-150 BC	**199 BC**	**1σ**	**199 BC**
X	700	A&C	variabl	781-700 BC	824-667 BC	**Mid VIII cent.**	**1σ**	**Mid VIII cent. BC**
XI	710	A&C	variabl	819-734 BC	861-705 BC	**Mid VIII cent.**	**1σ**	**Mid VIII cent. BC**
XII	919	A	variabl	[b]~ 2020-1635 BC				
Ein Feshkha seismites								
1	0.0	A	10	1300-1343 AD	1279-1421 AD	**1312 AD**	**1σ**	1293, **1303,1312**, 1401-8
2	12.0	A	7	1260-1293 AD	1239-1367 AD	**1293 AD**	**1σ**	**1293**,1303,1312
3	28.0	A	2	1199-1240 AD	1176-1267 AD	**1202/1212 AD**	**1σ**	1170, **1202,1212**
4	40.0	A	6	1150-1190 AD	1125-1210 AD	**1170 AD**	**1σ**	1138/9,1150,1156/7,1170,1202, 1212
5	48.0	A	2	1118-1155 AD	1091-1174 AD	**1117/1138 AD**	**1σ**	**1113/4,1114,1115,1117,1138/9 ,1150,1156**/7, 1170
6	66.0	A	1	1044-1084 AD	1017-1105 AD	**1068 AD**	**1σ**	1032,1033**,1042,1063,1068a,10 68b**
7	70.0	Q	1	1028-1067 AD	1002-1088 AD	**1063 AD**	**1σ**	991,**1032,1033,1042,1063,1068 a,1068b**
8	74.0	A	1.5	1013-1051 AD	986-1071 AD	**1033 AD**	**1σ**	991,**1032,1033,1042**,1063,1068 a,1068b
9	80.0	A	1.5	991-1026 AD	962-1045 AD	**991 AD**	**1σ**	952,956,**991,1032,1033**,1042
10	86.0	A	4	963-1005 AD	929-1023 AD	**956 AD, LS**	**1σ**	952,**956,991**,1032
11	104.0	D	6	885-939 AD	833-954 AD	**873 AD, LS**	**2σ**	835,847,853/4,859,873,952,956
12	110.5	Q	1.5	859-915 AD	801-926 AD	**859 AD, LS**	**1σ**	835,847,**853/4,859,873**
13	113.0	A	3	849-905 AD	788-915	**847 AD, LS**	**1σ**	835,**847,853/4,859,873**
14	125.0	A	1	801-861 AD	733-870 AD	**757 AD**	**2σ**	747/9,757,**835,847,853/4,859**,8 73
15	126.5	A	2.5	795-856 AD	729-865 AD	**748±1 AD**	**2σ**	747/9,757**,835,847,853/4,859**,8 73
16	157.0	B	3	666-747 AD	599-773 AD	**660 AD**	**1σ**	634,**660,747/9,757**
17	172.0	D	1	603-692 AD	538-727 AD	**634 AD**	**1σ**	500/502,551,**634,660**
18	186.5	Q	1	543-638 AD	476-681 AD	**551 AD**††	**1σ**	500/502,**551,634**,660
19	210.0	A	2	448-551 AD	376-605 AD	**419 AD**	**2σ**	419,**500/502,551**
20	212.5	Q	1	439-542 AD	365-595 AD			419,**500/502,551**
21	220.0	B	2	408-515 AD	334-570 AD	**363 AD**	**2σ**	349,362/3,**419,500/502**,551
22	228.0	A	1	372-487 AD	296-548 AD	**349 AD**	**2σ**	303,349,**363,419,**500/502,551

no.	Depth (cm) *	Type ¥	Thickness (cm)	†Modeled calendar age (68%, ~1 σ)	†Modeled calendar age (95%, ~2 σ)	Historic Earthquake correlation	‡Fit	¥¥ All possible events (within 2σ range, 1σ in bold)
23	338.0	B	1	25-100	20BC-142 AD	**33 AD**	**1σ**	**33,37,76,110**
24	364.0	B	1	57 BC-7 AD	94 BC-46 AD	**31 BC**	**1σ**	92BC,**64BC,31BC**,33,37
25	377.0	B	<1	96-41 BC	131-2 BC	**64 BC**	**1σ**	**92BC,64BC,31BC**
26	377.8	B	<1	101-42 BC	133-6 BC			**92BC,64BC**,31BC
27	387.0	B	1	126-76 BC	160-39 BC	**92 BC**	**1σ**	**92BC**,64BC,31BC
28	393.0	B	1	146-96 BC	177-61 BC	**mid-2nd century**	**1σ**	**92BC**,64BC, mid-2nd century BC
29	402.0	B	1.5	172-130 BC	204-95 BC	**mid-2nd century**	**1σ**	199BC, **mid-2nd century BC x 2**,92BC
30	425.0	B	2	243-202 BC	288-183 BC	**199**	**1σ**	**199BC**
31	428.0	D	2	252-212 BC	301-192 BC			199BC
32	438.0	A&E	2	286-240 BC	336-222 BC			331BC
33	447.0	B	2	321-267 BC	366-249 BC	**331 BC ****	**1σ**	**331BC**
34	473.0	A	1	412-346 BC	458-328 BC			331BC
35	478.5	Q	1	433-361 BC	477-346 BC			
36	483.0	A&E	1	447-375 BC	492-361 BC			
37	487.0	A&B	7.5	461-386 BC	507-373 BC			
38	495.0	A	5	489-408 BC	537-398 BC	**525 BC****	**2σ**	525BC
39	513.0	B	1.5	749-630 BC	817-577 BC			**Mid-8th century BC x 2**
40	515.0	B&E	2	784-661 BC	854-607 BC	**Mid-8th century BC**	**1σ**	**Mid-8th century BC x 2**
41	521.0	B	3	886-756 BC	963-699 BC	**mid-8th century BC**	**1σ**	**Mid-8th century BC x 2**
42	527.5	A	1.5	1002-862 BC	1076-801 BC			~1050BC
43	531.0	A	>9	1059-915 BC	1136-846 BC	**~1050 BC****	**1σ**	**~1050BC**
44	543.0	A	3-6	unmodeled				
45	547.0	B	1					
46	558.0	Q	0.7					
47	561.0	A	6					
48	572.0	B	1.5.					
49	574.5	A	0.5					
50	576.0	D	1					
51	578.0	A	0.6					
52	579.0	D	1					

Notes:

* Gully depth below fan delta surface

† Model ages of seismites extrapolated from deposition model (see text for details);

¥ Seismite type: A-Intraclast breccia layer, B-Microbreccia ("homogenite" to the naked eye), C-liquefied sand; D-Folded laminae; E-Small offsets; Q-Questionable as seismite. See Table 3.1.1, Fig. 3.1.2;

‡ Fit of historical earthquake dates within 1s or 2s calibrated age ranges of seismites. Although model ages are tabulated here with 1 year precision for convenience, event fit considers the realistic precision of 10 years (see text);

[a] Outside model range, extrapolated from model (Figure 3.1.4).

[b] Outside model range, estimated based on below and above radiocarbon ages (Figure 3.1.4).

** Events could have been caused by seismites below or above the one marked.

¥¥ All other possible events within the age probability range (1σ or 2 σ range) of the designated earthquake.

LS=local source, moderate earthquake, not appearing in the historical catalogues, may have produced these seismites.

††The seismites correlated to the 551 A.D. historic earthquake could also be accorded to the 597/598 A.D. earthquake discussed by *Rucker and Niemi* [2012] and noted by *Ambraseys* [2009].

Appendix C.1. Lisan Formation columnar section at Nahal Mishmar (MR), with emphasis on seismites and other deformations, sampling locations, and stratigraphic markers.

Mishmar -MR- columnar section

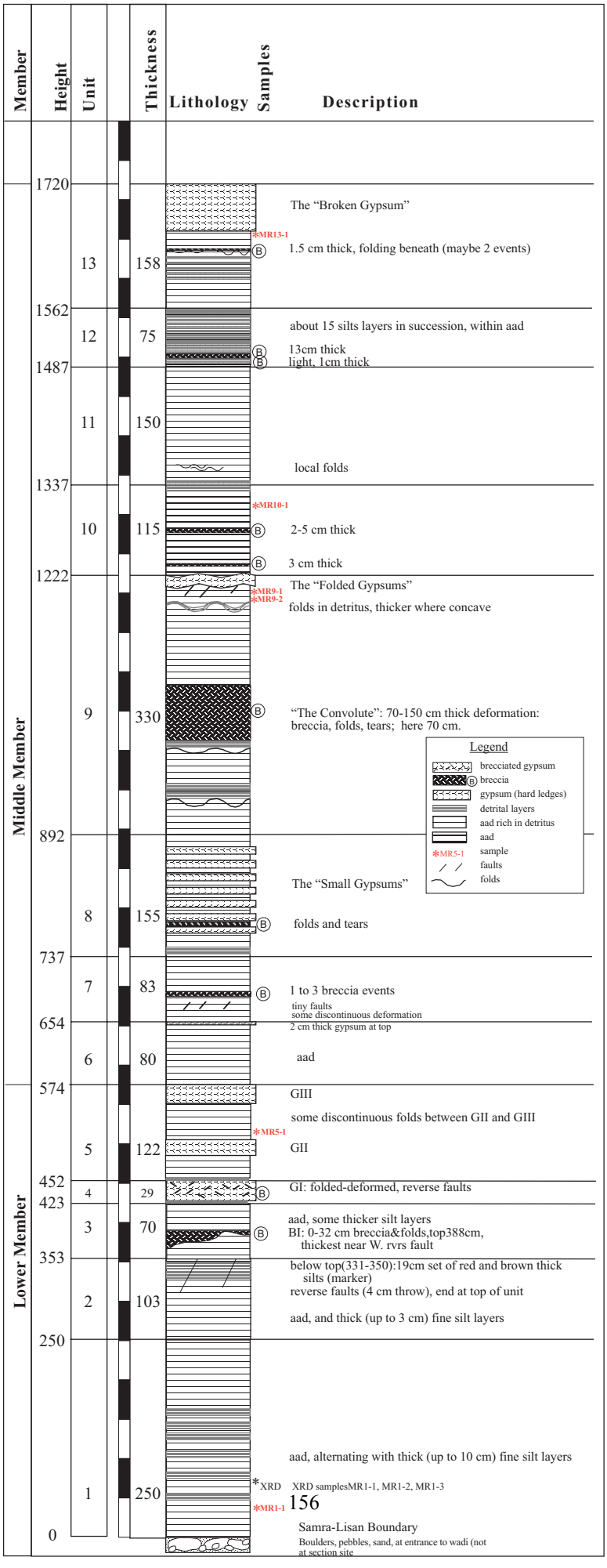

Appendix C.2

Association between asphalt and breccias in Lisan Formation

Can asphalt ejection be developed as an earthquake monitor and possibly as a precursor to earthquakes? A new direction in the paleoseismic study of the DST is related to the appearance of asphalt and oil in the sedimentary units. In the Lisan sediments asphalt and oil remnants have been identified and analyzed at various sites [Eli Tannenbaum, *pers comm.*]. The asphalt or oil migrated through the sedimentary fill of the Dead Sea basin to the surface and their source is the Upper Cretaceous (Senonian) bituminous rocks (also termed oil shales) buried in the graben [*Tannenbaum*, 1983; *Lewan et al*., 1997]. Petroleum migration depends on the local hydrodynamic conditions. In addition, the faults in the graben are major conduits for hydrocarbon migration. Factors that control this migration are the synchronous (ongoing) faulting activity (stress relief) and the hydrocarbon generation, and the distribution of the regional seal of the impermeable Sedom Group salts [Tannenbaum, *pers. comm.]*.

In the section studied, discrete pieces of asphalt and oil films appear within or in association with breccia layers (seismites), and also occasionally (in smaller quantities) within regular laminated (interseismic intervals) Lisan sediments. The appearance in association with seismites can be interpreted to represent an asphalt or oil discharge into the lake before a strong earthquake. The water turbulence after the earthquake can cause the floating asphalt or oil to be carried down to the sediment and buried there before oxidation can occur. Dating of asphalt-bearing seismites at different sites (publication in preparation) can reveal if the asphalt events were local or lake-wide and if there were discrete events of asphalt migration/expulsion, i.e. large earthquakes.

More than fifty U-Th dates have been measured on asphalt-bearing breccia layers from Sdom Mountain, Nahal Tamar, and Massada Plain. Results will be presented in a forthcoming paper.

Photograph of asphalt within Lisan brecciated layer, associated with earthquake shaking (Nahal Tamar).

בכל שלושת האתרים - IBS Intra Basin Seismites - מראים זמן חזרה ארוך מכפליים מכל הרעידות באתר בודד. בסביבה הקרסטית, ההשוואה בין מערות שורק-הר-טוב לבין מערת דניה היא היבט נוסף לגישה ה"רב-אתרית". במקרה הזה השוואת גילי הספליאוסייסמיטים איפשרה ניתוח של צימוד (coupling) אפשרי בין העתקים. באופן כללי יש הרבה יותר סייסמיטים בתווך האגמי מאשר בתווך הקארסטי, בהתאמה עם הנחה של סינון הרעידות הקטנות בסביבת ההשקעה של המערה וכן בגלל המרחק מהבקע.

המחקר הרב-אתרי בסביבות שונות מהווה קרש קפיצה להשוואה בין הארכיב הפליאוסייסמי המתוארך ארוך-הטווח מהמערות לבין הארכיב האגמי מתצורת הלשון (בנוסף לתצורת צאלים). יתכן שהשוואה זו תאפשר להפריד רעידות-ענק המשאירות את חותמן לכל אורך אגן ים המלח והרי יהודה וחוצות מגבלות ליתולוגיות. מוצגת בעבודה זו כרונולוגיה רב-אתרית משולבת לתצורת הלשון (ליסן) האגמי-גלציאלי (14-70 ka). כרונולוגיה זו מבוססת על תאריכים חדשים מחמישה אתרים לכל אורך אגם הלשון הקדום. סמנים (markers) סטרטיגרפיים בולטים איפשרו קורלציה סטרטיגרפית בין האתרים הליסניים, ויחד עם תיארוך אורניום-תוריום ושילוב של החתכים המתוארכים מספקים פריצת דרך בכרונולוגיה של אגמי האזור. מחקר זה מצביע כי עבודה רבה עוד לפנינו בפיענוח ההיסטוריה הסייסמית של אגן ים המלח, אך התוצאות מחדדות את ההבטחה הגלומה בהמשך מחקר זה.

גילי הפחמן -14 בסייסמיטים האגמיים ההולוקניים עובדו בתוכנת OxCal v 4.1 ובשימוש במודל השקעה בייסיאני (Bayesian). לגבי החתך בעין פשחה המודל נבדק בשני מצבים: (1) בלי שימוש במידע קודם על רעידות אדמה (מודל לא מעוגן), (2) שימוש בארבע רעידות היסטוריות מסוימות כעוגני גיל (מעוגן). המודל המעוגן סיפק דיאגרמת גיל-גובה עם מעטפת פזור מינימלית, אבל גם המודל הלא מעוגן סיפק תוצאה דומה ומרבית גילי 52 הסייסמיטים מראים קורלציה עם רעידות אדמה היסטוריות. לכן ניתן להשתמש במודל הלא מעוגן כמודל מועדף שמאפשר אנליזה פליאוסייסמית רב אתרית בהפרדה גבוהה.

משקעי מערות (ספליאותמים) שניזוקו ברעידות אדמה נחקרו במערות שורק והר-טוב. תופעות נזק במערות אלה כוללות: נטיפים נפולים, זקיפים נפולים או כרותים, תקרות ממוטטות, סדקים בספליאותמים והתמוטטות של בוץ. כאשר טיפטוף ממשיך במערה לאחר רעידת אדמה, המשקעים הניזוקים (גיל קדם-אירוע) מתכסים בגידול משני. גבישי הקלציט בשני צידי המגע (קדם ובתר) תוארכו בשיטת האורניום-תוריום ונמדדו ב-MC-ICP-MS במכון הגיאולוגי. היסטורית רעידות אדמה בת ארבע מאות אלף שנה נרשמה במערות המחקר ע"י דיגום של יותר מ-55 תופעות נזק. תופעות הנזק שתוארכו במאתיים אלף השנים האחרונות (200 ka) שויכו ל 26 אירועי רעידות אדמה שונים. מתוכם יש 21 אירועים המתוארכים ע"י גיל קדם ובתר או ע"י יותר מתופעת נזק אחת. שבע תקופות של שקט סייסמי ניכרות ללא גילי בתר או קדם. ארועי הרעידה מאז 200 ka מראים זמן חזרה של 6.8 אלפי שנים עם ערך אפיריודיות (aperiodicity מוגדרת כמנה בין סטיית התקן לממוצע) של 0.7, המצביע על התנהגות מחזורית למחצה (או קואזי-מחזורית). אם משתמשים ב-21 אירועים זמן החזרה גדל ל-7.8-8.6 אלף שנה עם ערך אפיריודיות (aperiodicity) של 0.5-0.6. זמן החזרה הינו ארוך בסדר גודל ממה שמוכר מהסייסמיטים האגמיים כנראה בגלל סינון של הרעידות הקטנות שלא נרשמו במערה בשל המרחק הרב מהטרנספורם ובשל המדיום השונה. גילי תופעות הנזק מפוזרים באופן די אקראי במרחב המערה. סוגים שונים של תופעות נזק התרחשו בזמנים מסוימים. שתי הבחנות אילו מחזקות את טענת המקור הסייסמי לתופעות נזק הללו.

השוואת ההיסטוריה הסייסמית ההולוקנית במערות שורק והר-טוב ובמערת דניה (חיפה) מאפשרת ניתוח היחס בין שני סקטורים של טרנספורם ים המלח (DST) וענף שלו – העתק הכרמל (CF), במרחק של 110 ק"מ זה מזה. אירוע סייסמו-טקטוני חזק במיוחד, שמשפיע על האזור כולו יכול להשאיר רישום שווה-גיל (בגדר אי-הודאות של התיארוך) במערות השונות. אירוע מקומי נפרד, מסקטור מסויים, יירשם בנפרד, באחד הארכיבים. תשעה סייסמיטים הולוקניים נמצאו במערת דניה, המייצגים שני אירועים סייסמיים (4.8±0.8 ka, 10.4±0.7 ka). באותה תקופה שישה סייסמיטים תוארכו במערות שורק והר-טוב, המתקבצים לשני אירועים (5 ka, 8.6 ka) . מחקרים פליאוסיסמיים נוספים באזור מראים קורלציה למערות בזמני רעידות אדמה המצביע על צימוד (coupling) בין ה-DST לבין ענף הכרמל. אירוע לפני כחמשת אלפים שנים נרשם היטב ע"י מספר רב של ספליאוסייסמיטים במערת דניה ובמערות שורק-הר-טוב. לעומת זאת, האירוע שלפני האחרון בדניה, ב-10.5 אלפי שנים לפני ההווה, נראה שנרשם רק באזור הצפוני. ייתכן שאירועים קרובים בזמן אינם ניתנים להפרדה בעקבות אי-ודאיות בתיארוך, אך התיארוכים מבליטים תקופות של שקט סייסמי וכן תקופה עם פעילות סייסמית מוגברת. תקופות של שקט סייסמי בין האירועים הגדולים שנרשמו במערות הינן בין 10 ka ל- 5 ka בדניה ובין 5 ka לתקופה ההיסטורית בהרי יהודה.

לסיכום, המחקר הפליאוסייסמי הרב-אתרי מאפשר השוואה בין ארכיבים פליאוסייסמיים שונים מאזורים שונים, סביבות השקעה שונות ותקופות שונות. במחקר הזה השוואת שלושת האתרים האגמיים איפשר אבחנה לגבי הרעידות ההיסטוריות השונות שגרמו לדפורמציה בסדימנטים והשערות לגבי ההעתקים אשר מהווים מקור לרעידות אלו. בנוסף רעידות שנרשמו

תקציר מורחב

המחקר הפליאוסייסמי, חקר רעידות אדמה בעבר, עוסק בתיעוד ותיארוך של רעידות אדמה כפי שנרשמו בארכיבים גיאולוגים. בדרך כלל דרושים סדימנטים שהשקעתם רציפה לאורך מאות, אלפי או עשרות אלפי השנים האחרונות. יעדיו של מחקר פליאוסייסמי הינם, בין היתר, שיחזור תאריכים שבהם התרחשו רעידות אדמה באזור מסוים, חישוב זמני חזרה של רעידות אדמה באזור הנחקר, בדיקת הקורלציה עם שיטות סייסמיות שונות באותו איזור, הערכה של עוצמות מקומיות או מגניטודות אשר גרמו להיוצרות התופעות המתועדות. בחקר האירועים האחרונים המחקרים מתרכזים בשחזור של תנועה על ההעתק (on-fault). בחקר רישום ארוך טווח ובמקרים בהם אין גישה לנתוני העתקה המחקרים מתמקדים בעדויות משניות הרושמות זעזועים במרחק מסוים מההעתק (off-fault) (למשל מעוות בסדימנטים).

ארכיון (archive) ארוך-טווח של פעילות רעידות אדמה, המתקבל ממידע פליאוסיימי, הכרחי להבנת תופעת הרעש ולהערכת סיכונים סייסמיים. רשומה פליאוסייסמית אמינה דורשת קביעת כרונולוגיה מהימנה וברזולוציה גבוהה, והבנה בהתנהגות של סממני רעידות האדמה (סייסמיטים). מחקרים פליאוסייסמיים באתרים רבים ומגוונים יכולים להניב ארכיונים ארוכי-טווח, לפצות על פערי זמן השקעה (היאטוסים) באתרים בודדים, להצביע על תגובות אתר ולזהות הבדלים בהקלטת אירועים סייסמיים במדיה שונים.

עבודת הדוקטורט התמקדה במחקר פליאוסייסמי של סדימנטים אגמיים ששקעו באגמי ים המלח ובמשקעי מערות בהרי יהודה. בארכיונים גיאולוגיים טבעיים אלה נרשמו עדויות לרעידות אדמה על בקע ים המלח בתקופת הרביעון המאוחר. האזור הזה נמצא בחזית המחקר הפליאוסייסמי והעבודה מוסיפה נדבכים בפיתוח המתודות של דיסציפלינה זו.

במסגרת המחקר נלמדו תצורת צאלים ההולוקנית ותצורת ליסן הגלציאלית שהניבו ארכיונים של שכבות רסק ומעוות ב-70 אלף השנים האחרונות, והראו תבניות של חזרתיות. מוצג כאן ארכיב חדש רב-אתרי מים המלח ההולוקני (2500 שנים אחרונות) אשר מבוסס על שני מודלים כרונולוגים של גיל-גובה בשני אתרים בחופי ים המלח המודרניים. שני האתרים שנחקרו בעבודה זו הינם: שמורת עין פשחה (עינות צוקים) בצפון האגן הצפוני בסמוך להעתק רוחב תת-ימי, ונחל צאלים בדרום האגן הצפוני של ים המלח. מודלים של גיל-גובה נקבעו לכל אתר בעזרת תיארוך פחמן-14 ב-AMS של חומרים אורגניים קצרי חיים. נעשתה השוואה בין גילי הסייסמיטים באתרים אלה ובין כרונולוגיית רעידות האדמה ההיסטוריות שנמצא להן התאמה בגלעין שנקדח בחוף מרחצאות עין גדי. המחשוף בעין פשחה מראה מספר רב ביותר של סייסמיטים (52) בתקופה הנחקרת, כאשר בצאלים ובעין גדי מופיעים 15 ו-36 סייסמיטים , בהתאמה. הסייסמיטים אינם מראים תלות בתנאים הסדימנטרים –לימנולוגיים באתרים השונים. תקופות של שקט סייסמי קיימות בכל שלושת האתרים מהמאה השנייה עד המאה הרביעית לספירה, ומ-500 עד 150 לפנה"ס בצאלים ועין גדי. בתקופות אלה כמעט ולא נרשמו אירועים היסטוריים, מה שתומך בתוצאות המחקר. מספר אירועי רעידות אדמה נרשמו בשלושת האתרים והם נקראים כאן סייסמיטים כלל אגניים - IBS. ארועים אלה התרחשו בשנים: 33 ,419 ,551 ,749 ,1202/1212 ,1293 ,1927 לספירה, ו-31 ואמצע המאה השניה לפנה"ס. זמן חזרה של ה-IBS הינו ~200 שנה (במהלך התקופה מהמאה השניה לפנ"ס עד המאה ה-14 לספירה), לעומת פחות ממאה שנים לכל הרעידות בעין גדי או עין פשחה. בדיאגרמה של מרחק מוקד לעומת מגניטודה, הרעידות ההיסטוריות שמתאימות ל-IBS נמצאות בשדה של עוצמה מקומית (Intensity) גבוהה. ה-IBS החזקים והרחוקים דורשים עוצמות מקומיות נמוכות יותר כדי להרשם בסדימנטים.

משרד האנרגיה והמים
המכון הגיאולוגי

פליאוסייסמולוגיה מרחבית ברבעון המאוחר באזור טרנספורם ים המלח: עדויות ממשקעי מערות ומשקעי אגם

אליסה קייגן

עבודה זו הוגשה כחיבור לקבלת תואר "דוקטור לפילוסופיה" לסינאט האוניברסיטה העברית, ירושלים

העבודה נעשתה בהדרכתם של:
פרופ' אמוץ עגנון, המכון למדעי כדור הארץ, האוניברסיטה העברית, ירושלים
פרופ' מרדכי שטיין, המכון הגיאולוגי הישראלי, ירושלים
דר' מרים בר-מטיוס, המכון הגיאולוגי הישראלי, ירושלים

דוח מס' GSI/17/2012 ירושלים, כסלו תשע"ג, נובמבר 2012